A MULTI-DIMENSIONAL TWO-PHASE FLOW MODELING FRAMEWORK FOR SEDIMENT TRANSPORT APPLICATIONS

by

Zhen Cheng

A dissertation submitted to the Faculty of the University of Delaware in partial fulfillment of the requirements for the degree of Doctor of Philosophy in Civil Engineering

Summer 2016

© 2016 Zhen Cheng
All Rights Reserved

ProQuest Number: 10191152

All rights reserved

INFORMATION TO ALL USERS
The quality of this reproduction is dependent upon the quality of the copy submitted.

In the unlikely event that the author did not send a complete manuscript
and there are missing pages, these will be noted. Also, if material had to be removed,
a note will indicate the deletion.

ProQuest 10191152

Published by ProQuest LLC (2016). Copyright of the Dissertation is held by the Author.

All rights reserved.
This work is protected against unauthorized copying under Title 17, United States Code
Microform Edition © ProQuest LLC.

ProQuest LLC.
789 East Eisenhower Parkway
P.O. Box 1346
Ann Arbor, MI 48106 - 1346

A MULTI-DIMENSIONAL TWO-PHASE FLOW MODELING FRAMEWORK FOR SEDIMENT TRANSPORT APPLICATIONS

by

Zhen Cheng

Approved: _____

Harry W. Shenton, Ph.D.
Chair of the Department of Civil and Environmental Engineering

Approved: _____

Babatunde A. Ogunnaike, Ph.D.
Dean of the College of Engineering

Approved: _____

Ann L. Ardis, Ph.D.
Senior Vice Provost for Graduate and Professional Education

I certify that I have read this dissertation and that in my opinion it meets the academic and professional standard required by the University as a dissertation for the degree of Doctor of Philosophy.

Signed: _____

Tian-Jian Hsu, Ph.D.
Professor in charge of dissertation

I certify that I have read this dissertation and that in my opinion it meets the academic and professional standard required by the University as a dissertation for the degree of Doctor of Philosophy.

Signed: _____

Jack A. Puleo, Ph.D.
Member of dissertation committee

I certify that I have read this dissertation and that in my opinion it meets the academic and professional standard required by the University as a dissertation for the degree of Doctor of Philosophy.

Signed: _____

Lian-Ping Wang, Ph.D.
Member of dissertation committee

I certify that I have read this dissertation and that in my opinion it meets the academic and professional standard required by the University as a dissertation for the degree of Doctor of Philosophy.

Signed: _____

Joseph Calantoni, Ph.D.
Member of dissertation committee

I certify that I have read this dissertation and that in my opinion it meets the academic and professional standard required by the University as a dissertation for the degree of Doctor of Philosophy.

Signed: _____

Julien Chauchat, Ph.D.
Member of dissertation committee

ACKNOWLEDGEMENTS

I would like to thank my advisor Prof. Tian-Jian (Tom) Hsu for patiently leading me to a wonderful field of scientific research, and shedding lights of sediment transport physics upon me. I'm grateful for invaluable suggestions, discussions, and all the opportunities that he has provided me. My sincere acknowledgement also goes to Dr. Julien Chauchat, whom I had a great pleasure working with and learning from during my last year in the University of Delaware. I also wish to thank Dr. Joseph Calantoni, Dr. Jack Puleo and Dr. Lian-Ping Wang for invaluable advices along the path of my research.

Numerous suggestions and helps from Dr. Fengyan Shi, Dr. Xiao Yu, Dr. Jialin Chen and many other lab mates must also be appreciated. They are great friends and colleagues, and I treasure the great memories in the Center for Applied Coastal Research (CACR) and laughters around the lunch tables of the main street. Without them, my 6-year PhD life cannot be so fun and enjoyable.

Major financial supports provided by Office of Naval Research (Littoral Geosciences and Optics; N00014-14-1-0586) and National Science Foundation (OCE-1130217; OCE-1537231; CMMI-1135026; OCE-1356855) and the high performance computing resources from the HPC Center of University of Delaware and XSEDE are also acknowledged.

Finally, I would like to thank my love Qi (Betty), my parents and my sister, who are always in support of me, and willing to share my happiness as well as sorrows.

TABLE OF CONTENTS

LIST OF TABLES . . . . . **x**
LIST OF FIGURES . . . . . **xi**
ABSTRACT . . . . . **xxii**

Chapter

1 INTRODUCTION **1**

1.1 General 1
1.2 Categories of Sediment Transport 3
1.3 Sediment Transport Methodology 8
1.4 Motivations 13

1.4.1 Fine sediment transport 13
1.4.2 Sand transport 15

1.5 Scope of This Thesis 19

2 ON THE TRANSPORT MODES OF FINE SEDIMENT IN THE WAVE BOUNDARY LAYER DUE TO RESUSPENSION/DEPOSITION — A TURBULENCE-RESOLVING NUMERICAL INVESTIGATION **21**

2.1 Introduction 22
2.2 Model Formulation 25

2.2.1 Governing equations 25
2.2.2 Model domain and boundary conditions 27
2.2.3 Numerical method 29

2.3 Model Results 30

2.3.1 Simulation setup 32

2.3.2 Transport modes under different critical shear stress of erosion 34
2.3.3 Transport modes under different settling velocities 46

2.4 Discussion 50
2.5 Conclusion 56
2.6 Acknowledgments 57

3 A NUMERICAL INVESTIGATION OF FINE SEDIMENT RESUSPENSION IN THE WAVE BOUNDARY LAYER – UNCERTAINTIES IN PARTICLE INERTIA AND HINDERED SETTLING 58

3.1 Introduction 59
3.2 Mathematical Formulations 63

3.2.1 Governing equation 63
3.2.2 Numerical implementation 66
3.2.3 Simulation setup 68

3.3 Effect of Particle Inertia 71

3.3.1 Model results 72

3.4 Effect of Hindered Settling 75

3.4.1 Model results 78

3.5 Discussion 88

3.5.1 Turbulence modulation due to increasing Stokes number . . . 88
3.5.2 Gelling ignition 92

3.6 Conclusion 96
3.7 Acknowledgments 98

4 EULERIAN TWO-PHASE FLOW GOVERNING EQUATIONS 99

4.1 Boltzmann Transport Equation 99
4.2 Two-phase Governing Equations 102

4.2.1 Fluid phase governing equations 102
4.2.2 Sediment phase governing equations 104
4.2.3 Particle stress model 105

4.2.4 Fluid-sediment momentum transfer . . . 109

4.3 Summary . . . 110

5 SEDFOAM: A MULTI-DIMENSIONAL EULERIAN TWO-PHASE MODEL FOR SEDIMENT TRANSPORT AND ITS APPLICATION TO MOMENTARY BED FAILURE . . . 111

5.1 Introduction . . . 111
5.2 Model Formulation . . . 114

5.2.1 Governing equations . . . 115
5.2.2 Closure models . . . 116

5.2.2.1 Inter-phase momentum transfer . . . 116
5.2.2.2 Fluid turbulence model . . . 116
5.2.2.3 Particle stress closure . . . 119

5.2.3 Numerical implementation . . . 120

5.3 Model Validation . . . 121

5.3.1 Steady sheet flow . . . 121
5.3.2 Oscillatory sheet flow . . . 125
5.3.3 Scour downstream of an apron . . . 129

5.4 Momentary Bed Failure in Sheet Flow . . . 135

5.4.1 1DV and 2DV sheet flow simulations . . . 137
5.4.2 Combined sheet flow and plug flow . . . 139
5.4.3 Discussion . . . 144

5.5 Conclusion . . . 147
5.6 Acknowledgements . . . 148

6 A LARGE EDDY SIMULATION TWO-PHASE MODEL FOR SEDIMENT TRANSPORT . . . 150

6.1 Introduction . . . 151
6.2 Mathematical Formulations . . . 153

6.2.1 Filtered two-phase Eulerian equations . . . 153
6.2.2 Subgrid drag model . . . 155

6.2.3 Subgrid turbulence closure . . . 158
6.2.4 Closures on particle stresses . . . 160

6.3 Model Validation—Steady Sheet Flow . . . 164

6.3.1 Computational domain and its discretization . . . 165
6.3.2 Mean quantities . . . 167
6.3.3 Turbulent kinetic energy budget . . . 173
6.3.4 Turbulence-sediment interactions . . . 176

6.4 Applications to Oscillatory Sheet Flow . . . 181

6.4.1 Model setup . . . 182
6.4.2 Medium sand . . . 183
6.4.3 Fine sand burst events . . . 186

6.5 Conclusion . . . 186
6.6 Acknowledgements . . . 189

7 FUTURE WORKS, DISCUSSION AND RECOMMENDATIONS 190

7.1 Grain Size Distribution . . . 190
7.2 Effect of Particle Shape . . . 194
7.3 Effect of Progressive Surface Waves . . . 198
7.4 Momentary Bed Failure/Plug Flow . . . 199
7.5 Experimental/DNS Data for Turbulence-resolving Model Assessment 200

BIBLIOGRAPHY . . . 202

Appendix

A IMPLEMENTATION OF TOP BOUNDARY FOR FINE SEDIMENT . . . 218
B INITIAL CONDITIONS FOR EULERIAN TWO-PHASE FLOW 220
C SOLUTION FOR SEDIMENT CONCENTRATION IN THE BED 222
D COPYRIGHT PERMISSION LETTERS . . . 225

D.1 Copyright 1 . . . 225
D.2 Copyright 2 . . . 225
D.3 Copyright 3 . . . 225
D.4 Copyright 4 . . . 226

LIST OF TABLES

1.1 Summary of Eulerian two-phase models for sediment transport applications 12

2.1 List of simulations presented in the study of fine sediment transport modes. 33

3.1 List of simulations presented in the study of particle inertia and hindered settling 70

5.1 List of coefficients in fluid turbulence closure (k-ϵ). 119

5.2 A summary of the fine sand (grain diameter $d = 0.13$ mm, specific gravity $s = 2.65$) experiments reported in Sumer et al. (1996) used here for model calibration. 122

5.3 Flow conditions in the study of momentary bed failure 137

6.1 The steady sheet flow experiment conditions in Revil-Baudard et al. (2015) 164

6.2 Numerical parameters for steady sheet flow experiments in Revil-Baudard et al. (2015) 165

6.3 Numerical parameters for oscillatory sheet flow experiments in O'Donoghue & Wright (2004) 182

7.1 List of simulations presented in the study of particle size distribution. 193

7.2 List of simulations presented in the study of particle shape. 197

LIST OF FIGURES

1.1 Schematic plots on the (a) modern sediment transport regimes and (b) bed-load and suspended load transport layers (Yu et al. 2012) (With permission from the Elsevier. This material may be downloaded for personal use only, and any other use requires prior permission of Elsevier). 6

1.2 A summary (Yu et al. 2014) on the existence of four flow regimes (I IV) reported by 3D turbulence-resolving simulations of Ozdemir et al. (2010) due to increasing sediment availability (or bulk Richardson number) under the same wave intensity (Stokes Reynolds number Re_Δ =1000) and settling velocity (≈0.5 mm/s). The second column shows snapshots of iso-surface of sediment concentration during flow peak for regime I, II and IV and during flow reversal for regime III. The third column shows averaged sediment concentration profile where the vertical axis is normalized by Stokes length scale and the horizontal axis is normalized by volume-averaged concentration, which is fixed in each simulation (With permission from the American Society of Civil Engineers. This material may be downloaded for personal use only, and any other use requires prior permission of ASCE). 16

2.1 Sketch of computation domain and definition of coordinate system. 28

2.2 (a) Time series of the nondimensional free-stream velocity; (b) Comparison of the magnitude of ensemble-averaged bottom shear stress for clear fluid condition (Case 0, solid curve) and the critical shear stress of erosion for Case 1 (curve with circle symbols), Case 2 (dashed curve), Case 3 (curve with cross symbols); Case 4 (curve with plus symbols). The logarithmic scale is used in y-axis for better illustration; (c) Time series of the domain-averaged sediment concentration for Case 1 (curve with circle symbols), Case 2 (dashed curve), Case 3 (curve with cross symbols); Case 4 (curve with plus symbols); (d) comparison of the wave- and domain-averaged sediment concentration for different critical shear stress of erosion. 35

2.3 Turbulent coherent structures for (a) Case 1, (d) Case 2 and (g) Case 4 visualized using the swirling strength (λ_{ci}) at flow peak ($\omega t = 0$). The contour level used here is 5% of the maximum λ_{ci} value in Case 4. (b), (d) and (h) show the corresponding iso-surface of near-bed sediment concentration at flow peak. The contour level is chosen to be the average concentration at $z = 2.5$ with $\phi = 0.005$, 8.2×10^{-3}, 9.2×10^{-5} for Case 1, Case 2 and Case 4, respectively. (c), (f) , (i) show the corresponding iso-surface of sediment concentration in the middle of the domain at flow peak. The contour level is chosen to be the average concentration at $z = 20$ with $\phi = 2.2 \times 10^{-5}$, $\phi = 6.8 \times 10^{-4}$, 7.6×10^{-5} for Case 1, Case 2 and Case 4, respectively. 37

2.4 Ensemble-averaged profiles of (a) sediment concentration, (b) non-dimensional streamwise velocity and (c) non-dimensional turbulence intensity during flow peak ($\omega t = 0$) for Case 1 (dashed curve), Case 2 (curve with triangle symbol), Case 4 (solid curve); The corresponding profiles during flow reversal ($\omega t = 3\pi/2$) are shown in (d), (e) and (f). In (a) and (d), the top x-axis is the concentration scale for Case 4, and the bottom axis is the concentration scale for Case 1 and Case 2. 39

2.5 (a) Time series of the nondimensional free stream velocity, U; (b) Time series of the ensemble-averaged bottom shear stress $|\langle\widetilde{\tau}_b\rangle|$ for Case 0 (circle symbol), Case 1 (dashed curve), Case 2 (curve with triangle symbol), Case 4 (solid curves). 41

2.6 (a) Time series of the domain averaged sediment concentration Φ (blue solid curve) and the ensemble-averaged bottom shear stress $|\langle\widetilde{\tau}_b\rangle|$ (red solid curve) for Case 1. The sampled instant shown (b),(c),(d) are denoted as blue dash lines. (b1-b4) present the ensemble-averaged profiles of streamwise velocity, sediment concentration, turbulence intensity, and iso-surface of concentration (=4Φ) at $t = 2T$. Similar plots are presented here at instant (c) $t = 3T$ and instant (d) $t = 14T$. In (c1), the laminar solution of streamwise velocity is shown as open circles. In (b3), (c3) and (d3), logarithmic scale is used in x-axis for a better illustration. 43

2.7 Flux Richardson number profiles of Case 1 at two different instants, (a) $t = 2T$ (see b in Figure 2.6); (b) $t = 3T$ (see c in Figure 2.6). The dash-doted lines denote the critical Richardson number of 0.25. . . 45

2.8 Ensemble-averaged profiles of (a) sediment concentration, (b) non-dimensional streamwise velocity and (c) non-dimensional turbulence intensity during flow peak ($\omega t = 0$) for Case 2 (solid curves), Case 5(dashed curves) and Case 6 (dash-dotted curves). Panels (d), (e), and (f) are the corresponding profiles during flow reversal ($\omega t = \pi/2$). 47

2.9 Wave- and domain-averaged sediment concentration $\overline{\Phi}_{eq}$ (or sediment availability) for cases of different settling velocity with a fixed $\widetilde{\tau}_c = 0.02$ Pa. Case 5 is shown in asterisk symbol and Case 2, 6, 7 and 8 are shown in circle symbol. The best-fit line (dashed) is $KW_s^{-1.4}$, where $K = 9.375 \times 10^{-8}$ is the proportional constant. 48

2.10 Schematic map of flow regime in terms of the bulk Richardson number Ri and the settling velocity W_s at Re_Δ=1000. The open symbols ($\diamondsuit$: regime I; $\triangle$: regime II; $\circ$: regime III; $\square$: regime IV) are earlier direct numerical simulations presented in (Ozdemir et al. 2011). Simulation results in the present paper (see Table 2.1) are consistent with (Ozdemir et al. 2011) for regime I (solid $\diamondsuit$) and regime II (solid $\triangle$). The dashed curves are the borders between the regimes, specifically the thick dashed curve denotes the onset of laminarization. 52

2.11 Peak bottom shear stress plotted against the Stokes Reynolds number Re_Δ for clear fluid discussed in (Ozdemir et al. 2014). DNS results are shown in the curve with triangle symbols, and analytical laminar solutions are shown in the curve with circle symbols. 53

2.12 Schematic map of transport mode in terms of the critical shear stress of erosion $\widetilde{\tau}_c$ (Pa) and the settling velocity $\widetilde{W}_s$ (mm/s) at Re_Δ=1000 obtained in the present simulations (see Table 2.1) for transport mode I ($\diamondsuit$), transport mode II ($\triangle$) and transport mode III ($\square$). The dashed curves represent the border between the transport modes described by equation (2.20). 54

3.1 Simulation results of turbulence dissipation rate at the flow peak for Case 0. 67

3.2 Comparison of the ensemble-averaged profiles of (a) sediment concentration, (b) streamwise velocity and (c) turbulence intensity during flow peak ($\omega t = 0$) for Case 0 (circle symbols), Case A1 (solid curve); The relative difference (%) of these flow quantities are shown in (d), (e) and (f), respectively; The levels of zero error are denoted as dashed lines in (d), (e) and (f). 72

3.3 (a) Time series of free-stream velocity $U(t)$. Three representative instants (b,c,d) are shown with open circles. The relative difference (%, solid curve) of effective settling velocities between Case 0 and Case A1 at these three representative instants are shown in (b) flow peak ($\omega t = 0$), (c) $\omega t = \pi/3$ and (d) $\omega t = 2\pi/3$; The levels of zero error are denoted as dashed lines in (b), (c) and (d). 74

3.4 Comparison of the ensemble-averaged profiles of (a) sediment concentration, (b) streamwise velocity and (c) turbulence intensity during flow the peak ($\omega t = 0$) for Case 0 (circle symbol), Case B1 (solid curve); The relative difference (%) of these flow quantities are shown in (d), (e) and (f), respectively; The levels of zero error are denoted as dashed lines in (d), (e) and (f). 77

3.5 Ensemble-averaged profiles of (a) sediment concentration, (b) streamwise velocity and (c) turbulent intensity during flow peak ($\omega t = 0$) for Case B1 (solid curve), Case B2 (dashed curve). (d), (e) and (f) are the corresponding profiles during flow reversal. 79

3.6 Turbulent coherent structures at flow peak ($\omega t = 0$) for (a) Case0, (c) Case B1, and (e) Case B2. The turbulent coherent structures are visualized using the swirling strength (λ_{ci}), and the contour level used here is 4% of the maximum λ_{ci} value in Case 0. The iso-surface of concentration ϕ field corresponding to (b) Case 0, (d) Case B1 and (f) Case B2 are also shown, and their contour levels are 8.2×10^{-3}, 9.8×10^{-3} and 0.015, respectively. 81

3.7 Normalized effective settling velocity profile for Case 0 (blue dashed curve), Case B1 (red solid curve), Case B2 (blue solid curve), Case B3 (black solid curve) and Case B4 (green solid curve) during flow peak ($t = 15T$). 82

3.8 Temporal evolution of (a) domain-averaged sediment concentration Φ and (b) ensemble-averaged sediment concentration at the bottom $\langle \phi_b \rangle$ for Case 0 (blue dashed curve), Case B1 (red solid curve), Case B2 (blue solid curve), Case B3 (black solid curve) and Case B4 (green solid curve). 83

3.9 Plane-averaged (a) sediment concentration profiles and (b) turbulent intensity profiles for Case B2 at five different instants: $t = 11T$ (blue solid curve), $t = 13T$ (dashed curve), $t = 15T$ (red solid curve), $t = 17T$ (dash-dot curve), $t = 19T$ (curve with circle symbols). The corresponding plane-averaged profiles for Case B4 are shown in (c) and (d) at five different instants: $t = 6T$ (blue solid curve), $t = 9T$ (dashed curve), $t = 12T$ (red solid curve), $t = 15T$ (dash-dot curve), $t = 18T$ (curve with circle symbols). 87

3.10 Comparisons of (a) sediment concentration, (b) streamwise velocity and (c) turbulence intensity for Case A1 (solid curve), Case A2 (dashed curve) and Case A3 (dash-dot curve). 89

3.11 Turbulent coherent structures at flow peak ($t = 10T$) for (a) Case 0 and (b) Case A3. The turbulent coherent structures are visualized using the second invariant Q, and the contour level used here is -0.04 (non-dimensional). The plane cuts of the concentration ϕ field at $z = 1.5$ are also shown. The sub-panels show enlarged views for better visualization of the preferential concentration effect. 91

3.12 Wave-averaged depositional flux $\overline{\widetilde{D}}$ as a function of wave-averaged bottom concentration $\overline{\phi_b}$ for Case B1 (red solid curve), Case B2 (blue solid curve), Case B3 (black solid curve) and Case B4 (green solid curve). The dashed curve $\overline{\widetilde{E}}_l$ is the wave-averaged erosion flux at the bottom calculated using laminar solution of bottom shear stress at $Re_\Delta = 1000$ (Cheng et al. 2015a). The dimensional value for the critical shear stress of erosion is $\widetilde{\tau}_c = 0.02$ Pa for all the cases. . . . 93

3.13 (a) A predictor of gelling ignition as a function of dimensional critical shear stress $\widetilde{\tau}_c$ and gelling concentration ϕ_{ref} at $Re_\Delta = 1000$. The black filled circles denote Cases B1-B4 in this study; (b) A predictor of gelling ignition as a function of $\widetilde{\tau}_c$ and ϕ_{ref} at $Re_\Delta = 500$ (solid curve); $Re_\Delta = 600$ (dashed curve); $Re_\Delta = 700$ (curve with circle symbols); $Re_\Delta = 800$ (curve with triangle symbols); $Re_\Delta = 1000$ (dash-dot curve). All the results shown here are for $\widetilde{W}_s$=0.5 mm/s and $\widetilde{m}_e = 3.05 \times 10^{-7}$ m/s. 97

5.1 Sketch of the domain setup for the present Eulerian two-phase flow model. 123

5.2 (a) Comparison of concentration profiles between numerical results (solid curve) and experiment data (circle symbols); (b) fluid velocity profile; (c) fluid turbulent kinetic energy (solid curve) and granular temperature(dashed curve) and (d) fluid shear stress (solid curve), sediment shear stress (dashed curve) and total shear stress (dash-dot curve) for steady sheet flow of at $\theta = 1.10$ (Sumer et al. 1996). The corresponding results for $\theta = 1.68$ ($\theta = 2.2$) are shown in (e), (f), (g) and (h) ((i), (j), (k) and (l)), respectively. The bed location $z = 0$ is defined as initial bed level. 124

5.3 (a) Time series of free-stream velocity, in which four representative instants are indicated: (b) $t = 0$; (c) $t = 1.6$ s; (d) $t = 3.2$ s and (e) $t = 5.36$ s; The corresponding comparison of sediment concentration profiles between the numerical results (solid curve) and measured data (symbols) from O'Donoghue & Wright (2004) are presented in panel (b), (c), (d) and (e), respectively. 126

5.4 (a) Time series of free stream velocity driven by Stokes second-order wave motion (MA7515, O'Donoghue & Wright (2004)); The comparisons of concentration time series for sheet flow of medium sand at four different vertical locations are shown in (b) $z = -0.95$ mm; (c) $z = -0.35$ mm; (d) $z = -0.15$ mm and (e) $z = 0.85$ mm. 127

5.5 (a) Time series of free-stream velocity, and (b) Comparison of erosion depth between numerical results (solid curve) and experiment data (symbols) of MA7515 in O'Donoghue & Wright (2004). 129

5.6 (a) Time series of free-stream velocity for MA7515 in O'Donoghue & Wright (2004), in which four representative instants are indicated: (b) $t = 0$; (c) $t = 1.6$ s; (d) $t = 3.2$ s and (e) $t = 5.36$ s; The corresponding comparison of fluid velocity profiles between the numerical results (solid curve) and measured data (symbols) at these four instants are shown in panel (b), (c), (d) and (e). 130

5.7 Sketch of scour downstream of an apron. 131

5.8 Velocity profiles at different locations downstream of the apron at (a) $t = 5$ s, (b) $t = 15$ s, and (c) $t = 45$ s; The background is the concentration contour. 133

5.9 (a) Evolution of maximum scour depth for model results (symbols) and the empirical formula of Eq. (5.18) with $T_s = 1100$ s and $n_s = 0.54$ (solid line); (b) Evolution of upstream scour angle between model results (dashed curve) and Eq. (5.19) with $T_{\alpha s} = 15.2$ s and $\alpha_{s0} = -14.55°$ (solid curve). 134

5.10 (a) Time series of free-stream velocity, in which four representative instants are indicated: (b) $t = 0$; (c) $t = 1.25$ s; (d) $t = 1.88$ s and (e) $t = 2.5$ s; The corresponding comparison of sediment concentration profiles between the numerical results (solid curve) and measured data (symbols) at these four instants for Case 1 (see Table 5.3) are shown in panel (b), (c), (d) and (e). 139

5.11 Snapshot of concentration field at (a) flow peak ($t = 0.45$ s) and (b) flow reversal ($t = 0.9$ s) for Case 3 (see Table 5.3); white arrows denotes the plane-averaged velocity vectors. 140

5.12 Sequence of four images (top to bottom) highlighting the development of instabilities and billows under combined sheet flow and plug flow conditions in a small oscillatory flow tunnel during half a wave cycle (Holway et al. 2012). The streamwise length (spanwise width) of the field of view in each snapshot is 128 cm (25 cm). . . . 141

5.13 Comparison of (a) sediment concentration profiles, (b) fluid velocity profiles and (c) sediment flux profiles of 1DV (dashed curves) and 2DV (solid curves) for Case 3 at flow peak. 142

5.14 Time series of free-stream velocity (panel (a)) and numerical results of the erosion depth (solid curves) for (b) Case 1 and (c) Case 3; In panel (b), the circle symbols represent measured data from O'Donoghue & Wright (2004). In panel (c), the dash-dot curve is the 1DV result. 143

5.15 The normalized half-wave-averaged transport rate in terms of Shields parameter θ. $\times$: 2D pure sheet flow of $d = 0.28$ mm; $\circ$: 2D sheet flow with momentary bed failure of $d = 0.28$ mm; $*$: 2D pure sheet flow of $d = 0.2$ mm; $\square$: 2D sheet flow with momentary bed failure of $d = 0.2$ mm; The solid curve shows the best-fit power law for pure sheet flow predicted by the present model ($M = 5.78$, $N = 1.65$) where $\theta_c = 0.05$ is the critical shields parameter. The dashed curve shows the best-fit power law for the combined sheet flow and plug flow condition ($M = 46.55$, $N = 1.81$). 145

5.16 Schematic map of sheet flow with momentary bed failure in terms of Sleath parameter S and Shields parameter θ. $\times$: sheet flows of $d = 0.28$ mm; $\circ$: momentary bed failure of 0.28 mm; $\triangle$: sheet flows of $d = 0.2$ mm; $\square$: momentary bed failure of 0.2 mm; dashed curve: proposed criteria for the occurrence of momentary bed failure (Eq. (5.26)). 147

6.1 Illustration of 3D domain for turbulence-resolving Eulerian two-phase flow model 154

6.2 Normalized autocorrelation of streamwise (solid curve), spanwise (dash-dot curve) and vertical (dashed curve) velocity components in streamwise (panel (a)) and spanwise (panel (b)) directions 166

6.3 Energy spectrum of streamwise (solid curve), spanwise (dash-dot curve) and vertical (dashed curve) velocity fluctuation components in streamwise (panel (a)) and spanwise (panel (b)) directions; In both panel (a) and (b), the thick curve denotes a slope of $-5/3$ 167

6.4 The comparison of numerical results (curves) and experiment results (symbols) of (a) Streamwise velocity (fluid velocity: solid curve, and particle velocity: dashed curve), (b) Sediment concentration, (c) Root-mean-square of velocity fluctuations and (d) Reynolds shear stress. In panel (c), cross and circle symbols denote the experiment results of the vertical and streamwise components of velocity fluctuation, while dashed curve and solid curves denote the numerical result of the vertical and streamwise components of velocity fluctuation 169

6.5 The model result (red-solid curve) of streamwise velocity profile in semi-logarithmic scale, the blue-dashed curve shows the fit with von Karman constant $\kappa = 0.25$, and the black-dashed-dot curve shows the slope of $\kappa = 0.41$ as in clear fluid. 170

6.6 The comparison of the mixing lengths from numerical result (solid curve) and experimental results (symbols). The dashed curve is the linear fit of the mixing length for numerical result with $\kappa = 0.25$, and the dashed-dot curve shows the linear fit of measured data with $\kappa = 0.23$. 171

6.7 The vertical structure (panel a) of turbulent eddy viscosity (mode result: solid curve, experiment data: circle symbols) and sediment diffusivity (mode result: dashed curve, experiment data: cross symbols); The corresponding vertical structure of Schmidt number ($Sc = \sigma_m/\sigma_p$) is plotted in panel b, model result: dashed curve; experiment data: circle symbols, and the dash-dot curve shows the mean level of Schmidt number. 172

6.8 The panel (a) shows the TKE budget for fluid phase. The turbulent production (solid curve), viscous dissipation (dashed curve), drag-induced dissipation (dash-dot), total transport (cross symbols); The comparison of production (numerical result: solid curve; experimental data: symbols) and energy dissipation (resolved dissipation: dashed curve; modeled dissipation: dash-dot curve) are shown in panel (b). 174

6.9 The comparison of density stratification effect (flux Richardson number: dashed curve; gradient Richardson number: dash-dot curve) and turbulence interactions (solid curve) due to drag. The gradient Richardson number obtained from the experiment is denoted as cross symbols. 177

6.10 Diagram illustrating the quadrant analysis of turbulent motions: Q_1, outward interactions ($u^{f'} > 0, w^{f'} > 0$); Q_2, ejection ($u^{f'} < 0, w^{f'} > 0$); Q_3, inward interactions ($u^{f'} < 0, w^{f'} < 0$); Q_4, sweep ($u^{f'} > 0, w^{f'} < 0$) 178

6.11 Panel (a) is the comparison of ratio $(\overline{u^{f'}w^{f'}})_i/\overline{u^{f'}w^{f'}}$ due to upward interactions ($i = 1$, numerical: thin solid curve; experiment: cross), ejection ($i = 2$, numerical: dashed curve; experiment: circles), downward interaction ($i = 3$, numerical: dash-dot curve; experiment: squares) and sweep events ($i = 4$, numerical: thick solid curve; experiment: triangles); The ratio of ejection/sweep contribution over interactions is shown in panel (b) and the ratio between ejection and sweep events is shown in panel (c), in both panel (b) and (c), the circle symbols denotes the measured data 179

6.12 The panel (a) shows the sediment vertical turbulent flux ($\overline{w^{s\prime}\phi'}$), which is positive in upward direction. Panel (b) shows the the contribution to the total vertical sediment flux ($(\overline{w^s\phi})_i$) due to upward interactions (1, '+'), ejection (2, solid curve), downward interaction (3, circles) and sweep events (4, dashed curve). 180

6.13 A 2D contour of sediment concentration field in terms of vertical elevation $(z - z_b)/d$ and time t (s). The sediment concentration is plotted in logarithmic scale, and the contours of ejection (dashed contour) and sweep (solid contours) events are also plotted. The contour level for the ejection and sweep are both chosen to be $-\overline{u^{f\prime} w^{f\prime}} = 0.001$. 181

6.14 Panel (a) shows the free-stream velocity time series, and the comparison of sediment concentration profiles between turbulence-averaged model(dashed curve), turbulence-resolving model (solid curve) at four different instant are shown in (b) $t = T/12$; (c) $t = T/6$; (d) $t = T/4$; (e) $t = T/3$. 184

6.15 The comparison of time series of sediment concentration against measured data (O'Donoghue & Wright 2004, symbols), turbulence-averaged model results (dashed curve), turbulence-resolving model (solid curve) at (a) $z = -1.25$ mm (pick-up layer); (b) $z = -0.05$ mm (near initial bed); (c) $z = 0.85$ mm (suspension layer). 185

6.16 Iso-surfaces of concentration at $\phi = 0.005$ (brown) and $\phi = 0.3$ (dark gray) during flow peak (panel (a)) and flow reversal (panel (b)) for medium sand (Case M512, see table 6.3). Similar iso-surfaces of sediment concentration for fine sand (Case F512, see table 6.3) during flow peak and flow reversal are also plotted in panel (c) and (d), respectively. 187

7.1 Illustration of the armoring effect in Case A2, where (a) is the initial bed, and (b) is the bed at flow peak when the flow is quasi-steady state. The particles are colored with the respective diameter, and the vectors denote the velocity. 193

7.2 (a) Time series of the free-stream velocity. (b) Comparison of the time series of sediment transport rate for Case 0 (red solid curve), Case A1 (blue dashed curve), Case A2 (black dash-dot curve), Case A3 (blue solid curve) and Case A4 (green solid curve). 195

7.3 Illustration of the composite particle; (a) 3D view of the composite particle, the plane coincide with the intersection plane of the two partial spheres; (b) plan view of the composite particle, where $z = 0$ is located at the intersection plane of the two partial spheres, and z-axis coincide with the center of the two partial spheres (O_1, O_2, respectively), and it intersects with the intersection plane at the origin of the coordinate O. R_1, R_2 are the radius of the two partial spheres, respectively, and the angles γ_1 and γ_2 are measured from the positive z-axis about the center of each respective partial spheres. CM is the center of mass for the composite particle. 196

7.4 Illustration of particle shape of Case 0, B1, B2 and B3 (see Table 7.2). 197

7.5 (a) Time series of the free-stream velocity; (b) Comparison of the time series of the sediment transport rate for Case 0 (circle symbols), Case B1(red solid curve), Case B2 (black solid curve), Case B3 (green solid curve) 198

C.1 (a) Sediment concentration profiles with $n = 2$ (dashed curve) and $m = 3$ (solid curve) in the frictional stress model (see equation C.1), $m = 5$, $\phi_{max} = 0.635$, and $\phi = 0.57$; (b) Sediment concentration profiles with $\phi_{max} = 0.635$ (solid curve) and $\phi_{max} = 0.65$ (dashed curve) in the frictional stress model (see equation C.1), $m = 5$, $n = 3$, and $\phi_f = 0.57$ 223

D.1 Permission letter from Advances in Water Resources (Elsevier) for the reuse of figure 1 in the article by Yu et al. (2012) 227

D.2 Permission letter from ASCE for the reuse of figure 1 in the article by Yu et al. (2014) 228

D.3 Permission letter from the Journal of Geophysical Research (John Wiley and Sons) for the reuse of the article by Cheng et al. (2015a) 229

D.4 Permission letter from Computers & Geosciences (Elsevier) for the reuse of the article by Cheng et al. (2015b) 230

ABSTRACT

Studying coastal processes is essential for the sustainability of human habitat and vibrancy of coastal economy. Coastal morphological evolution is caused by a wide range of coupled cross-shore and alongshore sediment transport processes associated with short waves, infra-gravity waves, and wave-induced currents. One of the key challenges was that the major transport occurs within bottom boundary layers and it is dictated by turbulence-sediment interactions and inter-granular interactions. Therefore, this study focuses on numerical investigations of sediment transport in the bottom wave boundary layers on continental shelves and nearshore zones, with emphasis on both fine sediment (mud) and sand transports.

On the continental shelves, the sea floor is often covered with fine sediments (with settling velocity no more than a few mm/s). Wave-induced resuspension has been identified as one of the major mechanisms in the offshore delivery for fine sediments. A series of turbulence-resolving simulations were carried out to study the role of sediment resuspension/deposition on the bottom sediment transport. Specifically, we focus on how the critical shear stress of erosion and the settling velocity can determine the transport modes. At a given wave intensity associated with more energetic muddy shelves, three transport modes, namely the well-mixed transport (mode I), two-layer like transport with the formation of lutocline (mode II) and laminarized transport (mode III), are obtained by varying the critical shear stress of erosion or the settling velocity. A 2D parametric map is proposed to characterize the transition between transport modes as a function of the critical shear stress and the settling velocity at a fixed wave intensity. In addition, the uncertainties due to hindered settling and particle inertia effects on the transport modes were further studied. Simulation results confirmed that the effect of particle inertia is negligible for fine sediment in typical

wave condition on continental shelves. On the other hand, the hindered settling with low gelling concentration can play a key role in sustaining a large amount of suspended sediments and results in the laminarized transport (mode III). Low gelling concentrations can also trigger the occurrence of gelling ignition, a state in which the erosion rate always exceeds the deposition rate. A sufficient condition for the occurrence of gelling ignition is hypothesized for a range of wave intensities as a function of sediment/floc properties and erodibility parameters.

In the more energetic nearshore zones, the sea floor is often covered with sand (with settling velocity exceeds 1 cm/s). Based on the open-source CFD toolbox OpenFOAM, a multi-dimensional Eulerian two-phase modeling framework is developed for sediment transport applications. With closures of particle stresses and fluid-particle interactions, the model is able to resolve full sediment transport profiles without conventional bedload/suspended load assumptions. The turbulence-averaged model is based on a modified k-ϵ closure for the carrier flow turbulence and it was used to study momentary bed failure under sheet flow conditions. Model results revealed that the momentary bed failure and the resulting large transport rate were associated with a large erosion depth, which was triggered by the combination of large bed shear stresses and large horizontal pressure gradients. In order to better resolve turbulence-sediment interactions, the modeling framework was also extended with a 3D turbulence-resolving capability, where most of the turbulence-sediment interactions are directly resolved. The model is validated against a steady sheet flow experiment for coarse light particles. It is found that the drag-induced turbulence damping effect was more significant than the well-known density stratification for the flow condition and grain properties considered. Meanwhile, the turbulence-resolving model is able to reproduce bed intermittency, which was driven by turbulent ejection and sweep motions, similar to the laboratory observation. Finally, simulations for fine sand transport in oscillatory sheet flow demonstrate that the turbulence-resolving model is able to capture the enhanced transport layer thickness for fine sand, which may be related to the burst events near flow reversal. Several future research directions, including further improvements of the

present modeling framework and science issues that may be significantly benefited from the present turbulence-resolving sediment transport framework, are recommended.

Chapter 1

INTRODUCTION

1.1 General

The coastal zone, a dynamic interface between the ocean and the land, is of high ecological diversity and economic importance. Over 38% of the world's population live within 100 km of the coast, and population densities in coastal regions are about three times higher than the global average (Small & Nicholls 2003). Thus, maintaining the ecosystem in coastal zone is essential for the sustainability of human habitat and vibrancy of coastal economy. Due to global accelerated sea level rise, the coastal zone becomes increasingly vulnerable to anthropogenic impact and natural hazards, such as storm surge and hurricane waves, which may cause severe shoreline erosion and coastal flooding. Generally, coastline morphology is controlled by coupled longshore and cross-shore sediment transport driven by waves, currents, tides and river discharges. Studying sediment transport under waves and currents in the coastal environments is a vital discipline to further understand coastal evolution, vulnerability of coastal infrastructure and resiliency of ecosystem (e.g., the fate of carbon, nutrient and pollutant, etc).

Sediment transport is a challenging subject because it involves a wide range of flow conditions and sediment properties, which further results in complicated flow-sediment interactions. In outer part of the continental shelves where the flow depth is typically greater than about 100 m, the surface waves have little effects on the sediment motion at the sea bed. The dominant sediments in deeper oceanic water are carbonate ooze, thus studying sediment supply and deliveries to the shelf edges are key elements of sea floor evolutions and ocean resources. One of the major sediment transport

mechanisms in deeper oceanic water is the downslope gravity current. In the inner to mid continental shelves, where the water depth is less than 100 m, the bottom slope is usually less than 0.005, and they are often covered with fine sediments (sediments of settling velocity no more than a few mm/s). Sediment suspension due to strong currents and waves can cause strong density anomaly and drive offshore delivery of fine sediment to the shelf breaks (e.g., Wheatcroft & Borgeld 2000, Fan et al. 2004, Bever et al. 2011). However, previous studies on the fine sediment transport assumed a fixed supply of fine sediments, and the resuspension/deposition of sediment at the bottom was neglected (Ozdemir et al. 2010, 2011, Yu et al. 2014). One of the goals in this thesis is to study the role of sediment resuspension/deposition on muddy continental shelves.

In the nearshore (littoral) zone, where the water depth is usually shallower than $10 \sim 15$ m, and surface waves and wave-induced circulations are important driving force for sediment transport. Because flow is more energetic, the nearshore sea floor is often covered with sand (with settling velocity exceeding 1 cm/s), and the understanding of onshore/offshore sediment transport mechanisms is critical to the prediction of coastal morphology and beach erosion/recovery. As waves shoal in the shallow water region, they become skewed (peaky crests and flat troughs) and asymmetric (steep front faces and gently sloping rear faces). It has been shown that wave skewness (Ruessink et al. 2007), wave asymmetry (Drake & Calantoni 2001, Hoefel & Elgar 2003), wave boundary layer streaming (Henderson et al. 2004, Kranenburg et al. 2014, Yu et al. 2010) and undertow currents (Gallagher et al. 1998) are important mechanisms for nearshore sediment transport. As the waves enters the surf zone and breaks, the sediment transport is further complicated by various processes associated with wave breaking. The breaking wave turbulence (Sumer et al. 2011) can induced large bottom shear stress and strong horizontal pressure gradient, which may further cause significant sediment transport. With successes in understanding some of these sediment transport mechanisms, dominant mechanisms under extreme events remains unclear (Ruessink & Kuriyama 2008). This deficiency serves as the main motivation

for the work presented in this dissertation.

This thesis focuses on numerical investigations of sediment transport in the bottom boundary layers of continental shelves and nearshore zones, with emphasis on both fine sediment (mud) and sand transport processes. The goal is to understand the fundamental sediment transport mechanisms, and in the scope of this thesis, no free-surface is explicitly considered, and flow conditions are similar to that in an enclosed channel or an oscillatory water tunnel. As an introduction, a brief description of sediment properties and transport layers are given in section 1.2, and literatures of existing sediment transport models are reviewed in section 1.3. Motivations of the present research is discussed in section 1.4, and the outline of this thesis and the relevant research questions are listed in section 1.5.

1.2 Categories of Sediment Transport

Sediments are of different grain sizes across the coastal environments. Depending on the grain sizes, sediments are typically divided into two categories, cohesive and non-cohesive sediments. Their properties and transport mechanisms differ and hereby need to be investigated individually before a mixed transport can be studied in detail. Cohesive sediments, alternatively called mud, are fine-grain sediments with grain size typically smaller than about 63 μm, and they are primarily composed of clay, silt, and organic matter. Heavy metals and organic chemicals are particularly susceptible to fine-grained sediments. They are often found in continental shelves and estuaries where the flow is less energetic or there exist a large supply nearby (e.g., river input). Cohesive sediments may stick to each other due to the action of electrostatical forces. This process is called flocculation (Dyer & Manning 1999). Cohesive sediments are mainly transported as flocs, rather than individual grain particles. As the flocs are transported through advection, turbulent/molecular diffusion and gravitational settling, flocs may deform, aggregate or breakup. Flocculation makes the cohesive sediment transport process complicated, and difficult to study. Many processes can affect the process of flocculation, such as sediment size distribution and concentration, flow turbulence,

salinity and temperature. The floc structure can be quantitatively characterized by the fractal dimensions n_f:

$$N = (D_f/d)^{n_f} \tag{1.1}$$

where N is the number of primary fine sediment particles within the floc, d is the primary particle diameter and D_f is the floc diameter. The floc properties such as density can be evaluated from the fractal dimension. The fractal dimension n_f is known to vary with shear rate (Maggi 2007), electrolyte concentration, presence of microbial biomass. Moreover, high sediment concentration may increase the effective viscosity or more generally modifies the rheological stresses with a non-Newtonian behavior, which could also affect the flow structures and sediment transport (Vinzon & Mehta 2000).

Once flocs settle to the bed, they may consolidate due to gravity and overlaying pressure. As a result of the consolidation, the pore water is generally expulsed, and bed density and strength are increased. Changes in the flow condition may drive the erosion and deposition of fine sediments. When the bottom shear stress exceeds the critical shear stress, erosion may occur. Since the fine sediments are not likely to be eroded grain by grain, the critical shear stress does not vary with the primary grain size. Instead, the critical shear stress for mud erosion may vary with the depth into the bed due to the consolidation process (Parchure & Mehta 1985, Sanford & Maa 2001)

Non-cohesive sediment, for which the grain size d is much larger than 63 μm, is typically called sand. The particle size in this class can vary from 0.063 mm to about 20 mm, and they can be further divided into fine sand ($d < 0.15$ mm), medium sand ($0.15 < d < 0.5$ mm), and coarse sand ($d > 0.5$ mm). In nature, the sediment in coastal environments are often of mixed grain sizes, and the size distribution depends on the source of sediment, and flow conditions. Even though the particles are rarely spherical, it is often practical to describe the sediment as a sphere with an equivalent grain diameter. For a mixture of different grain sizes, the medium sediment diameter (d_{50}) is often used. In the state-of-the-art sediment transport theory, the sediment transport modes are commonly divided into bed-load and suspended load (see Figure

1.1b). The bedload is defined as the motion of rolling, sliding and saltation of sand particles on the sediment bed when the threshold of sediment motion is exceeded. It is often assumed that the incipient motion of sediment can be quantified by the Shields parameter:

$$\theta = \frac{\tau_b}{\rho^f (s-1) g d}, \tag{1.2}$$

where τ_b is the bottom shear stress, $s = \rho^s / \rho^f$ is the ratio of sediment density ρ^s to the fluid density ρ^f, and g is the gravitational acceleration. The Shields parameter can be interpreted as the ratio of mobilizing forces (i.e., fluid drag, lift force, etc.) and stabilizing force of immersed weight. Typically when the Shields parameter exceeds about 0.05, sediment particles are mobilized. When $\theta << 0.8$, ripples and small bedforms may form. When $\theta > 0.8$, sheet flow can occur, and the intense sediment motion can wash out the small bed forms. In sheet flow, the bed becomes flat, and the concentrated transport layer can extend to several tens of grain diameters. However, under wave motions, it has recently been found that the incipient motion of sediment are triggered by the combined bottom shear stress and horizontal pressure gradient (Frank et al. 2015b), and the critical Shields parameter could be lower than 0.05. As flow and turbulent stress become sufficient intense to overcome the submerge weight of the particles, the particles are suspended into the water column and get transported by the flow turbulence. The relative dominance between bedload and suspended load can be estimated by the Rouse number:

$$Ro = \frac{W_s}{\kappa u_*}, \tag{1.3}$$

where W_s is the settling velocity, κ is the von Karman constant, and u_* is the bottom shear velocity, $u_* = \sqrt{\tau_b / \rho^f}$. When the Rouse number $Ro > 2.5$, the bedload is usually found to be dominate, while the suspended load dominates the transport when $Ro < 1.2$ (Nino et al. 2003).

A modern description of the non-cohesive sediment transport considers four transport layers, as shown in figure 1.1a (Yu et al. 2012): (1) immobile bed layer, where

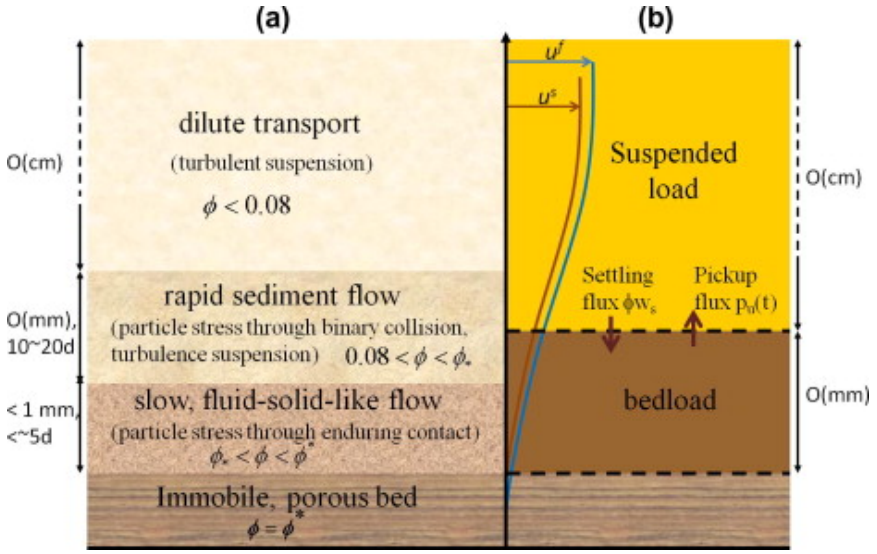

Figure 1.1: Schematic plots on the (a) modern sediment transport regimes and (b) bed-load and suspended load transport layers (Yu et al. 2012) (With permission from the Elsevier. This material may be downloaded for personal use only, and any other use requires prior permission of Elsevier).

the sediment bed is closely packed, and the sediment concentration is near close packing limit. For spherical particles, the close packing volumetric concentration is about 0.635 (Torquato et al. 2000), while particle with irregular shape could have a slightly different packing concentration. The flow velocity in this layer is nearly zero, and the sediment bed is essentially a porous media; (2) Above the immobile bed, a slowly moving layer can be triggered by the shear flow and hydrodynamic pressure gradient. Particles are in constant contact with other particles, and the frictional force among particles dominates the particle-particle interaction. Due to the shear induced motion, a bed of particles will dilate, and particle concentration drops between close packing limit and loose packing limit (volumetric concentration about 0.57); (3) Exerted by the turbulent agitation and short-duration particle-particle collision, a rapid sediment transport layer exists. The thickness of this layer becomes more significant in the more energetic sheet flow condition. The sediment concentration in this regime is between loose packing limit and about 0.08, where the average particle skin distance is about one diameter (Lanckriet et al. 2013). (4) When the sediment concentration is smaller

than about 0.08, the average particle-particle distance is more than one diameter, and particle-particle collision in this regime is less important, flow turbulence becomes the dominant mechanism driving sediment suspension.

In the aforementioned description of sediment transport layers, we can see two key mechanisms are responsible for the sediment suspension: particle-particle interaction, and turbulence agitation. To quantify the particle-particle interactions, a one-dimensional parameter called Bagnold number can be used (Hunt et al. 2002):

$$N = \frac{\sqrt{\lambda} s d^2}{\nu} \frac{\partial u}{\partial z}, \tag{1.4}$$

where λ is the so-called linear concentration related to the sediment volumetric concentration by:

$$\lambda = \frac{1}{(\phi_m/\phi)^{1/3} - 1}, \tag{1.5}$$

where ϕ_m is the maximum sediment concentration at dense packing. Geometrically, d/λ is a measure for the average distance between two particles. Bagnold number N is the ratio of the dispersive stress due to particle inertia over the fluid viscous effect, and it can be rewritten as $N = 18\sqrt{\lambda}\tau_p \partial u/\partial z$, where $\tau_p = sd^2/(18\nu)$ is the particle response time. The ratio of τ_p to the characteristic fluid time scale is the so-called particle Stokes number, which is a non-dimensional description of particle inertia. The particle Stokes number describes how rapidly the particles will follow the fluid motion. With larger St, the particles are hardly disturbed by the fluid motion. It is found that when $N < 40$, the viscous effect of interstitial fluid dominates the sediment dispersion (viscous regime), while when $N > 450$, the particles are in inertial regime, and the particle inertia becomes increasingly important and direct collision dominates. When the Bagnold number falls between 40 and 450, it is a transitional regime, and interstitial fluid viscous effect and direct particle collisions are both important. It is critical to understand sediment transport mechanisms as a function of grain size because it leads to vastly different Bagnold number and Stokes number.

1.3 Sediment Transport Methodology

As discussed in section 1.2, there is a wide range of sediment properties as well as flow conditions across the coastal zone. Therefore, different flow-sediment interactions are resulted. To successfully model sediment transport, and better predict coastal morphology, researchers have developed several types of numerical models for various sediment transport applications. These models can be divided into two categories. In the single-phase model, sediment transport is divided into bedload and suspended load (see figure 1.1b). In the state-of-the-art single-phase sediment transport models, the bedload is not directly resolved but parameterized with empirical formulations, which are usually obtained from steady flow experiments (e.g., Meyer-Peter & Muller 1948, Einstein 1950, Bagnold 1966, van Rijn 1984*a*):

$$\frac{\Psi_B}{\sqrt{(s-1)gd^3}} = C(\theta - \theta_c)^b, \tag{1.6}$$

where C and b are empirical coefficients, and θ_c is the critical Shields parameter. The reported value of C can vary from 8 to 12, and the power b varies from 1.5 to 1.8 (Bagnold 1966, van Rijn 1984*a*). To resolve suspended load, the dilute flow assumptions are invoked, and a vertical sediment flux boundary condition is needed (pick-up flux). The pick-up flux is also parameterized with bed-shear-stress-based near-bed suspension flux or near-bed reference concentration (Rijn 1984, Engelund & Fredsoe 1976). The single phase model has been widely used because of its simplicity and numerical efficiency, and it has been integrated into meso/large scale models, such as Delft3D (Lesser et al. 2004, Hu et al. 2009), XBeach (Roelvink et al. 2009) and ROMS (Warner et al. 2008). Despite their ability to predict long-term regional morphology in littoral zones, there are several challenges to model sediment transport using such single-phase methodology. Firstly, major transport in sheet flow occurs within about 1 cm above the bed. Hence, the resolved suspended load layer only accounts for a minor portion of transport while the majority of the predicted transport relies on the empirical bedload parameterization. Secondly, most of the existing formulae for bedload transport

and suspension flux are developed for steady flow and hence their applicability to the highly unsteady wave-induced transport is questionable (Yu et al. 2012). Thirdly, the particle-particle collisions and frictions in the high concentration regions are assumed to be negligible, and entrained sediments are assumed to be suspended immediately by the flow turbulence. In addition, the bed erosion/deposition and its impact on the sediment concentration distribution and the carrier flow fields are largely neglected. Liu & Garcia (2008) successfully studied the local scour by tracking the bed elevation changes based on the continuity of sediment in a finite volume scheme, and the numerical meshes are deformed accordingly. The numerical model is limited to small bed geometry changes, as large mesh distortion may result in numerical instabilities. Chou & Fringer (2010) employed a Lagrangian-Eulerian moving mesh scheme to simulate flow over time-dependent moving bed geometries in the curvilinear coordinate system. The model succeeded in modeling two-dimensional and three-dimensional bedforms, however, the bedload needs to be neglected in order to match experimental observations.

Another alternative for sediment transport modeling is the two-phase flow approach, which only caught researchers' attention for sediment transport applications during the past two decades. In the two-phase modeling framework, both the sediment motion and fluid phase are solved separately, either using a Eulerian approach (Eulerian-Eulerian model) or a Eulerian-Lagrangian approach. Sediment-fluid interactions can therefore be naturally represented and full transport profiles from dilute transport to the immobile bed can be obtained without the assumption of bedload and suspended loads. In Eulerian-Eulerian model, both the fluid phase and the sediment phase are treated as a continuum. Fluid and sediment momentums can be coupled by inter-phase drag forces, added mass and lift forces, while particle stresses due to collisions and frictions are modeled with additional closure. In the past two decades, several numerical models for sheet flow sediment transport have been developed based on the Eulerian two-phase flow approach (e.g., Jenkins & Hanes 1998, Dong & Zhang 1999, Hsu et al. 2004, Revil-Baudard & Chauchat 2013). Asano (1990) and Li & Sawamoto

(1995) are among the earliest work. However, these models include insufficient representation of sediment-flow interactions. Dong & Zhang (1999) first established a complete two-phase model based on a mixing length closure for flow turbulence under oscillatory flows, and it was later used to study sheet flow under combined wave-current flow conditions (Dong & Zhang 2002). However, the quasi-static regime where the sediment concentration is close to the packing limit is not resolved, and instead, a constant sediment concentration is specified at the bottom boundary. Hsu et al. (2004) incorporated an empirical sediment stress closure in the enduring contact layer, and adopted kinetic theory for inter-granular stress in the collisional sediment transport regimes. The model adopted a closure of the fluid turbulence based on modified $k-\epsilon$ equations, and through derivation from two-phase equations, the damping effect due to the existence of sediment is included. Although the model of Hsu et al. (2004) is more theoretically complete, it still lacks the capability for medium to fine sand particles. Amoudry et al. (2008) addressed this issue with some success by changing the coefficients in the ϵ equations to take into account of the effect of particles on the fluid turbulence. However, the model is still inadequate for fine sand. Amoudry (2014) further incorporated the k-ω model into Eulerian two-phase model. However, similar results as the k-ϵ model were obtained, and it does not improve the prediction for fine sand. Li et al. (2008) developed a new two-phase model based on a modified one-equation turbulence closure, and succeeded in reproducing the sheet flow layer thickness. However, they also failed to reproduce the sediment burst events during the flow reversal. Recently, new development on the models for the particle stresses were carried out using phenomenological laws for dense granular rheology (Revil-Baudard & Chauchat 2013). With a mixing length approach, Revil-Baudard & Chauchat (2013) showed that granular rheology can produce similar predictions of sediment transport as other models using the kinetic theory. With the above mentioned success in multi-phase Eulerian two-phase modeling of sediment transport, several improvement are warranted. For example, the existing models are mostly limited to one-dimensional-vertical (1DV), namely, the models are limited to the assumption that the flow and

sediment fields are homogenous in the two horizontal directions. Meanwhile, critical mechanisms that allow more accurate prediction for wave-driven fine sand transport remain unclear.

In contrast with the Eulerian two-phase models, in which the particle-particle interactions are modeled with either kinetic theory or granular rheology, the Euler-Lagrangian model directly resolves the particle-particle interactions to the individual grain level, and tracks each sediment particles by using Newton's second law. Drake & Calantoni (2001) coupled 3D Discrete Element model (DEM) directly with a 1DV mixing length turbulence model for sheet flow sediment transport in the nearshore zone. One advantage of Euler-Lagrangian model is that it can explicitly study the particle shape and poly-dispersed sediment transport. Calantoni et al. (2004) presented a DEM to represent the natural sand with non-spherical particles for sheet flow transport. Calantoni & Thaxton (2008) studied the transport ratio for bimodal distributions of coarse sediments under monochromatic waves using DEM, and a simple power law was proposed for the prediction of the transport rates of each size fraction in the bimodal distribution. The above mentioned models rely on a Reynolds averaged turbulence model, thus the turbulence-particles interactions are not properly included. Schmeeckle (2014) coupled a turbulence-resolving large eddy simulation scheme with discrete particle models. The model was able to predict the bedload transport rate as well as the bed response to the fluid turbulent motions. However, the computational cost and memory requirement for such numerical approach is much larger than the Eulerian-Eulerian models, especially when the particle size is small. Hence, its applicability to sheet flow transport has not yet been demonstrated.

To summarize, the numerical simulation approach has been developed rapidly during the past two decades, and various numerical models were developed for sediment transport (see a brief summary in table 1.1). With closures for particle-particle interactions, and turbulence-sediment interactions, the Eulerian two-phase model excels the single phase sediment transport models in several aspects, and provide us new insight into sediment transport mechanisms, especially in sheet flow. Considering the high

Table 1.1: Summary of Eulerian two-phase models for sediment transport applications

Eulerian two-phase models				
Authors	Turbulence model	Particle stress	Sediment sizes	Comments
Asano (1990)	mixing length	Bagnold	coarse	first numerical model
Li & Sawamoto (1995)	mixing length	Bagnold	coarse	improved upon Asano (1990)
Dong & Zhang (2002)	mixing length	Bagnold	fine to medium	immobile bed not resolved
Hsu et al. (2004)	$k-\epsilon$	kinetic theory	massive	1DV, immobile bed resolved
Amoudry et al. (2008)	$k-\epsilon$	kinetic theory	medium and coarse	modified based on Hsu et al. (2004)
Li et al. (2008)	k equation	Bagnold	fine	immobile bed not resolved
Amoudry (2014)	$k-\omega$	kinetic theory	medium and coarse	performance similar to Amoudry et al. (2008)
Yu et al. (2010), Kranenburg et al. (2014)	$k-\epsilon$	kinetic theory	medium and coarse	boundary streaming included
Revil-Baudard & Chauchat (2013)	mixing length	granular rheology	massive	steady flow applications

computational costs of Euler-Lagrangian approach, this thesis will focus on improving the Eulerian two-phase model based on the development of Hsu et al. (2004) for multidimensional simulations. The field and laboratory findings that form the foundation of the research questions in this study will be discussed in the next section.

1.4 Motivations

This section describes several observations from the recent field/laboratory experiments and numerical studies, and provide motivations for the numerical studies presented in this thesis. As discussed in section 1.3, two-phase sediment transport model provides several features superior to the state-of-the-art bedload/suspended load sediment transport. Our numerical study will focus on the two-phase models. For fine sediment in continental shelves, the particle size is usually very small, and particle Stokes number $St < 0.2$, according to (Balachandar & Eaton 2010), the two-phase formulations can be simplified by the equilibrium Eulerian approximation (Balachandar & Eaton 2010), that is, the particle velocity can be expressed as a vectorial sum of the local fluid velocity, the settling velocity and additional particle inertia terms associated with the Stokes number. However, for sand particle, where the Stokes number is usually larger than 0.2, full mass and momentum equations of the two-phase flow system need to be solved.

1.4.1 Fine sediment transport

In many estuaries and continental shelves, the delivery and dispersal of fine sediments play a critical role in fate of seabed state and carbon cycles (Goldsmith et al. 2008). Due to horizontal sediment flux convergence (Wright & Friedrichs 2006) via trapping in the frontal zones in large rivers (e.g., Amazon: Kineke et al. 1996) or episodic river flooding in small mountainous rivers (Ogston et al. 2000), a large availability of fine sediment in the inner shelves is commonly observed. The subsequent delivery of these fine sediments on continental shelves are mainly driven by bottom resuspension (e.g., Wheatcroft & Borgeld 2000, Fan et al. 2004, Bever et al.

2011). Wave-induced fine sediment resuspension has been identified as one of the major mechanisms in sediment source to sink (e.g., Wiberg et al. 1994, Harris & Wiberg 1997, Traykovski et al. 2000, Wright & Friedrichs 2006), and cause offshore delivery processes due to sediment flux gradients (Ogston et al. 2000, Harris & Wiberg 2002, Hale et al. 2014) and sediment-driven gravity flows (Traykovski et al. 2000). Thus, characterizing the resuspension of fine sediment in the wave bottom boundary layer is an important segment of sediment source to sink.

One key complexity of fine sediment transport is its coupling with turbulence. Firstly, the presence of suspended fine sediment may attenuate the carrier flow turbulence (e.g., Trowbridge & Kineke 1994, Winterwerp 2006). Ozdemir et al. (2010, 2011) carried out a series of three-dimensional turbulence-resolving simulation of fine sediment in oscillatory channel flow with wave condition similar to an energetic muddy continental shelf (Stokes Reynolds number Re_Δ =1000). Simulation results revealed that at a given Reynolds number, the prescribed sediment load and settling velocity determine the degree of sediment-induced density stratification and lead to four distinct flow regimes (see figure 1.2): Regime I is of very dilute flow (sediment mass concentration is much smaller than $\sim$ 1 g/L). Sediments in the wave boundary layer is well-mixed and carrier fluid turbulence remains intact within the boundary layer. Regime II occurs when the near-bed sediment concentration is in the range of $O\big(1 \sim 10\big)$ g/L, and a lutocline, i.e., a sharp negative concentration gradient, is formed. Above the lutocline, the flow becomes quasi-laminar but the flow remains turbulent beneath. Regime III takes place when the near bed sediment concentration approaches several tens of g/L. Carrier fluid turbulence is significantly attenuated, and the flow becomes nearly laminar. However, due to shear instability, sediment burst events can be triggered during flow reversal. Regime IV is observed at sediment concentration of $O\big(100\big)$ g/L or greater, in which a completely laminarized flow throughout the wave cycle is observed. Yu et al. (2014) later extended the work of Ozdemir et al. (2010) to allow a variable viscosity in order to investigate the rheological effect (mixture viscosity increases as a function of sediment concentration). It was found that the enhanced viscosity tends to

further attenuate turbulence via reduced near-bed velocity gradient and hence weaker turbulent production.

The discovery of the above transport regimes and their transition due to sediment-turbulence interactions have critical implications to our capability in assessing the state of the muddy seabed and to further understand various applications related to the fine sediment transport. In typical continental shelves, wave-induced bottom shear stress varies in time, and sediment can be resuspended/deposited when the flow intensity becomes stronger/weaker. However, the studies by Ozdemir et al. (2010, 2011) and Yu et al. (2014) are based on a prescribed fixed sediment availability in the domain. To make the model more realistic, an erosion-deposition bottom boundary for suspended sediments is required to allow a net erosion/deposition from/to the bed. A key research question to be investigated is to understand how flow-sediment interactions can affect the sediment availability and the resulting sediment transport.

In addition, in previous studies by Ozdemir et al. (2010, 2011) and Yu et al. (2014), the particle velocity can be calculated by the equilibrium Eulerian approximation (Balachandar & Eaton 2010) as a vectorial sum of the local fluid velocity, the settling velocity and additional particle inertia terms associated with the Stokes number. However, the particle inertia terms are neglected by assuming that particle Stokes number is much smaller than unity. Meanwhile, hindered settling effect is also neglected. However, Ozdemir et al. (2011) demonstrated that the settling velocity plays a key role in determining the vertical sediment flux budget, and vertical distribution of sediment concentration. Therefore, there is a need to quantify the effect of neglecting the particle inertia and hindered settling on fine sediment transport for typical wave conditions encountered in the continental shelves.

1.4.2 Sand transport

As reviewed in section 1.3, several numerical models for sheet flow sediment transport have been developed based on the Eulerian two-phase flow approach (e.g., Jenkins & Hanes 1998, Dong & Zhang 1999, Hsu et al. 2004, Revil-Baudard & Chauchat

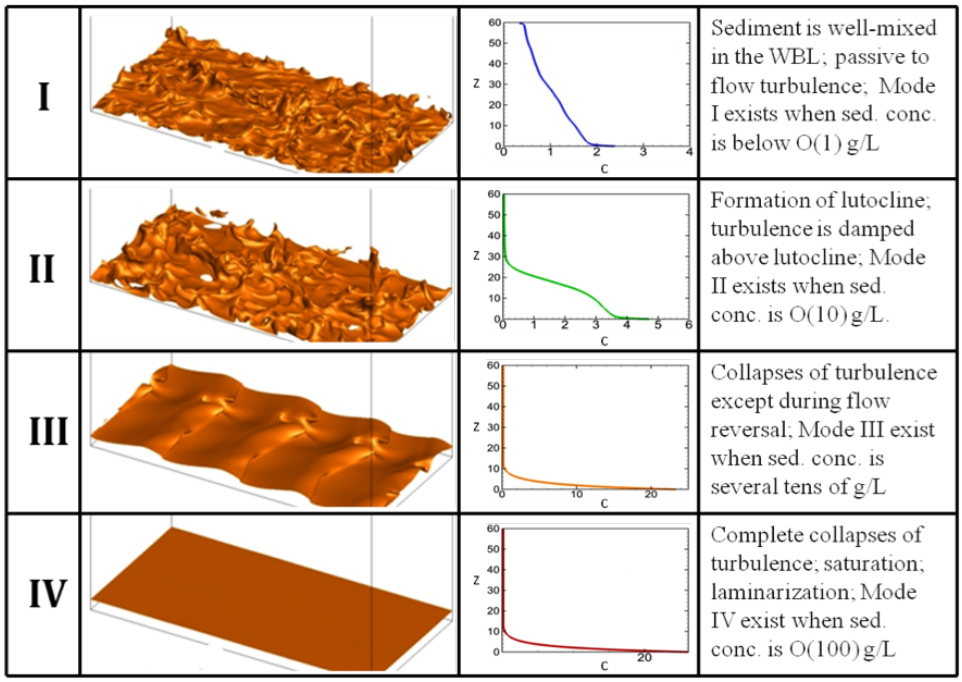

Figure 1.2: A summary (Yu et al. 2014) on the existence of four flow regimes (I IV) reported by 3D turbulence-resolving simulations of Ozdemir et al. (2010) due to increasing sediment availability (or bulk Richardson number) under the same wave intensity (Stokes Reynolds number Re_Δ =1000) and settling velocity (≈0.5 mm/s). The second column shows snapshots of iso-surface of sediment concentration during flow peak for regime I, II and IV and during flow reversal for regime III. The third column shows averaged sediment concentration profile where the vertical axis is normalized by Stokes length scale and the horizontal axis is normalized by volume-averaged concentration, which is fixed in each simulation (With permission from the American Society of Civil Engineers. This material may be downloaded for personal use only, and any other use requires prior permission of ASCE).

2013). These two-phase flow models have been adopted to study several onshore/offshore sediment transport mechanisms such as nonlinear wave shapes (e.g., Dong & Zhang 2002, Hsu & Hanes 2004, Liu & Sato 2006) and boundary layer streaming (Yu et al. 2010, Kranenburg et al. 2014), the parameterization of suspension flux under waves (Amoudry & Liu 2010, Yu et al. 2012), and inner-surf/swash sediment transport (Bakhtyar et al. 2010). These modeling studies successfully demonstrated that the two-phase flow approach can be an effective tool to study coastal sediment transport, however, several mechanisms for energetic flow conditions, and especially for fine sand still remains unclear and major improvements are warranted.

Sediment transport rate is often parameterized by the bottom shear stress, which works reasonably well for moderate wave conditions. However, during large wave events associated with intense storms, the predicted morphological evolution is less satisfactory (Ruessink & Kuriyama 2008) and hence researchers start to concern about other mechanisms that may not be parameterized by bottom stress stress. It was found that horizontal pressure gradient also play a role for sediment transport rate (Calantoni & Puleo 2006, Frank et al. 2015b), and significant bed mobilization, called momentary bed failure or plug flow, may occur during the passage of steep waves (Madsen 1974, Sleath 1999, Foster et al. 2006). The non-dimensional number, called Sleath parameter $S_p = (\partial p/\partial x)/[(s-1)g]$ was introduced to quantify the importance of horizontal pressure gradient. Based on the field observation, the plug flow occurs when $S_p > 0.1 \sim 0.2$. However, according to the laboratory experiment of Sleath (1999), the plug flow could occur when $S_p > 0.3$. There seems to be no consensus on the threshold for the occurrence of plug flow. In addition, as described in Conley & Inman (1992), when momentary bed failure occurs, sediment transport may become inhomogeneous with small "tufts" appearing in the transport layer. The formation of small tufts may violate the commonly used 1DV sheet flow assumption. Meanwhile, there are many sediment transport problems that are essentially not homogenous in horizontal directions, such as ripple dynamics and scour around objects. We are therefore motivated to develop a multi-dimensional sediment transport model.

Existing Eulerian two-phase models are mostly developed using a turbulence-averaged approach, and turbulence-sediment interactions are modeled with highly empirical closures. These sediment transport models works well for medium sand and coarse sand. However, no satisfactory predictions of fine sand has been reported. For instance, it is well-known that in the laboratory experiments of sheet flow in oscillatory flows, measured maximum sheet flow layer thickness δ_s, when nondimensionalized by mean grain size d, scales well with the Shields parameter θ. Specifically, Dohmen-Janssen et al. (2001) demonstrated that for medium sand (mean grain diameter d = 0.21 mm and 0.32 mm), the resulting δ_s agrees with the well-known formula developed for steady flow (Wilson 1987), $\delta_s/d = C_\delta\theta$, with the empirical coefficient C_δ = 10. However, for fine sand with d=0.13 mm in oscillatory sheet flow, the empirical coefficient C_δ increases significantly to about 30. Under progressive waves, several large wave flume studies also reveal enhanced sheet flow layer thickness (Dohmen-Janssen & Hanes 2002, Mieras et al. 2016). To our knowledge, the enhanced sheet layer thickness for fine sand cannot be reproduced by the turbulence-averaged two-phase flow model unless the particular coefficient in the turbulence closure is recalibrated for fine sand. In addition, experiment data for fine sand (O'Donoghue & Wright 2004, Dohmen-Janssen et al. 2001, Li et al. 2004) reveals sediment concentration bursts during the flow reversal. Though the velocity during the flow reversal is small, depending on the wave shape and wave period, the bursted sediment may have a dramatic effect on the net onshore/offshore transport. According to the previous turbulence-resolving simulation of fine sediments (Ozdemir et al. 2011), turbulence-sediment interaction plays an important role in fine sediment transport. Moreover, flow condition in coastal environment is often of transitional turbulent flows, while typical turbulence-averaged closures only works for fully turbulent flow. Therefore, we are motivated to develop a 3D turbulence-resolving model to fully understand sand transport for a full range of grain sizes., We hypothesize that a 3D turbulence-resolving Eulerian two-phase model can capture these missing mechanisms, and provide insights on improvements for turbulence-average models.

1.5 Scope of This Thesis

The main objective of this study is to develop a comprehensive and physical-based numerical modeling framework to study key processes of sediment transport. Due to different mechanisms involved in sediment transport associated with different grain sizes, we adopted different mathematical governing equations for fine sediment and sand transport.

For fine sediment transport, we utilize the simplified governing equations for fine sediment using the Equilibrium Eulerian approximations (chapter 1), and major transport physics due to sediment resuspension/deposition are investigated in chapter 2. Specifically, we focus on how the critical shear stress of erosion and the settling velocity, can determine the sediment availability and the resulting fine sediment transport modes. A 2D parametric map is proposed to characterize the transition from one transport mode to another as a function of the critical shear stress and the settling velocity at a given wave intensity.

Chapter 3 further investigates the uncertainties of the particle velocity approximations adopted in chapter 2, particularly the hindered settling and particle inertia effects. The effects of particle inertia and hindered settling on the switch in sediment transport modes are described in chapter 3. The occurrence of gelling ignition associated with large hindered settling effect is discussed, which leads to a state in which the erosion rate is always higher than the deposition rate for flocs with a low gelling concentration. A sufficient condition for the occurrence of gelling ignition is hypothesized for a range of wave intensities as a function of sediment/floc properties and erodibility parameters.

To model sand transport, a multi-dimensional Eulerian two-phase flow model is developed. The complete set of Eulerian governing equations for sediment transport in the two-phase flow system, before further applying any turbulence-averaging or scale-separation scheme is first presented in chapter 4. Particle stresses due to collisions and frictions are also discussed in detail.

In chapter 5, the turbulence-averaged multi-dimensional Eulerian two-phase

model is developed to study the mechanisms for the momentary bed failure in sheet flow. An attempt to describe the criteria for the occurrence of momentary bed failure is made using this turbulence-averaged model, and its effect on the sediment transport rate is discussed.

In chapter 6, the turbulence-averaged model is extended to a turbulence-resolving model by using the large eddy simulation methodology. The model formulation, subgrid closures for fluid and particle stresses, and fluid-sediment interactions are discussed. A detail model-data comparison with a recent laboratory experiment of steady sheet flow (Revil-Baudard et al. 2015) is carried out and numerical investigation of fine sand burst under oscillatory sheet flows (O'Donoghue & Wright 2004) is also presented.

Finally, the chapter 7 closes this thesis with discussions and future works. Applications of the multi-dimensional Eulerian two-phase model are discussed, and future directions for the model improvements are discussed. In addition, a preview of ongoing and future work related to expanding the modeling framework for Euler-Lagrangian scheme in order to study poly-dispersed sediment transport is presented.

Chapter 2

ON THE TRANSPORT MODES OF FINE SEDIMENT IN THE WAVE BOUNDARY LAYER DUE TO RESUSPENSION/DEPOSITION — A TURBULENCE-RESOLVING NUMERICAL INVESTIGATION

Previous field observations revealed that the wave boundary layer is one of the main conduits delivering fine sediments from the nearshore to continental shelves. Recently, a series of turbulence-resolving simulations further demonstrated the existence of a range of flow regimes due to different degrees of sediment-induced density stratification controlled by the sediment availability. In this study, we investigate the scenario in which sediment availability is governed by the resuspension/deposition from/to the bed. Specifically, we focus on how the critical shear stress of erosion and the settling velocity, can determine the modes of transport. Simulations reveal that at a given wave intensity, which is associated with more energetic muddy shelves and a settling velocity of about 0.5 mm/s, three transport modes, ranging from the well-mixed transport (mode I), two-layer like transport with the formation of lutocline (mode II) and laminarized transport (mode III) are obtained as the critical shear stress of erosion reduces. Moreover, reductions in the settling velocity also yield similar transitions of transport modes. We also demonstrate that the onset of laminarization can be well-explained by the reduction of wave-averaged bottom stress to about 0.39 Pa due to attenuated turbulence by sediments. A 2D parametric map is proposed to characterize the transition from one transport mode to another as a function of the critical shear stress and the settling velocity at a fixed wave intensity. Major contents to be presented in this chapter have been published in Cheng et al. (2015a).

2.1 Introduction

In many estuaries and continental shelves, the delivery and dispersal of fine riverine sediment play a critical role in determining seabed state, coastal geomorphology (Friedrichs & Wright 2004) and carbon cycle (Goldsmith et al. 2008). Due to horizontal sediment flux convergence (Wright & Friedrichs 2006) via trapping at estuarine-like shelf fronts in large rivers (e.g., Amazon: Kineke et al. 1996) or episodic river flooding in small mountainous rivers (Ogston et al. 2000), a large availability of fine sediment in the inner shelves is commonly observed. The subsequent delivery of these fine sediments are mainly driven by bottom resuspension (e.g., Wheatcroft & Borgeld 2000, Fan et al. 2004, Bever et al. 2011). Although both strong currents and waves are responsible for the sediment resuspension on continental shelves, it has been reported that waves are the dominant factors in resuspending sediment from the seabed (Wiberg et al. 1994, Harris & Wiberg 1997), and cause offshore delivery processes due to sediment flux gradients (Ogston et al. 2000, Harris & Wiberg 2002, Hale et al. 2014) and sediment-driven gravity flows (Traykovski et al. 2000). Thus, characterizing the resuspension of fine sediment in the wave bottom boundary layer (WBBL) is an important segment of sediment source to sink.

The complexity of fine sediment resuspension and deposition in the wave boundary layer is due to highly coupled interactions between surface waves and bottom fine sediment, as well as the knowledge gap on fine sediment resuspension. Firstly, the presence of suspended fine sediment may attenuate the carrier flow turbulence (e.g., Trowbridge & Kineke 1994, Winterwerp 2006). To understand the fine sediment transport in the wave boundary layer due to occasional river floods, where the sediment supply is controlled by the river input, a series of three-dimensional (3D) turbulence-resolving simulation of fine sediment in oscillatory channel flow were carried out (Ozdemir et al. 2010, 2011). Simulation results revealed that at a given Reynolds number, the prescribed sediment load and settling velocity determine the degree of sediment-induced density stratification and lead to four distinct flow regimes: Regime I is of very dilute flow (sediment concentration is much smaller than $\sim$ 1 g/L), sediment is well-mixed

and carrier fluid turbulence remains intact within the boundary layer. Regime II occurs when the near-bed sediment concentration is in the range of $O(1 \sim 10)$ g/L, and a lutocline, i.e., a sharp negative concentration gradient, is formed. Above the lutocline, the flow becomes quasi-laminar but it remains turbulent beneath. Regime III takes place when the near bed sediment concentration approaches several tens of g/L, carrier fluid turbulence is significantly attenuated, and the flow becomes nearly laminar. However, due to shear instability sediment, burst events occur during flow reversal. Regime IV is observed at sediment concentration of $O(100)$ g/L or greater, in which a completely laminarized flow throughout the wave cycle is observed. The existence of these regimes and the transition from one regime to the other have critical implications to our capability in assessing the state of the muddy seabed and to further understand various applications related to the fine sediment transport.

Secondly, the lack of knowledge on fine sediment resuspension, such as the magnitude of critical shear stress of erosion and other bed erodibility parameters, also stands as a difficulty in sediment transport modeling. In typical continental shelves, wave-induced bottom shear stress varies in time, and sediment can be resuspended/deposited when the flow intensity becomes stronger/weaker. However, the studies by Ozdemir et al. (2010, 2011) and Yu et al. (2014) are based on a prescribed fixed sediment availability in the domain. To make the model more realistic, an erosion-deposition bottom boundary for suspended sediments is required to allow a net erosion/deposition from/to the bed. It is generally agreed that wave- and current-induced bottom shear stresses are the dominant factors that cause erosion, and a critical shear stress for erosion exists. Two major erosion types have been proposed to model fine sediment erosions (Sanford & Maa 2001). Type I erosion model assumes that the critical shear stress for fine sediment increases with depth into the sediment bed (Parchure & Mehta 1985, Sanford & Maa 2001), while type II erosion adopts a constant critical shear stress, which is physically more appropriate for noncohesive sediments. In general, the critical shear stress for the erosion of muddy seabed is difficult to determine

due to possible consolidation, flocculation, and biological effects (Sanford 2008, Winterwerp et al. 2012), and it is typically determined through in-situ measurements or laboratory tests. Using a one-dimensional-vertical Reynolds-averaged model for fine sediment transport, Hsu et al. (2009) compared type I and type II erosion models for wave-supported gravity-driven mudflows and found that results of these two types of erosion model are similar due to the small timescale of wave forcing compared to that of settling in WBBL.

Although many insights have been gained into the fine sediment resuspension and deposition for tidal bottom boundary layers (e.g., Winterwerp 2006, Byun & Wang 2005) and WBBL (e.g., Hsu et al. 2009), these numerical studies are based on Reynolds-averaged models. Due to underlying assumptions adopted in the turbulence closure (for example, the assumption of fully turbulent flow), Reynolds-averaged models may not be sufficiently accurate to investigate the effect of turbulence modulation due to sediment, especially when it is related to the onset of laminarization. The objective of this paper is twofold: the first objective is to characterize sediment transport dynamics on an erodible bed, which allows sediments to be eroded/deposited from/to the bottom by turbulence-resolving simulations. Our second objective is to revisit the existence and transition of fine sediment flow regimes in erodible bed conditions (Ozdemir et al. 2010, 2011). Through allowing sediments to be resuspended and deposited at the bottom boundary, sediment availability in the domain in each simulation becomes part of the solution of the numerical model. This paper is organized as follows. Model formulation and numerical methodology are presented in section 2.2, as well as specific details on the new implementation of bottom erosional/depositional boundary condition are presented in the same section. In section 2.3, results of numerical experiments are presented to illustrate the effect of sediment erodibility and settling velocity on controlling the resulting transport characteristics. Further numerical experiments and analyses on the parameterization of these transport characteristics are discussed in section 2.4. Finally, concluding remarks are given in section 2.5.

2.2 Model Formulation

2.2.1 Governing equations

In this study, a simplified Eulerian two-phase flow formulation for fine sediment transport is adopted (Ferry & Balachandar 2001). By applying the equilibrium Eulerian approximation, the particle phase velocity $\widetilde{v}_i$ is expressed as a vectorial sum of fluid velocity $\widetilde{u}_i$, sediment settling velocity $\widetilde{W}_s$, and Stokes number, St, dependent inertia terms. This approximation is justified for fine particulate flows where the particle Stokes number St (the ratio of particle response time to the characteristic timescale of fluid) is sufficiently smaller than unity (Ferry et al. 2003). Following the previous turbulence-resolving simulation studies adopting this approach for fine sediment transport (Cantero et al. 2009, Ozdemir et al. 2010, Yu et al. 2014), inertia terms associated with St are neglected and hence the sediment phase velocity can be expressed as (Balachandar & Eaton 2010):

$$\widetilde{v}_i = \widetilde{u}_i - \widetilde{W}_s \delta_{i3}, \tag{2.1}$$

where $i = 1, 2, 3$ represents streamwise (x), spanwise (y) and vertical (z) directions, respectively. In this paper, except for physical constants such as the fluid density ρ_f, the sediment density ρ_s, the fluid kinematic viscosity ν, the gravitational acceleration g and the sediment diffusivity κ, variables without overhead '$\widetilde{\ }$' are non-dimensional variables.

For the suspended sediment transport in typical continental shelves, the volumetric concentration of sediment is usually not significant (< 0.05) (Traykovski et al. 2007). Therefore, the density variation is sufficiently small such that the Boussinesq approximation can be adopted to simplify the governing equations (Cantero et al. 2008). The resulting continuity and momentum equations for the fluid flow read as:

$$\frac{\partial \widetilde{u}_i}{\partial \widetilde{x}_i} = 0, \tag{2.2}$$

$$\frac{\partial \widetilde{u}_i}{\partial \widetilde{t}} + \widetilde{u}_j \frac{\partial \widetilde{u}_i}{\partial \widetilde{x}_j} = -\frac{1}{\rho_f}\frac{\partial \widetilde{p}}{\partial \widetilde{x}_i} - \widetilde{U}_0 \widetilde{\omega} \sin\left(\widetilde{\omega}\widetilde{t}\right)\delta_{i1} + \nu \frac{\partial^2 \widetilde{u}_i}{\partial \widetilde{x}_j \partial \widetilde{x}_j} - (s-1)g\phi\delta_{i3}, \tag{2.3}$$

where the fluid dynamic pressure is represented by $\widetilde{p}$, and ϕ is the volumetric concentration of sediment, which is dimensionless. $s = \rho_s/\rho_f = 2.65$ is the specific gravity of sediment, and the gravitational acceleration $g = 9.81$ m/s^2. The second term on the right-hand-side of equation (2.3) is the streamwise pressure gradient that drives the oscillatory fluid motion with a free-stream velocity amplitude of $\widetilde{U}_0$, and an angular wave frequency of $\widetilde{\omega}$, and $\widetilde{\omega} = 2\pi/\widetilde{T}$, where $\widetilde{T}$ is the wave period. The last term on the right-hand-side of equation (2.3) is the buoyancy term, which is resulted from simplifying the drag force using the equilibrium Eulerian approximation (Cantero et al. 2008). This term represents the coupling between the sediment and the carrier fluid via the sediment-induced density stratification.

By consistently applying the equilibrium Eulerian approximation to the mass conservation of sediment, the governing equation of sediment concentration is written as:

$$\frac{\partial \phi}{\partial \widetilde{t}} + \frac{\partial \phi(\widetilde{u}_i - \widetilde{W}_s\delta_{i3})}{\partial \widetilde{x}_i} = \kappa \frac{\partial^2 \phi}{\partial \widetilde{x}_i \partial \widetilde{x}_i}. \tag{2.4}$$

In this study, the free-stream velocity amplitude $\widetilde{U}_0$ is chosen as the characteristic velocity scale, and the Stokes boundary layer thickness $\widetilde{\Delta}$ is selected to be the characteristic length scale of the flow:

$$\widetilde{\Delta} = \sqrt{\frac{2\nu}{\widetilde{\omega}}}. \tag{2.5}$$

Consequently, the flow characteristic time scale is calculated as $\widetilde{\tau}_l = \widetilde{\Delta}/\widetilde{U}_0$, and the non-dimensional flow variables can be defined as:

$$x_i = \frac{\widetilde{x}_i}{\widetilde{\Delta}}, t = \frac{\widetilde{t}}{\widetilde{\tau}_l}, u_i = \frac{\widetilde{u}_i}{\widetilde{U}_0}, W_s = \frac{\widetilde{W}_s}{\widetilde{U}_0}, p = \frac{\widetilde{p}}{\rho_f \widetilde{U}_0^2}. \tag{2.6}$$

The resulting non-dimensional continuity and momentum equations for fluid flow are

written as:

$$\frac{\partial u_i}{\partial x_i} = 0, \tag{2.7}$$

$$\frac{\partial u_i}{\partial t} + u_j \frac{\partial u_i}{\partial x_j} = -\frac{\partial p}{\partial x_i} - \frac{2}{Re_\Delta} \sin\left(\frac{2t}{Re_\Delta}\right)\delta_{i1} + \frac{1}{Re_\Delta}\frac{\partial^2 u_i}{\partial x_j \partial x_j} - \frac{1}{Fr^2}\phi\delta_{i3}, \tag{2.8}$$

where $Re_\Delta = \widetilde{U}_0\widetilde{\Delta}/\nu$ is the Stokes Reynolds number, which is used to quantify the wave intensity. In the previous studies by Ozdemir et al. (2010, 2011), the total amount of sediment in the domain is constant throughout each simulation and hence the last term in equation (2.8) is represented by a bulk Richardson number (see definition in equation (2.19)). Different from Ozdemir et al. (2010, 2011), the bottom stress can suspend sediments from the bottom boundary and the total amount of sediment in the domain is part of the solution of the model. Therefore, the particle Froude number $Fr = \widetilde{U}_0/\sqrt{(s-1)g\widetilde{\Delta}}$ is introduced instead in this study.

The non-dimensional transport equation for sediment concentration is written as:

$$\frac{\partial \phi}{\partial t} + \frac{\partial \phi(u_i - W_s\delta_{i3})}{\partial x_i} = \frac{1}{Re_\Delta Sc}\frac{\partial^2 \phi}{\partial x_i \partial x_i}, \tag{2.9}$$

where Sc is the Schmidt number, $Sc = \nu/\kappa$. The right-hand-side of equation (2.9) accounts for the sub-grid scale particle motion. Following the previous studies by Ozdemir et al. (2010) and Yu et al. (2014), Sc is chosen to be 0.5.

2.2.2 Model domain and boundary conditions

In this study, we idealize the bottom boundary layer to be statistically homogeneous in streamwise (x) and spanwise (y) directions. The domain is bounded by wall boundaries in the vertical direction (see Figure 2.1). For fluid phase velocity, wall boundaries are assumed to be hydraulically smooth, and no-slip and no-penetration boundary conditions are imposed at these walls. With this assumption, any effect due to the existence of bedforms is ignored. Periodic conditions are implemented at the streamwise and spanwise boundaries. Similarly, periodic boundary conditions are adopted for sediment concentration at the streamwise and spanwise boundaries. As

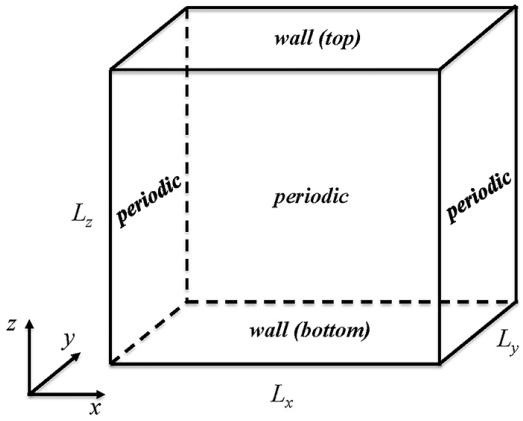

Figure 2.1: Sketch of computation domain and definition of coordinate system.

it is illustrated in the following sections, the domain height is sufficiently large, and we assume no mass exchange through the top wall boundary and no-flux boundary condition is specified:

$$-W_s\phi - \frac{1}{Re_\Delta Sc}\frac{\partial\phi}{\partial z}\Big|_{z=L_z} = 0, \tag{2.10}$$

where $z = L_z$ is located at the top of the domain.

To allow sediments to be resuspended/deposited from/to the bottom, the erodible/depositional boundary condition is implemented at the bottom boundary:

$$-W_s\phi - \frac{1}{Re_\Delta Sc}\frac{\partial\phi}{\partial z}\Big|_{z=0} = E - D, \tag{2.11}$$

where E and D are the non-dimensional erosional and depositional fluxes at the bottom, respectively, and both E and D are normalized by the free-stream velocity magnitude $\widetilde{U}_0$. Since many empirical parameters involved in erosional/depositional formulas are measured or presented in dimensional forms (e.g., Hill et al. 2000, Sanford & Maa 2001), the dimensional forms of the depositional flux and the erosional flux are discussed here. The depositional flux is specified following the continuous erosion-deposition

formulation (Sanford & Maa 2001, Winterwerp 2007):

$$\widetilde{D} = \widetilde{W}_s \phi \Big|_{\widetilde{z}=0}. \tag{2.12}$$

The erosion rate $\widetilde{E}$ is calculated by the Partheniades-Ariathurai type formulation (e.g., Sanford & Maa 2001), and it is presented here in the non-dimensional form:

$$\widetilde{E} = \begin{cases} \widetilde{m}_e \left(\frac{|\widetilde{\tau}_b|}{\widetilde{\tau}_c} - 1 \right), & |\widetilde{\tau}_b| \geq \widetilde{\tau}_c \\ 0, & |\widetilde{\tau}_b| < \widetilde{\tau}_c \end{cases}, \tag{2.13}$$

where $\widetilde{m}_e$ is the dimensional empirical coefficient of erosion rate, $|\widetilde{\tau}_b|$ is the magnitude of the bottom shear stress, and it is calculated as:

$$|\widetilde{\tau}_b| = \rho_f \nu \left| \frac{\partial \widetilde{u}}{\partial \widetilde{z}} \right|_{\widetilde{z}=0}, \tag{2.14}$$

and the critical shear stress of erosion is represented by $\widetilde{\tau}_c$. For fine sediments, both $\widetilde{m}_e$ and $\widetilde{\tau}_c$ depend on the degree of consolidation, and need to be determined from erosion tests. In this paper, $\widetilde{m}_e$ is assumed to be constant and its dimensional value is specified to be 3.05×10^{-7} m/s for all the cases, and the selected values of $\widetilde{\tau}_c$ range from 0.01 to 0.6 Pa in order to study the effect of critical shear stress on a diverse range of transport characteristics. Due to consolidation, the critical shear stress may increase with depth in the sediment bed (e.g., Parchure & Mehta 1985, Sanford & Maa 2001). However, this level of complexity is beyond the scope of the present study, and $\widetilde{\tau}_c$ is kept constant in each simulation.

2.2.3 Numerical method

A recently developed turbulence-resolving hybrid spectral-compact finite difference scheme for fine sediment transport in the bottom boundary layer (Yu et al. 2013) is utilized in this study. In a turbulence-resolving approach, high resolution three-dimensional grid points are employed to directly resolve flow instabilities, nonlinear growth of turbulent fluctuations and their evolution and dissipation. At the Stokes

Reynolds number selected in this study ($Re_\Delta = 1000$), all the essential turbulence scales, including the Kolmogorov scale estimated for clear flow (sediment-free) condition, are resolved (Yu et al. 2014, Ozdemir et al. 2014). Fourier expansions are adopted in both streamwise and spanwise directions, which enforce the periodic boundary conditions in these directions. More details on the pseudo-spectral scheme of the present model can be found in Cortese & Balachandar (1995). In the vertical (wall-normal) direction, a sixth-order centered compact finite difference scheme is implemented on Chebyshev-Gauss-Lobatto points, where more grid points are clustered at both the top and the bottom boundaries. With this extension, more complicated (nonlinear) boundary conditions, such as erodible/depositional boundary condition for sediments, can be implemented while maintaining spectral-like accuracy. More details on the compact finite difference scheme of the present model can be found in Yu et al. (2013, 2014). Equations (2.7) and (2.8) are solved with a standard projection method (Chorin 1968). For diffusion terms, the Crank-Nicolson scheme is used. Non-linear advection terms are calculated by the Arakawa method (Arakawa & Lamb 1981) with the 2/3 de-aliasing law, and integrated by a third-order low-storage Runge-Kutta scheme. A direct solver (Yu et al. 2013) is used to solve the pressure Poisson equation. For the equation of sediment concentration, same numerical methods are used where applicable.

2.3 Model Results

Compared to Ozdemir et al. (2010, 2011), where the sediment availability is kept constant, an additional layer of complexity is introduced by the erodible bed condition in this study. Therefore, it is instructive to examine the mechanism controlling the sediment availability in the present model in order to motivate the scientific issues to be investigated here.

In this study, the initial condition for fluid flow is chosen to be the fully-developed clear fluid oscillatory flow of $Re_\Delta = 1000$ (Case 0 in Table 2.1) for each numerical simulation. Once the bottom stress exceeds the threshold value of erosion, sediments are then suspended from the bottom boundary following equation (2.13).

Meanwhile, sediments will deposit to the bottom through equation (2.12). The net flux through the bottom boundary adjusts the total amount of sediment in the domain and if the wave forcing condition remains unchanged, a statistical equilibrium can be reached where the time-averaged net sediment flux over one wave period eventually become zero, or $\overline{\widetilde{E}} = \overline{\widetilde{D}}$, where '$\overline{\ }$' represents wave-averaged quantities, i.e., time average over one wave cycle. Using equations (2.12) and (2.13), we obtain the following approximated relationship controlling the wave-averaged bottom stress at equilibrium:

$$\overline{\widetilde{\tau}}_{eq} \approx \left(\frac{\widetilde{W}_s \overline{\phi}_{eq}}{\widetilde{m}_e} + 1 \right) \widetilde{\tau}_c, \tag{2.15}$$

where $\overline{\phi}_{eq}$ is the wave-averaged equilibrium sediment concentration at the bottom. This equation is only an approximated relationship to estimate $\overline{\widetilde{\tau}}_{eq}$ because there is always a portion of the wave cycle when bottom stress is below the critical shear stress of erosion (e.g., see Figure 2.2(b)). However, for cases with low $\widetilde{\tau}_c$, equation (2.15) is expected to be reasonably accurate. The physical interpretation of this relationship can be explained as follows. As sediments are suspended into the domain, the bottom shear stress is reduced due to attenuated turbulence via sediment-induced density stratification. According to equation (2.15), the equilibrium state is established when the wave-averaged bottom stress is reduced to $\overline{\widetilde{\tau}}_{eq}$, which is a function of erodibility parameters, namely, the critical shear stress of erosion $\widetilde{\tau}_c$ and m_e, and settling velocity. Moreover, smaller $\overline{\widetilde{\tau}}_{eq}$ indicates larger sediment availability (or larger wave- and domain-averaged sediment concentration), because sediment availability is proportional to the difference between initial bottom stress without sediment (wave-averaged bottom stress in the clear fluid condition) and $\overline{\widetilde{\tau}}_{eq}$. In other words, equation (2.15) provides an approximated relationship between sediment availability and sediment/bed properties. Thus, our goal is to study the interplay between resuspension and deposition, which determines sediment availability and thereby the resulting transport modes.

2.3.1 Simulation setup

Following previous studies (Ozdemir et al. 2010, Yu et al. 2014), we choose a wave condition with free-stream velocity amplitude $\widetilde{U}_0 = 0.56$ m/s, and period $\widetilde{T} = 10$ s to represent a more energetic flow condition when fine sediments form high concentration suspension on continental shelves (Traykovski et al. 2000). In the following sections, we will mostly interpret the results in dimensional quantities under this specific wave condition. The resulting Stokes boundary layer thickness is calculated to be $\widetilde{\Delta} = 1.78$ mm, and the Stokes Reynolds number is $Re_\Delta = 1000$. The given Stokes Reynolds number lies in the range of intermittently turbulent flow where the flow can reach fully turbulent only for a portion of the wave cycle (e.g., Jensen et al. 1989, Ozdemir et al. 2014). Following the direct numerical simulation of oscillatory turbulent channel flow (Spalart & Baldwin 1989) at $Re_\Delta = 1000$, the domain size is selected to be $\widetilde{L}_x \times \widetilde{L}_y \times \widetilde{L}_z = 60\widetilde{\Delta} \times 30\widetilde{\Delta} \times 60\widetilde{\Delta}$. This domain size is demonstrated to be large enough to resolve the largest turbulent eddies (Ozdemir et al. 2010). The number of grid points is given as $N_x \times N_y \times N_z = 128 \times 128 \times 257$ with uniform grids in both streamwise and spanwise directions. In the vertical direction, Chebyshev-Gauss-Lobatto collocation points are used. The given discretization is the same as Yu et al. (2014), and has been verified to be sufficient to resolve turbulent scales.

In this study, sixteen numerical simulations are presented to study the effects of the sediment availability through resuspension/deposition on controlling the transport characteristics (see Table 2.1). The sediment availability in the domain is controlled by two competing mechanisms at the bottom boundary, i.e., the erosion and the deposition flux. Due to consolidation, sand content and bio-chemical effects, a wide range of the critical shear stress of erosion has been observed (e.g., Stevens et al. 2007). It has been reported that a loosely consolidated fine sediment layer is resuspended by the bottom shear stress as low as 0.01 Pa (Curran et al. 2007). Therefore, we consider critical shear stress to be in the range of $\widetilde{\tau}_c = 0.01 \sim 0.6$ Pa (see Table 2.1). Within this range, significant variations in the flow transport characteristics are observed. On the other hand, the deposition flux, which is mainly controlled by the settling velocity, depends

Table 2.1: List of simulations presented in the study of fine sediment transport modes.

Case	$\widetilde{\tau}_c$(Pa)	W_s	$\widetilde{W}_s(mm/s)$	$\overline{\Phi}_{eq}$	$\overline{\widetilde{\tau}}_{eq}$(Pa)	Transport mode
0	NA	NA	NA	NA	0.45	NA
1	0.01	9.0×10^{-4}	0.5	6.2×10^{-4}	0.28	III
2	0.02	9.0×10^{-4}	0.5	1.8×10^{-3}	0.39	II
3	0.05	9.0×10^{-4}	0.5	1×10^{-3}	0.43	II
4	0.6	9.0×10^{-4}	0.5	4.9×10^{-5}	0.45	I
5	0.02	3.0×10^{-4}	0.17	3.1×10^{-3}	0.28	III
6	0.02	18×10^{-4}	1.0	6.9×10^{-4}	0.42	II
7	0.02	21×10^{-4}	1.17	5.6×10^{-4}	0.42	II
8	0.02	27×10^{-4}	1.5	3.6×10^{-4}	0.43	II
9	0.3	27×10^{-4}	1.5	1.8×10^{-5}	0.45	I
10	0.01	27×10^{-4}	1.5	4.8×10^{-4}	0.40	II
11	0.01	18×10^{-4}	1.0	1.6×10^{-4}	0.28	III
12	0.1	18×10^{-4}	1.0	1.8×10^{-4}	0.44	II
13	0.2	18×10^{-4}	1.0	7.8×10^{-5}	0.45	II
14	0.3	18×10^{-4}	1.0	4.2×10^{-5}	0.45	I
15	0.4	9×10^{-4}	0.5	8×10^{-5}	0.44	II

on sediment properties, namely particle size and density. Although the settling velocity is a variable due to flocculation and hindered settling, it is more insightful at this point to use a constant settling velocity to investigate the interplay between the sediment exchange with the bed and turbulence modulation in determining the resulting flow transport mode. We consider fine sediments with non-dimensional settling velocity between 3×10^{-4} and 27×10^{-4}, which corresponds to the commonly encountered dimensional settling velocity that ranges between 0.17 mm/s and 1.5 mm/s (see Table 2.1). For non-cohesive sediment, both the settling velocity and the critical shear stress are dependent on sediment properties (e.g., grain size and density) (Shields 1936), and therefore they are directly related. However, for cohesive sediment, there is no universal relationship between the settling velocity and the critical shear stress due to flocculation, consolidation and chemical-biological effects (Sanford & Maa 2001). Thus the critical shear stress of erosion and the settling velocity are considered to vary independently in this study.

2.3.2 Transport modes under different critical shear stress of erosion

According to equation (2.15), the critical shear stress of erosion $\widetilde{\tau}_c$ plays a key role in controlling the sediment availability and hence the resulting transport characteristics. This conjecture is demonstrated in this section. We discuss simulation results due to different $\widetilde{\tau}_c$ by comparing Cases 1-4 (see Table 2.1). Figure 2.2(a) shows time series of the non-dimensional free stream velocity. The definition of the wave phase (ωt) is also shown in this figure, that is, $\omega t = 0$ ($\omega t = \pi$) corresponds to the positive (negative) peak of free-stream velocity, and $\omega t = \pi/2$ and $3\pi/2$ correspond to flow reversals. The comparison between the ensemble-averaged bottom shear stress of clear flow condition and $\widetilde{\tau}_c$ associated with each case is shown in Figure 2.2(b). The magnitude of the ensemble-averaged bottom shear stress is calculated from the simulation results by averaging over the x-y plane, which is denoted by '$\langle\ \ \rangle$'. We can see that although the bottom shear stress varies over the entire wave cycle in each case, there is always a portion of the wave cycle where the bottom stress magnitude exceeds the critical shear stress. Therefore, in all the cases sediment is suspended. It is also noted that the difference between the critical shear stress and the peak bottom shear stress is largest for Case 1, and is smallest for Case 4. Thus, from the erosion rate formulation (see equation (2.13)), it is expected that the sediment availability is the largest for Case 1, while the smallest for Case 4.

Figure 2.2(c) shows the temporal variation of domain-averaged suspended sediment concentration, which is defined as:

$$\Phi = \frac{1}{L_z}\int_0^{L_z} \langle\phi\rangle dz. \tag{2.16}$$

We can see that a lower critical shear stress generally leads to a higher Φ in the domain except for Case 1. When the domain-averaged sediment concentration increases to about $\Phi = 1.3 \times 10^{-3}$ in Case 1, a decrease in Φ is observed after the third cycle. As we will demonstrate later (e.g., see Figure 2.6), due to the rapid resuspension associated with the low critical shear stress, the flow turbulence in Case 1 is completely attenuated

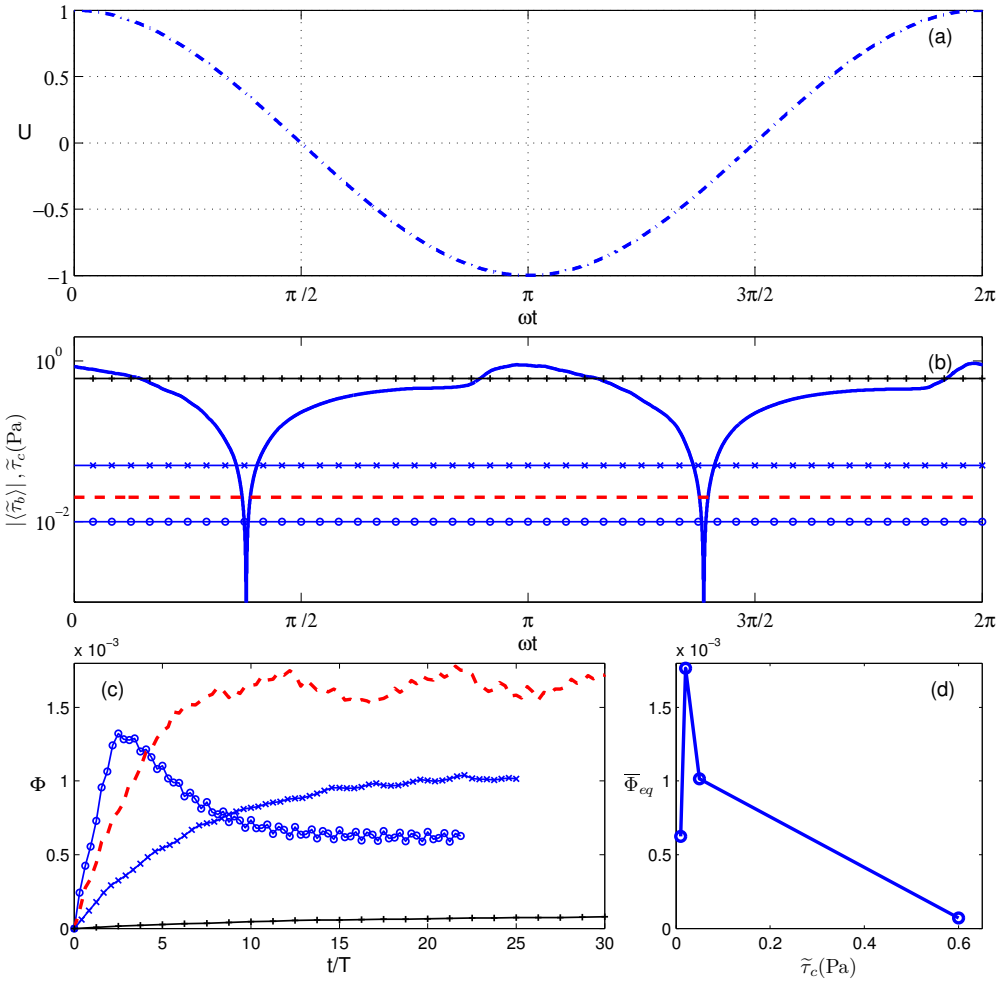

Figure 2.2: (a) Time series of the nondimensional free-stream velocity; (b) Comparison of the magnitude of ensemble-averaged bottom shear stress for clear fluid condition (Case 0, solid curve) and the critical shear stress of erosion for Case 1 (curve with circle symbols), Case 2 (dashed curve), Case 3 (curve with cross symbols); Case 4 (curve with plus symbols). The logarithmic scale is used in y-axis for better illustration; (c) Time series of the domain-averaged sediment concentration for Case 1 (curve with circle symbols), Case 2 (dashed curve), Case 3 (curve with cross symbols); Case 4 (curve with plus symbols); (d) comparison of the wave- and domain-averaged sediment concentration for different critical shear stress of erosion.

after a couple of wave cycles, and the flow eventually becomes laminar. For Cases 2-4, the corresponding $\widetilde{\tau}_c$ is larger and the amount of resuspended sediment from the bottom

at the initial stage increases more gradually (see Figure 2.2(c)). Hence, the flows are still turbulent and the domain-averaged sediment concentrations keep increasing until a quasi-equilibrium state (an equilibrium balance between the erosion flux $\overline{E}$ and the settling flux $\overline{D}$) has been reached. A comparison of the wave- and domain-averaged sediment concentration at the quasi-equilibrium state $\overline{\Phi}_{eq}$ for Cases 1-4 is shown in Figure 2.2(d). From now on, we will refer to $\overline{\Phi}_{eq}$ as sediment availability. For Cases 2-4, as the critical shear stress increases, it is evident that sediment availability decrease (see Figure 2.2 (d)). However, the results also indicate that $\overline{\Phi}_{eq}$ in Case 1 (lowest critical shear stress) is less than that in Case 2 or Case 3. This seemingly unexpected trend for Case 1 is due to the reduction in bottom shear stress. Therefore, the sediment availability is not solely related to the critical shear stress, but also affected by the sediment-turbulence interaction. The turbulence structures under different critical shear stresses for Case 1, 2 and 4 are further illustrated by the iso-surfaces of local swirling strength (λ_{ci}) during flow peak (see Figure 2.3 (a),(d),(g)). λ_{ci} is the imaginary part of the complex eigenvalue of the velocity gradient tensor and its magnitude can be used to quantify the strength of local swirling motion (Zhou et al. 1999). In Cases 2 and 4 (see Figure 2.3 (d) and (g)), some vortex structures are clearly observed over a portion of the bed. However, for Case 1 with the lowest critical shear stress of 0.01 Pa, no vortex structure is observed (see Figure 2.3(a)). Meanwhile, the corresponding iso-surfaces of concentration are also shown in Figure 2.3 (b) to (i). To better illustrate the resulting sediment concentration field near the bed (or in the middle of the domain), the contour level for the concentration iso-surface in Figure 2.3 (b), (e) and (h) (or (c), (f) and (i)) is chosen to be the plane-averaged concentration at $z = 2.5$ (or $z = 20$) in each case. Since there are no turbulent coherent structures observed in Case 1 (Figure 2.3(a)), a flat near-bed iso-surface of concentration field is obtained in Figure 2.3(b), which further indicates that the flow turbulence is suppressed in the lower part of the channel. However, irregular structures of very dilute concentration can still be observed at around $z = 20$ due to turbulence generated from the top wall (see Figure 2.3(c)). As the critical shear stress is increased to 0.02 Pa in Case 2, sparse coherent

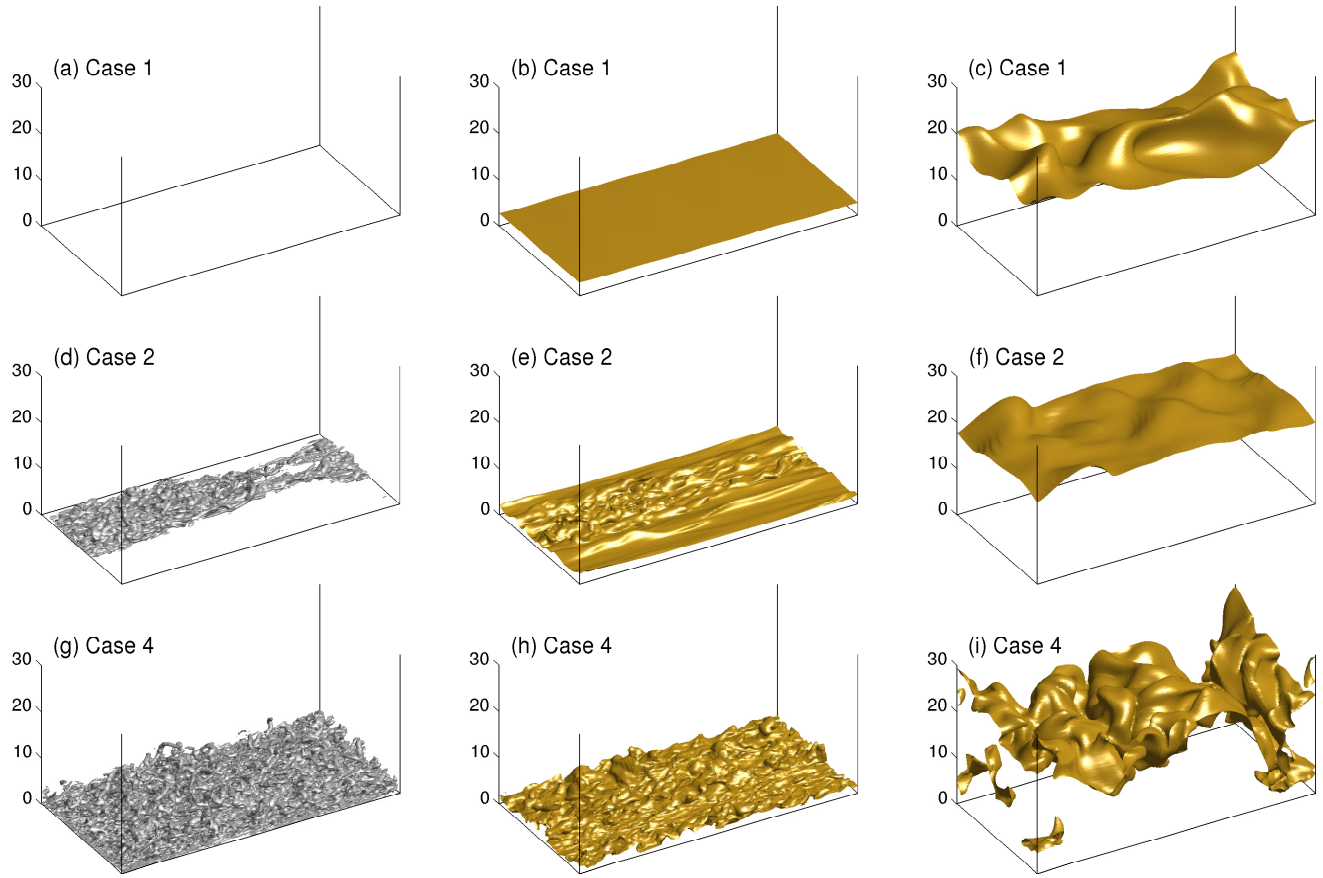

Figure 2.3: Turbulent coherent structures for (a) Case 1, (d) Case 2 and (g) Case 4 visualized using the swirling strength (λ_{ci}) at flow peak ($\omega t = 0$). The contour level used here is 5% of the maximum λ_{ci} value in Case 4. (b), (d) and (h) show the corresponding iso-surface of near-bed sediment concentration at flow peak. The contour level is chosen to be the average concentration at $z = 2.5$ with $\phi = 0.005$, 8.2×10^{-3}, 9.2×10^{-5} for Case 1, Case 2 and Case 4, respectively. (c), (f) , (i) show the corresponding iso-surface of sediment concentration in the middle of the domain at flow peak. The contour level is chosen to be the average concentration at $z = 20$ with $\phi = 2.2 \times 10^{-5}$, $\phi = 6.8 \times 10^{-4}$, 7.6×10^{-5} for Case 1, Case 2 and Case 4, respectively.

vortex structures can be observed over a portion of the near-bed region (see Figure 2.3(d)). This region is corresponding to a stripe of more irregular/chaotic sediment concentration structures shown in Figure 2.3(e). In the middle of the channel at $z = 20$ (see Figure 2.3(f)), the iso-surface of sediment concentration is much less chaotic, which suggests a much weaker turbulence. As the critical shear stress is further increased to 0.6 Pa in Case 4, it is evident that the turbulence near the bed is much stronger with denser near-bed turbulent structures (see Figure 2.3(g)). In this case, the iso-surface of sediment concentration in the middle of the domain (at $z = 20$, see Figure 2.3(i)) is similarly chaotic, suggesting that turbulence is sufficiently large throughout the domain. Comparing to iso-surface of sediment concentration in Case 2, it is clear that fluctuations in sediment concentration are much stronger in Case 4 (Figure 2.3(i)), implying that the turbulence in Case 2 is significantly suppressed in the middle of the domain despite the flow remains turbulent near the bed.

More quantitative comparisons on how the critical shear stress determines the sediment availability and the resulting flow field are presented through ensemble-averaged flow statistics. Figure 2.4 shows ensemble-averaged profiles of sediment concentration, streamwise velocity and turbulent intensity during flow peak and flow reversal for Case 1, 2 and 4. For a better illustration, only the bottom half channel ($z = 0 \sim 30$) is shown here. Several distinct features can be observed from the concentration profiles (Figure 2.4 (a),(d)). Firstly, sediment concentration profile of Case 4 is relatively uniform throughout the lower half of the domain and although not shown here, the profiles of turbulent intensity and streamwise velocity in Case 4 is almost identical to those of the clear fluid condition. The high critical shear stress of Case 4 significantly limits sediment availability and available sediments have almost no impact on the flow turbulence throughout the boundary layer (Figure 2.4 (c),(f)). Hence, the flow features observed in Case 4 show quite similar characteristics of a well-mixed condition (regime I) that was previously reported by Ozdemir et al. (2010) due to a very low sediment availability.

On the contrary, concentration profiles of Case 1 are distinctly different from

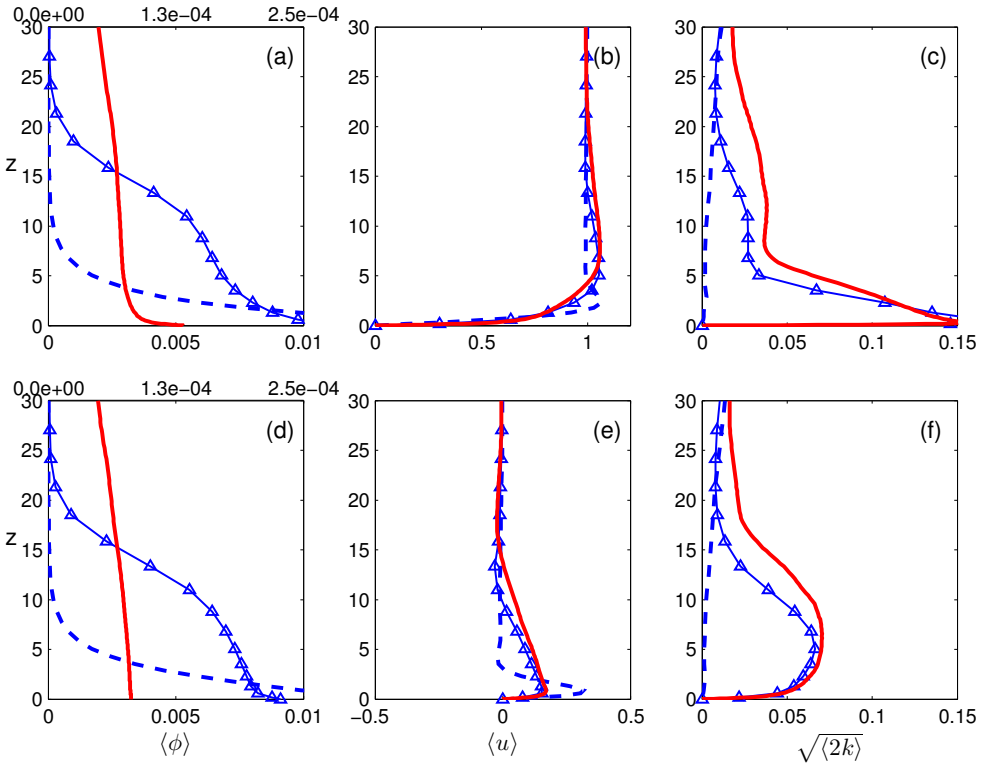

Figure 2.4: Ensemble-averaged profiles of (a) sediment concentration, (b) non-dimensional streamwise velocity and (c) non-dimensional turbulence intensity during flow peak ($\omega t = 0$) for Case 1 (dashed curve), Case 2 (curve with triangle symbol), Case 4 (solid curve); The corresponding profiles during flow reversal ($\omega t = 3\pi/2$) are shown in (d), (e) and (f). In (a) and (d), the top x-axis is the concentration scale for Case 4, and the bottom axis is the concentration scale for Case 1 and Case 2.

those of Case 4. High sediment concentration only accumulates very close to the bed and decays rapidly away from the bed. The sharp decrease of concentration is clearly associated with nearly zero turbulent intensity (see Figure2.4 (c),(f)) throughout the lower half of the channel. The streamwise velocity profile in Figure 2.4(b) shows that the boundary layer thickness is about 3 times smaller than that in Case 4 (or the clear fluid condition), consistent with nearly annihilated turbulence and mixing. Although not shown, the streamwise velocity profiles at different wave phases are basically identical to the laminar flow solution. Flow features presented here are consistent with the

regime IV reported by Ozdemir et al. (2010), where the flow is completely laminarized by a large availability of sediment. However, the initial large sediment availability obtained here is controlled by a very low critical shear stress.

For Case 2, where its $\widetilde{\tau}_c$ is two times larger than that of Case 1, a relatively sharp negative gradient of sediment concentration (lutocline) can be seen around $z = 10 \sim 15$, while this feature is absent in Case 1 and Case 4. Through sediment-induced density stratification, the lutocline separates the upper quasi-laminar layer from the lower turbulent layer, and hence a classic two-layer system in stably stratified flow is obtained. Such feature can be clearly seen in the profiles of turbulent intensity shown in Figure 2.4 (c) and (f). Below $z = 10$, the turbulent intensity of Case 2 is comparable to that of Case 4 (or the clear fluid condition). However, the turbulent intensity above $z = 15$ is less than 50% of that in Case 4. The two-layer-like features of Case 2 are consistent with the regime II reported by Ozdemir et al. (2010) for moderate sediment availabilities. In summary, by varying the critical shear stress of erosion to control the sediment availability, simulation results presented here demonstrate the existence of three distinct transport modes over a range of critical shear stresses, namely, a well-mixed condition (transport mode I), the formation of lutocline and two-layer-like system (transport mode II) and a laminarized transport (transport mode III). Probably due to the highly transitional and ephemeral nature of regime III reported by Ozdemir et al. (2010), where shear instabilities are observed in the laminarized transport during flow reversal, we do not observe such flow feature here. However, the main transport characteristics of regime III are essentially laminarized flow and we will only categorize three transport modes in this study.

Figure 2.5 shows the time series of bottom shear stress associated with different critical shear stresses of erosion (Cases 1, 2, and 4) and the sediment-free case (Case 0). Case 4 (large $\widetilde{\tau}_c$ and transport mode I) shows the typical turbulent behavior of bottom shear stress (Spalart & Baldwin 1989, Jensen et al. 1989). At the reversal of bottom shear stress ($\widetilde{\tau}_b = 0$), the phase lead between the bottom shear stress and free stream velocity is about 25°. The burst of bottom shear stress occurs during the

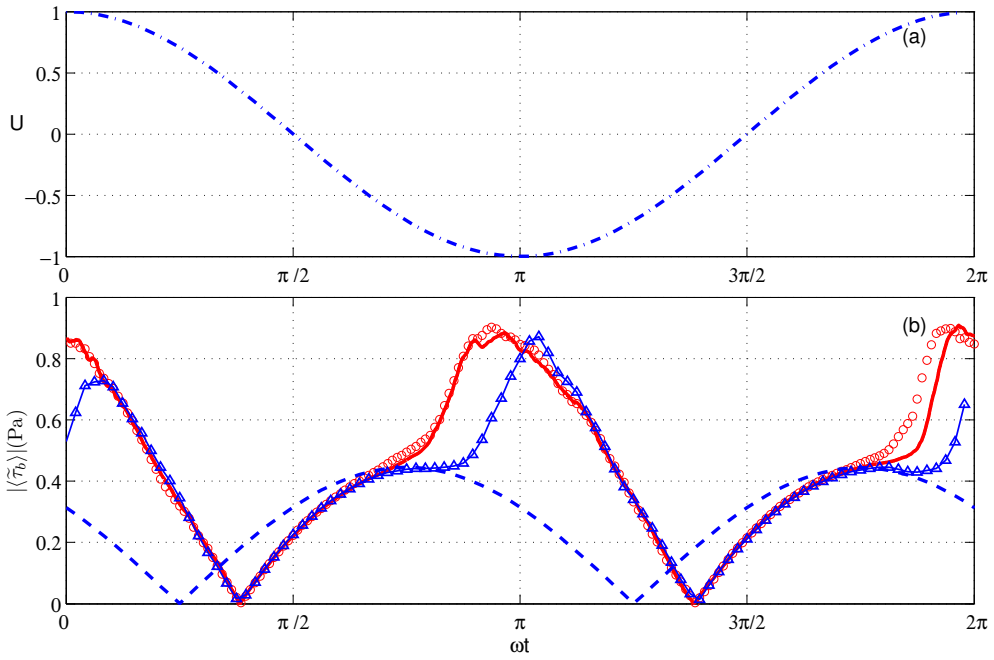

Figure 2.5: (a) Time series of the nondimensional free stream velocity, U; (b) Time series of the ensemble-averaged bottom shear stress $|\langle\widetilde{\tau}_b\rangle|$ for Case 0 (circle symbol), Case 1 (dashed curve), Case 2 (curve with triangle symbol), Case 4 (solid curves).

end of acceleration phase (at about $\omega t = 3/4\pi$), which then peaks shortly before the free-steam velocity reaches its maximum. The time series of bottom stress obtained for Case 4 is quite similar to that of the clear fluid condition, except for very slight temporal delay associated with the initiation of the burst. However, for Case 2 with smaller $\widetilde{\tau}_c$ (transport mode II), the burst of bottom stress occurs later during the deceleration phase and peaks shortly before flow reversal. Moreover, a reduction of peak bottom shear stress associated with the burst is also observed. This reduction of peak shear stress is consistent with the turbulence attenuation by sediment-induced density stratification. However, we would also like to point out that in terms of phase lead with respect to the free-stream velocity, Case 2 is very close to that of Case 4, suggesting the flow near the bed in Case 2 remains to be turbulent. On the other hand, the bottom shear stress time series of Case 1 clearly shows distinctly different

behaviors as compared to Case 2 and Case 4. No burst of bottom shear stress is observed throughout the wave cycle, and the phase lead between bottom shear stress and free stream velocity becomes 45°, which is exactly the same as that of laminar flow. In fact, the time series of bottom shear stress is identical to the laminar solution of oscillatory flow, which is consistent with Figure 2.4 that the turbulence in Case 1 is completely attenuated by the sediment-induced density stratification.

Because each simulation is carried out with no initial sediment in the domain, the development into laminarized transport mode III can also be observed through the temporal evolution of the flow field in Case 1 (see Figure 2.6). As the bottom shear stress exceeds the threshold of erosion $\widetilde{\tau}_c$, sediments are suspended from the bottom, and the domain-averaged sediment concentration increases rapidly for the first two waves (see Figure 2.6(a)). Notice that during the first two wave cycles, the time-series of bottom stress shows typical turbulent features. The plane-averaged velocity profile at $t = 2T$ shows that the shear associated with the bottom boundary layer extends to about $z = 15$ (see Figure 2.6(b1)) and within which, sediments are also suspended (Figure 2.6(b2)). The turbulent intensity is significant below $z = 5$ at this early stage of simulation (Figure 2.6(b3)). Also, chaotic motions can be identified through the iso-surface of sediment concentration near the bed (Figure 2.6(b4)). At the third wave cycle, more sediments are suspended and the domain-averaged sediment concentration time series reaches its peak value. However, at the same time, we also observe that the bottom shear stress is significantly reduced and becomes identical to the laminar solution. From the iso-surface of sediment concentration, the flow field is much less chaotic (see Figure 2.6(c4)) and only some mild wave-like features can be observed. It is also evident from approximately 98% reduction in the turbulent intensity (Figure 2.6(c3)) that the turbulence is significantly suppressed and consequently, the boundary layer thickness is also reduced (see velocity profile shown in Figure 2.6(c1)). Due to considerable turbulence attenuation, the flow becomes insufficient to keep such amount of sediment suspended, and the domain-averaged sediment concentration begins to cease after $t = 3T$. Eventually, the flow turbulence is terminated (see Figure 2.6(d3)), and

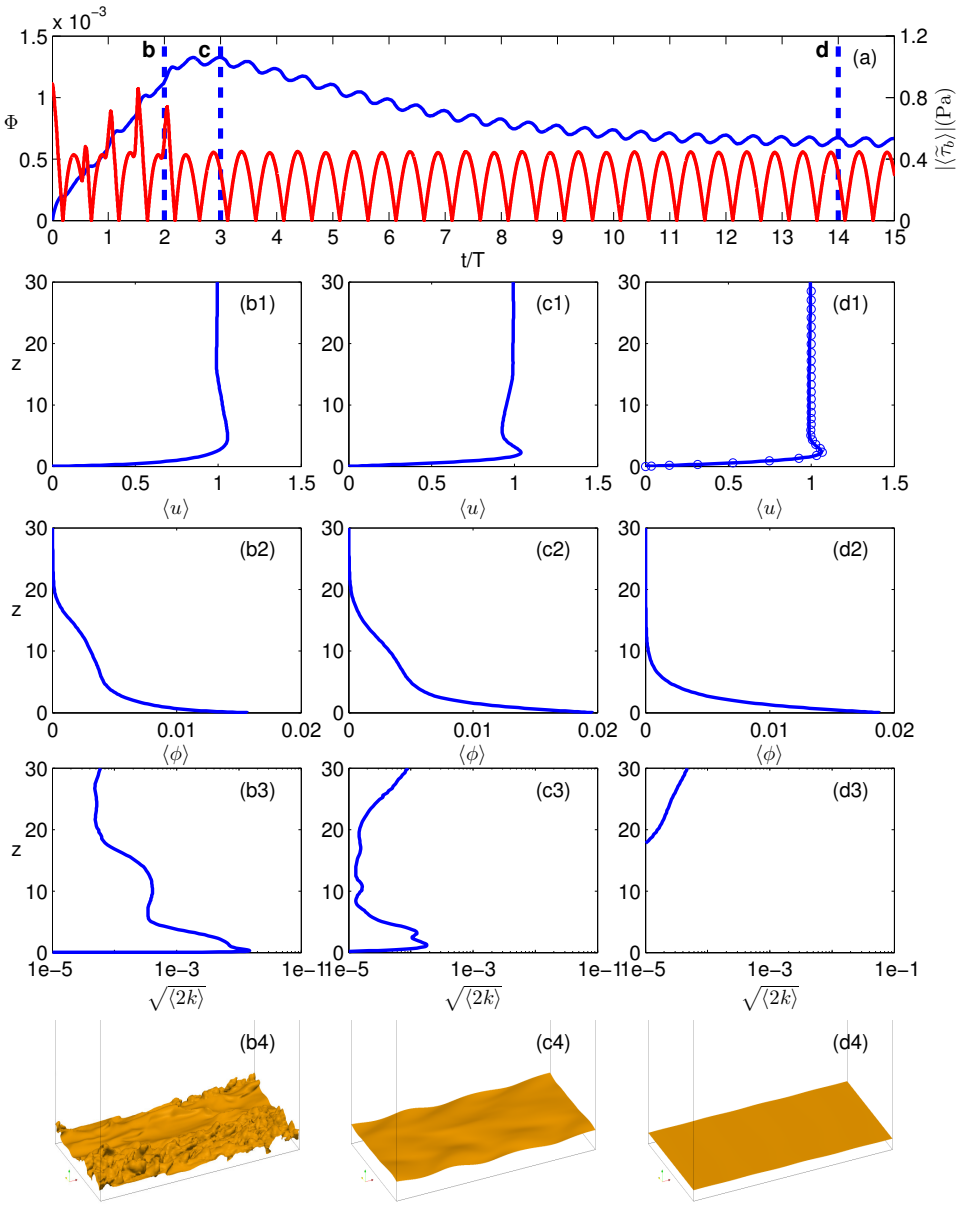

Figure 2.6: (a) Time series of the domain averaged sediment concentration Φ (blue solid curve) and the ensemble-averaged bottom shear stress $|\langle\widetilde{\tau}_b\rangle|$ (red solid curve) for Case 1. The sampled instant shown (b),(c),(d) are denoted as blue dash lines. (b1-b4) present the ensemble-averaged profiles of streamwise velocity, sediment concentration, turbulence intensity, and iso-surface of concentration (=4Φ) at $t = 2T$. Similar plots are presented here at instant (c) $t = 3T$ and instant (d) $t = 14T$. In (c1), the laminar solution of streamwise velocity is shown as open circles. In (b3), (c3) and (d3), logarithmic scale is used in x-axis for a better illustration.

the domain-averaged sediment concentration reaches a statistical equilibrium, where the settling flux is balanced with the viscous suspension, and hence the sediment availability in the laminarized flow further depends on the Schmidt number Sc value used (see Ozdemir et al. (2010) for more detail). In this equilibrium state, the streamwise velocity profile becomes identical to the laminar solution (see Figure 2.6(d1)).

Regarding the laminarized flow mode obtained in the present simulation, we like to make a few comments regarding its relevance to reality. Because the perturbation is not continuously applied in the simulation (except in the initial condition), the flow turbulence is not re-energized in the simulation in the post-laminarization stage even when the sediment availability in the domain later reduces due to deposition. In reality, perturbations may be persistent and the dynamics in the post-laminarization stage may be more complex. Moreover, it is also likely that the final flow mode may depend on the initial condition, especially under the critical condition for flow laminarization (e.g., Shringarpure et al. 2012). In fact, these critical flow scenarios can be associated with the surging and waning of a storm and they will be investigated in the future.

The transition of flow transport modes in Case 1 is further illustrated by profiles of the flux Richardson number (Ri_f), which is defined as:

$$Ri_f = -\frac{(s-1)g\widetilde{\Delta}\langle\phi' w'\rangle}{\widetilde{U}_0^2\langle u'w'\rangle\frac{\partial\langle u\rangle}{\partial z}}, \tag{2.17}$$

where primes denotes fluctuations from the ensemble-averaged quantities. The flux Richardson number is the ratio of stable density stratification term (dissipation of turbulence) to turbulence production term in the turbulent kinetic energy (TKE) budget, and it is often used to quantify the degree of the stable density stratification effect on the flow turbulence. In Figure 2.7, the flux Richardson number profiles at $t = 2T$ and $t = 3T$ in Case 1 are presented. After the first two wave cycles during which finite amount of sediments are suspended from the bottom (see Figure 2.6(a)), the flow remains turbulent, and the flux Richardson number is below the critical value of 0.25 near the bed ($z < 5$). Between $z = 4.5 \sim 5$, where a lutocline is present, the flux

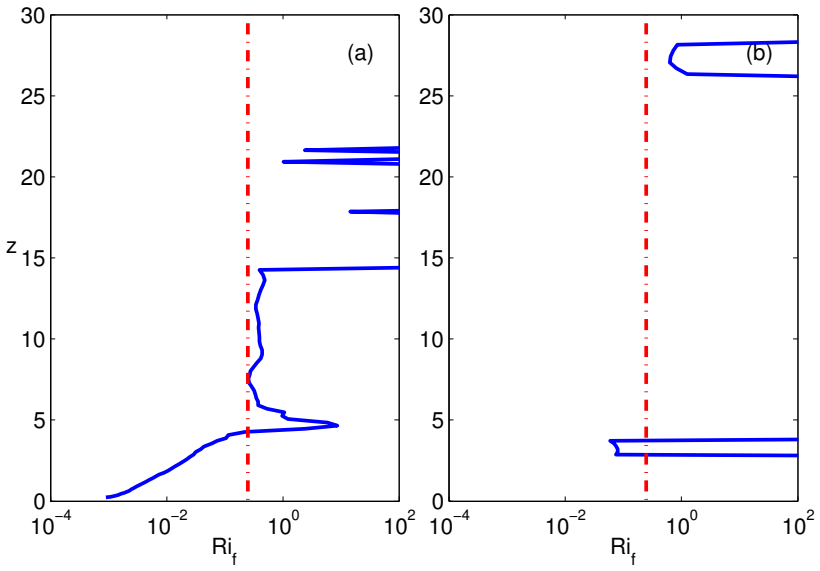

Figure 2.7: Flux Richardson number profiles of Case 1 at two different instants, (a) $t = 2T$ (see b in Figure 2.6); (b) $t = 3T$ (see c in Figure 2.6). The dash-doted lines denote the critical Richardson number of 0.25.

Richardson number increases rapidly and exceeds 0.25, suggesting that a significantly attenuated turbulence at around $z = 5$ is observed. Between $z = 6 \sim 15$, the flux Richardson number approaches a constant but the turbulence intensity here is one order of magnitude lower than that below the lutocline. In other words, at this early stage of sediment suspension in Case 1, the flow is similar to transport mode II. However, after one more wave at $t = 3T$ (see Figure 2.7(b)), the flux Richardson number exceeds 0.25 for almost the entire channel, indicating a collapse of turbulence. This collapse is also consistent with the laminar flow feature described in Figure 2.6 (c1) $\sim$ (c4).

Based on the results presented so far, we observe three distinct transport modes by varying the critical shear stress of erosion in order to control the sediment availability. The resulting three transport modes are similar to the flow regimes I, II and IV described by Ozdemir et al. (2010). It is found that under the Stokes Reynolds number $Re_\Delta = 1000$ and a fixed settling velocity of $\widetilde{W}_s = 0.5$ mm/s, a very low critical shear stress (very high erodibility) as low as 0.01 Pa can cause significant

turbulence suppression by sediment induced stable density stratification that further leads to laminarized flow (transport mode III). Interestingly, a slightly increased critical shear stress ($\widetilde{\tau}_c \geq 0.02$ Pa) causes lower sediment availability, much less turbulence attenuation and the formation of lutocline that separates the turbulent layer from the upper quasi-laminar layer (transport mode II). When the critical shear stress is sufficiently large ($\widetilde{\tau}_c \geq 0.6$ Pa), the sediment availability is very low such that the effect sediment-induced density stratification on the turbulence is negligible (transport mode I).

2.3.3 Transport modes under different settling velocities

The previous section discussed how the critical shear stress of erosion $\widetilde{\tau}_c$ can control the sediment availability and the resulting transport mode for a fixed settling velocity. Further investigations on the effect of settling velocity for a fixed $\widetilde{\tau}_c$ are necessary. Although this study does not explicitly incorporate flocculation dynamics, we consider sediment settling velocity in the range of $0.17 \sim 1.5$ mm/s which is typical for fine sediment in the field condition (e.g., Hill et al. 2000). The study by Ozdemir et al. (2011) demonstrated that when the sediment availability is held constant in the domain, larger settling velocity leads to a sharper negative gradient of sediment concentration and hence a more intense turbulence attenuation via stable stratification. In this study, the sediment availability (or bottom stress at equilibrium) is controlled by equation (2.15), which also depends on the settling velocity. In fact, a more careful examination of equation (2.15) suggests that a larger settling velocity leads to a larger bottom stress at equilibrium and hence a lower sediment availability. When the sediment availability is lower, as shown in the previous section, the attenuation of turbulence is less pronounced. Therefore, the outcome of turbulence modulation due to varying settling velocity is not obvious without further numerical investigations.

Figure 2.8 compares profiles of the ensemble-averaged concentration, the streamwise velocity and the turbulent intensity for cases with a small (Case 5), medium (Case

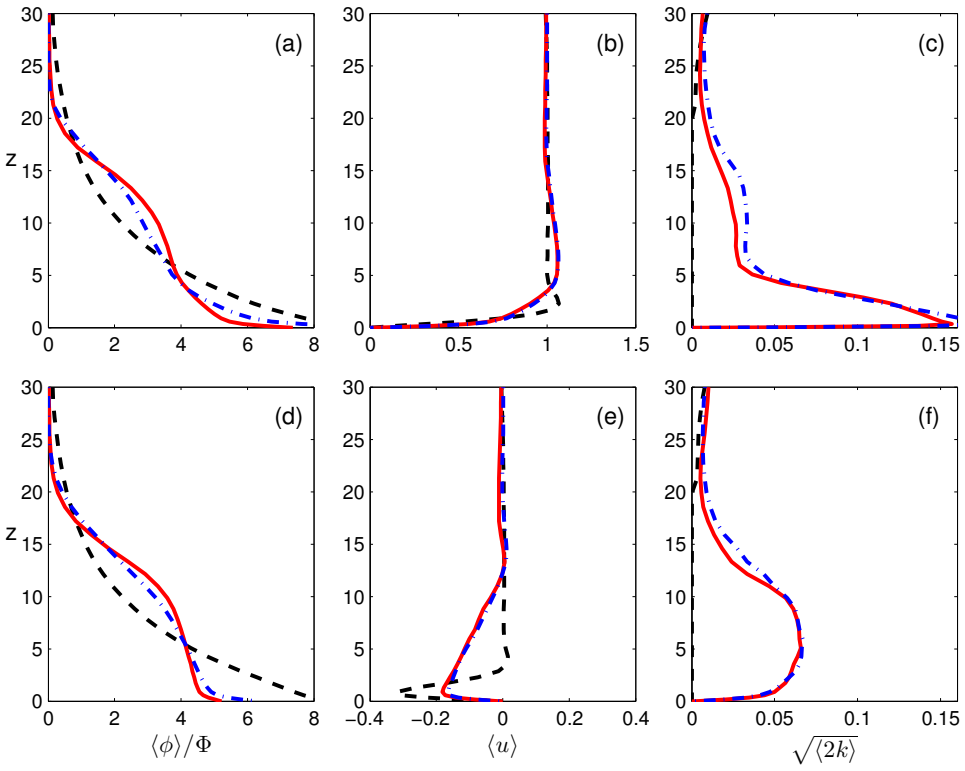

Figure 2.8: Ensemble-averaged profiles of (a) sediment concentration, (b) non-dimensional streamwise velocity and (c) non-dimensional turbulence intensity during flow peak ($\omega t = 0$) for Case 2 (solid curves), Case 5(dashed curves) and Case 6 (dash-dotted curves). Panels (d), (e), and (f) are the corresponding profiles during flow reversal ($\omega t = \pi/2$).

2) and large (Case 6) settling velocity at a fixed $\widetilde{\tau}_c = 0.02$ Pa (see Table 2.1). By keeping the critical shear stress constant, it is shown here that different transport modes are realized with different settling velocities. To better illustrate the differences, sediment concentrations are normalized by the domain-averaged sediment concentration. As discussed previously, Case 2 with $\widetilde{W}_s = 0.5$ mm/s corresponds to transport mode II. Decreasing the settling velocity to $\widetilde{W}_s = 0.17$ mm/s in Case 5 shows a significantly different concentration profile (Figure 2.8 (a),(d)). The lutocline is not present in the concentration profile of Case 5 and it is clear from Figure 2.8 (c),(f) that flow turbulence in Case 5 is completely suppressed. In Figure 2.8 (b),(e), it can be observed that the velocity profiles are identical to the laminar solution. With a three-fold reduction

of the settling velocity to $\widetilde{W}_s = 0.17$ mm/s, the laminarized transport mode III is observed in Case 5.

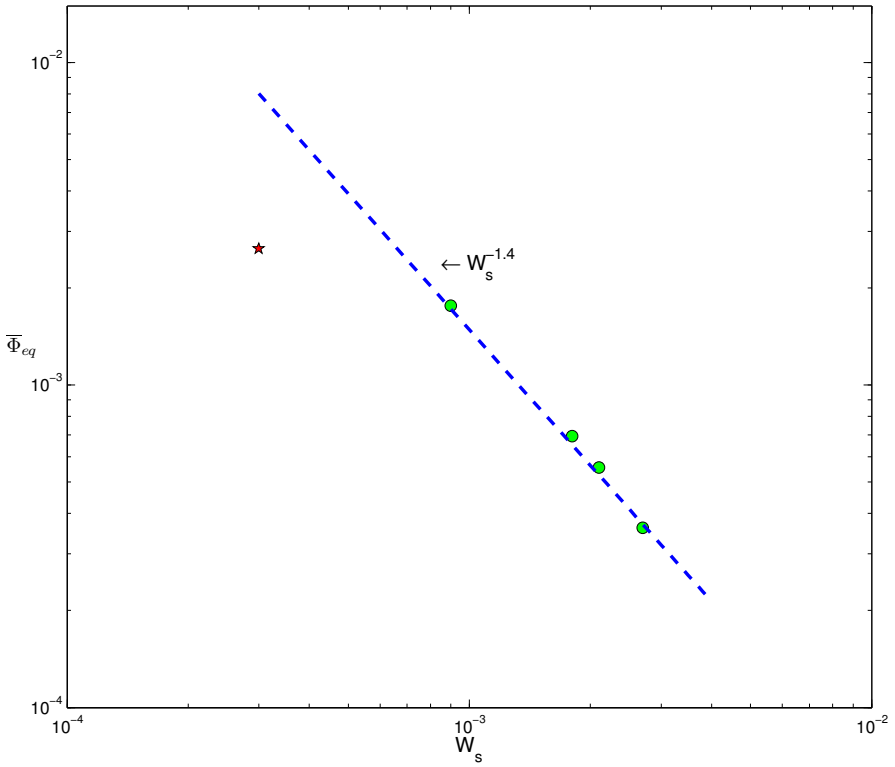

Figure 2.9: Wave- and domain-averaged sediment concentration $\overline{\Phi}_{eq}$ (or sediment availability) for cases of different settling velocity with a fixed $\widetilde{\tau}_c = 0.02$ Pa. Case 5 is shown in asterisk symbol and Case 2, 6, 7 and 8 are shown in circle symbol. The best-fit line (dashed) is $KW_s^{-1.4}$, where $K = 9.375 \times 10^{-8}$ is the proportional constant.

On the other hand, increasing the settling velocity from $\widetilde{W}_s = 0.5$ mm/s to $\widetilde{W}_s = 1.0$ mm/s (Case 6) still produces the transport mode II (see Figure 2.8). However, there is a slight increase in the lutocline elevation. In Case 2, the lutocline is located at around $z = 13$, while increasing the settling velocity twice (Case 6), the lutocline moves upward to about $z = 16$. Moreover, the turbulent intensity above $z = 5$ in Case 6 is also larger. By examining the sediment availability represented by the domain-averaged sediment concentration at equilibrium (see $\overline{\Phi}_{eq}$ in Table 1), it is

clear that Case 6 with a larger settling velocity has a much lower sediment availability. Hence, the higher lutocline location and stronger turbulence (weaker turbulence attenuation) in Case 6 can be explained by the lower sediment availability. In contrast, laminarized transport mode III, Case 5, is caused by the high sediment availability and the significant turbulence attenuation. Ozdemir et al. (2011) reported that, when the sediment availability is held constant in each simulation, a larger settling velocity leads to a more pronounced lutocline and stronger turbulence attenuation due to sediment-induced stable density stratification. However, numerical simulations where the sediment availability is determined by the bottom resuspension/deposition (i.e., equation (2.15)), suggest that the effect of setting velocity on the sediment availability is more significant than that on the vertical concentration profile in controlling the resulting fine sediment transport modes.

The carrying capacity concept provides a criterion on how available sediments and their settling velocities lead to laminarization in a steady boundary layer. Through utilizing the critical Richardson number for steady-state turbulent velocities and concentration profiles, the following relation is proposed (Winterwerp 2001):

$$\Phi_s = K_s \frac{\widetilde{u}_*^3}{(s-1)gh\widetilde{W}_s}, \tag{2.18}$$

where $\widetilde{u}_*$ is the friction velocity associated with the current, h is the flow depth and K_s is an empirical coefficient. The use of the given relation to calculate the saturation concentration in this study is not straightforward especially due to its dependence on the bottom shear stress through $\widetilde{u}_*$ and the time-periodic nature of the oscillatory flow. In addition, co-variability of the depositional and the erosional fluxes as a result of time-dependent flow characteristics should also be considered. However, for transport mode III, time-averaged laminar concentration profile reveals that the domain-averaged sediment concentration (sediment availability) is proportional to W_s^{-2}. Similarly, for transport mode I, approximating the concentration profile to a constant, the sediment availability is obtained to be proportional to W_s^{-1}. The sediment availability versus

the settling velocity is shown in Figure 2.9 for $\widetilde{\tau}_c = 0.02$ Pa (Cases 2, 5, 6, 7, and 8). Except for Case 2, where the flow becomes laminar, the sediment availability varies roughly linearly with $W_s^{-1.4}$. This sharper (milder) variation of available sediment concentration with respect to transport mode I (III) clearly identifies the role of the sediment-induced density stratification on the carrying capacity of the flow in a WBBL.

In summary, the settling velocity plays an important role in determining the sediment availability and the vertical structure of sediment concentration. For a low critical shear stress, the change in settling velocity is more dominant in controlling sediment availability than the vertical structure and hence a smaller settling velocity results in a larger sediment availability and a more significant sediment-induced density stratification which may lead to laminarized transport mode III. Simulation results also suggest that when the flow remains turbulent in transport mode II, the sediment availability $\overline{\Phi}_{eq}$ depends on non-dimensional settling velocity through a power law. Hence, the concept of carrying capacity may be used to parameterize the sediment availability in oscillatory bottom boundary layer for transport mode II.

2.4 Discussion

Ozdemir et al. (2011) summarized all the simulations carried out with fixed/prescribed sediment availability in a flow regime map (see Figure 2.10, open symbols) as a function of non-dimensional settling velocity W_s and a bulk Richardson number:

$$Ri = \frac{(s-1)g\widetilde{\Delta}}{\widetilde{U}_0^2}\Phi_0, \tag{2.19}$$

where Φ_0 is the prescribed domain-averaged sediment concentration. In the present study, sediments are allowed to be resuspended/deposited from/to the bottom depending on the flow intensity, the critical shear stress of erosion and the settling velocity. Hence, the domain-averaged concentration becomes a flow variable. However, using the domain- and wave-averaged sediment concentration at equilibrium $\overline{\Phi}_{eq}$ to replace Φ_0 in equation (2.19), the results obtained in this study (see solid symbols in Figure 2.10)

are plotted into the regime map proposed by Ozdemir et al. (2011). The transport modes I and II obtained from the present study are consistent with those reported by Ozdemir et al. (2011). Particularly, both models predict similar curves for the transition from turbulent to laminar state (see the thick dashed curve), which confirms that laminarization is directly triggered by sediment-induced density stratification. The resuspension/deposition mechanism implemented in the present study determines the transition between transport modes indirectly through controlling sediment availability. Notice that in the present simulations, once the flow becomes laminarized, i.e., mode III, the domain-averaged concentration starts to decrease and reaches another equilibrium in laminar flow with lower $\overline{\Phi}_{eq}$ (not shown here). Since bottom resuspension/deposition is a common scenario in fine sediment transport, it is crucial to further understand the criterion through which a sufficiently large sediment availability can be established and laminarization can occur. Such criterion is also useful toward developing a predictor for the onset of laminarization (transition from transport mode II to III). As sediments are suspended into the domain, the bottom stress is reduced due to the turbulence attenuation (see Figure 2.5(b)). The resulting wave-averaged equilibrium stress $\overline{\overline{\tau}}_{eq}$ is dependent on the settling velocity and the critical shear stress (see equation (2.15)), and their values are reported in Table 2.1 for all the cases considered in this study. Firstly, for those cases of transport mode III (laminarized transport, see Case 1, Case 5 and Case 11), we obtain that $\overline{\overline{\tau}}_{eq} = 0.28$ Pa, which is the value associated with laminar solution. Further examining Case 2 (or Case 10), where transport mode II is observed, but which is very close to transport mode III, the resulting wave-averaged equilibrium stress is $\overline{\overline{\tau}}_{eq} = 0.39$ Pa (or $\overline{\overline{\tau}}_{eq} = 0.4$ Pa). Therefore, the simulation results presented here suggest a transition from transport mode II to III, i.e., the onset of laminarization, occurs when the wave-averaged equilibrium bottom stress is reduced to below 0.39 Pa due to the turbulence attenuation by suspended sediments. The reason why this critical value leads to the onset of laminarization due to suspended sediments is elucidated next.

Ozdemir et al. (2014) carried out a series of direct numerical simulation (DNS) of

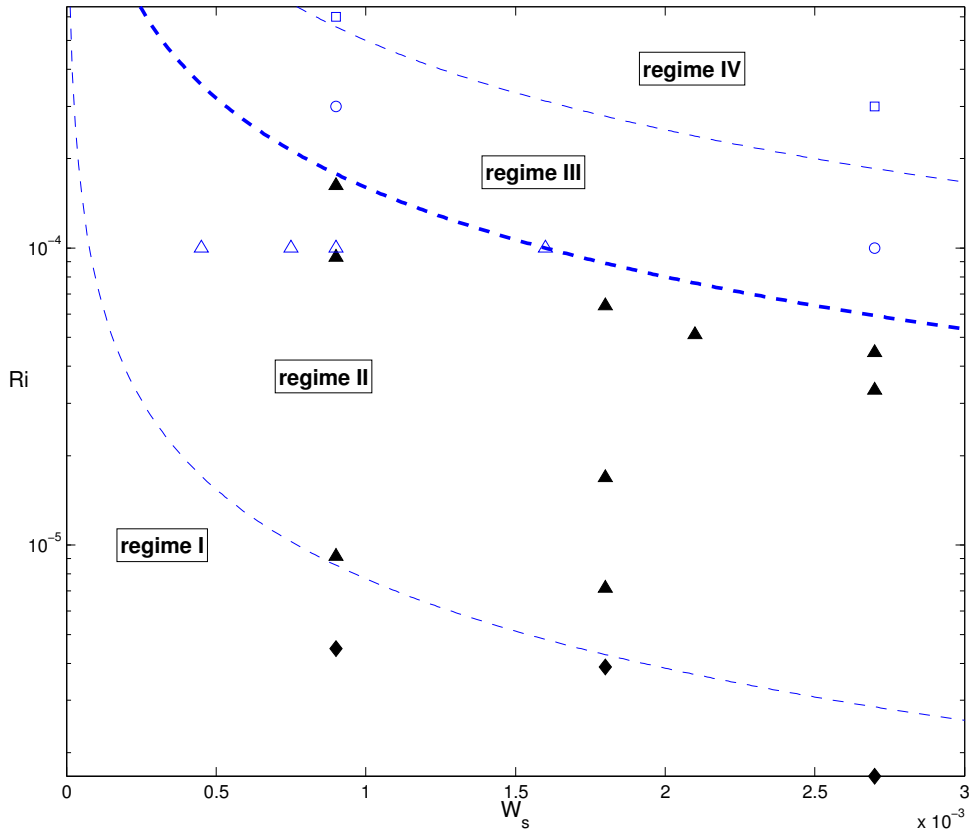

Figure 2.10: Schematic map of flow regime in terms of the bulk Richardson number Ri and the settling velocity W_s at Re_Δ=1000. The open symbols (♢: regime I; △: regime II; ○: regime III; □: regime IV) are earlier direct numerical simulations presented in (Ozdemir et al. 2011). Simulation results in the present paper (see Table 2.1) are consistent with (Ozdemir et al. 2011) for regime I (solid ♢) and regime II (solid △). The dashed curves are the borders between the regimes, specifically the thick dashed curve denotes the onset of laminarization.

clear fluid oscillatory boundary layer for Reynolds number ranging from $Re_\Delta = 500 \sim 1000$. The peak bottom shear stress value over one wave period at various Reynolds numbers are shown in Figure 2.11 (the curve with triangle symbols). The corresponding laminar peak bottom shear stresses are also shown (see the curve with circle symbols). As elaborated in Ozdemir et al. (2014), the flow in the range of $Re_\Delta = 550 \sim 700$ is classified as self-sustaining transitional flow in which flow instabilities can become

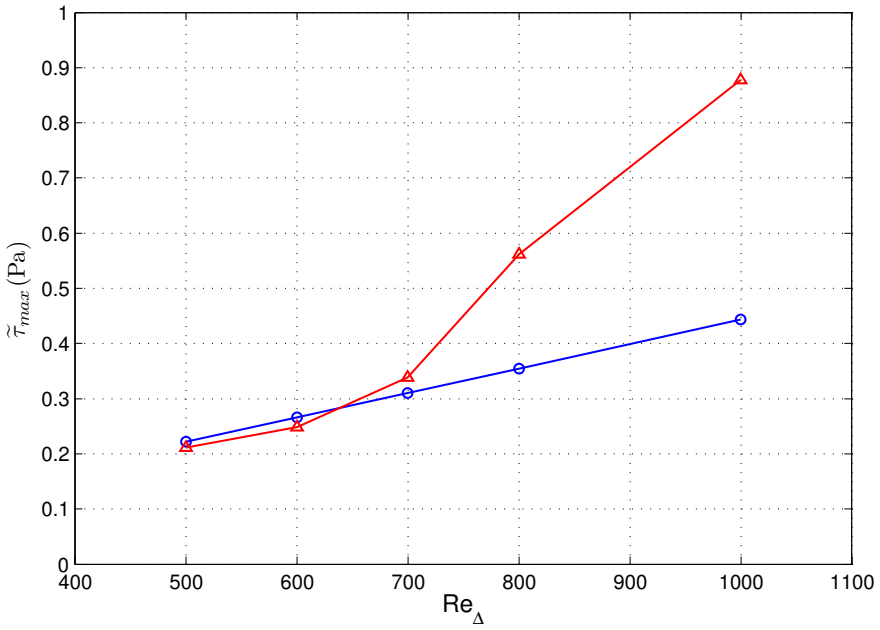

Figure 2.11: Peak bottom shear stress plotted against the Stokes Reynolds number Re_Δ for clear fluid discussed in (Ozdemir et al. 2014). DNS results are shown in the curve with triangle symbols, and analytical laminar solutions are shown in the curve with circle symbols.

nonlinear and sustain throughout the wave cycle. However, strictly speaking, the flow is not fully turbulent and a logarithmic velocity profile does not form at any instant. In the same study, the peak bottom stress in cases below $Re_\Delta \approx 700$ is close to the analytical laminar solution. However, the peak bottom shear stress starts to increase rapidly as the Reynolds number exceeds $Re_\Delta \approx 700$, at which the peak bottom shear stress is about 0.34 Pa. Inspired by the clear fluid simulation results, we observe a consistent result for sediment-laden condition. Namely, as $\widetilde{\overline{\tau}}_{eq}$ is reduced to below 0.39 Pa or possibly near 0.34 Pa due to the sediment-induced density stratification, the flow starts to show more or less laminar flow features, such as observed in Case 2.

Parameterizations or criteria for transition between the transport modes are important for the prediction of fine sediment transport in coastal environments. For example, the initiation of wave-supported gravity-driven mudflows (Traykovski et al. 2000) may require the formation of lutocline (i.e., transport mode II) in order to

accumulate sufficient buoyancy anomaly to drive downslope gravity flow. When the flow is laminarized, deposition occurs and wave-supported gravity-driven mudflows may be either terminated or sustained by hindered settling and enhanced viscosity due to rheological stress (Kampf & Myrow 2014). Although these important sediment transport processes are outside the scope of the present study, we would like to focus on providing a criterion to quantify the transition between the transport modes by utilizing the 15 cases presented here at the Stokes Reynolds number of Re_Δ=1000.

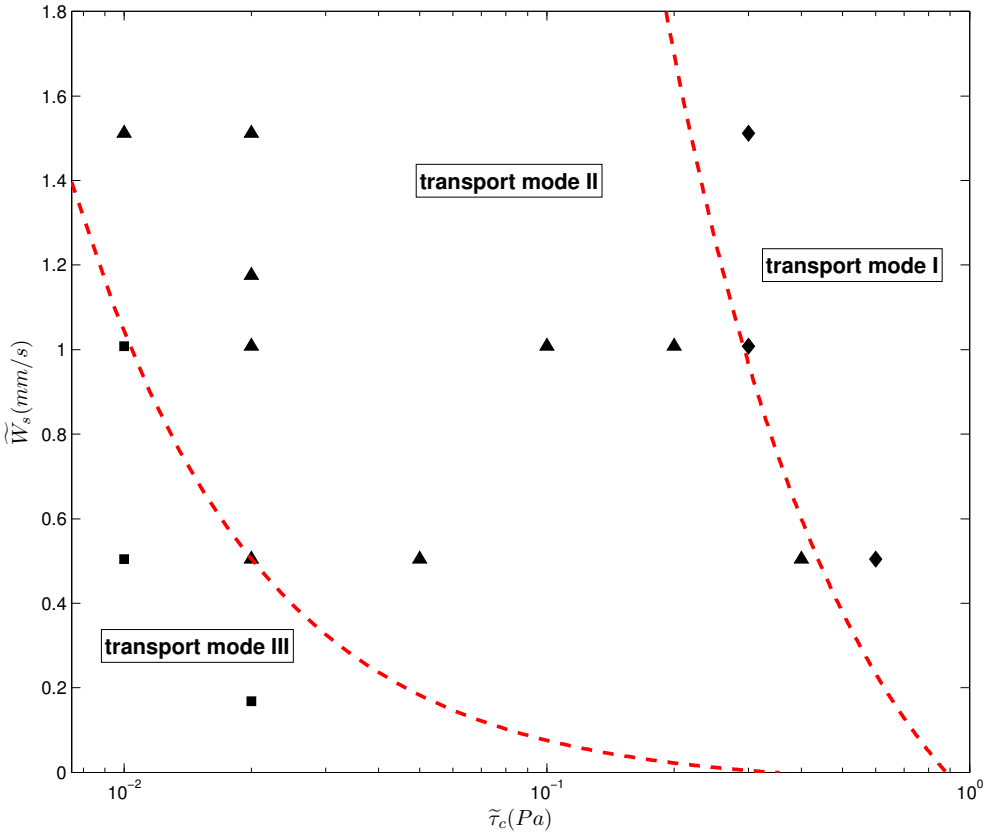

Figure 2.12: Schematic map of transport mode in terms of the critical shear stress of erosion $\widetilde{\tau}_c$ (Pa) and the settling velocity $\widetilde{W}_s$ (mm/s) at Re_Δ=1000 obtained in the present simulations (see Table 2.1) for transport mode I ($\diamondsuit$), transport mode II ($\triangle$) and transport mode III ($\square$). The dashed curves represent the border between the transport modes described by equation (2.20).

Given that the Stokes Reynolds number is fixed, the resulting transport modes must depend on the critical shear stress of erosion $\widetilde{\tau}_c$ and the settling velocity $\widetilde{W}_s$. A summary of all the cases investigated in this study is presented in Figure 2.12. A large critical shear stress represents a more consolidated bed or a limited supply of fine sediment, and hence a well-mixed dilute sediment suspension (transport mode I) is obtained. As $\widetilde{\tau}_c$ or $\widetilde{W}_s$ becomes smaller, more sediments are suspended in the domain (see equation (2.15)) and more pronounced sediment-induced density stratification can lead to the formation of lutocline (transport mode II) and eventually the laminarization of the entire boundary layer (transport mode III). Moreover, we also observe that the dependence of the transport mode is more sensitive on the critical shear stress of erosion than the settling velocity. To further describe the transition of these transport modes, namely the curves separating these three transport modes, a relationship that describes sediment availability is sought since it is the sediment availability that governs the turbulence attenuation and the resulting transport modes. Hence, rearranging equation (2.15), we propose the following semi-empirical relationship:

$$\frac{1}{\widetilde{W}_s}\left(\frac{\widetilde{\tau}_{tc}}{\widetilde{\tau}_c}-1\right)=\widetilde{K}_0=f(Re_\Delta,\widetilde{m}_e,\overline{\phi}_{eq}), \tag{2.20}$$

where $\widetilde{\tau}_{tc}$ is a characteristic shear stress to describe the transition of transport mode and $\widetilde{K}_0$, according to equation (2.15), should depend on the erodibility parameter $\widetilde{m}_e$, the sediment availability and the flow intensity. As the transition between transport mode II to III is simply a laminarization criterion, we adopt $\widetilde{\tau}_{tc}=0.34$ Pa, which shows hybrid characteristics of intermittently turbulent and self-sustaining transitional flows (Ozdemir et al. 2014). With $\widetilde{K}_0=32$ s/mm, the resulting semi-empirical relationship (equation (2.20)) follows the dashed curve in Figure 2.12. Meanwhile, for the border between transport modes I and II, we use $\widetilde{\tau}_{tc}=0.88$ Pa which corresponds to the peak bottom stress for a clear fluid condition at $Re_\Delta=1000$. The corresponding coefficient $\widetilde{K}_0$ is specified to be 2 s/mm.

2.5 Conclusion

The effects of the critical shear stress of erosion and the settling velocity on fine sediment transport in the oscillatory bottom boundary layer are investigated using a 3D turbulence-resolving model. Comparing to the earlier turbulence-resolving numerical studies with a fixed sediment availability (Ozdemir et al. 2010, 2011), this new model employs a widely used bottom erosional/depositional boundary condition for sediment concentration. Hence, the numerical model simulates a more common scenario where the amount of suspended sediment in the domain is part of the solution in each simulation. Model results reveal the existence of three transport modes, namely, the dilute suspension in well-mixed condition (transport mode I), the formation of lutocline due to moderately attenuated turbulence by sediment-induced stable density stratification (transport mode II), and laminarized flow due to a significant turbulence attenuation (transport mode III). The characteristics of these transport modes are similar to the flow regimes reported by Ozdemir et al. (2010, 2011). However, we further demonstrate that the transition of these transport modes is determined by the adopted erosional/depositional formulation, which controls the sediment availability and hence the degree of turbulence modulation. Particularly, a lower critical shear stress of erosion (high erodibility) leads to a larger sediment availability and a transport mode that represents more turbulence attenuation. Reducing the settling velocity also increases the sediment availability although its effect is less pronounced than the critical shear stress of erosion. We also demonstrate that the transition between different flow modes can be explained by the reduction of bottom stress due to the sediment-induced turbulence attenuation. Therefore, utilizing the bottom erosion/deposition formulation adopted in this study, semi-empirical relationships are proposed. The present study elucidates the mechanisms through which the sediment availability is controlled by bottom erosion/deposition that further leads to different transport modes of fine sediment in the oscillatory boundary layer. Our findings can be the foundation to explain transport modes observed under more complicated bottom erosion/deposition condition and different wave intensities.

2.6 Acknowledgments

This work is supported by National Science Foundation (OCE-1130217) and Office of Naval Research (N00014-14-1-0586) to the University of Delaware and National Science Foundation (OCE-1131016) to the University of Florida. Simulations presented in this paper are carried out on Chimera at the University of Delaware with funding supported by the National Science Foundation (CNS-0958512) and the Extreme Science and Engineering Discovery Environment, which is supported by National Science Foundation Grant No. TG-OCE100015. We thank Carl Friedrichs and an anonymous reviewer for their valuable comments.

Chapter 3

A NUMERICAL INVESTIGATION OF FINE SEDIMENT RESUSPENSION IN THE WAVE BOUNDARY LAYER – UNCERTAINTIES IN PARTICLE INERTIA AND HINDERED SETTLING

The wave bottom boundary layer is a major conduit delivering fine terrestrial sediments to continental margins. Hence, studying fine sediment resuspensions in the wave boundary layer is crucial to the understanding of various components of the earth system, such as carbon cycles. By assuming the settling velocity to be a constant in each simulation, previous turbulence-resolving numerical simulations reveal the existence of three transport modes in the wave boundary layer associated with sediment availabilities. As the sediment availability and hence the sediment-induced stable stratification increases, a sequence of transport modes, namely, (I) well-mixed transport, (II) formulation of lutocline resembling a two-layer system, and (III) completely laminarized transport are observed. In general, the settling velocity is a flow variable due to hindered settling and particle inertia effects. Present numerical simulations including the particle inertia suggest that for a typical wave condition in continental shelves, the effect of particle inertia is negligible. Through additional numerical experiments, we also confirm that the particle inertia tends (up to the Stokes number $St = 0.2$) to attenuate flow turbulence. On the other hand, for flocs with lower gelling concentrations, the hindered settling can play a key role in sustaining a large amount of suspended sediments and results in the laminarized transport (III). For the simulation with a very significant hindered settling effect due to a low gelling concentration, results also indicate the occurrence of gelling ignition, a state in which the erosion rate is always higher than the deposition rate. A sufficient condition for the occurrence of gelling ignition is hypothesized for a range of wave intensities as a function of sediment/floc

properties and erodibility parameters. Major content to be presented in this chapter has been published in Cheng et al. (2015b).

3.1 Introduction

Fine sediments delivered by rivers are the main vehicle to carry terrestrial organic carbon, nutrients and anthropogenic contaminants to the ocean (e.g., Milliman & Farnsworth 2011). According to Hedges et al. (1997), about 1.5×10^{14} g of particulate organic carbon (POC) is delivered to the ocean annually. However, only a very small amount of POC is preserved. Therefore, studying the fate of terrestrial sediment in continental margins, such as the physical mechanisms that control the delivery processes (e.g., Hale et al. 2014, Kniskern et al. 2014, Kolker et al. 2014) is one of the essential steps to better understand the global carbon cycle. The physical processes driving sediment source to sink are classified into three stages, namely, initial deposition, resuspension and final deposition (Wright & Nittrouer 1995). Due to a variety of mechanisms associated with sediment-laden riverine outflow dynamics (e.g., trapping, flocculation), initial deposition of fine sediment is typically located within the inner-shelf (e.g., Geyer et al. 2000, Bever et al. 2011). Hence, resuspension can play a crucial role to further deliver fine sediment offshore. In the past decade, it has been well-established in many systems, for example, Eel river (Traykovski et al. 2000, Ogston et al. 2000), Po delta (Traykovski et al. 2007), Waiapu (Ma et al. 2008) and Waipaoa (Hale et al. 2014), that during large wave events, concentrated fine sediment suspension can be maintained in the wave-current bottom boundary layer and the resulting high buoyancy anomaly drives offshore transport of fine sediment even over relatively mild shelf slopes. This process is referred to as the wave-supported sediment-driven gravity flow.

A high buoyancy anomaly is clearly prerequisite for offshore-directed gravity flow (Wright et al. 1988, Sternberg et al. 1996). Field observations by Traykovski et al. (2000, 2007) suggest that the occurrence of high buoyancy anomaly in fine sediment transport requires sufficiently strong turbulence as well as the formation of a lutocline, a

sharp negative sediment concentration gradient near the top of the wave boundary layer (Ross & Mehta 1989). The existence of a lutocline indicates that the flow turbulence is suppressed by the sediment-induced stable density stratification, which effectively traps suspended sediments within a few centimeters near the bed, i.e., a form of convergence typically found during the formation of gravity flow (Ogston et al. 2000). Yet, the flow below the lutocline remains turbulent (Noh & Fernando 1991, Trowbridge & Kineke 1994) or at least transitionally turbulent (Ozdemir et al. 2010), so that the suspension is sufficiently mobile to drive gravity flows on mild slopes.

Due to interactions among descending particles, upward flow motions are generated and hence the collective settling velocity of particles is reduced from the single particle settling velocity. This is the well-known hindered settling effect (e.g., Winterwerp & Van Kesteren 2004, Fredsoe & Deigaard 1992). For non-cohesive sediments, hindered settling is a relatively well-constrained process (Richardson & Zaki 1954, Jimenez & Madsen 2003). For example, the reference concentration, often introduced in the hindered settling parameterization, is generally agreed to be the random-close-packing concentration of sediment (around 0.6 in terms of volumetric concentration). For fine sediments that often become cohesive in the coastal waters, the hindered settling plays a critical role in the slow deposition and consolidation processes. However, the parameterization of hindered settling for cohesive sediment is poorly constrained due to uncertainties in flocculation. When flocs are considered, the 'gelling concentration' is typically introduced to replace the reference concentration in the hindered settling parameterization (Dankers & Winterwerp 2007), and it is defined as the concentration at which floc aggregates form concentrated aggregate networks (Winterwerp & Van Kesteren 2004). However, the gelling concentration has a wide range of values due to variabilities in floc structures. For more organic and porous flocs with low fractal dimensions, the gelling concentration can be as low as $\sim$100 g/L. In this case, Kampf & Myrow (2014) argue that the fine sediment transport in the bottom boundary layer can fall into a situation, called gelling ignition, in which the deposition flux is always lower than the erosion flux, and this gelling ignition will lead to a net increase

of suspended sediment.

To understand fine sediment transport in the wave boundary layer due to episodic river floodings where the sediment supply is controlled by the river input, a series of three-dimensional (3D) turbulence-resolving numerical simulations based on a highly accurate pseudo-spectral scheme were carried out by Ozdemir et al. (2010) at the Stokes Reynolds number of $Re_\Delta = 1000$. This Re_Δ corresponds to a most energetic wave condition at Eel River inner shelf with near bed wave-induced velocity amplitude of 0.56 m/s and wave period of 10 s (Traykovski et al. 2000). With a prescribed/fixed amount of sediments in the domain in each simulation, model results demonstrated that the effect of sediment-induced density stratification is associated with the prescribed sediment load and the settling velocity, which leads to several distinct flow regimes. However, a more common scenario of sediment supply in the bottom boundary layer is due to the bottom resuspension/deposition where sediment availability is also a flow variable. Yu et al. (2013) developed a hybrid spectral-compact finite difference simulation model to study the fine sediment transport in the bottom boundary layer. Comparing to the pseudo-spectral scheme, this hybrid scheme is more flexible to incorporate variable viscosity, and nonlinear boundary conditions. Cheng et al. (2015a) adopt this new scheme to study how a range of sediment/bed properties associated with resuspension can control the sediment availability and the resulting transport. Simulation results reveal that the sediment availability is highly dependent on the resuspension/deposition mechanism from/to the bed. Specifically, a decrease (increase) of critical shear stress of erosion or settling velocity causes a growth (reduction) of sediment availability and three distinct transport modes are revealed: Transport mode I is of dilute, well-mixed sediment distribution where the attenuation of turbulence by sediments is negligible due to a low sediment concentration ($\ll$1 g/L); Transport mode II is similar to the two-layer flow in stably stratified flow signified by the formation of lutocline due to moderate turbulence attenuation by sediment-induced density stratification. A high concentration mud suspension layer occurs near the bed with a typical layer thickness of no more than $O(10)$ cm; Transport mode III is characterized by very

significant attenuation of turbulence due to the presence of high sediment concentration which laminarizes the bottom boundary layer. As similar transport modes are observed in the field or in the laboratory (Traykovski et al. 2007, Lamb et al. 2004, Sahin et al. 2012, Traykovski et al. 2015), it is important to better quantify the occurrence of these transport modes because they directly control sediment fluxes. For example, the transport mode I is the familiar dilute suspension and the net transport is determined by the flux divergence of suspended load (Harris & Wiberg 2002). When transport mode II occurs, large buoyancy anomaly caused by high suspended sediment concentration can encourage offshore delivery of fine sediments through gravity flows. When transport mode III occurs, it is believed that gravity flows may be terminated or maintained by gelling ignition due to the predominance of hindered settling effect (Kampf & Myrow 2014).

In most of the numerical models for fine sediment transport, the particle velocity can be calculated by the equilibrium Eulerian approximation (Balachandar & Eaton 2010), that is, a vectorial sum of the local fluid velocity, the settling velocity and additional particle inertia terms associated with the Stokes number. This approximation is only appropriate for particles of Stokes number much smaller than unity. From the theoretical perspective (Balachandar & Eaton 2010), the particle inertia effect is another mechanism to deviate the particle velocity from the fluid velocity, especially in turbulent flows with high accelerations (Cantero et al. 2008). However, these additional terms are also ignored in the aforementioned turbulence-resolving studies. There is a need to quantify the effect of neglecting the particle inertia on fine sediment transport for typical wave conditions encountered in the continental shelves.

The purpose of this study is to evaluate and quantify the uncertainties associated with the parameterization of particle velocity of fine sediment transport in the wave boundary layer using a series of turbulence-resolving simulation. Model formulations are discussed in Section 3.2. The sensitivity of the particle inertial effect for typical energetic wave conditions in the inner-shelves is first evaluated (Section 3.3), and the effect of different degrees of hindered settling due to a range of gelling concentrations

is then investigated in Section 3.4. Further discussions on the particle inertia effect on turbulence modulation and gelling ignition are presented in Section 3.5. Concluding remarks are given in Section 3.6.

3.2 Mathematical Formulations

3.2.1 Governing equation

Following previous studies (Ozdemir et al. 2010, Cheng et al. 2015a), the wave condition with a free-stream velocity magnitude $\widetilde{U}_0 = 0.56$ m/s and a wave period $\widetilde{T}$=10 s is considered to represent a relatively energetic flow condition when fine sediments form high concentration suspensions on continental shelves (e.g., Traykovski et al. 2000). The Stokes boundary layer thickness is calculated to be $\widetilde{\Delta} = \sqrt{2\nu/\widetilde{\omega}} = 1.78$ mm, in which ν is the fluid kinematic viscosity and $\widetilde{\omega} = 2\pi/T$ is the wave angular frequency. The resulting Stokes Reynolds number is $Re_\Delta = \widetilde{U}_0\widetilde{\Delta}/\nu = 1000$. This Stokes Reynolds number is in the range of intermittently turbulent flow where the fully turbulent condition can only be attained for a portion of the wave cycle (e.g., Jensen et al. 1989). The dimensional settling velocity is set to be $\widetilde{W}_{s0} = 0.5$ mm/s, which is typical for fine sediments in marine environments (Hill et al. 2000).

To generalize the simulation results, flow variables are nondimensionalized and a set of dimensionless equations are solved in this study. We choose the free-stream velocity amplitude $\widetilde{U}_0$ as the characteristic velocity scale, and the Stokes boundary layer thickness $\widetilde{\Delta}$ as the characteristic length scale. Consequently, the characteristic time scale of fluid flow is calculated as $\widetilde{t}_l = \widetilde{\Delta}/\widetilde{U}_0$. Hence, the non-dimensional flow variables are defined as:

$$x_i = \frac{\widetilde{x}_i}{\widetilde{\Delta}}, t = \frac{\widetilde{t}}{\widetilde{t}_l}, u_i = \frac{\widetilde{u}_i}{\widetilde{U}_0}, u_i^s = \frac{\widetilde{u}_i^s}{\widetilde{U}_0}, W_{s0} = \frac{\widetilde{W}_{s0}}{\widetilde{U}_0}, p = \frac{\widetilde{p}}{\rho_f \widetilde{U}_0^2}. \tag{3.1}$$

where $\widetilde{p}$ is the dynamic pressure, ρ_f is the fluid density, $\widetilde{u}_i$, $\widetilde{u}_i^s$ are the non-dimensional fluid and sediment velocities, respectively, and $i = 1, 2, 3$ represents streamwise (x), spanwise (y) and vertical (z) components, respectively (see Fig. 2.1 in chapter 2). In

this paper, except for physical constants such as ρ_f, ν, and the gravitational acceleration g, variables without overhead '$\sim$' are non-dimensional variables.

In particle-laden turbulent flows, the degree of coupling between the carrier flow and dispersed particles is often characterized by comparing the characteristic time scale of fluid flow $\widetilde{t_l}$ with the particle response time $\widetilde{t_p}$, which is defined as:

$$\widetilde{t_p} = \frac{s\widetilde{d}^2}{18\nu}, \tag{3.2}$$

where $s = \rho_s/\rho_f$ is the particle specific gravity, ρ_s is the sediment density, and $\widetilde{d}$ is the particle diameter. When $\widetilde{t_p}$ is relatively small compared with $\widetilde{t_l}$, the equilibrium Eulerian approximation (Balachandar & Eaton 2010) can be applied. Thus, the particle velocity u_i^s can be simplified to be an algebraic sum of the fluid velocity u_i, the settling velocity W_{s0} and an expansion in terms of the particle Stokes number St:

$$u_i^s = u_i - W_{s0}\delta_{i3} - St(1 - \frac{1}{s})\frac{Du_i}{Dt} + \mathcal{O}(St), \tag{3.3}$$

where the particle Stokes number $St = \widetilde{t_p}/\widetilde{t_l}$ is introduced to quantify the particle inertia relative to the flow inertia.

By substituting Eqn. (3.3) into the Eulerian two-phase equations for the fluid phase (Cantero et al. 2008), and adopting the Boussinesq approximation, which is appropriate for the relatively small volumetric concentration of suspended fine sediment on continental shelves (Traykovski et al. 2007), the resulting non-dimensional continuity and momentum equations of the fluid phase are written as (Cheng et al. 2015a):

$$\frac{\partial u_i}{\partial x_i} = 0, \tag{3.4}$$

$$\frac{\partial u_i}{\partial t} + u_j\frac{\partial u_i}{\partial x_j} = -\frac{\partial p}{\partial x_i} - \frac{2}{Re_\Delta}\sin\left(\frac{2t}{Re_\Delta}\right)\delta_{i1} + \frac{1}{Re_\Delta}\frac{\partial^2 u_i}{\partial x_j \partial x_j} - \frac{1}{Fr^2}\phi\delta_{i3}, \tag{3.5}$$

where the second term on the right-hand-side of Eqn. (3.5) represents the streamwise

pressure gradient that drives the prescribed wave motion. The last term on the right-hand-side of Eqn. (3.5) results from the momentum exchange between the sediment phase and the carrier fluid with ϕ representing the volumetric concentration of sediment and the particle Froude number $Fr = \widetilde{U}_0/\sqrt{(s-1)g\widetilde{\Delta}}$ is also introduced. For the bottom resuspension, this term typically represents sediment-induced stable density stratification, which can attenuate the carrier flow turbulence (Cheng et al. 2015a).

The non-dimensional mass conservation equation of the sediment phase is written as:

$$\frac{\partial \phi}{\partial t} + \frac{\partial \phi u_i^s}{\partial x_i} = \frac{1}{Re_\Delta Sc} \frac{\partial^2 \phi}{\partial x_i \partial x_i}, \tag{3.6}$$

where $Sc = \nu/\kappa$ is the Schmidt number with κ denoting the sediment diffusivity. The Schmidt number is chosen to be $Sc = 0.5$ in this study (Ozdemir et al. 2010, Yu et al. 2013).

The bottom boundary layer is idealized to be statistically homogeneous in streamwise (x) and spanwise (y) directions (see Fig. 2.1 in chapter 2). Periodic boundary conditions are used along streamwise and spanwise boundaries for fluid phase velocities and the sediment concentration. Two walls are located at the top and bottom boundaries and no-slip and no-penetration wall boundary conditions are implemented for the fluid velocity. For the sediment concentration, a no-flux boundary condition is applied at the top boundary:

$$w^s \phi - \frac{1}{Re_\Delta Sc} \frac{\partial \phi}{\partial z}\Big|_{z=L_z} = 0, \tag{3.7}$$

where $z = L_z$ is located at the top of the domain, and w^s is the vertical component of the sediment velocity.

At the bottom boundary, an erodible/depositional boundary condition is implemented for sediment concentration to allow resuspension/deposition at the bottom:

$$w^s \phi - \frac{1}{Re_\Delta Sc} \frac{\partial \phi}{\partial z}\Big|_{z=0} = E - D, \tag{3.8}$$

where E and D are non-dimensional erosional and depositional fluxes from/to the bottom, respectively, and both E and D are nondimensionalized by the free-stream velocity magnitude $\widetilde{U}_0$. The continuous non-dimensional depositional flux is specified as (Sanford & Maa 2001, Winterwerp 2007):

$$D = -w^s \phi\Big|_{z=0}. \tag{3.9}$$

The non-dimensional erosion rate E is calculated by the Partheniades-Ariathurai type formulation (e.g., Sanford & Maa 2001):

$$E = \begin{cases} m_e\left(\frac{|\tau_b|}{\tau_c} - 1\right), & |\tau_b| \geq \tau_c \\ 0, & |\tau_b| < \tau_c \end{cases}, \tag{3.10}$$

where m_e is the non-dimensional empirical coefficient of erosion rate (normalized by $\widetilde{U}_0$), τ_b is the non-dimensional bottom shear stress and the non-dimensional critical shear stress of erosion is represented by τ_c. Both τ_b and τ_c are normalized by $\rho_f \widetilde{U}_0^2$.

3.2.2 Numerical implementation

In this study, the computational domain (see Fig. 2.1 in chapter 2) is kept the same as the previous study of Ozdemir et al. (2010), which is $\widetilde{L}_x \times \widetilde{L}_y \times \widetilde{L}_z = 60\widetilde{\Delta} \times 30\widetilde{\Delta} \times 60\widetilde{\Delta}$, and it has been shown to be sufficient to resolve the largest turbulent eddies at the Stokes Reynolds number of Re_Δ=1000. Following Cheng et al. (2015a), the model domain is discretized into $N_x \times N_y \times N_z = 128 \times 128 \times 257$ with uniform grids in both streamwise and spanwise directions, and Chebyshev collocation points are used in the vertical direction. A more detailed discussion is given later to demonstrate that the present numerical resolution is sufficient. Taking advantage of the statistical homogeneity in the streamwise (x) and spanwise (y) directions, ensemble-averaged (turbulence-averaged) flow quantities can be calculated approximately by averaging over the $x - y$ plane. A hybrid numerical scheme which maintains Fourier expansions

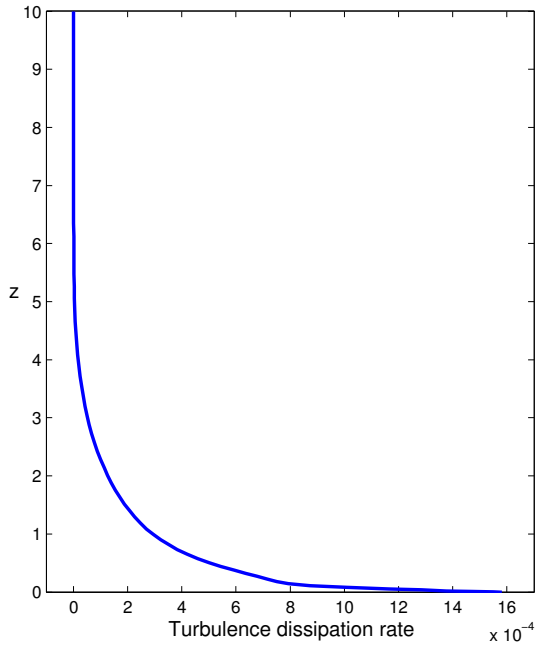

Figure 3.1: Simulation results of turbulence dissipation rate at the flow peak for Case 0.

in homogeneous directions (streamwise and spanwise) and implements sixth-order centered compact finite difference method in the wall-normal direction (Yu et al. 2013) is utilized in this study. With this hybrid scheme, flow-dependent properties and more flexible boundary conditions become relatively straightforward to implement. Uniform grids are used in the two homogeneous directions and Chebyshev collocation points are used in the vertical direction in order to better resolve the flow near the wall/bed. Eqns. (3.4) and (3.5) are solved with a standard projection method (Chorin 1968). The velocity field is first advanced to the intermediate level. For diffusion terms, the Crank-Nicolson scheme is used. Nonlinear advection terms are calculated by the Arakawa method (Arakawa & Lamb 1981) with the 2/3 de-aliasing law. To preserve the accuracy of the 128 grids used in the x and y directions, the nonlinear products are computed on 192 grids, while 128 unfiltered wave-numbers are retained. The temporal integration is performed using a third-order low-storage Runge-Kutta scheme. A direct solver is used to solve the pressure Poisson equation, and once the pressure is

determined, the intermediate velocity field is corrected to satisfy Eqn. (3.4). For the sediment concentration equation, similar numerical scheme are used. More detailed discussions on the numerical schemes and implementations can be found in Cortese & Balachandar (1995) and Yu et al. (2013). The implementation of the top boundary condition (Eqn. (3.7)) is discussed in detail in the Appendix. Yu et al. (2014) has demonstrated that the same grid resolution and domain size used in the present study is sufficient to reproduce the DNS results of clear fluid oscillatory wave boundary layer at $Re_\Delta = 1000$ of Spalart & Baldwin (1989). An additional evidence for sediment-laden condition is given here using Case 0 (see Table 1). The grid resolution can be verified by comparing with the Kolmogorov length scale, which can be estimated from the simulation results of turbulence dissipation rate. Fig. 3.1 shows the turbulence dissipation rate during the flow peak, the moment that the turbulence dissipation rate is the largest throughout the wave cycle. We can observe that the maximum non-dimensional turbulence dissipation rate ϵ occurs very close to the bed, which is about 1.6×10^{-3}. Therefore, the smallest non-dimensional Kolmogorov length scale is estimated to be about $\eta = (1/(\epsilon Re_\Delta^3))^{1/4} = 2.8 \times 10^{-2}$. According to Pope (2000), $l = 60\eta$ is the length scale representing the upper bound of dissipative ranges. We can verify that the non-dimensional grid size adopted here is $dx = 0.47$ is about 4 times smaller than $l = 60\eta$. Hence, we verify that the grid resolution can capture sufficient turbulence scales for the cases considered in this study.

3.2.3 Simulation setup

In the previous studies (Ozdemir et al. 2010, Cheng et al. 2015a), the inertia terms associated with the particle Stokes number St in the particle velocity expression (Eqn. (3.3)) are neglected by assuming that the Stokes number St is sufficiently small, and the particle velocity is calculated as:

$$u_i^s = u_i - W_{s0}\delta_{i3}. \tag{3.11}$$

The dimensional settling velocity $\widetilde{W}_{s0}$ is calculated via the Stokes drag law:

$$\widetilde{W}_{s0} = \frac{(s-1)g\widetilde{d}^2}{18\nu}. \tag{3.12}$$

Hence, by specifying $\widetilde{W}_{s0} = 0.5$ mm/s (or $W_{s0} = 9 \times 10^{-4}$), these simulations can be interpreted as corresponding to fine silt (no flocculation) with a particle size of $\widetilde{d} = 24$ μm and the specific gravity is $s = 2.65$.

As one of the objectives in this study is to evaluate the uncertainties associated with the parameterization of settling velocity adopted by the previous studies, namely, Eqn. (3.11), simulations are designed to vary the selected parameters that stem from the baseline Case 0 (see Table 3.1). Case 0 is identical to a case reported in Cheng et al. (2015a), which belongs to transport mode II. Specifically, the fine sediment transport of $W_{s0} = 9 \times 10^{-4}$ with a relative low dimensional critical shear stress of erosion of $\widetilde{\tau}_c = 0.02$ Pa in the wave condition of Re_Δ=1000 is studied in Case 0. As reported in Cheng et al. (2015a), although transport mode II is obtained for Case 0 where the flow is turbulent below the lutocline, the resulting sediment availability is in fact quite large and further reducing $\widetilde{\tau}_c$ to 0.01 Pa produces laminarized transport mode III. Therefore, in this study we focus on varying the parameterizations of settling velocity and evaluate the results especially in terms of the transition of transport modes. Following Cheng et al. (2015a), we also set $m_e = 5.4 \times 10^{-7}$.

For Case 0, the particle response time and characteristic flow time scale are $\widetilde{t}_p = 8.5 \times 10^{-5}$ s and $\widetilde{t}_l \approx 3.2 \times 10^{-3}$ s, respectively. The resulting Stokes number is $St = \widetilde{t}_p/\widetilde{t}_l \approx 0.03$, which is much smaller than unity. However, the non-dimensional settling velocity $W_{s0} = 9 \times 10^{-4}$ is also quite small. Hence, it is not obvious if the third term in Eqn. (3.3), representing the inertia effect, is always smaller than the second term (Stokes settling velocity) unless flow acceleration is small. In the present boundary layer setting with gravitational acceleration acting only in the z direction, the main difference is that the second term in Eqn. (3.3) is persistent throughout the simulation while since there is no ensemble-averaged mean flow in the z direction, the

Table 3.1: List of simulations presented in the study of particle inertia and hindered settling

Case	St	ϕ_{ref}	$\widetilde{d}$ (μm)	$\widetilde{D}_f$ (μm)	n_f	$\overline{\widetilde{\tau}}_{eq}$ (Pa)	$\overline{\Phi}_{eq}$	ϕ_{max}	Transport mode
0	NA	NA	24	NA	NA	0.39	1.76×10^{-3}	0.012	II
$A1$	0.03	NA	24	NA	NA	0.38	1.8×10^{-3}	0.013	II
$A2$	0.1	NA	NA	NA	NA	NA	NA	NA	II
$A3$	0.2	NA	NA	NA	NA	NA	NA	NA	III
$B1$	NA	0.63	24	NA	NA	0.38	1.95×10^{-3}	0.014	II
$B2$	NA	0.2	4	52.7	2.38	0.28	4.7×10^{-4}	0.021	III
$B3$	NA	0.13	4	66.6	2.27	0.28	7.0×10^{-4}	0.026	III
$B4$	NA	0.05	4	107.3	2.09	0.28	NA	0.05	III

Note: All simulations presented in this study are corresponding to non-dimensional parameters Re_Δ=1000, $W_{s0} = 9 \times 10^{-4}$, $\tau_c = 6.4 \times 10^{-5}$ and $m_e = 5.4 \times 10^{-7}$.

third term in Eqn. (3.3) can only be large instantaneously. Because the system is nonlinear, it remains necessary to evaluate the importance of the third term on the resulting sediment transport at $St = 0.03$ and Case A1 shown in Table 1 is presented for this purpose. To further emphasize the effect of particle inertia, two additional numerical experiments (Case A2 and A3) with higher Stokes numbers are carried out, while the other non-dimensional quantities, namely, Re_Δ, W_{s0} and Fr are kept the same as Case 0. The equilibrium Eulerian approximation is fairly accurate for $St \leq 0.2$ (Balachandar & Eaton 2010), thus the largest St is chosen to be 0.2 (Case A3).

In addition, the hindered settling effects were neglected in the previous studies (Ozdemir et al. 2010, Cheng et al. 2015a). To incorporate the effect of hindered settling, the bulk settling velocity W_s is corrected with a hindered settling function $f(\phi)$:

$$W_s = W_{s0} f(\phi). \tag{3.13}$$

In this study, we choose the model of Richardson & Zaki (1954) to parameterize the hindered settling effect:

$$f(\phi) = \big(1 - \frac{\phi}{\phi_{ref}}\big)^m, \tag{3.14}$$

where ϕ_{ref} is the reference concentration, i.e., a maximum packing concentration

(Richardson & Zaki 1954, Mehta 1986, Dankers & Winterwerp 2007). Clearly, the degree of hindered settling and hence the resulting transport is highly dependent on ϕ_{ref}. For non-cohesive sediments, ϕ_{ref} corresponds to the maximum packing limit, which is around 0.63, at which the mean distance between the edges of the nearest neighbors is nearly zero (Berryman 1983). For cohesive sediments, fine particles (primary particles) are transported as flocs and the gelling concentration is often used for ϕ_{ref}. As the gelling concentration is defined as the concentration at which floc aggregates form concentrated networks, it depends on the floc structures and may vary due to floc dynamics (Winterwerp 1998, Dyer & Manning 1999). In this study, we investigate four cases with different reference/gelling concentrations associated with non-cohesive particles (see Case B1 in Table 3.1), and different floc structures (Case B2∼B4 in Table 3.1). The empirical exponent m is related to the particle Reynolds number ($Re_p = \widetilde{W}_{s0}\widetilde{d}/\nu$). As will be demonstrated later, the particle size (or floc size) considered in this study is small ($Re_p < 0.2$) and the exponent m is kept constant as $m = 4.6$ (Richardson & Zaki 1954).

3.3 Effect of Particle Inertia

To study the effect of particle inertia, four numerical experiments are carried out and results are compared in non-dimensional quantities. In Case 0 (see Table 3.1), the inertia terms in the sediment velocity expression are neglected and Eqn. (3.11) is used. In Case A1−A3 (see Table 3.1), the first-order inertia term in the sediment velocity expression is kept:

$$u_i^s = u_i - W_{s0}\delta_{i3} - St(1 - \frac{1}{s})\frac{Du_i}{Dt}. \tag{3.15}$$

Except for the difference in the particle velocity expressions, other non-dimensional flow and sediment parameters in Case 0 and Case A1−A3 are kept the same, and thus any difference between these cases is due to the extra inertia term in the particle velocity expression.

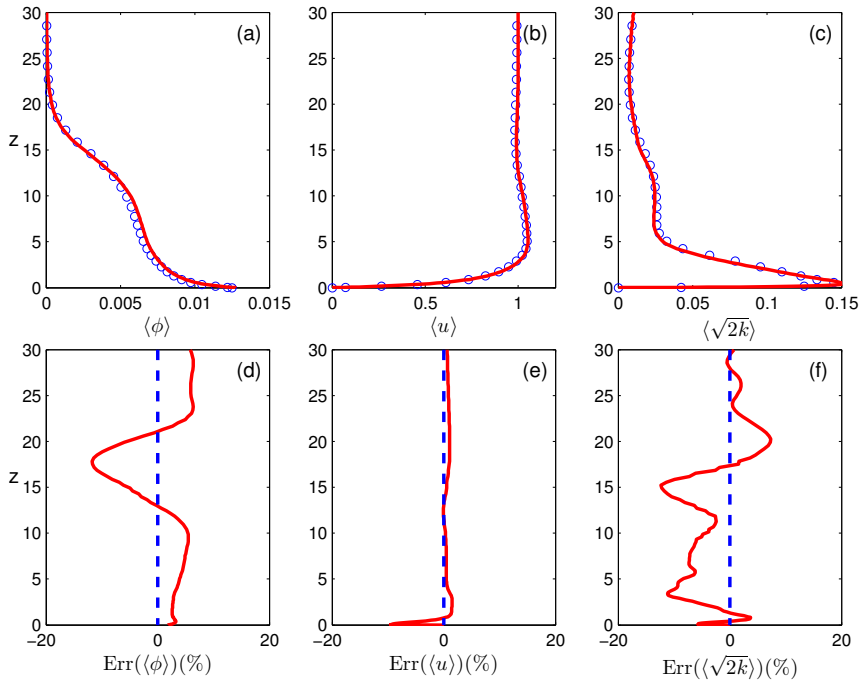

Figure 3.2: Comparison of the ensemble-averaged profiles of (a) sediment concentration, (b) streamwise velocity and (c) turbulence intensity during flow peak ($\omega t = 0$) for Case 0 (circle symbols), Case A1 (solid curve); The relative difference (%) of these flow quantities are shown in (d), (e) and (f), respectively; The levels of zero error are denoted as dashed lines in (d), (e) and (f).

3.3.1 Model results

The sensitivity of the particle inertia is first investigated by comparing the ensemble-averaged profiles (see Fig. 3.2) of sediment concentration, non-dimensional streamwise velocity and non-dimensional turbulence intensity for Case 0 (inertia effect neglected) and Case A1 (St=0.03). The turbulence intensity is defined as $\langle\sqrt{2k}\rangle$, where '$\langle\ \ \rangle$' denotes the averaging operation over the $x-y$ plane, and k is the turbulent kinetic energy:

$$k = \frac{1}{2}(u'^2 + v'^2 + w'^2), \tag{3.16}$$

where u', v' and w' are the velocity fluctuations of streamwise, spanwise and vertical velocity components, respectively. It is reminded here that Case 0 belongs to transport

mode II, in which the lutocline separates the upper quasi-laminar layer from the lower turbulent layer. In this case, the lutocline is located approximately at $z = 13 \sim 14$ (see circle symbols in Fig. 3.2(a)). By including the first-order inertia term, the resulting sediment concentration profile (see Fig. 3.2(a)) is very similar to that of Case 0. Moreover, the relative difference of the sediment concentration is shown in Fig. 3.2(d), which is defined as:

$$\mathrm{Err}(\langle\phi\rangle) = \frac{\langle\phi_A\rangle - \langle\phi_0\rangle}{\langle\phi_0\rangle} \times 100\%, \tag{3.17}$$

where $\langle\phi_0\rangle$ is the plane-averaged sediment concentration in Case 0, and $\langle\phi_A\rangle$ is the plane-averaged sediment concentration in Case A1. The relative difference of the streamwise velocity $\mathrm{Err}(\langle u\rangle)$ and the turbulent intensity $\mathrm{Err}(\langle\sqrt{2k}\rangle)$ can be calculated in a similar manner. We can see that the overall relative difference is small ($< 10\%$). A reduction of sediment concentration can be observed in the range of $13 < z < 21$, and the peak difference appears at around $z = 18$ (about -10%), which is close to the lutocline. On the contrary, sediment concentration below $z = 13$ is increased by about 7%. This observation suggests the lowering of lutocline when inertia effect is considered. Meanwhile, the streamwise velocities (see Fig. 3.2(b)) of both cases are again very similar, and the relative difference (see Fig. 3.2(e)) is generally smaller than 5%, and the peak value can be observed near the bottom. Furthermore, the comparison of turbulence intensity is shown in Fig. 3.2(c). Although the turbulence intensity profiles from Case 0 and Case A1 are also very close, it is evident that the predicted turbulence is slightly lower by including the inertia effect with the peak attenuation occurs at around $z = 15$ near the lutocline. More attenuated turbulence is consistent with the lowered lutocline.

Moreover, the relative differences in effective settling velocities at three representative instants are discussed in Fig. 3.3. The relative difference in the effective settling velocity is calculated by the ensemble-average of the additional term associated

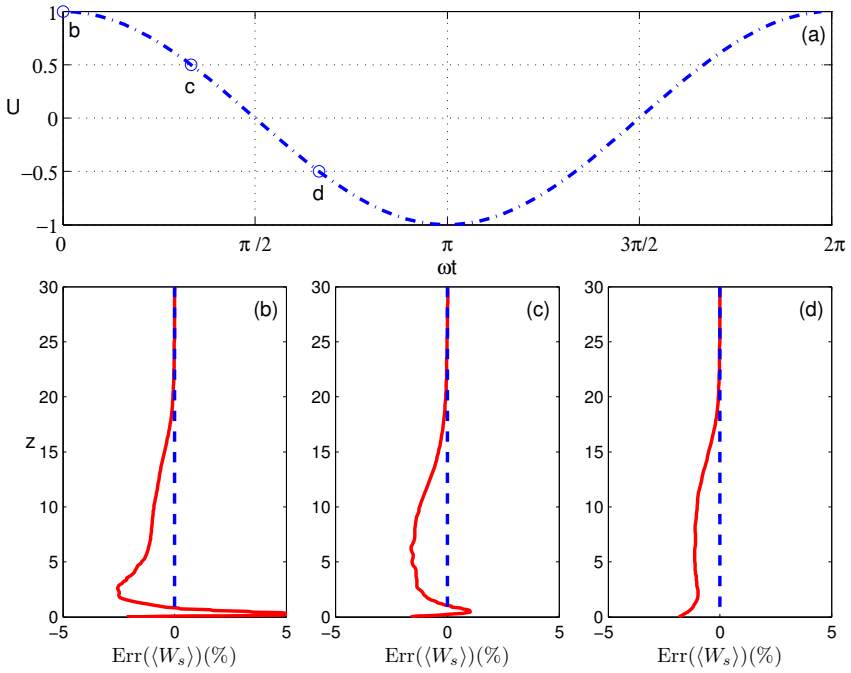

Figure 3.3: (a) Time series of free-stream velocity $U(t)$. Three representative instants (b,c,d) are shown with open circles. The relative difference (%, solid curve) of effective settling velocities between Case 0 and Case A1 at these three representative instants are shown in (b) flow peak ($\omega t = 0$), (c) $\omega t = \pi/3$ and (d) $\omega t = 2\pi/3$; The levels of zero error are denoted as dashed lines in (b), (c) and (d).

with the inertia effect normalized by W_{s0}:

$$\mathrm{Err}(\langle W_s \rangle) = St(1 - \frac{1}{s})\frac{\langle \frac{Dw}{Dt} \rangle}{W_{s0}} \times 100\% \tag{3.18}$$

In Fig. 3.3(a), the wave phase (ωt) is defined such that $\omega t = 0$ ($\omega t = \pi$) corresponds to the positive (negative) peak of free-stream velocity, and $\omega t = \pi/2$ and $3\pi/2$ correspond to flow reversals. From the comparison of effective settling velocities (Fig. 3.3(b,c,d)), we can see that the effective settling velocity is nearly unaffected above $z = 20$ due to very low turbulence above the lutocline. Between $1.5 < z < 20$, including the particle inertia reduces the effective settling velocity. However, the reduction is only within 3%. Moreover, an increase of the effective settling velocity can be observed near the

bottom $0 < z < 1.5$, and the peak value of the increment is about 5% at flow peak. However, the effective settling velocity at the bottom is still reduced by about 2%. As the flow decelerates to $\omega t = \pi/3$, the increment of effective settling velocity at around $z = 1.5$ is decreased to about 1%. After the flow reserves and accelerates to $\omega t = 2\pi/3$, a uniform reduction of effective settling velocity can be observed below the lutocline, and the reduction is less than 2%. Overall, the inertia effect slightly reduces velocity fluctuations in the z-direction and hence the Reynolds stress is reduced (not shown here for conciseness). This can further lead to a reduction of turbulent production and hence more attenuation of turbulence. However, the Stokes number considered here remains to be too small ($St = 0.03$) to trigger the transition to transport mode III.

As discussed in this section, by retaining the first order St term in the particle velocity expansion based on Case 0 with $St = 0.03$, the inertia effect is demonstrated to be small on concentration profiles, velocity profiles and turbulent intensity. This negligible effect is consistent with the small $\mathrm{Err}(\langle W_s \rangle)$ which is generally within 5%. This sensitivity study of inertia effect justifies the previous studies where the inertia terms are neglected. Simulation results for Case A2 and A3 demonstrating more pronounced evidence that particle inertia effect can attenuate turbulence are presented in Discussion (Section 5.1).

3.4 Effect of Hindered Settling

Ozdemir et al. (2011) has demonstrated that the settling velocity plays a key role in determining the vertical sediment flux budget, and vertical distribution of sediment concentration. Meanwhile, it has been shown that the settling velocity directly affects the deposition flux at the bottom, and therefore determines the sediment availability (Cheng et al. 2015a). Both sediment availability and vertical structure of sediment concentration have significant impacts on the carrier flow turbulence characteristics via stable density stratification. Therefore, it is intrinsic to study the effect of hindered settling on fine sediment transport. As demonstrated in Section 3, the particle inertia has negligible effects on the fine sediment transport for Stokes number St up to 0.03.

Therefore, in the study of hindered settling effects, the inertia effect is neglected. Neglecting the inertia effect in particle velocity parameterization also allows us to easily isolate the hindered settling effect. In this section, the particle velocity is expressed to account for the hindered settling correction:

$$u_i^s = u_i - W_{s0} f(\phi) \delta_{i3}. \tag{3.19}$$

When fine sediments are considered non-cohesive, the reference concentration is chosen to be $\phi_{ref} = 0.63$, which corresponds to Case B1 in Table 3.1, and the dimensional Stokes settling velocity $\widetilde{W}_{s0}$ is calculated by Eqn. (3.12). Hence, for Case 0 and Case B1, a dimensional settling velocity of $\widetilde{W}_{s0}$=0.5 mm/s corresponds to fine silt of grain diameter $\widetilde{d} = 24\mu$m. For cohesive sediments forming floc aggregates, the dimensional Stokes settling velocity should be determined by floc properties (Kranenburg 1994):

$$\widetilde{W}_{s0} = \frac{(s^{floc} - 1) g \widetilde{D}_f^2}{18\nu}, \tag{3.20}$$

where $\widetilde{D}_f$ is the floc size, and $s^{floc} = \rho^{floc}/\rho^f$ is the specific gravity of flocs with ρ^{floc} being the density of flocs. The floc density depends on floc structures, and it is calculated by adopting the fractal model (Kranenburg 1994) as:

$$\rho^{floc} = \rho^f + (\rho^s - \rho^f) \Big(\frac{\widetilde{D}_f}{\widetilde{d}} \Big)^{(n_f - 3)}, \tag{3.21}$$

where n_f is the fractal dimension and $\widetilde{d}$ is interpreted here as the primary particle size. For flocs, the gelling concentration is used as the reference concentration (see Eqn. (3.14)). The gelling concentration is also determined by floc structures, which is calculated as (e.g., Winterwerp & Van Kesteren 2004):

$$\phi_{gel} = \Big(\frac{\widetilde{D}_f}{\widetilde{d}} \Big)^{n_f - 3} = \frac{\rho^{floc} - \rho^f}{\rho^s - \rho^f}. \tag{3.22}$$

Due to complicated processes of floc aggregation and breakup, floc properties may vary

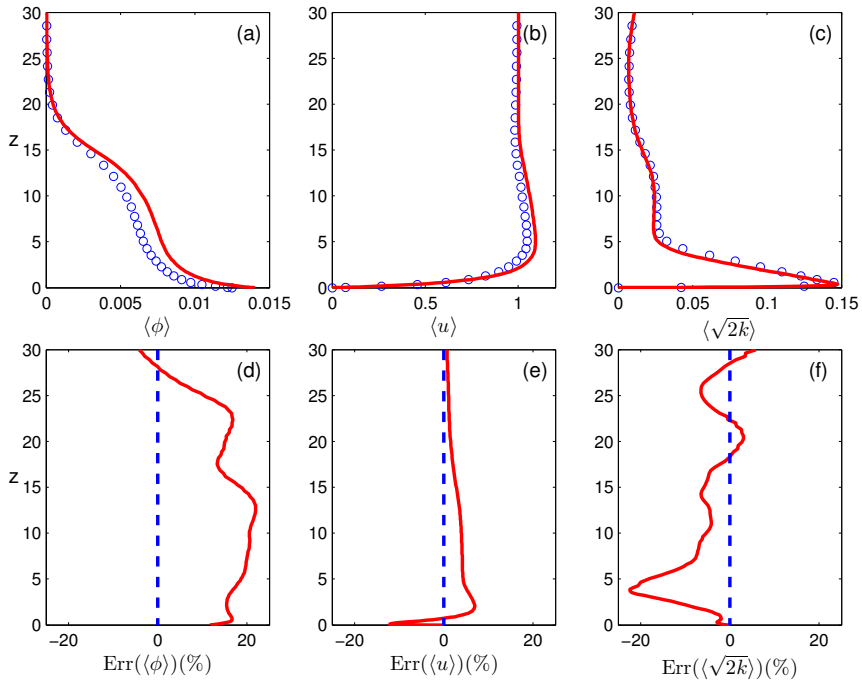

Figure 3.4: Comparison of the ensemble-averaged profiles of (a) sediment concentration, (b) streamwise velocity and (c) turbulence intensity during flow the peak ($\omega t = 0$) for Case 0 (circle symbol), Case B1 (solid curve); The relative difference (%) of these flow quantities are shown in (d), (e) and (f), respectively; The levels of zero error are denoted as dashed lines in (d), (e) and (f).

with flow shear and floc-floc interactions (Dyer & Manning 1999, Winterwerp 1998). However, this level of complexity is beyond the scope of this study, and floc properties are assumed to be constant in each simulation. We consider the primary particle size to be $\widetilde{d} = 4\mu$m, the floc size $\widetilde{D}_f$ and fractal dimension n_f are then determined by keeping the Stokes settling velocity the same as Case 0, i.e., $\widetilde{W}_{s0} = 0.5$ mm/s (or $W_{s0} = 9 \times 10^{-4}$). For example, in Case B2 we specify the gelling concentration to be $\phi_{gel} = 0.2$. Matching the Stokes settling velocity of $\widetilde{W}_{s0} = 0.5$ mm/s gives a floc size of $\widetilde{D}_f = 53.7$ μm with the fractal dimension n_f=2.38. This corresponds to typical inorganic flocs with n_f significantly greater than 2.0. On the other hand, Case B4 with a gelling concentration of $\phi_{gel} = 0.05$ gives a floc size of $\widetilde{D}_f = 107$ μm and n_f=2.09, which corresponds to more porous and organic flocs. The floc properties for all the

cases considered in this study are summarized in Table 3.1. We can check that the maximum particle Reynolds number considered in Table 3.1 remains to be very small $Re_p = 0.06$. Thus, a constant $m = 4.6$ (see Eqn. (3.14)) can be used in all the cases.

3.4.1 Model results

Using the model of Cheng et al. (2015a), the sediment availability in this study is determined by the interplay of erosion and deposition at the bottom boundary. However, the hindered settling adds another layer of complexity, since the settling velocity becomes a function of sediment concentration (see Eqn. (3.13)) and the deposition flux is now a nonlinear function of sediment concentration. Hence, it is crucial to study the uncertainty introduced by hindered settling on the transport mode of fine sediment.

Firstly, the ensemble-averaged flow statistics in Case 0 and Case B1 are compared in Fig. 3.4 to study the sensitivity of the hindered settling for non-flocculated condition ($\phi_{ref} = 0.63$). Case 0 and Case B1 show a similar feature of concentration profiles (Fig. 3.4(a)). Since the lutoclines are observed in both Case 0 and Case B1 near $z = 14$, transport mode II is also obtained for Case B1. However, Case B1 shows slightly increased sediment concentrations below the lutocline. Although the increase is within 20%, this notable increment of total load in the domain is clearly associated with the reduced settling velocity through hindered settling. Meanwhile, the streamwise velocity profiles (see Fig. 3.4(b)) show that the overshoot near the bottom in Case B1 is slightly larger (within 10%) than that of Case 0. Below the lutocline, the turbulent intensity in Case B1 is consistently lower that that of Case 0 by about 5% to 20% (see Fig. 3.4(f)). When settling velocity is effectively reduced by hindered settling effect, more sediments are suspended in the domain (Cheng et al. 2015a), which leads to an enhanced sediment-induced density stratification and a stronger attenuation of turbulence is observed. However, both Case 0 and Case B1 are in transport mode II, which verifies the simulations of Cheng et al. (2015a), where the hindered settling effect is neglected as sediments are assumed to be non-flocculated.

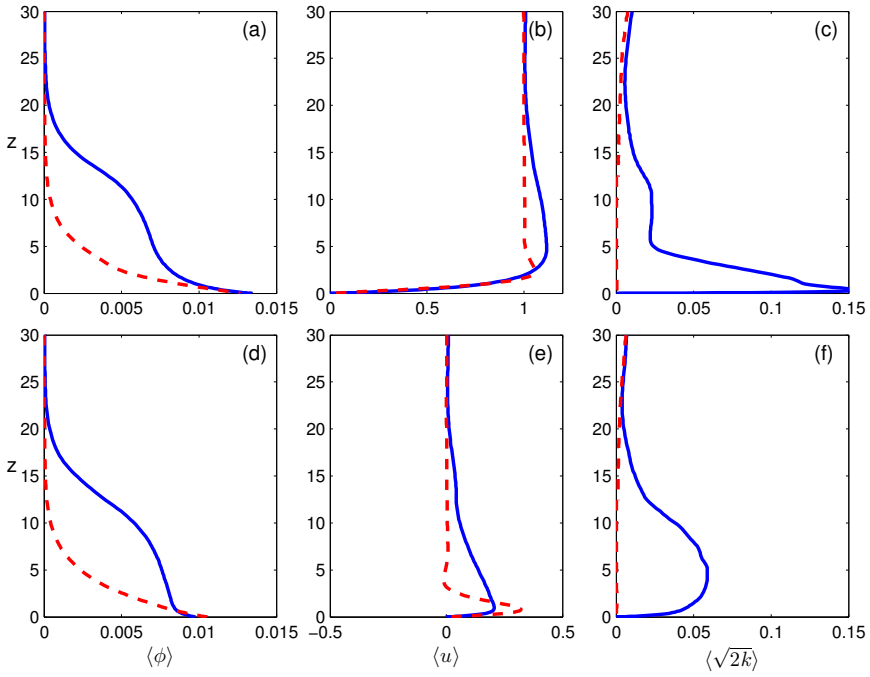

Figure 3.5: Ensemble-averaged profiles of (a) sediment concentration, (b) streamwise velocity and (c) turbulent intensity during flow peak ($\omega t = 0$) for Case B1 (solid curve), Case B2 (dashed curve). (d), (e) and (f) are the corresponding profiles during flow reversal.

Though the transport mode is not altered, a noticeable damping effect of flow turbulence is observed when the hindered settling is considered. It is motivated to further investigate the hindered settling effect with different reference (gelling) concentrations (see Cases B2-B4 with different gelling concentration shown in Table 3.1). As a result of different gelling concentrations, distinct transport modes are observed. These distinct transport modes are first examined from the ensemble-averaged flow statistics for Case B1 and B2. Fig. 3.5 illustrates the hindered settling effect on the vertical structure of sediment concentration, streamwise velocity and turbulent intensity. As discussed before, transport mode II with a lutocline is observed for Case B1 (see solid curves in Fig. 3.5(a) and (d)). By reducing the reference (gelling) concentration from $\phi_{ref} = 0.63$ to $\phi_{ref} = 0.2$, Case B2 (see dashed curve in Fig. 3.5(a) and (d)) shows a very different feature of sediment concentration. The lutocline is not observed in the

concentration profile of Case B2, and nearly exponential profile is obtained. From the velocity profiles shown in Fig. 3.5(b) and (e), a reduction of bottom boundary layer thickness is also observed. More importantly, the turbulent intensity below $z = 14$ is completely suppressed in Case B2, which indicates that the flow turbulence is completely attenuated by sediment-induced stable density stratification. Above $z = 14$, a weak turbulent intensity can still be observed, and this is introduced by the turbulent fluctuation from the upper wall. During the flow reversal, significantly attenuated turbulence (or laminar-like features) is also obtained for Case B2. From the flow statistics, we observe that Case B1 is in transport mode II, while further reducing the reference (gelling) concentration associated with hindered settling triggers the transition from transport mode II to laminarized transport mode III.

To further illustrate the effect of hindered settling on the turbulent structure and the resulting turbulence-sediment interaction, the iso-surfaces of local swirling strength λ_{ci} are shown along with the iso-surface of sediment concentration for Case 0, B1 and B2 during the flow peak in Fig. 3.6. λ_{ci} is the imaginary part of the complex eigenvalue of the velocity gradient tensor and its magnitude can be used to quantify the strength of local swirling motion (Zhou et al. 1999). The threshold is chosen here to be 4% of the maximum value obtained in Case 0, and this threshold value is applied to the other cases to facilitate the comparison. It is evident that sparse coherent vortex structures can be observed in part of the near-bed region in Case 0 (see Fig. 3.6(a)). This region is corresponding to a stripe of more irregular/chaotic and higher sediment concentration structures. In regions where no coherent turbulence structures are observed, a regularly spaced streaks of lower sediment concentration are observed. When hindered settling is considered with reference concentration $\phi_{ref} = 0.63$ (see Case B1 in Fig. 3.6(b)), similar sparse coherent vortex structures can be seen but with slightly sparser distribution than that in Case 0. On the other hand, no coherent vortex structures can be observed in Case B2 (see Fig. 3.6(c)), which indicates that the turbulence in Case B2 is completely suppressed. As a result, a nearly uniform sediment concentration structures appears in the sediment concentration field of Case B2. Although not shown here, further

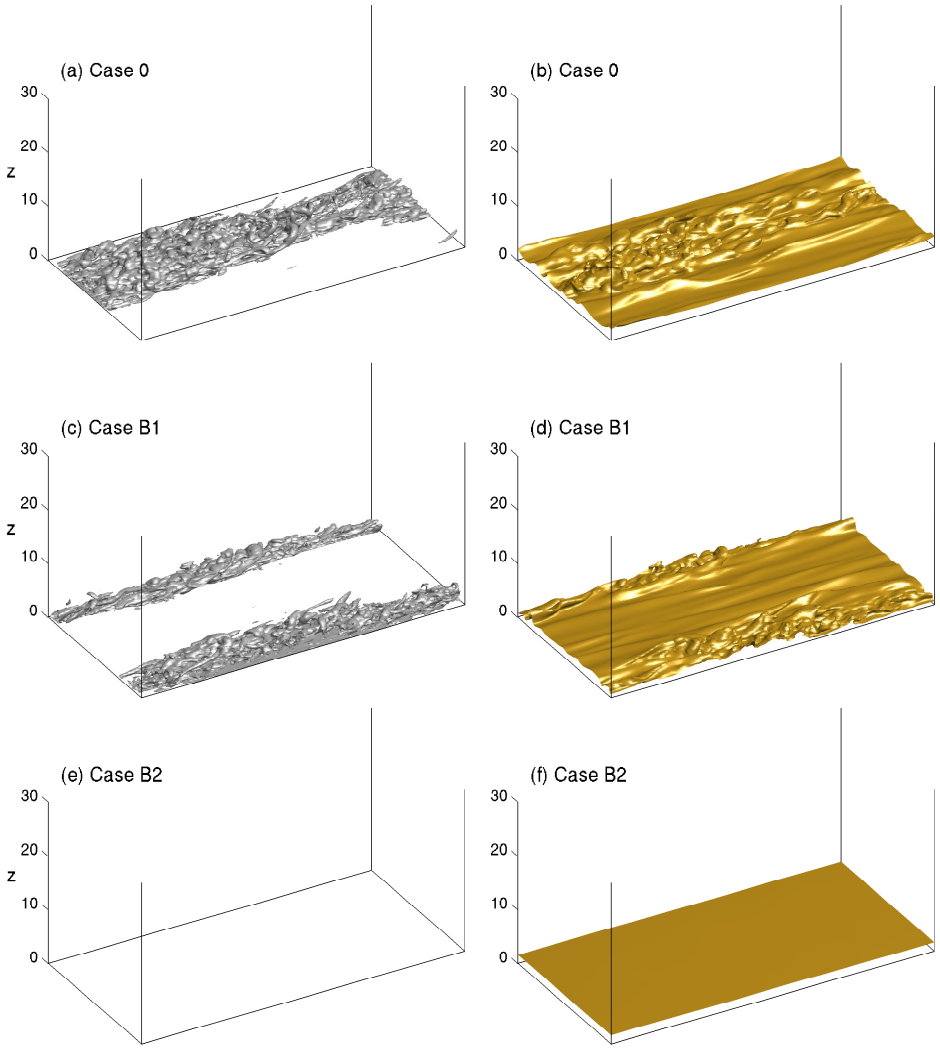

Figure 3.6: Turbulent coherent structures at flow peak ($\omega t = 0$) for (a) Case0, (c) Case B1, and (e) Case B2. The turbulent coherent structures are visualized using the swirling strength (λ_{ci}), and the contour level used here is 4% of the maximum λ_{ci} value in Case 0. The iso-surface of concentration ϕ field corresponding to (b) Case 0, (d) Case B1 and (f) Case B2 are also shown, and their contour levels are 8.2×10^{-3}, 9.8×10^{-3} and 0.015, respectively.

reducing the reference concentration to $\phi_{ref} = 0.13$ (Case B3) and $\phi_{ref} = 0.05$ (Case B4) also shifts the flow to laminarized transport mode III, and the flow turbulence structures for Case B3 and Case B4 are similar to Case B2.

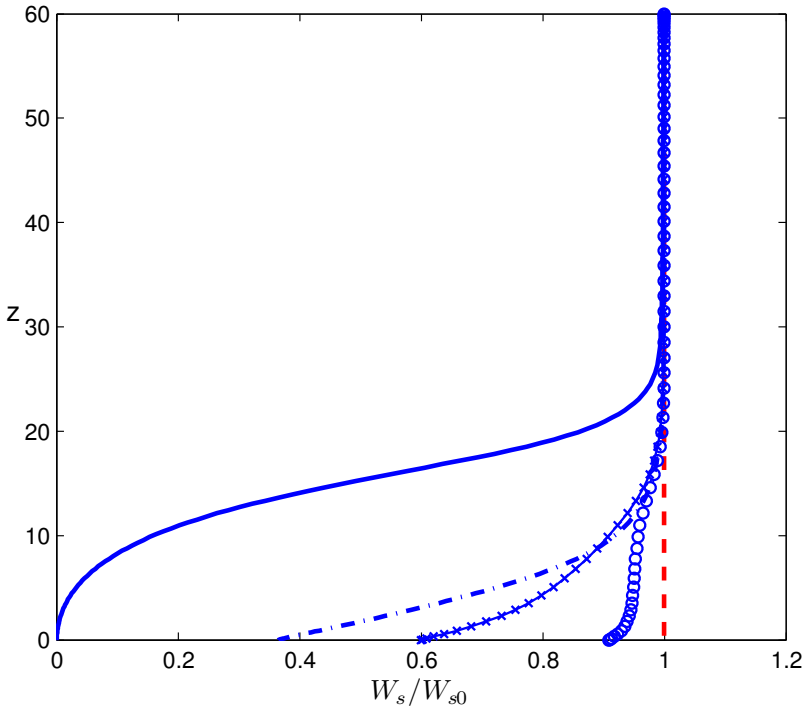

Figure 3.7: Normalized effective settling velocity profile for Case 0 (blue dashed curve), Case B1 (red solid curve), Case B2 (blue solid curve), Case B3 (black solid curve) and Case B4 (green solid curve) during flow peak ($t = 15T$).

These distinct flow features are caused by different degrees of hindered settling effect. Fig. 3.7 presents the normalized effective settling velocity, which is defined as the difference between the sediment velocity and the fluid velocity in the z-direction normalized by the Stokes settling velocity. Since the features are similar during the entire wave cycle, only the comparison at the flow peak is shown here. We can see that different reference (gelling) concentrations render different degrees of reduction in the effective settling velocity, and the reduction of effective settling velocity is larger near the bottom, where the sediment concentration is larger. For Case B1 ($\phi_{ref} = 0.63$),

the reduction is less than 10%. When the reference concentration ϕ_{ref} is reduced to 0.2 (or 0.13) in Case B2 (in Case B3), the reduction of settling velocity is significantly enhanced and near the bed, the effective settling is only 60% (37%) of that in Case 0. Finally, the complete hindered effect, where the effective settling velocity approaches zero near the bottom is observed for reference concentration $\phi_{ref} = 0.05$ (Case B4).

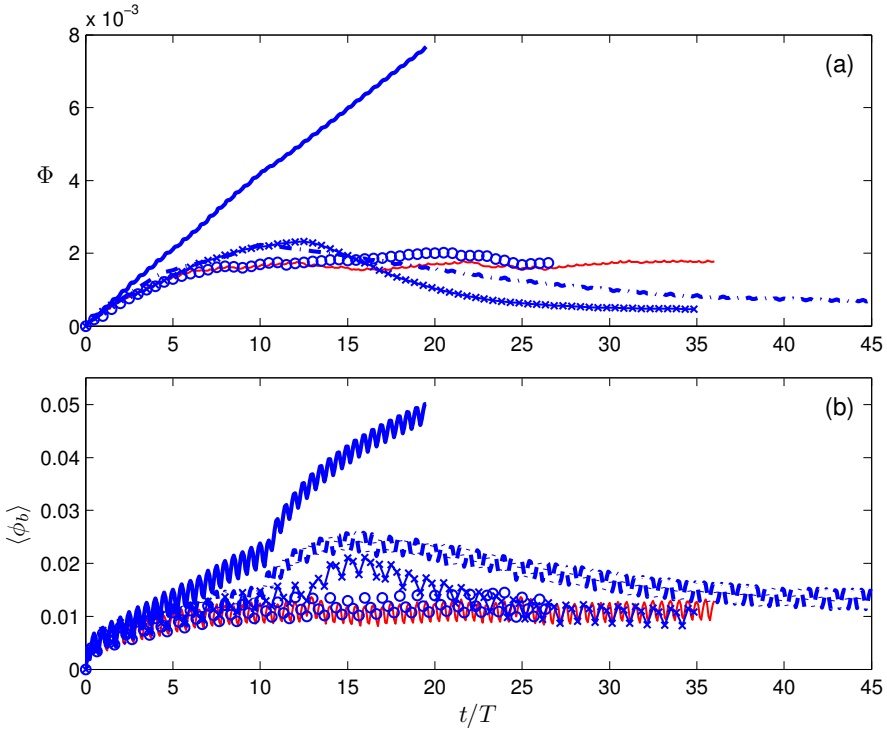

Figure 3.8: Temporal evolution of (a) domain-averaged sediment concentration Φ and (b) ensemble-averaged sediment concentration at the bottom $\langle\phi_b\rangle$ for Case 0 (blue dashed curve), Case B1 (red solid curve), Case B2 (blue solid curve), Case B3 (black solid curve) and Case B4 (green solid curve).

It has been revealed that settling velocities play an important role in vertical structure of sediment-induced density stratification (Ozdemir et al. 2011) and sediment availability (Cheng et al. 2015a), which determines the flow transport modes. Fig.

3.8(a) further illustrates the hindered settling effect on the time series of domain-averaged sediment concentration, which is defined as:

$$\Phi = \frac{1}{L_z}\int_0^{L_z} \langle\phi\rangle dz. \tag{3.23}$$

It is evident from Fig. 3.8(a) that Φ is significantly affected by the hindered settling. For non-flocculated condition (Case B1, $\phi_{ref} = 0.63$), the temporal variation of domain-averaged sediment concentration is similar to that of Case 0. An equilibrium state in transport mode II is estabilished, in which the wave-averaged erosion flux $\overline{E}$ balances the wave-averaged deposition flux $\overline{D}$ with '$\overline{\ }$' representing wave-averaged operator. The deposition flux at the bottom boundary is determined by the bottom concentration, which plays a key role in controlling the sediment availability in the domain. Therefore, the evolution of the ensemble-averaged bottom concentration $\langle\phi_b\rangle$ is also presented in Fig. 3.8(b). For both Case 0 and Case B1, time series of $\langle\phi_b\rangle$ are similar to that of Φ and an equilibrium state is achieved after about 20 repeated wave motions. To facilitate the comparison, we also examine the time averaged Φ over one wave period at the equilibrium stage and formally define it as sediment availability $\overline{\Phi}_{eq}$ (see Table 1). The sediment availability for Case B1 ($\overline{\Phi}_{eq} = 1.95 \times 10^{-3}$) is slightly greater than that of Case 0 ($\overline{\Phi}_{eq} = 1.76 \times 10^{-3}$), which is consistent with the slightly lower settling velocity in Case B1. This equilibrium state reflects transport mode II and the turbulent nature of this mode sustain a notable amount of sediment (see Table 3.1).

However, when the gelling concentration is further reduced to $\phi_{ref} = 0.2$ and $\phi_{ref} = 0.13$, a different trend of sediment concentration evolution can be observed. The domain-averaged sediment concentration Φ increases to about 2.1×10^{-3} (2.4×10^{-3}) in Case B2 (Case B3) at $t/T = 10$ ($t/T = 12$). Afterward, Φ starts to decrease. As discussed previously (see Fig. 3.5 and Fig. 3.6(c)), the flow turbulence in Case B2 (or Case B3) is completely suppressed (laminarized transport mode III) and the viscous suspension alone can not sustain such amount of sediment in the domain. As

a result, the domain-averaged concentration drops until a final equilibrium state in the laminarized transport mode III is reached and a much lower $\overline{\Phi}_{eq}$ is found. Notice that the decreasing rate of domain-averaged sediment concentration in Case B3 is smaller than that in Case B2, and this difference can be explained by the different effective settling velocities as shown in Fig. 3.7.

More insights can be revealed by examining the time series of bottom concentration $\langle\phi_b\rangle$. In in Fig. 3.8(b), $\langle\phi_b\rangle$ of Case B2 increases slightly faster than that of Case B1 (compare the blue curve with the red curve). Similar features in the bottom concentrations are also observed for Case B3 (black curve in Fig. 3.8(b)). This sharper increase of bottom concentration is clearly associated with the collapse of flow turbulence at around $t = 13T$ for Case B2 (or $t = 10T$ for Case B3), and hence a larger increment rate of the bottom concentration must then occur for the next couple of wave cycles. This process is more clearly demonstrated in Fig. 3.9 (a) and (b). Before the flow laminarizes ($t < 13T$), the flow is evidently turbulent with peak turbulent intensity exceeding 0.15 (see Fig. 3.9(b)), and a lutocline is observed from the corresponding concentration profiles. At $t = 13T$, the turbulent intensity drops significantly and the peak value is of no more than 0.04. Two more wave periods later at $t = 15T$, the turbulent intensity is almost vanished. To respond to the suppression of turbulence, sediment concentrations in the range of $5 < z < 20$ is reduced. Meanwhile, an accumulation of sediment concentration near the bottom ($z < 5$) is observed. The increased sediment concentration near the bed can further reduce the effective settling velocity (see Eqn. (3.14)), however the deposition rate is increased (demonstrated later in Fig. 3.12), thus the bottom concentration then generally drops until the final equilibrium state is reached (see Fig. 3.8(b)). The interplay between the deposition flux and bottom concentration after laminarization further determines the equilibrium balance between erosion flux and deposition flux. Quantitatively, the erosion flux after laminarization in the numerical simulation is only determined by viscous suspension, which is sensitive to the Schmidt number Sc specified. However, the qualitative feature discussed here is unaffected by the value used for Sc.

From the above discussions, we can clearly observe that significantly suppressed turbulence and laminarized transport mode III is obtained for Cases B2 and B3 due to initially high sediment availability, which is consistent with the finding discussed in Cheng et al. (2015a). However, in Cheng et al. (2015a), the high sediment availability is obtained via a lower critical shear stress of erosion (lower than the value used here), while in this study, the higher sediment availability is associated with a significant hindered settling effect. Indeed, Cheng et al. (2015a) also demonstrated that by systematically reducing the settling velocity used in each simulation, larger availability is obtained which can also lead to laminarization.

If we further reduce the reference concentration as in Case B4 ($\phi_{ref} = 0.05$), we would expect laminarized transport mode III with even lower sediment availability $\overline{\Phi}_{eq}$ that that in Case B3. However, the time series of domain-averaged concentration shows unexpected features. We can observe that the domain-averaged concentration continue to increase as wave motion persists. Eventually the increment rate becomes relatively constant, however, an equilibrium state such as those of Case B1-B3 cannot be established. This unbounded mode of suspended sediment load in the domain is caused by the significantly reduced deposition flux (or nearly zero deposition flux) associated with very large hindered settling effect.

According to the time series of bottom concentration of Case B4 shown in Fig. 3.8(b), the larger increment rate after the laminarization at $t = 10T$ is consistent with that of Cases B2 and B3. However, the subsequent time series of $\langle\phi_b\rangle$ of Case B4 again shows a trend of continue increment, which indicates that the equilibrium balance between the erosion flux and the deposition flux cannot be established. From the snapshots of sediment concentration and turbulent intensity profiles (see Fig. 3.9(c) and (d)), during the early stage of the simulation at $t = 6T$ (or $t = 9T$), a lutocline can be observed in the concentration profile and the flow is turbulent. After the onset of laminarization, the flow turbulence is almost completely suppressed (see $t = 12T$) and the sediment concentration shows the expected concave-upward profile. What is unexpected is that by comparing the concentration profile between $t = 15T$ and $t = 18T$, it

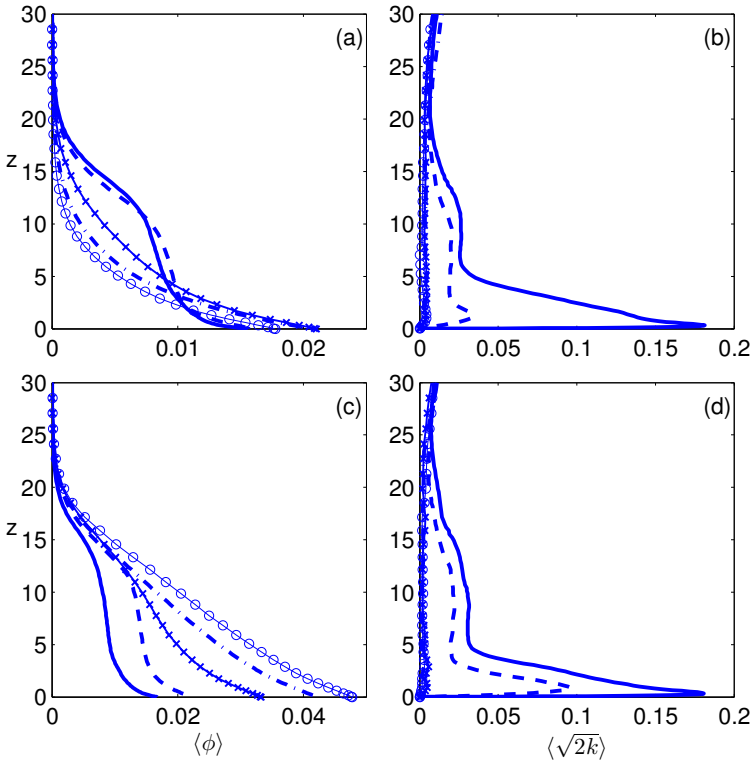

Figure 3.9: Plane-averaged (a) sediment concentration profiles and (b) turbulent intensity profiles for Case B2 at five different instants: $t = 11T$ (blue solid curve), $t = 13T$ (dashed curve), $t = 15T$ (red solid curve), $t = 17T$ (dash-dot curve), $t = 19T$ (curve with circle symbols). The corresponding plane-averaged profiles for Case B4 are shown in (c) and (d) at five different instants: $t = 6T$ (blue solid curve), $t = 9T$ (dashed curve), $t = 12T$ (red solid curve), $t = 15T$ (dash-dot curve), $t = 18T$ (curve with circle symbols).

becomes clear that the total amount of suspended sediment in the domain (or sediment availability) continue to increase cycle by cycle. Hence, by considering the hindered settling with a very low gelling concentration, the flow feature obtained in Case B4 after the onset of laminarization is distinctly different from that of Cases B2 and B3. The flow feature demonstrated in Case B4 is similar to the gelling ignition discussed in Kampf & Myrow (2014). It is reminded that when the sediment concentration becomes large, the assumptions of the equilibrium Eulerian approximation and Boussinesq approximation may be violated. To confirm this, the maximum concentrations ϕ_{max} in

each case are also shown in Table 1. We can see that the maximum concentration in each is no more than 0.05, which is sufficiently small. In Case B4, the simulation is terminated as the bottom concentration exceeds 0.05, however, the fate of the sediment transport at this point is already clear.

In summary, the transition from transport mode II to transport mode III can be triggered by the hindered settling with a low reference (gelling) concentration. This transition of transport modes is due to the reduction in the effective settling velocity when the hindered settling is considered. As discussed in Cheng et al. (2015a), the reduced settling velocity can increase the sediment availability, and the resulting sediment-induced stable density stratification is enhanced that further trigger the flow laminarization. Interestingly, in the laminarized transport mode III, an unstable mode, where the deposition flux becomes always smaller than the erosion flux, is obtained when a sufficiently low gelling concentration is used. In the next section, we will show that the observed unstable mode is indeed the gelling ignition as described in Kampf & Myrow (2014) and a sufficient condition for its occurrence is proposed.

3.5 Discussion

3.5.1 Turbulence modulation due to increasing Stokes number

Although including the inertia terms in the particle velocity expression for fine sediment in typical continental shelf condition ($St = 0.03$) makes no more than %10 difference on the mean quantities (see Fig. 3.2), it is likely that the inertia effect can be more pronounced when the Stokes number St is larger in Case A2 and Case A3 (see Table 1). We like to also point out that Case A2 and A3 are numerical experiments with increased Stokes number, while other non-dimensional parameters are kept the same. Since the physical condition of Case A2 and A3 may not occur for typical fine sediment in the continental shelf, we focus on comparing non-dimensional quantities and turbulence modulation.

Ensemble-averaged sediment concentration, fluid streamwise velocity and turbulent intensity are compared in Fig. 3.10 for cases with different Stokes numbers

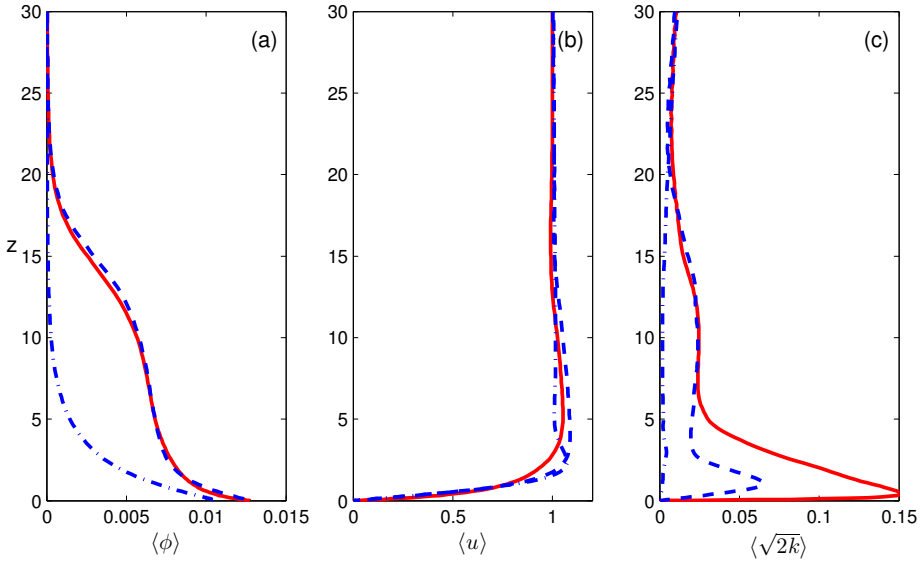

Figure 3.10: Comparisons of (a) sediment concentration, (b) streamwise velocity and (c) turbulence intensity for Case A1 (solid curve), Case A2 (dashed curve) and Case A3 (dash-dot curve).

(Case A1-A3). From the concentration profiles (Fig. 3.10(a)), we can see that the lutoclines, which is typical for transport mode II, appear in both Case A1 and A2. However, the lutocline is absent in Case A3, and a rapid decaying sediment concentration is observed. The boundary layer thickness is significantly reduced in Case A3, which is evident in the streamwise velocity profiles (Fig. 3.10(b)). Meanwhile, from the turbulence intensity profile, we observe that increasing the Stokes number, the flow turbulence is evidently decreased. Particularly, for Case A3 with $St = 0.2$, the flow turbulence is almost completely suppressed. By increasing the St to about 0.2, laminarized mode III is obtained.

Previous studies found that intense and persistent local vortical structures can influence the local particle concentration field, and the effect of large particle inertia would bias the particle trajectory towards regions of high strain rate and low vorticity due to the centrifugal effect. This biased distribution of inertia particles has been identified as preferential accumulation (e.g., Wang & Maxey 1993). If we take the

divergence of the particle velocity shown in Eqn. (3.15), due to the incompressibility of the carrier flow, the following relationship is obtained:

$$\frac{\partial u_i^s}{\partial x_i} = St(1 - \frac{1}{s})(\|\Omega\|^2 - \|S\|^2) = 2St(1 - \frac{1}{s})Q, \tag{3.24}$$

where $\|S\|$ is the magnitude of strain-rate tensor, and $\|\Omega\|$ is the magnitude rotation-rate tensor. In an incompressible flow, the second invariant $Q = 1/2(\|\Omega\|^2 - \|S\|^2)$ is a local measure of the excess rotation rate relative to the strain rate (Chakraborty et al. 2005). When $s > 1$, i.e. particles are denser than the carrier fluid, the divergence of particle velocity has the same sign as Q, indicating that the particles tend to accumulate in regions where the strain rate is larger than the rotation rate, (i.e. $\|S\|^2 > \|\Omega\|^2$). Meanwhile, it is noted that the effect of particle inertia grows as the particle Stokes number increases, which is evident from Eqn. (3.24).

To identify the preferential concentration phenomenon, the iso-surface of the second invariant Q field is plotted against the plane cut ($z = 1.5$) of the sediment concentration field at $t = 10T$ for Case 0 and Case A3 (see Fig. 3.11). At the moment of $t = 10T$ presented here, both cases are still turbulent. As discussed before, denser-than-fluid inertial particles prefer to concentrate in regions of low vorticity and high strain rate. Hence, we expect that negative Q value regions would correspond to high concentration field. From Fig. 3.11(a), we can see that when inertia terms are ignored in the sediment velocity (Eqn. (3.15)), the turbulence structures represented by negative Q value typically covers both high and low concentration regions (see the sub-panels in (a) for enlarged view). However, when the inertia terms are included with high $St = 0.2$ (see Fig. 3.11(b)), the high correlation between turbulence structures represented by negative Q and high sediment concentration region can be observed (the sub-panels in (b) for enlarged view). It is evident that the inertia terms in the sediment velocity expression is responsible for the preferential concentration of sediment observed in Fig. 3.11(b).

In summary, two additional numerical experiments are carried out by increasing

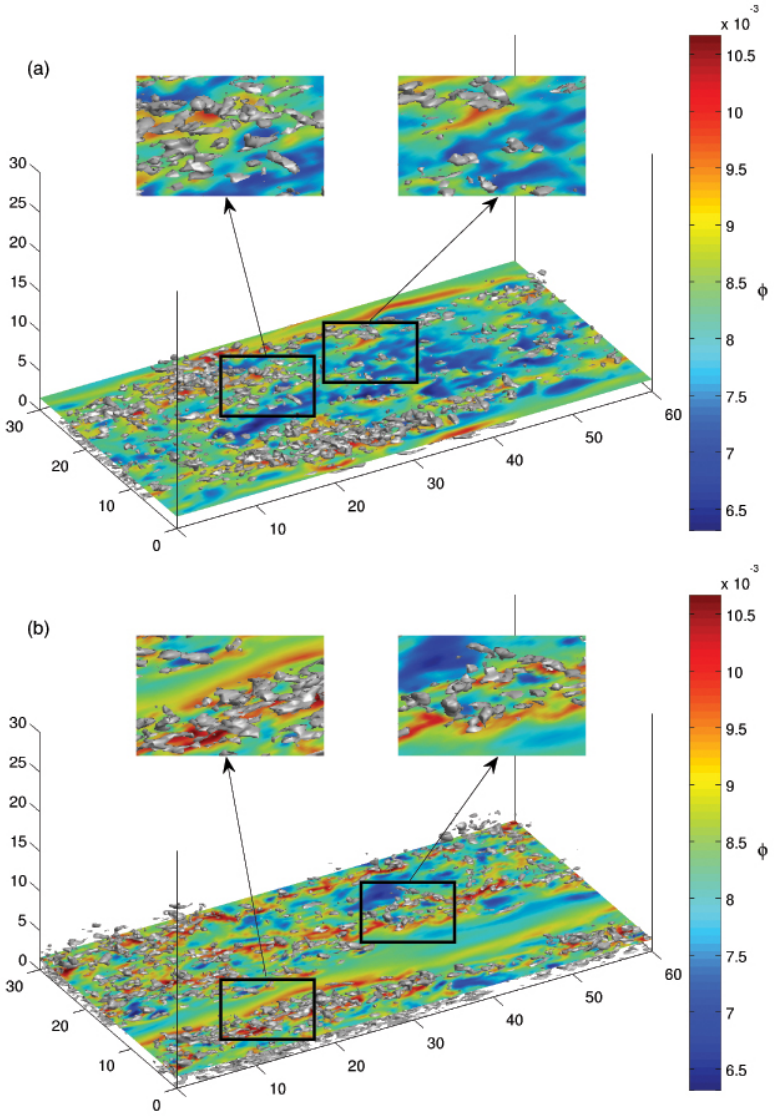

Figure 3.11: Turbulent coherent structures at flow peak ($t = 10T$) for (a) Case 0 and (b) Case A3. The turbulent coherent structures are visualized using the second invariant Q, and the contour level used here is -0.04 (non-dimensional). The plane cuts of the concentration ϕ field at $z = 1.5$ are also shown. The sub-panels show enlarged views for better visualization of the preferential concentration effect.

St, while keeping the other non-dimensional parameters the same as Case 0. Analysis of the mean profiles reveals that large particle inertia tends to attenuate flow turbulence. The well-known preferential concentration effect is illustrated using Case A3.

3.5.2 Gelling ignition

The unbounded resuspension of sediments in Case B4 is an interesting phenomenon, which may have profound implications on the fine sediment transport on continental shelves. Similar results are also reported by Kampf & Myrow (2014) using an eddy-viscosity based model, and it is named gelling ignition. Here, the more sophisticated turbulence-resolving simulation results are used to further investigate the occurrance of gelling ignition. The time-averaged deposition flux over one wave cycle $\overline{\widetilde{D}}$ is calculated and approximated as:

$$\overline{\widetilde{D}} = \widetilde{W}_{s0}\overline{\phi_b\Big(1-\frac{\phi_b}{\phi_{ref}}\Big)^m} \approx \widetilde{W}_{s0}\overline{\phi_b}\Big(1-\frac{\overline{\phi_b}}{\phi_{ref}}\Big)^m. \tag{3.25}$$

We need to point out that this approximation shown on the right-hand-side is only appropriate when the variation of bottom concentration during one wave cycle is small (see Fig. 3.8(b)). Since $m \neq 0$, the wave-averaged deposition flux is clearly a nonlinear function of wave-averaged bottom sediment concentration that also depends on the reference (gelling) concentration ϕ_{ref}. In Fig. 3.12, $\overline{\widetilde{D}}$ is plotted against $\overline{\phi_b}$ with $m = 4.6$ for four different ϕ_{ref} considered in this study. It is noted that for a given ϕ_{ref}, there exists a maximum $\overline{\widetilde{D}}$ and this maximum deposition flux is smaller for lower gelling concentration due to hindered settling effect. On the other hand, the erosional flux averaged over one wave cycle is calculated as:

$$\overline{\widetilde{E}} \approx \widetilde{m}_e\Big(\frac{\overline{|\widetilde{\tau}_b|}}{\widetilde{\tau}_c}-1\Big), \tag{3.26}$$

where the approximation of the wave-averaged erosional flux is appropriate for relatively small critical shear stress (Cheng et al. 2015a). Once the wave-averaged bottom shear stress $\overline{|\widetilde{\tau}_b|}$ can be estimated, $\overline{\widetilde{E}}$ is determined. Two scenarios can be expected. If $\overline{\widetilde{E}}$ is lower than the the maximum $\overline{\widetilde{D}}$, an equilibrium state exists, which corresponds to one of the interceptions between $\overline{\widetilde{E}}$ and $\overline{\widetilde{D}}$ (see Fig. 3.12). The transport mode of this equilibrium state is further determined by the degree of sediment-induced density

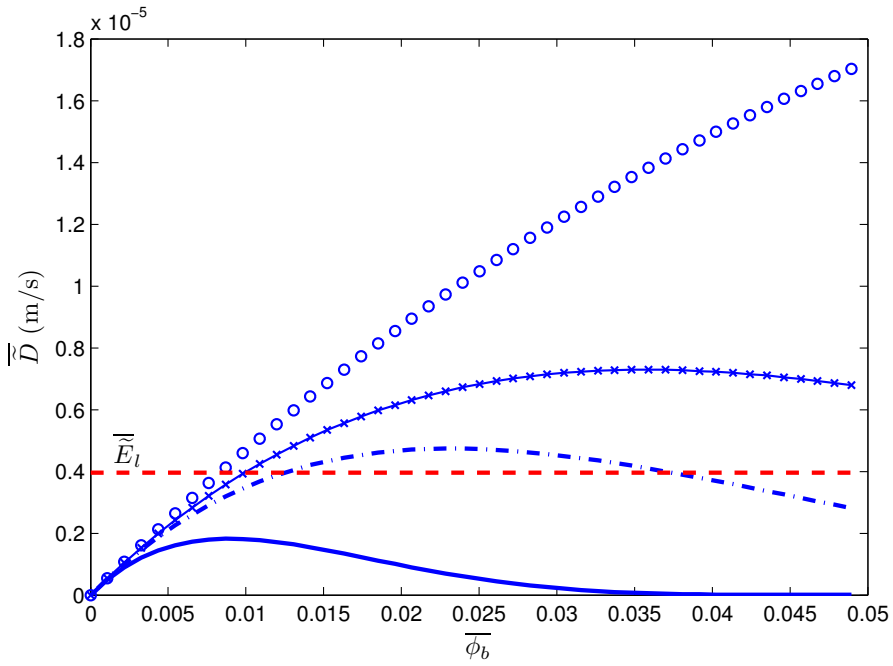

Figure 3.12: Wave-averaged depositional flux $\overline{\widetilde{D}}$ as a function of wave-averaged bottom concentration $\overline{\phi_b}$ for Case B1 (red solid curve), Case B2 (blue solid curve), Case B3 (black solid curve) and Case B4 (green solid curve). The dashed curve $\overline{\widetilde{E}_l}$ is the wave-averaged erosion flux at the bottom calculated using laminar solution of bottom shear stress at $Re_\Delta = 1000$ (Cheng et al. 2015a). The dimensional value for the critical shear stress of erosion is $\widetilde{\tau}_c = 0.02$ Pa for all the cases.

stratification (Ozdemir et al. 2010, Cheng et al. 2015a). On the other hand, if the erosion flux is always greater than the deposition flux, no equilibrium state exists, and this will further result in the unlimited resuspension, or gelling ignition, as observed previously.

Because sediments can attenuate the flow turbulence and hence reduce the bottom stress, in general it is not straightforward to estimate the wave-averaged bottom stress magnitude $\overline{|\widetilde{\tau}_b|}$ in order to estimate $\overline{\widetilde{E}}$. Numerical simulation carried out in this study can provide information on bottom stress and $\overline{|\widetilde{\tau}_b|}$ at the equilibrium state are shown as $\overline{\widetilde{\tau}}_{eq}$ in Table 3.1. Because a large (or unlimited) supply of resuspended sediment is expected when gelling ignition occurs, laminarized transport mode III is surely

to follow. Indeed, model results discussed here suggest when gelling ignition occurs in Case B4, $\overline{|\widetilde{\tau}_b|}$ reduces to 0.28 Pa (Table 3.1), which is identical to the laminar solution at Stokes Reynolds number of Re_Δ=1000 (Cheng et al. 2015a). The corresponding erosion flux $\overline{\widetilde{E}}_l$ associated with $\overline{|\widetilde{\tau}_b|}$=0.28 Pa is shown in Fig. 3.12 (see the dashed line). It is evident that the deposition flux associated with a gelling concentration of ϕ_{ref}=0.05 is always lower than $\overline{\widetilde{E}}_l$ while for Cases B1, B2 and B3 with higher gelling (reference) concentration, there are always interceptions between $\overline{\widetilde{D}}$ and $\overline{\widetilde{E}}_l$.

Through the above analysis, we can see that the gelling ignition can be triggered by a low gelling (reference) concentration in the hindered settling model. When the gelling concentration is low enough, the deposition flux curve is always below the erosional flux line. Consequently, the net flux at the bottom boundary is always positive (net erosional), and more sediments are resuspended into the domain. In this process, although the flow is initially turbulent, as the sediment availability increases, the sediment-induced density stratification is enhanced. Eventually, the laminarized transport mode III is obtained. It is noted that even in the laminarized stage, the viscous suspension in the laminarized flow can keep sediment suspended. In reality, viscous suspension further depends on the closure of rheological stress, which is neglected here, and we parameterize the viscous suspension process simply with a constant Schmidt number $Sc = 0.5$.

With findings learned so far, it is possible to propose a simple parameterization for the occurrence of the gelling ignition. We consider that the critical condition to initiate gelling ignition is when the wave-averaged erosion flux at equilibrium balances the maximum wave-averaged depositional flux. For the deposition/erosion formulations adopted here and the resulting wave-averaged form shown in Eqns. (3.25) and (3.26), the critical condition occurs at $\phi_b = \phi_{ref}/(m+1)$ with

$$\overline{\widetilde{D}}_{max} = \widetilde{W}_{s0}\phi_{ref}\frac{m^m}{(m+1)^{m+1}}. \tag{3.27}$$

By evaluating $\overline{\widetilde{E}} = \overline{\widetilde{D}}_{max}$ at equilibrium, we obtain:

$$\phi_{ref} = \frac{\widetilde{m}_e}{\widetilde{W}_{s0}} \frac{(m+1)^{m+1}}{m^m} \Big(\frac{\overline{|\widetilde{\tau}_b|}}{\widetilde{\tau}_c} - 1 \Big), \tag{3.28}$$

For cohesive sediments, this expression involves several empirical parameters associated with flocs, including the floc settling velocity $\widetilde{W}_{s0}$, and erodibility parameters $\widetilde{m}_e$ and $\widetilde{\tau}_c$. It is reminded that the floc properties are assumed to be constant throughout the simulation, and the complexity of variable viscosity due to rheology is neglected. This assumption may not be held true in reality. Nevertheless, our model results provides the first step to understand the condition for the occurrence of gelling ignition. As demonstrated in this study, the gelling ignition is likely to occur near laminarization, we specify $\overline{|\widetilde{\tau}_b|} = 0.28$ Pa as in the laminarized flow at Stokes Reynolds number Re_Δ=1000. Using the values of $\widetilde{m}_e$ and $\widetilde{W}_{s0}$ identical to those used in the numerical simulations (see Table 3.1), a 2D map for the occurrence of gelling ignition as a function of critical shear stress of erosion and gelling (reference) concentration is shown in Fig. 3.13(a). The curve shown in Fig. 3.13(a) represents Eqn. (3.28) with $\overline{|\widetilde{\tau}_b|} = 0.28$ Pa and the region below the curve signifies the occurrence of gelling ignition. The corresponding values for Cases B1-B4 are also plotted, and the prediction of Eqn.(3.28) is consistent with the numerical results of this study for Re_Δ=1000. Since the main flow variable in Eqn. (3.28) is the wave-averaged bottom stress $\overline{|\widetilde{\tau}_b|}$ and we have demonstrated that the laminar solution value is appropriate for the present purpose, we can further present the prediction formula of Eqn. (3.28) for other (lower) Stokes Reynolds number by specifying $\overline{|\widetilde{\tau}_b|}$ using the corresponding value obtained from the laminar solution (see Fig. 3.13(b)). As mentioned before, the gelling concentration can be related to the fractal dimension n_f, and more porous, organic flocs tend to have lower n_f and hence lower gelling concentration. Fig. 3.13(b) indicates that for cohesive sediment with lower critical shear stress of erosion $\widetilde{\tau}_c$, gelling ignition can be triggered at higher gelling concentration (higher n_f). Moreover, when the oscillatory flow is more energetic (larger Re_Δ), the gelling ignition can also be triggered at higher

gelling concentration (higher n_f).

3.6 Conclusion

In this study, the uncertainties due to model simplifications in sediment phase velocity, namely particle inertia and hindered settling for fine sediment transport in the wave boundary layer are investigated. Continuing the work of Cheng et al. (2015a), fine sediment resuspension/deposition in the oscillatory boundary layer with Stokes Reynolds number $Re_\Delta = 1000$ is carried out by using a highly accurate turbulence-resolving model (Yu et al. 2013, Cheng et al. 2015a). It is revealed that retaining the particle inertia at the Stokes number of $St = 0.03$, which corresponds to the value typical for fine sediment transport in energetic continental shelves, makes a very minor difference in the numerical results. Attenuation of flow turbulence is increased by no more than 10% by considering the particle inertia at $St = 0.03$ and the resulting transport mode is unchanged. Therefore, previous numerical studies neglecting the particle inertia effect at Stokes number up to 0.03 is justified. However, further numerical experiments with larger St reveal that particle inertia tends to damp flow turbulence, and the transport mode II in Case 0 shifts to transport mode III when the Stokes number St increases to 0.2.

At a fixed critical shear stress ($\widetilde{\tau}_c = 0.02$ Pa) for erosion, the sediment availability in the domain is increased due to the reduced deposition flux by hindered settling. However, the degree of hindered settling is highly dependent on the reference (gelling) concentration used. For non-flocculated sediment with ϕ_{ref}=0.63, the increase of sediment availability is only about 10%, while the turbulence attenuation is slightly increased, no shift of transport modes is observed. However, when flocs of relatively high fractal dimension are considered, which results in ϕ_{ref}=0.2 and 0.13, more significant hindered settling effect enhances sediment availability, significantly attenuates flow turbulence and a laminarized transport mode III is obtained. After laminarization, an equilibrium state can be established with a balance between the depositional flux and the erosion flux due to viscous suspension. However, for more porous flocs

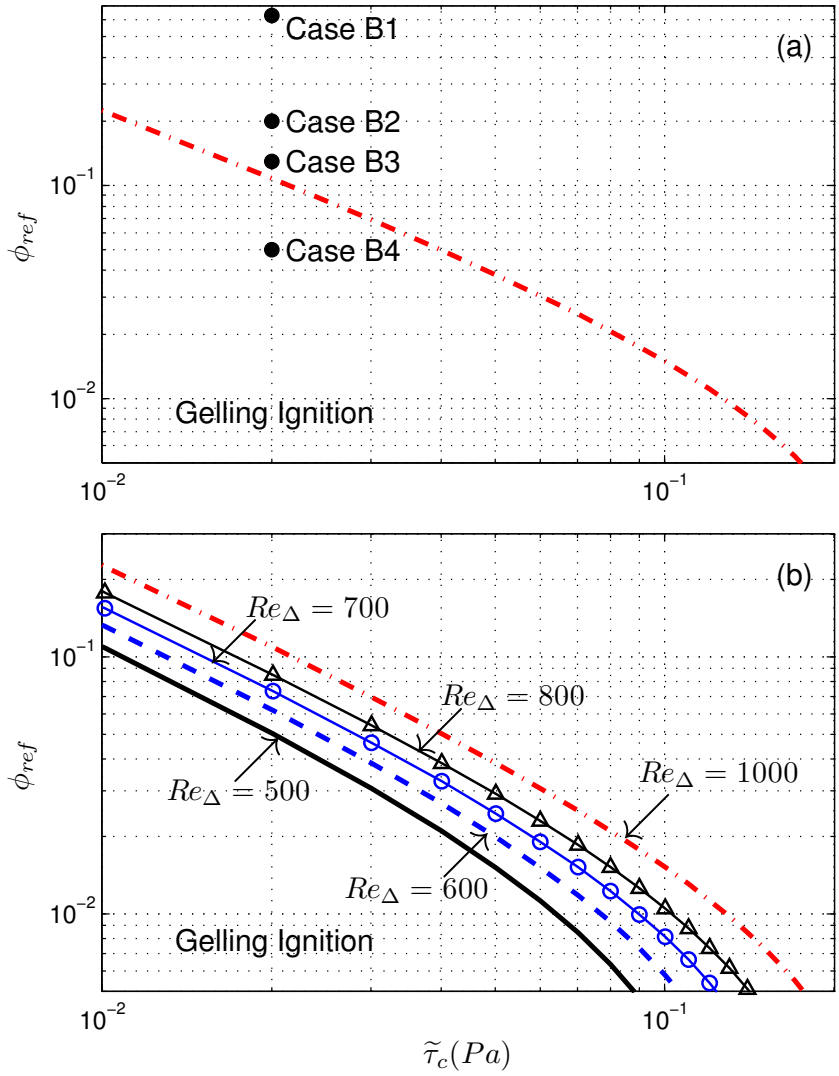

Figure 3.13: (a) A predictor of gelling ignition as a function of dimensional critical shear stress $\widetilde{\tau}_c$ and gelling concentration ϕ_{ref} at $Re_\Delta = 1000$. The black filled circles denote Cases B1-B4 in this study; (b) A predictor of gelling ignition as a function of $\widetilde{\tau}_c$ and ϕ_{ref} at $Re_\Delta = 500$ (solid curve); $Re_\Delta = 600$ (dashed curve); $Re_\Delta = 700$ (curve with circle symbols); $Re_\Delta = 800$ (curve with triangle symbols); $Re_\Delta = 1000$ (dash-dot curve). All the results shown here are for $\widetilde{W}_s$=0.5 mm/s and $\widetilde{m}_e = 3.05 \times 10^{-7}$ m/s.

of a low fractal dimension that gives ϕ_{ref}=0.05, we demonstrate that an equilibrium state cannot be achieved. An unlimited increase of sediment in the domain is obtained in the simulation because the depositional flux is always lower than the erosion flux. This unlimited sediment availability is caused by the gelling ignition as described in Kampf & Myrow (2014).

Simulations carried out in the previous studies (Ozdemir et al. 2010, Cheng et al. 2015a) and this study show a bimodal behavior, in which large amount of fine sediments can be kept in suspension driven by an energetic wave condition at high gelling concentration (ϕ_{ref}=0.63) in the turbulent transport mode II and at very low gelling concentration in laminarized transport mode III as the gelling ignition is triggered. These findings provide critical insights into the formation and the fate of wave supported sediment-driven gravity flows.

Finally, a criterion for the occurrence of gelling ignition is proposed. From the theoretical perspective, we provide a framework of such criteria and demonstrate that the laminar solution can be used for the specification of bottom stress. However, we need to also note that other critical quantities related to floc structures, such as the Stokes settling velocity, erodibility parameters (e.g., $\widetilde{\tau}_c$ and $\widetilde{m}_e$) and gelling concentration are still highly empirical and rely on in-situ data. Characterizing and modeling those parameters for cohesive sediment is complex due to consolidation, sand content and bio-chemical effects, thus more future studies are needed.

3.7 Acknowledgments

This work is supported by National Science Foundation (OCE-1130217) and Office of Naval Research (N00014-14-1-0586) to the University of Delaware and National Science Foundation (OCE-1131016) to the University of Florida. Simulations presented in this paper are carried out on Chimera and Mills at the University of Delaware and the Extreme Science and Engineering Discovery Environment, which is supported by National Science Foundation Grant No. TG-OCE100015.

Chapter 4

EULERIAN TWO-PHASE FLOW GOVERNING EQUATIONS

In this chapter, a general Eulerian two-phase flow equations for modeling fluid-particle system is presented. The derivation begins at the Boltzmann transport equation to describe the probability of finding particles or fluid parcel (mesoscale) within a small position range and velocity range at a certain instant. By further adopting the Maxwellian velocity distribution for the change rate of probability density function due to collisions of particles or fluid parcels, the macroscopic continuity and momentum equations for the fluid and sediment phase can be derived. In the derivation, no ensemble-averaging or scale-separation for flow turbulence is assumed, and the governing equations are the foundation for turbulence-averaged model (chapter 5) and turbulence-resolving model (chapter 6).

4.1 Boltzmann Transport Equation

We consider a large collection of granular particles or fluid parcels (both are uniform and spherical), and they are collectively referred to as particles hereafter. A statistical description of a large collection of particles can be explained by a velocity distribution function $f(\boldsymbol{r}, \boldsymbol{c}, t)$, where $\boldsymbol{r}$ is the position vector, and $\boldsymbol{c}$ is the velocity vector. $f(\boldsymbol{r}, \boldsymbol{c}, t)$ is defined such that $f d\boldsymbol{c}$ is the differential number of particles per unit volume with velocities within the range between $\boldsymbol{c}$ and $\boldsymbol{c} + d\boldsymbol{c}$. If we consider the particles are forced by the external force $\boldsymbol{F}$, according to the momentum theorem, the number of particles initially in the range of $(\boldsymbol{r}, \boldsymbol{c}, t)$ will remain the same after time dt in the range of $(\boldsymbol{r} + \boldsymbol{c}dt, \boldsymbol{c} + \boldsymbol{F}dt, t + dt)$. If we take account of the the rate of change

in the distribution function due to collisions, we can have the Boltzmann transport equation:

$$\frac{\partial f}{\partial t} + c_i \frac{\partial f}{\partial x_i} + F_i \frac{\partial f}{\partial c_i} = \Omega_c(f) \tag{4.1}$$

where $\Omega_c(f)$ is the collisional rate of change in the distribution function f. The particle macroscopic quantities $M(\psi)$ can be easily related to the mesoscale quantities ψ by:

$$M(\psi) = \frac{1}{n} \int \psi f d\mathbf{c}, \tag{4.2}$$

where n is the particle number density,

$$n = \int f d\mathbf{c}, \tag{4.3}$$

The transport equation of any macroscopic quantity $M(\psi)$ can be derived by multiplying the Boltzmann equation by $\psi d\boldsymbol{c}$ and integrating over the velocity space:

$$\frac{\partial n M(\psi)}{\partial t} + \frac{\partial n M(c_i \psi)}{\partial x_i} - n \left[M\left(\frac{\partial \psi}{\partial t}\right) + M\left(c_i \frac{\partial \psi}{\partial x_i}\right) + F_i M\left(\frac{\partial \psi}{\partial c_i}\right) \right] = \Omega_c(\Psi) \tag{4.4}$$

In the scope of this chapter, we only consider ψ to be a function of $\boldsymbol{c}$, so the terms $\partial\psi/\partial t$, $\partial\psi/\partial x_i$ drops. The transport equation is hereby simplified to be:

$$\frac{\partial n M(\psi)}{\partial t} + \frac{\partial n M(c_i \psi)}{\partial x_i} - n \left[F_i M\left(\frac{\partial \psi}{\partial c_i}\right) \right] = \Omega_c(\psi) \tag{4.5}$$

However, assumptions of collisional rate of change has to be made to close the problem. If we assume that only binary collisions between particles are dominant, for example, consider the collision between particle 1 and particle 2 with the same particle diameter d_p, the probable number of collisions per unit time such that particle 1 and particle 2 are within the collision cylinder of volume $d_p^2(\boldsymbol{c_{12}} \cdot \boldsymbol{k}) d\boldsymbol{k}$ per unit time can be quantified by a pair-distribution function, which is defined such that $f^{(2)} d\boldsymbol{r_1} d\boldsymbol{r_1} d\boldsymbol{c_1} d\boldsymbol{c_1}$ is the probability of finding a pair of particles centered at $\boldsymbol{r_1}$ and $\boldsymbol{r_2}$ and have a velocity

within the range of $\boldsymbol{c_1}$ to $\boldsymbol{c_1} + d\boldsymbol{c_1}$, and $\boldsymbol{c_2}$ to $\boldsymbol{c_2} + d\boldsymbol{c_2}$.

$$f^{(2)}(\boldsymbol{r}, \boldsymbol{c_1}; \boldsymbol{r} + d_p\boldsymbol{k}, \boldsymbol{c_2}; t) d_p^2 (\boldsymbol{c_{12}} \cdot \boldsymbol{k}) d\boldsymbol{k} d\boldsymbol{c_1} \boldsymbol{c_2} d\boldsymbol{r}, \tag{4.6}$$

Due to the collisions, the quantity ψ_1 of particle 1 changes to ψ_1', and the collisional rate of change for ψ_1 per unit volume is (Lun et al. 1984):

$$\Omega_c(\psi) = \int_{\boldsymbol{c_{12}} \cdot \boldsymbol{k} > \boldsymbol{0}} (\psi_1' - \psi_1)(\boldsymbol{c_{12}} \cdot \boldsymbol{k}) f^{(2)}(\boldsymbol{r} - d_p\boldsymbol{k}, \boldsymbol{c_1}; \boldsymbol{r}, \boldsymbol{c_2}; t) d\boldsymbol{k} d\boldsymbol{c_1}) d\boldsymbol{c_2}, \tag{4.7}$$

Since the collision is symmetric, we can directly write the collision rate of change for ψ_2 per unit volume is:

$$\Omega_c(\psi) = \int_{\boldsymbol{c_{12}} \cdot \boldsymbol{k} > \boldsymbol{0}} (\psi_2' - \psi_2)(\boldsymbol{c_{12}} \cdot \boldsymbol{k}) f^{(2)}(\boldsymbol{r} + d_p\boldsymbol{k}, \boldsymbol{c_1}; \boldsymbol{r}, \boldsymbol{c_2}; t) d\boldsymbol{k} d\boldsymbol{c_1}) d\boldsymbol{c_2}, \tag{4.8}$$

After expanding the pair-distribution function $f^{(2)}(\boldsymbol{r}, \boldsymbol{c_1}; \boldsymbol{r} + d_p\boldsymbol{k}, \boldsymbol{c_2}; t)$ in a Taylor series, and only keep the first order involving the spatial derivatives:

$$\begin{aligned} f^{(2)}(\boldsymbol{r}, \boldsymbol{c_1}; \boldsymbol{r} + d_p\boldsymbol{k}, \boldsymbol{c_2}; t) &= f^{(2)}(\boldsymbol{r} - d_p\boldsymbol{k}, \boldsymbol{c_1}; \boldsymbol{r}, \boldsymbol{c_2}; t) \\ &\quad + d_p\boldsymbol{k} \cdot \nabla f^{(2)}(\boldsymbol{r} - d_p\boldsymbol{k}, \boldsymbol{c_1}; \boldsymbol{r}, \boldsymbol{c_2}; t), \end{aligned} \tag{4.9}$$

Combining equation 4.7-4.9, we can get the rate of change in ψ due to collision can be calculated as:

$$\Omega_c(\psi) = \nabla \cdot \boldsymbol{T}(\psi) + \chi(\psi), \tag{4.10}$$

where

$$\boldsymbol{T}(\psi) = \frac{d_p}{2} \int_{\boldsymbol{c_{12}} \cdot \boldsymbol{k} > \boldsymbol{0}} (\psi_1' - \psi_1)(\boldsymbol{c_{12}} \cdot \boldsymbol{k}) f^{(2)}(\boldsymbol{r_1}, \boldsymbol{c_1}; \boldsymbol{r_2}, \boldsymbol{c_2}; t) d\boldsymbol{k} d\boldsymbol{c_1}) d\boldsymbol{c_2}, \tag{4.11}$$

$$\chi(\psi) = \frac{1}{2} \int_{\boldsymbol{c_{12}} \cdot \boldsymbol{k} > \boldsymbol{0}} (\psi_1' + \psi_2' - \psi_1 - \psi_2)(\boldsymbol{c_{12}} \cdot \boldsymbol{k}) f^{(2)}(\boldsymbol{r_1}, \boldsymbol{c_1}; \boldsymbol{r_2}, \boldsymbol{c_2}; t) d\boldsymbol{k} d\boldsymbol{c_1}) d\boldsymbol{c_2}, \tag{4.12}$$

4.2 Two-phase Governing Equations

The macroscopic governing equations of two-phase flow can be derived from the mesoscale Boltzmann transport equation. As discussed above, the collisional rate of change needs a priori assumption of the pair-distribution of $f^{(2)}(\boldsymbol{r_1}, \boldsymbol{c_1}; \boldsymbol{r_2}, \boldsymbol{c_2}; t)$. In the section, we adopt Maxwellian velocity distribution and Enskog assumption, and a derivation of the fluid mass conservation, momentum equation for fluid phase and sediment phase is briefly presented, as well as the kinetin energy transport equations for the granular temperature.

4.2.1 Fluid phase governing equations

For the fluid phase, considering the fluid mass per unit volume as: $\phi^f \rho^f = n^f m^f$, where ϕ^f is the fluid volume concentration, n^f is the number density of fluid parcel, and m^f is the mass of fluid parcel. We can obtain the conservation of mass by substituting $\psi = m^f$ into equation 4.5, we can get:

$$\frac{\partial n^f m^f}{\partial t} + \frac{\partial n^f M(c_i m^f)}{\partial x_i} - n^f \left[F_i M \left(\frac{\partial m^f}{\partial c_i} \right) \right] = \Omega_c(m^f), \tag{4.13}$$

where the relation $M(m^f) = m^f$ is used, because we assume that there is no phase changes. For the same reason, the third term on the left-hand-side (LHS) of equation 4.13 is zero, and It is evident that $M(c_i m^f) = m^f u_i^f$, where u_i^f is the macroscopic velocity, and $i = 1, 2, 3$ represents streamwise, spanwise and vertical components, respectively. The righ-hand-side (RHS) vanished because collisions do not create or destroy particles/mass. The mass conservation equation is derived as:

$$\frac{\partial \phi^f \rho^f}{\partial t} + \frac{\partial \phi^f \rho^f u_i^f}{\partial x_i} = 0, \tag{4.14}$$

We further substitute $\psi = m^f c_j$ into equation 4.5, we obtain,

$$\frac{\partial n^f M(m^f c_i)}{\partial t} + \frac{\partial n^f M(m^f c_i c_j)}{\partial x_j} - n^f \left[F_j^f M \left(\frac{\partial m^f c_i}{\partial c_j} \right) \right] = \Omega_c(m^f c_i), \tag{4.15}$$

and we assume that total momenta is conserved, namely, the total momenta of particle 1 and particle 2 after the collision remain the same as before the collision: $\psi_1' + \psi_2' = \psi_1 + \psi_2$. Meanwhile, the fluid phase is assumed to be incompressible and isothermal, and hence the RHS of equation 4.15 also vanishes (see equation 4.10). The first term on LHS of equation 4.15 is

$$\frac{\partial \phi^f \rho^f u_i^f}{\partial t}, \tag{4.16}$$

The second term of equation 4.15 is

$$\frac{\partial n^f M(m^f c_i c_j)}{\partial x_j} = \frac{\partial}{\partial x_i}\left[\phi^f \rho^f (u_i^f u_j^f) + \phi^f \rho^f M[(c_i - u_i^f)(c_j - u_j^f)]\right], \tag{4.17}$$

where the last term is due to the 'random' motion of fluid parcels, and this term can be closed with a constitute law, where the diagonal contribution is termed as pressure (p^f), and off-diagonal part is called viscous shear stress (τ_{ij}^f):

$$p^f = \rho^f M[(c_i - u_i^f)(c_i - u_i^f)], \tag{4.18}$$

$$\tau_{ij}^f = p^f \delta_{ij} - \rho^f M[(c_i - u_i^f)(c_j - u_j^f)], \tag{4.19}$$

where δ_{ij} is the Kronecker delta, and the third term of equation 4.15 is

$$-n^f \left[F_j M\left(\frac{\partial m^f c_i}{\partial c_j}\right)\right] = -n^f m^f F_j \delta_{ij} = -\phi^f \rho^f F_i, \tag{4.20}$$

The external force for the fluid includes the gravity g_i and inter-phase momentum transfer from sediment phase M_i^{fs}, which will be discussed in section 4.2.4. Consequently, we have derived the conservation equations for mass and momentum of the fluid phase as:

$$\frac{\partial \phi^f \rho^f}{\partial t} + \frac{\partial \phi^f \rho^f u_i^f}{\partial x_i} = 0, \tag{4.21}$$

$$\frac{\partial \phi^f \rho^f u_i^f}{\partial t} + \frac{\partial \phi^f \rho^f u_i^f u_j^f}{\partial x_i} = -\frac{\partial \phi^f p^f}{\partial x_i} + \frac{\partial \phi^f \tau_{ij}^f}{\partial x_j} + \phi^f \rho^f g_i + M_i^{fs}, \tag{4.22}$$

4.2.2 Sediment phase governing equations

In a similar manner, the mass conservation equations for the sediment phase can be obtained by setting $\psi = m^s$, and the resulting equation is written as:

$$\frac{\partial \phi^s}{\partial t} + \frac{\partial \phi^s u_i^s}{\partial x_i} = 0, \tag{4.23}$$

where ϕ^s is the sediment volumetric concentration, u_i^s is the macroscopic sediment velocity. Taking $\psi = m^s c_i$ and substituting it to equation 4.5, the momentum equations for sediment phase can be written as,

$$\frac{\partial \rho^s \phi u_i^s}{\partial t} + \frac{\partial \rho^s \phi u_i^s u_j^s}{\partial x_j} = n(F_j^s \frac{\partial m_p c_i}{\partial c_j})_m + \frac{\partial (\Gamma_{ij}^{sk} + \Gamma_{ij}^{sc})}{\partial x_j} \tag{4.24}$$

where F_i^s is the force acting on each particles, and as formulated in Bouillard et al. (1989), the force can include gravity, fluid pressure gradient force, and inter-phase momentum transfer force M_i^{sf}. $\Gamma_{ij}^{sk} = -\phi^s \rho^s M(C_i C_j)$ is the kinetic contribution of the stress tensor, and $C_i = c_i - u_i^s$ is the uncorrelated particle velocity. The collisional contribution of the stress tensor is $\Gamma_{ij}^{sc} = T_i(m^s c_j)$. It is often convenient to decompose the stress tensor into diagonal part, $p^{skc} = 1/3(\Gamma_{ij}^{sk} + \Gamma_{ij}^{sk})\delta_{ij}$, and off-diagonal part, $\tau_{ij}^{skc} = p^{skc}\delta_{ij} + \Gamma_{ij}^{sk} + \Gamma_{ij}^{sc}$.

It shall be noted that the above derivation assumes binary collisions between particles, this assumption holds reasonably well until the sediment concentration ϕ^s is larger than the random loose packing limit, where the particles are constantly in contact with each other. In order to model a full profile of sediment transport, the closure of particle stresses includes two components. For low to moderate sediment concentration, inter-granular interaction is assumed to be dominated by binary collisions and a closure based on kinetic theory is adopted. For large sediment concentration,

binary collision becomes unlikely and inter-granular interaction is dominated by enduring contact/frictional forces among particles (Tardos 1997). For the present sediment transport application where the immobile bed and concentrated region of transport are also resolved (Hsu et al. 2004), we assume that particle pressure and particle stress both consist of a collisional-kinetic component (super-script 'sc') and a frictional component (super-script 'sf') (Johnson & Jackson 1987),

$$p^s = p^{skc} + p^{sf}, \tag{4.25}$$

$$\tau_{ij}^s = \tau_{ij}^{skc} + \tau_{ij}^{sf}. \tag{4.26}$$

Thus the governing equations for the sediment phase can be summarized as:

$$\frac{\partial \phi^s \rho^s}{\partial t} + \frac{\partial \phi^s \rho^s u_i^s}{\partial x_i} = 0, \tag{4.27}$$

$$\frac{\partial \phi^s \rho^s u_i^s}{\partial t} + \frac{\partial \phi^s \rho^s u_i^s u_j^s}{\partial x_i} = -\frac{\partial \phi^s p^f}{\partial x_i} - \frac{\partial p^s}{\partial x_i} + \frac{\partial \tau_{ij}^s}{\partial x_j} + \phi^s \rho^s g_i + M_i^{sf}, \tag{4.28}$$

So far, the above equations are not closed because of unknown velocity distribution function and particle collision rate. Following Gidaspow (1994), Lun et al. (1984), Hsu et al. (2004), the particle stress closures are given in section 4.2.3.

4.2.3 Particle stress model

The closures for both τ_{ij}^{sc} and τ_{ij}^{sk} requires the knowledge of single-particle distribution function $f(\boldsymbol{r}, \boldsymbol{c}, t)$ and the pair-distribution function $f^{(2)}(\boldsymbol{r_1}, \boldsymbol{c_1}; \boldsymbol{r_2}, \boldsymbol{c_2}; t)$. Here we take the Maxwellian velocity distribution function as the single-particle distribution (Lun et al. 1984):

$$f(\boldsymbol{r}, \boldsymbol{c}, t) = \frac{n}{(2\pi\Theta)^{(3/2)}} exp\left[-\frac{(\boldsymbol{c} - \boldsymbol{u^s})}{2\Theta}\right] \tag{4.29}$$

where $\Theta = 1/3M(C_iC_i)$ is the granular temperature. The pair-distribution function can be obtained by taking the Enskog assumption, that is

$$f(\boldsymbol{r_1}, \boldsymbol{c_1}; \boldsymbol{r_2}, \boldsymbol{c_2}; t) = g_{s0}(\phi^s) f(\boldsymbol{r_1}, \boldsymbol{c_1}, t) f(\boldsymbol{r_2}, \boldsymbol{c_2}, t) \tag{4.30}$$

where radial distribution function g_{s0} is introduced to describe the crowdiness of particle, which is a sharp increasing function of sediment concentration, ϕ. It has been demonstrated that the formula of Carnahan & Starling (1969) under-predicts g_{s0} when concentration $\phi^s > 0.57$ (Ding & Gidaspow 1990, Sinclair & Jackson 1989). However, it is noted that in the present study when $\phi^s > 0.57$, inter-granular interactions are dominated by enduring contact/frictional component of the stress. In fact, granular temperature modeled by the kinetic theory reduces to nearly zero when particle concentration is approaching $\phi^s = 0.57$. Therefore, for simplicity, we still adopt the radial distribution function of Carnahan & Starling (1969):

$$g_{s0} = \frac{2 - \phi^s}{2(1 - \phi^s)^3}. \tag{4.31}$$

The transport equation for the granular temperature Θ can be obtained by take $\psi = 1/2 m^s C_i C_i$ in equation 4.5:

$$\frac{3}{2}\Big[\frac{\partial \phi^s \rho^s \Theta}{\partial t} + \frac{\partial \phi^s \rho^s u_j^s \Theta}{\partial x_j}\Big] = \big(-p^{skc}\delta_{ij} + \tau_{ij}^{skc}\big)\frac{\partial u_i^s}{\partial x_j} - \frac{\partial q_j}{\partial x_j} - \gamma_s + J_{int}, \tag{4.32}$$

where terms on the RHS are the production of granular temperature, the flux of granular temperature $q_j = \phi^s \rho^s M(C_i C_i C_j) - T_j(1/2 m^s C_i C_i)$, the energy dissipation rate due to inelastic collision $\gamma_s = -\chi(1/2 m^s C_i C_i)$ and the production (or dissipation) due to the interaction with the carrier fluid phase $J_{int} = \beta[M(C_{go} C_i) - 3\Theta]$ is the correlation term between uncorrelated fluid velocity and particle velocities, which needs to be modeled. Following Lun et al. (1984) and Ding & Gidaspow (1990), closure of particle pressure is written as,

$$p^{sc} = \rho^s \phi^s [1 + 2(1 + e)\phi^s g_{s0}]\Theta, \tag{4.33}$$

where e is the coefficient of restitution during collision. Following Gidaspow (1994), the particle stress is calculated as,

$$\tau_{ij}^{skc} = \mu^{sc}\Big[\frac{\partial u_i^s}{\partial x_j} + \frac{\partial u_j^s}{\partial x_i}\Big] + \big(\lambda - \frac{2}{3}\mu^{sc}\big)\frac{\partial u_k^s}{\partial x_k}\delta_{ij}. \tag{4.34}$$

Through the kinetic theory, the particle shear viscosity is calculated as a function of granular temperature and radial distribution function,

$$\mu^{sc} = \rho^s d\sqrt{\Theta}\Big[\frac{4}{5}\frac{\phi^{s2} g_{s0}(1+e)}{\sqrt{\pi}} + \frac{\sqrt{\pi} g_{s0}(1+e)(3e-1)\phi^{s2}}{15(3-e)} + \frac{\sqrt{\pi}\phi^s}{6(3-e)}\Big]. \tag{4.35}$$

Similarly, the bulk viscosity is calculated as,

$$\lambda = \frac{4}{3}\phi^{s2}\rho^s d g_{s0}(1+e)\sqrt{\frac{\Theta}{\pi}}. \tag{4.36}$$

The closure of granular temperature flux is assumed to be analogous to the Fourier's law of conduction,

$$q_j = -\kappa^{sc}\frac{\partial \Theta}{\partial x_j}, \tag{4.37}$$

where the κ^{sc} is the conductivity of granular temperature, calculated as,

$$\kappa^{sc} = \rho^s d\sqrt{\Theta}\Big[\frac{2\phi^{s2} g_{s0}(1+e)}{\sqrt{\pi}} + \frac{9\sqrt{\pi} g_{s0}(1+e)^2(2e-1)\phi^{s2}}{2(49-33e)} + \frac{5\sqrt{\pi}\phi^s}{2(49-33e)}\Big]. \tag{4.38}$$

The dissipation rate due to inelastic collision is calculated based on that proposed by Ding & Gidaspow (1990),

$$\gamma_s = 3(1-e^2)\phi^{s2}\rho^s g_{s0}\Theta\Big[\frac{4}{d}\Big(\frac{\Theta}{\pi}\Big)^{1/2} - \frac{\partial u_j^s}{\partial x_j}\Big]. \tag{4.39}$$

Due to the presence of carrier fluid phase, carrier flow turbulence can also induce particle fluctuations. However, due to the difficulty of estimating the fluctuating interaction of fluid phase and sediment phase, the transfer of the fluctuation energy J_{int} between the two phases may require a turbulence closure for the fluid phase in the presence of sediment phase (e.g., Hsu et al. 2004).

When the volumetric concentration of particles becomes close to random loose packing ($\phi^s \approx 0.57$ for uniform, spherical particles), particles are constantly in contact with one another, and most of the particle phase energy is dissipated by friction between sliding particles, rather than inelastic collision (Tardos 1997). In this condition, the

normal stress acts to support the particles and the sediment bed behaves like a solid. In other words, when the sediment concentration exceeds certain threshold value ϕ_f, sediment transport is in the stage of enduring contact, kinetic theory is no longer valid, and a frictional stress model needs to be incorporated. Following Johnson & Jackson (1987), the enduring contact component of particle pressure is calculated as,

$$p^{sf} = \begin{cases} 0, \phi^s < \phi_f \\ F\frac{(\phi^s - \phi_f)^m}{(\phi_{max} - \phi^s)^n}, \phi^s \geq \phi_f, \end{cases} \tag{4.40}$$

where ϕ_f is the random loose packing limit, ϕ_{max} is the close packing limit, which depends on the particle properties such as particle shape, size distribution. For uniform and spherical particles, $\phi_f = 0.57$ and $\phi_{max} = 0.635$ is used. F, m and n are empirical coefficients calibrated to ensure a stable sediment bed can be established. The particle stress due to frictional contact is calculated by,

$$\tau_{ij}^{sf} = -2\mu^{sf} S_{ij}^s, \tag{4.41}$$

where μ^{sf} is the frictional viscosity and S_{ij}^s is the deviatoric part of strain rate tensor of sediment phase,

$$S_{ij}^s = \frac{1}{2}\left(\frac{\partial u_i^s}{\partial x_j} + \frac{\partial u_j^s}{\partial x_i}\right) - \frac{1}{3}\frac{\partial u_k^s}{\partial x_k}\delta_{ij}. \tag{4.42}$$

Srivastava & Sundaresan (2003) combine the frictional normal stress model of Johnson & Jackson (1987) and the frictional viscosity from Schaeffer (1987) model, and suggest the friction viscosity to be calculated by,

$$\mu^{sf} = \frac{\sqrt{2}p^{sf}\sin(\theta_f)}{2\sqrt{S_{ij}^s \cdot S_{ij}^s}}, \tag{4.43}$$

where θ_f is the angle of repose and is taken to be $\theta_f = 28^\circ \sim 40^\circ$ for sand.

In sediment transport, the frictional components of particle pressure and particle stress play a definite role to ensure the existence of an immobile sediment bed and above which, a low mobility layer of enduring contact can be modeled (Hsu et al. 2004). This

frictional shear viscosity model has the capability to capture the transition between solid-like feature and fluid-like feature of the sediment bed. In the original model of Srivastava & Sundaresan (2003), a correction of Θ/d_p^2 is added to the denominator of Eq. (4.43) for numerical stability. However, we found that in the present sediment transport application, the shear rate in the concentrated region of transport was rather small. Therefore, the correction of Θ/d_p^2 can introduce large error. In this study, this extra term was replaced by a small number of 10^{-20} to ensure numerical stability.

4.2.4 Fluid-sediment momentum transfer

In the two-phase flow formulation, the momentum exchange of the fluid phase and particle phase are coupled through the inter-phase momentum transfer terms (Maxey & Riley 1983). For simplicity, only the dominant terms, namely the drag force and the buoyancy force are included in the present study. Thus the momentum exchange has the following form,

$$M_i^{fs} = -M_i^{sf} = -\phi^s \beta (u_i^f - u_i^s) + p^f \frac{\partial \phi^f}{\partial x_i}. \tag{4.44}$$

The first two terms on the right-hand-side (RHS) are due to drag force with β as the drag parameter. For the closure of the drag parameter β, we follow Ding & Gidaspow (1990), who combined the model of Ergun (1952) for dense sediment concentration ($\phi^s \geq 0.2$) and the model of Wen & Yu (1966) for lower sediment concentration ($\phi^s < 0.2$),

$$\beta = \begin{cases} \frac{150\phi^s \nu^f \rho^f}{(1-\phi^s)d^2} + \frac{1.75\rho^f |u^f - u^s|}{d}, \phi^s \geq 0.2 \\ \frac{0.75 C_d \rho^f |u^f - u^s| (1-\phi^s)^{-1.65}}{d}, \phi^s < 0.2 \end{cases}, \tag{4.45}$$

where d is the sediment diameter, and the drag coefficient C_d is calculated as:

$$C_d = \begin{cases} \frac{24(1+0.15 Re_p^{0.687})}{Re_p}, Re_p \leq 1000 \\ 0.44, Re_p > 1000 \end{cases}, \tag{4.46}$$

in which, $Re_p = (1-\phi^s)\left|u^f - u^s\right| d/\nu^f$ is the particle Reynolds number, and ν^f is the fluid molecular viscosity.

4.3 Summary

In this chapter, we derived the macroscopic Eulerian two-phase governing equations from the Boltzmann equations. The macroscopic continuum description of sediment transport can be obtained by considering a statistical descriptions of the discrete sediment particles and fluid parcels at the mesoscale. In the process of derivation, no turbulence-averaging or scale separation was assumed. Therefore, these Eulerian two-phase governing equations are the bases for the turbulence-averaging model and turbulence-resolving model to be discussed in chapter 5 and 6, respectively.

It should be pointed out here that several assumptions were adopted in the derivation, which may limit the applications of the current Eulerian two-phase flow models. For example, the kinetic theory for the sediment phase is based on the assumption of binary collisions, which may be problematic when the sediment concentration becomes high. In the present model, the kinetic theory is stretched to the random loose packing limit, where particles are constantly in contact with each other. Above the loose packing limit, a phenomenological friction stress model is used to model the immobile/solid-fluid like bed. This frictional stress model simplifies the Coulomb failure criteria, and assumes a constant angle of repose inside the bed. However, due to consolidation and different properties in the bed, the frictional stress model may be too simple to model the bed features. In addition, the inelasticity of particle collision assumes a constant restitution coefficient, this assumption may become inaccurate due to strong inter-particle fluid effect (low Bagnold number), in which the restitution coefficient may depend on the particle Stokes number. The Eulerian two-phase flow formulation and the kinetic theory of granular flow assume that the particles are spherical particles of uniform size. However, in natural environments, the particles are often heterogeneous, and this may also limit the application for the present Eulerian two-phase model. More discussions can also be found in chapter 7.

Chapter 5

SEDFOAM: A MULTI-DIMENSIONAL EULERIAN TWO-PHASE MODEL FOR SEDIMENT TRANSPORT AND ITS APPLICATION TO MOMENTARY BED FAILURE

A multi-dimensional Eulerian two-phase model for sediment transport, called SedFoam, is presented. The model was developed under the open-source framework via the CFD toolbox OpenFOAM. With closures of particle stresses and fluid-particle interactions, the model is able to resolve processes in the concentrated region of sediment transport and hence does not require conventional bedload/suspended load assumptions. A modified $k-\epsilon$ closure was adopted for the carrier flow turbulence. The model was validated for Reynolds-averaged steady and oscillatory sheet flows and verified with empirical formulae for scour downstream of an apron. The model was used to study momentary bed failure (or plug flow) under sheet flow conditions. Model results revealed the existence of instabilities of the near-bed transport layer when momentary bed failure criteria was exceeded. These instabilities evolved into $5-10$ cm billows and were responsible for the large transport rate. The instabilities were associated with a large erosion depth, which was triggered by the combination of large bed shear stresses and large horizontal pressure gradients. Further numerical experiments confirmed the conjecture by previous studies that a criterion for onset of momentary bed failure in oscillatory sheet flow was a function of both the Shields parameter and Sleath parameter. This chapter is adapted from a manuscript submitted to Coastal Engineering (Cheng et al. 2016).

5.1 Introduction

The coastal zone is one of the most economically vibrant and culturally diverse human habitats. However, it is vulnerable to sea-level rise and intense storm events.

Coastal morphological evolution is caused by a wide range of coupled cross-shore and alongshore sediment transport processes driven by waves, wave-induced currents and wave-breaking turbulence (e.g., Roelvink et al. 2009). At operational forecasting scales, parameterizations of sediment transport rate associated with these hydrodynamic forcing mechanisms are needed. Typically, sediment transport rate is parameterized by the bottom shear stress (e.g., Ribberink 1998, van Rijn 1984*a*), which works reasonably well for moderate wave conditions. However, during large wave events associated with intense storms, the predicted morphological evolution is less satisfactory (Ruessink & Kuriyama 2008) and other mechanisms that are not parameterized by bottom shear stress may become dominant.

For example, laboratory experiments (Madsen 1974, Sleath 1999, Liu & Sato 2005, Holway et al. 2012) and field observations (Conley & Inman 1992, Foster et al. 2006) demonstrate that significant bed mobilization, called momentary bed failure or plug flow, may occur during the passage of steep waves. Although transport often occurs as sheet flow under steep waves, the timing of such large bed mobilization coincides with large horizontal pressure gradients. Moreover, momentary bed failure/plug flow can cause much larger transport than is predicted by typical sheet flow formula, and hence it is an essential process that should be included for the prediction of beach evolution during large wave events.

Our capability to resolve key mechanisms in the concentrated region of transport remains limited. Numerical models for coastal morphological evolution (Jacobsen et al. 2012, Warner et al. 2008, Lesser et al. 2004), local scour around structures (Hoffmans & Pilarczyk 1995, Liu & Garcia 2008) and bedform dynamics (Marieu et al. 2008, Chou & Fringer 2010) typically separate the total sediment transport into bedload and suspended load components. Partitioning is necessary in order to efficiently model morphological evolution or to better resolve turbulence. However, bedload transport and erosion flux (pick up flux) are then parameterized semi-empirically (Ribberink 1998, van Rijn 1984*b*). Presently, these parameterizations do not explicitly include the effect of momentary bed failure.

On the other hand, the two-phase flow approach can resolve concentrated region of sediment transport by including closures of particle stresses and fluid-particle interactions in the governing equations. In the past decades, several two-phase numerical models have been developed, where the sediment phase is modeled either with an Eulerian scheme (e.g., Dong & Zhang 1999, 2002, Hsu et al. 2004, Li et al. 2008, Amoudry & Liu 2009, Bakhtyar et al. 2010) or a Lagrangian scheme (e.g., Drake & Calantoni 2001, Calantoni & Puleo 2006, Calantoni & Thaxton 2008, Heald et al. 2004). These two-phase models can resolve the full profiles of sediment transport without the need to divide the transport into bedload and suspended load components. For instance, one-dimensional-vertical (1DV) two-phase models are used to improve the parameterization of pickup flux in suspended load module under waves in sheet flow condition (Amoudry & Liu 2010, Yu et al. 2012).

Due to the complexity of the model formulation, most of the existing two-phase models are based on the Reynolds-averaged approach and simplified into 1DV formulation. 1DV models cannot capture the development of inhomogeneous flow features (e.g., bedforms), flow instabilities (Charru & Mouilleron-Arnould 2002) and scour (Amoudry & Liu 2009). Hence, existing two-phase models are mainly restricted to sheet flow applications where the ensemble-averaged flow field is more or less fully developed in the streamwise and spanwise directions. Also, a model developed for 1DV cannot resolve turbulence, which is inherently three-dimensional. Amoudry & Liu (2009) developed a two-dimensional (2D) two-phase model to study scour downstream of an apron, and good agreements are obtained for the development of the 2D scour characteristics. A two-phase model has been developed by Bakhtyar et al. (2010) to study surf and swash zones sediment transport under the influence of wave breaking and wave runup/rundown. The model is shown to be capable of reproducing the observed beach profile evolution in the surf and swash zones qualitatively.

Motivated by this need, we have recently developed a multi-dimensional model for sediment transport that solves the complete Eulerian two-phase equations following the mathematical formulation similar to that of Hsu et al. (2004) and Yu et al.

(2012). The mathematical formulation is solved numerically using the open-source CFD toolbox, OpenFOAM. OpenFOAM includes several multiphase flow modeling capabilities, such as bubbly flow (Rusche 2002). Specifically, a two-phase flow solver in OpenFOAM called, twoPhaseEulerFoam (Rusche 2002, Weller 2002, Passalacqua & Fox 2011) was adopted as the baseline. The numerical stability of the solver was improved and additional capabilities needed for coastal sediment transport applications were implemented. This new sediment transport model is called SedFoam. Although the numerical model was written in three spatial dimensions, the current version of the model has only been validated/verified for 2DV Reynolds-averaged condition.

The purpose of this study is to describe this new multi-dimensional model, SedFoam, its validation and its application to investigate momentary bed failure. The mathematical formulation of the model is discussed in Section 5.2. The numerical methodology is discussed in Section 5.2.1 and 5.2.2 . Model validation for the present 2DV Reynolds-averaged formulation is presented in Section 5.3. The numerical investigation of momentary bed failures/plug flows is presented in Section 5.4, and concluding remarks are given in Sections 5.5, respectively.

5.2 Model Formulation

In this study, we utilize the complete set of Eulerian two-phase flow governing equations as derived in chapter 4. In order to efficiently apply these equations to turbulent flow, in which turbulent motions are generated by flow shear much larger than the grain scale, additional turbulence averaging or filtering is necessary. Through Reynolds-averaging, Hsu et al. (2004) developed the turbulence-averaged Eulerian two-phase model and simplified the model to 1DV to study sheet flow sediment transport. In this study, we adopted similar turbulence-averaged governing equations and closures to develop the numerical model in 3D. All the quantities in this chapter are turbulence-averaged, and the averaging operator are omitted for simplicity.

5.2.1 Governing equations

Assuming that there is no mass transfer between the two phases, the mass conservation equations for fluid phase and sediment phase can be written as,

$$\frac{\partial(1-\phi)}{\partial t}+\frac{\partial(1-\phi)u_i^f}{\partial x_i}=0, \tag{5.1}$$

$$\frac{\partial\phi}{\partial t}+\frac{\partial\phi u_i^s}{\partial x_i}=0 \tag{5.2}$$

where ϕ is the sediment volumetric concentration, u_i^f is the fluid velocity, and u_i^s is the sediment velocity. In this study, $i=1,2,3$ represents streamwise, spanwise and vertical components, respectively. The momentum equations for fluid and particle phases are expressed as,

$$\begin{aligned}\frac{\partial\rho^f(1-\phi)u_i^f}{\partial t}+\frac{\partial\rho^f(1-\phi)u_i^fu_j^f}{\partial x_j}= & -\frac{\partial(1-\phi)p^f}{\partial x_i}+(1-\phi)f_i+\frac{\partial\tau_{ij}^f}{\partial x_j}\\ & +\rho^f(1-\phi)g\delta_{i3}+M_i^{fs},\end{aligned} \tag{5.3}$$

and

$$\frac{\partial\rho^s\phi u_i^s}{\partial t}+\frac{\partial\rho^s\phi u_i^su_j^s}{\partial x_j}=-\frac{\partial\phi p^f}{\partial x_i}+\phi f_i-\frac{\partial p^s}{\partial x_i}+\frac{\partial\tau_{ij}^s}{\partial x_j}+\rho^s\phi g\delta_{i3}+M_i^{sf}, \tag{5.4}$$

where ρ^f and ρ^s are fluid and sediment density, respectively, g_i is the gravitational acceleration and p^f is the fluid pressure. The external pressure gradient that drives the flow is written as f_i. The fluid stress τ_{ij}^f includes the grain-scale (viscous) stress and the turbulent Reynolds stress, which are calculated with a two-equation turbulence model. The particle normal stress p^s and shear stress τ_{ij}^s are modeled with the kinetic theory of granular flow and a phenomenological closure of frictional contact stresses. Finally, M_i^{fs} and M_i^{sf} represent the inter-phase momentum transfer between fluid and particle phase, and $M_i^{fs}=-M_i^{sf}$ follows the Newton's 3rd law.

5.2.2 Closure models

5.2.2.1 Inter-phase momentum transfer

In the two-phase flow formulation, the momentum exchange of the fluid phase and particle phase are coupled through the inter-phase momentum transfer terms (Maxey & Riley 1983). For simplicity, only the dominant terms, namely the drag force and the buoyancy force are included in the present study. Thus the momentum exchange has the following form,

$$M_i^{fs} = -\phi\beta(u_i^f - u_i^s) + \beta\frac{\nu^{ft}}{\sigma_c}\frac{\partial\phi}{\partial x_i} + p^f\frac{\partial(1-\phi)}{\partial x_i}. \tag{5.5}$$

The first two terms on the right-hand-side (RHS) are due to drag force with β as the drag parameter, the closure of β is kept the same as described in chapter 4. The first term represents averaged drag force due to mean velocity difference between fluid and particle phases. The second term is the fluid turbulent suspension term, which results from the correlation of sediment concentration and fluid velocity fluctuations. The gradient transport assumption was adopted here with a closure for ν^{ft} representing the turbulent viscosity, which was calculated with a turbulence closure (see Section 5.2.2.2), and σ_c is the Schmidt number (see Table 5.1). The last term on the RHS of Eq. (5.5) represents the averaged buoyancy force. The correlation term between sediment concentration and fluid pressure is ignored in the turbulence averaged momentum equations. However, in the closure of eddy viscosity, the effect is included via buoyancy terms in the $k-\epsilon$ equations.

5.2.2.2 Fluid turbulence model

Because the present model equations were obtained by averaging over turbulence, the fluid stresses consist of a large-scale component R_{ij}^{ft} (i.e., Reynolds stress) and a grain-scale component r_{ij}^f, which includes the viscous stress and an additional effect due to fluid-particle interaction at grain scale. In the present study, this later

effect is ignored and only viscous stress is considered. Thus, the total fluid stress is written as,

$$\tau_{ij}^f = R_{ij}^{ft} + r_{ij}^f = \rho^f(1-\phi)\Big[(\nu^{ft}+\nu^f)\Big(\frac{\partial u_i^f}{\partial x_j} + \frac{\partial u_j^f}{\partial x_i} - \frac{2}{3}\frac{\partial u_k^f}{\partial x_k}\delta_{ij}\Big) - \frac{2}{3}k^f\delta_{ij}\Big]. \tag{5.6}$$

The turbulent eddy viscosity ν^{ft} is calculated by the fluid turbulence kinetic energy k^f and turbulent dissipation rate ϵ^f,

$$\nu^{ft} = C_\mu \frac{(k^f)^2}{\epsilon^f}, \tag{5.7}$$

where C_μ is an empirical coefficient (see Table 5.1). The turbulent kinetic energy k^f (TKE) is calculated by its balance equation appropriate for sand particles in water (Yu et al. 2010),

$$\begin{aligned}\frac{\partial k^f}{\partial t} + u_j^f\frac{\partial k^f}{\partial x_j} = {} & \frac{R_{ij}^{ft}}{\rho^f}\frac{\partial u_i^f}{\partial x_j} + \frac{\partial}{\partial x_j}\Big[\Big(\nu^f + \frac{\nu^{ft}}{\sigma_k}\Big)\frac{\partial k^f}{\partial x_j}\Big] - \epsilon^f - \frac{2\beta(1-\alpha)\phi k^f}{\rho^f(1-\phi)} \\ & - \frac{1}{(1-\phi)}\frac{\nu^{ft}}{\sigma_c}\frac{\partial \phi}{\partial x_j}(s-1)g_j.\end{aligned} \tag{5.8}$$

Except for the last two terms on the RHS, the rest of terms in the present k^f equation are similar to those in the clear fluid TKE equation. The last term in Eq. (5.8) represents the buoyancy effect. For typical sediment concentration with an upward decaying profile, the buoyancy term represents the well-known sediment-induced density stratification that can attenuate turbulence. The fourth term on the RHS represents attenuation of TKE due to drag. The parameter α is proposed to characterize the degree that particles follow the fluid velocity fluctuations and it can be quantified by the Stokes number $St = t_p/t_l$ (Balachandar & Eaton 2010), where $t_p = \rho^s/\beta$ is the particle response time, and $t_l = k^f/(6\epsilon^f)$ is the characteristic time scale of energetic eddies. Considering a given particle encounters a turbulent eddy on its path, if the particle has very small inertia ($St \ll 1$), it can closely follow the eddy motion. However, if $St{\sim}O(1)$, the particle cannot completely follow the eddy motion and may cause

disturbance to the eddy. Finally, if $St \gg 1$, the particle trajectory is hardly affected by the eddy motion. With these observations, Danon et al. (1977) and Chen & Wood (1985) proposed an exponential function for α,

$$\alpha = e^{-B \cdot St}, \tag{5.9}$$

where B is an empirical coefficient. It is evident from the model that the fourth term in Eq. (5.8) represents a dissipation mechanism for the turbulent kinetic energy. It is also possible that the presence of particle provides a generation mechanism of flow turbulence. However, this is observed for particles with very large Stokes number. For sand transport in water considered in this study, this turbulence generation mechanism is unlikely and it is neglected.

Finally, the balance equation for the rate of turbulent kinetic energy dissipation ϵ^f is written as,

$$\begin{aligned} \frac{\partial \epsilon^f}{\partial t} + \quad u_j^f \frac{\partial \epsilon^f}{\partial x_j} &= C_{1\epsilon} \frac{\epsilon^f}{k^f} \frac{R_{ij}^{ft}}{\rho^f} \frac{\partial u_i^f}{\partial x_j} + \frac{\partial}{\partial x_j} \left[\left(\nu^f + \frac{\nu^{ft}}{\sigma_\epsilon} \right) \frac{\partial \epsilon^f}{\partial x_j} \right] - C_{2\epsilon} \frac{\epsilon^f}{k^f} \epsilon^f \\ &- C_{3\epsilon} \frac{\epsilon^f}{k^f} \frac{2\beta(1-\alpha)\phi k^f}{\rho^f (1-\phi)} - C_{4\epsilon} \frac{\epsilon^f}{k^f} \frac{1}{(1-\phi)} \frac{\nu^{ft}}{\sigma_c} \frac{\partial \phi}{\partial x_j} (s-1) g_j. \end{aligned} \tag{5.10}$$

As discussed in Hsu et al. (2004), due to lack of comprehensive experimental data, the coefficients associated with the present two-equation closure are adopted from their clear fluid counterpart. The coefficient $C_{3\epsilon}$ in Eq. (5.10) is chosen to be 1.2. For the coefficient associated with the buoyancy term, $C_{4\epsilon} = 0$ is used in stably stratified condition, while it is set to 1 for unstably stratified condition. Table 5.1 summarizes the coefficients used for the present turbulence closure. The coefficient B in Eq. (5.9) is left as the only free model parameter to be calibrated with measured data.

Table 5.1: List of coefficients in fluid turbulence closure (k-ϵ).

C_μ	$C_{1\epsilon}$	$C_{2\epsilon}$	$C_{3\epsilon}$	$C_{4\epsilon}$	σ_k	σ_ϵ	σ_c
0.09	1.44	1.92	1.2	0 or 1.0	1.0	1.3	1.0

5.2.2.3 Particle stress closure

Following the derivation in chapter 4, the closure of particle stresses includes collisional-kinetic component and frictional component:

$$p^s = p^{skc} + p^{sf}, \tag{5.11}$$

$$\tau_{ij}^s = \tau_{ij}^{skc} + \tau_{ij}^{sf}. \tag{5.12}$$

The closure of the collisional-kinetic component is based on the kinetic theory of granular flow where particle stress and particle pressure are quantified by the granular temperature, Θ. The turbulence-averaged transport equation for the granular temperature is similar to equation **??** in chapter 4, except that the interaction term J_{int} needs further closure. Following Hsu et al. (2004), the fluid-particle interaction term is given as,

$$J_{int} = \phi\beta(2\alpha k^f - 3\Theta). \tag{5.13}$$

When the sediment concentration exceeds random loose packing ($\phi \approx 0.57$), sediment transport is in the stage of enduring contact, kinetic theory is no longer valid, and a frictional stress model needs to be incorporated. Following the discussion in chapter 4, the frictional component of particle pressure is calculated by equation 6.34 in chapter 4. In sediment transport, the frictional components of particle pressure and particle stress play a definite role to ensure the existence of an immobile sediment bed and above which, a low mobility layer of enduring contact can be modeled (Hsu et al. 2004). Hence, the empirical coefficients in Eq. (6.34) were calibrated to ensure a

stable sediment bed can be established. The following values are adopted,

$$F = 0.05, m = 3, n = 5. \tag{5.14}$$

With this new frictional stress model and choice of empirical coefficients, the sediment concentration becomes close but rarely exceeds the maximum packing limit of 0.635. Notice that in the original model of Johnson & Jackson (1987) applied to debris flow, these coefficients are suggested to be $F = 0.05$, $m = 2$ and $n = 5$. Hence, the present model applied to sediment transport in a bottom boundary layer also gives similar values.

5.2.3 Numerical implementation

The numerical implementation of the present model utilizes the open-source CFD toolbox OpenFOAM, which provides a variety of finite volume method libraries and solvers. OpenFOAM includes several single phase and multiphase flow solvers. Specifically, the mathematical formulations presented above were implemented by modifying a two-phase flow solver, twoPhaseEulerFoam (Rusche 2002, Weller 2002, Passalacqua & Fox 2011).

The standard PIMPLE procedure, which is a merged PISO-SIMPLE algorithm, is used after the version 2.1.0 of OpenFOAM. The intermediate velocities are first solved using the momentum equation without the pressure gradient term. To ensure the Newton's third law in the momentum equations of the fluid phase and sediment phase, the drag force is calculated explicitly using the velocities at the previous time step. The pressure equation is constructed and solved by considering the continuity equations for both phases. In the present model, collocated variables are solved at cell centers, and the method of Rhie & Chow (1983) is adopted for solving the pressure equations to prevent velocity-pressure decoupling and oscillation in the pressure field. After solving the pressure, the fluid and sediment velocities are updated, and the resulting fluid phase and particle phase velocities both satisfy their mass conservation. The

velocities are then used to update the volumetric sediment concentrations, turbulence quantities, fluid stresses, granular temperature and particle stresses. The advection terms in the governing equations are solved using a second-order TVD scheme, based on the Sweby limiter (Sweby 1984). Two special versions of this scheme are available in OpenFOAM: (1) limitedLinearV, which is specifically for vectors, and the limiter is applied independently in each direction; (2) limitedLinear01, which ensures the scalar variable is bounded between 0 and 1, is adopted to solve the volumetric concentration ϕ. In this manner, the convective terms are treated implicitly after being linearised using the value of the velocity flux at the previous iteration. The central difference schemes are used for diffusion terms, and the standard Crank-Nicolson scheme is used for time integration. The time step is updated every cycle to satisfy the Courant–Friedrichs–Lewy (CFL) condition and it is adjusted in a smooth fashion to ensure numerical stability. More details about the numerical implementations can be found in Cheng & Hsu (2014*a*).

5.3 Model Validation

The model was first calibrated/validated with laboratory flume data of Sumer et al. (1996) for sand transport in steady channel flow under the sheet flow condition. Then, the calibrated model was further validated with measured sheet flow sediment concentration and flow velocity for 1DV/2DV oscillatory flow (O'Donoghue & Wright 2004) and 2DV scour development downstream of an apron (Amoudry & Liu 2009).

5.3.1 Steady sheet flow

The intensity of sediment transport is often quantified by the bed shear stress τ_b. The non-dimensional bed shear stress, called the Shields parameter, is defined as, $\theta = \tau_b/(\rho^s - \rho^f)gd$. Compared with Hsu et al. (2004), the present model adopts a new turbulence modulation parameterization for α in the $k-\epsilon$ equations as well as in the granular temperature equation. The improved α parameterization model is expected to be more robust in predicting sediment suspension over a wider range of sediment

Table 5.2: A summary of the fine sand (grain diameter $d = 0.13$ mm, specific gravity $s = 2.65$) experiments reported in Sumer et al. (1996) used here for model calibration.

Shields parameter θ	τ_b (Pa)	h (cm)	f_x (Pa/m)
1.10	2.31	10.5	52
1.68	3.54	10.8	82
2.20	4.63	11.2	110

size and density (Kranenburg et al. 2014). We first calibrate the model with fine sand (d=0.13 mm; $\rho^s = 2650$ kg/m^3) in the sheet flow condition driven by steady flows in a channel (Sumer et al. 1996). Specifically, the model coefficient B in Eq. (5.9) associated with turbulence modulation due to sediment is calibrated and demonstrated to work well for Shields parameter ranging from 1.0 to 2.2.

As shown in Table 5.2, the three different Shields parameters modeled here cover a range from θ =1.1 to 2.2. In the numerical simulation, both the flow depth and bottom shear stress were kept the same as Sumer et al. (1996). The flow was driven by a prescribed constant streamwise pressure gradient, which was determined by matching the targeted bottom shear stress at the bed. Since sheet flow is typically assumed to be statistically homogeneous in the streamwise and spanwise directions, 1DV simulations were carried out, i.e., L_x and L_y in the streamwise and spanwise directions are reduced to one grid cell (see Fig. 5.1). Periodic boundary conditions were used in the streamwise direction. For 2D simulation in the OpenFOAM framework, a dummy boundary condition called 'empty' can be used in the spanwise direction. Wall boundaries were imposed on both the top and bottom boundary of the computational domain. The total domain height is set to be $L_z = 0.15$ m with an initial sediment bed depth of $h_b = 0.05$ m. We use 600 uniformly spaced grid points in the vertical direction, and the grid resolution is $\Delta_z = 0.25$ mm.

When using $B = 0.22$, we obtained good agreement with measured sediment concentration profiles for Shields parameter in the range of $\theta = 1.1$ to 2.2 for fine sand (Fig. 5.2(a),(e),(i)). Although the fluid and sediment velocities were not measured, the

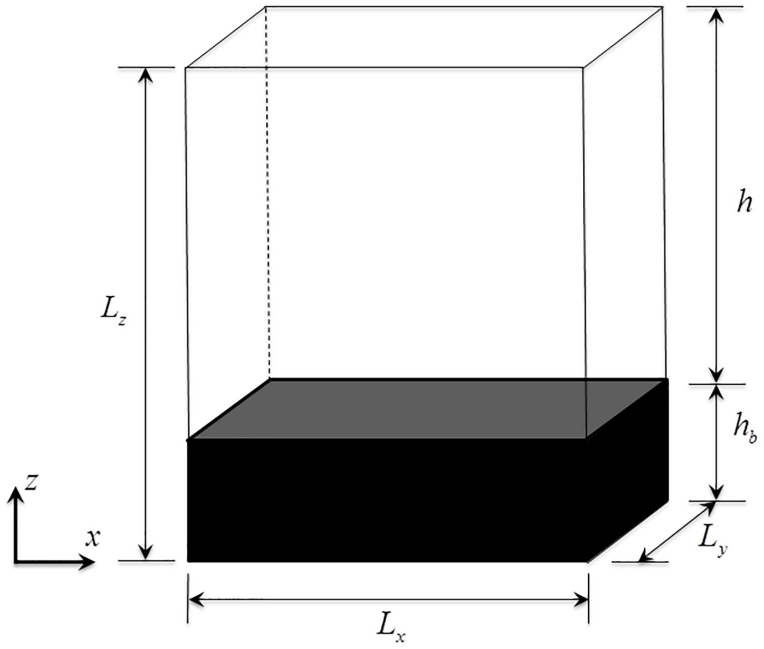

Figure 5.1: Sketch of the domain setup for the present Eulerian two-phase flow model.

model results for the streamwise fluid velocity were shown in Fig. 5.2 (b),(f),(j). Due to the small particle size considered here, the difference between the fluid phase and sediment phase velocity was within 0.01 m/s and hence the sediment phase velocities are not shown here for brevity. The model also provided profiles of fluid turbulent kinetic energy and granular temperature (see Fig. 5.2 (c),(g),(k)). The velocity fluctuation energies were both zero in the bed, while the fluid turbulent kinetic energy increased rapidly to its peak value several millimeters above the bed due to large flow shear. Similar behavior can be observed for granular temperature. The fluid shear stress and particle shear stress are shown in Fig. 5.2 (d),(h),(l). It can be observed that the particle shear stress increased rapidly in the sheet layer and peaked at the immobile bed. On the other hand, the fluid shear stress dropped sharply in the sheet flow layer, and became close to zero at the immobile bed. The summation of particle shear stress and fluid (mostly turbulent) shear stress gave the expected linear profile of total shear stress in a steady channel flow. The calibrated value of $B = 0.22$ will be used for the

remainder of this paper.

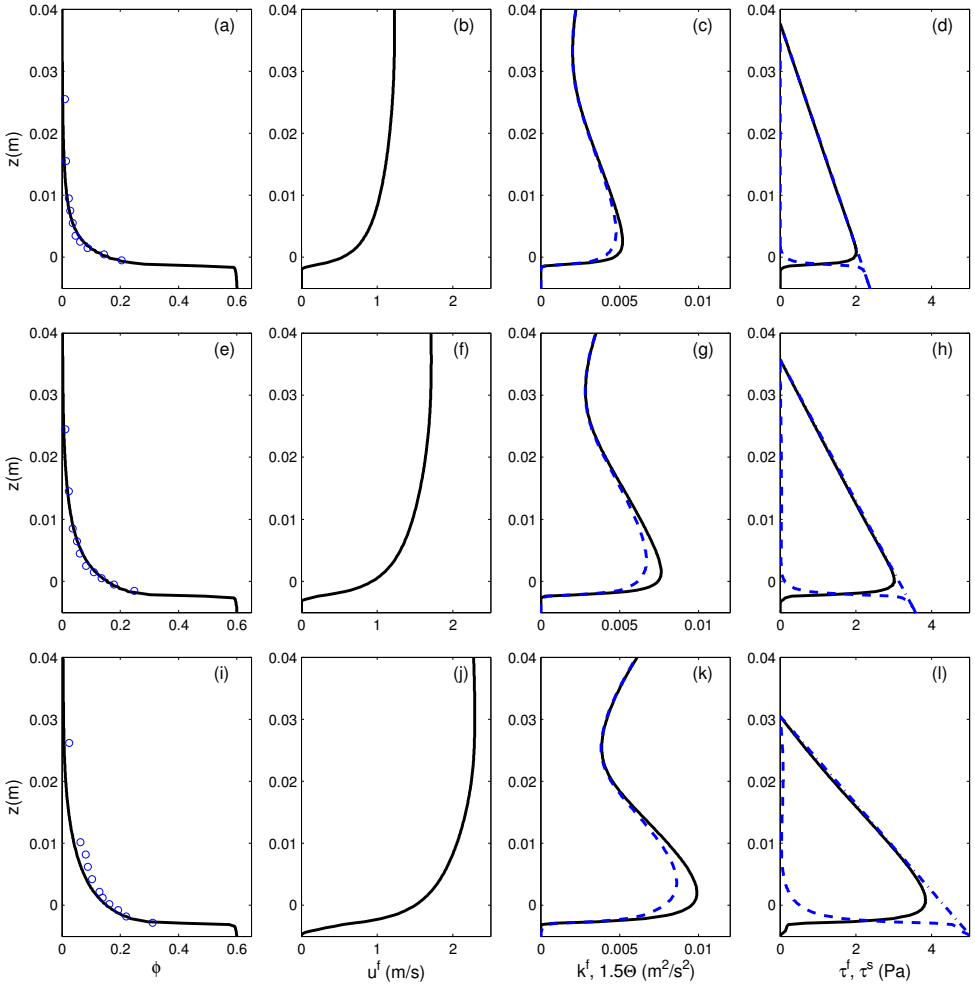

Figure 5.2: (a) Comparison of concentration profiles between numerical results (solid curve) and experiment data (circle symbols); (b) fluid velocity profile; (c) fluid turbulent kinetic energy (solid curve) and granular temperature(dashed curve) and (d) fluid shear stress (solid curve), sediment shear stress (dashed curve) and total shear stress (dash-dot curve) for steady sheet flow of at $\theta = 1.10$ (Sumer et al. 1996). The corresponding results for $\theta = 1.68$ ($\theta = 2.2$) are shown in (e), (f), (g) and (h) ((i), (j), (k) and (l)), respectively. The bed location $z = 0$ is defined as initial bed level.

5.3.2 Oscillatory sheet flow

O'Donoghue & Wright (2004) measured sediment concentration and flow velocity in the concentrated region of transport under a range of oscillatory sheet flow conditions. The experimental results have been used by many researchers to validate their models (e.g., Li et al. 2008, Chen et al. 2011, Yu et al. 2012). The calibrated model coefficient $B = 0.22$ was used here to validate sheet flow of medium sand ($d = 0.28$ mm) under oscillatory flow condition.

In the numerical model, the oscillatory flow is driven by a mean streamwise pressure gradient. Outside the wave boundary layer, the shear stress vanishes, and the momentum equation reduces to,

$$f_x = \rho^f \frac{\partial U_0}{\partial t}, \tag{5.15}$$

where U_0 is the free stream velocity. Following O'Donoghue & Wright (2004), the asymmetric flow was forced by the second-order Stokes wave motion,

$$U_0(t) = U_1 \sin(\omega t + \sigma_0) - U_2 \cos(2\omega t + 2\sigma_0), \tag{5.16}$$

where U_1 and U_2 are velocity amplitudes for each harmonic, $\omega = 2\pi/T$ is the oscillatory frequency, T is the oscillatory period and σ_0 is the a phase lag, which is chosen such that the free-stream velocity is zero at $t = 0$. The flow asymmetry is defined as, $a = U_{max}/(U_{max} - U_{min})$, in which U_{max} and U_{min} are maximum and minimum free-stream velocities, respectively. Here, we consider the asymmetric flow case with wave period $T = 7.5$ s and maximum velocity $U_{max} = 1.5$ m/s with $a = 0.63$ (MA7515 in O'Donoghue & Wright 2004). A 1DV simulation was first carried out, and the domain height is $L_z = 0.3$ m, with an initial sediment bed depth $h_b = 0.05$ m. A total of 240 grid points are used in the vertical direction with finer grid resolutions of $\Delta_z = 0.5$ mm around the initial bed level and the grid resolution increases gradually away from the initial bed level to a maximum grid size of $\Delta_z = 2$ mm near the top boundary.

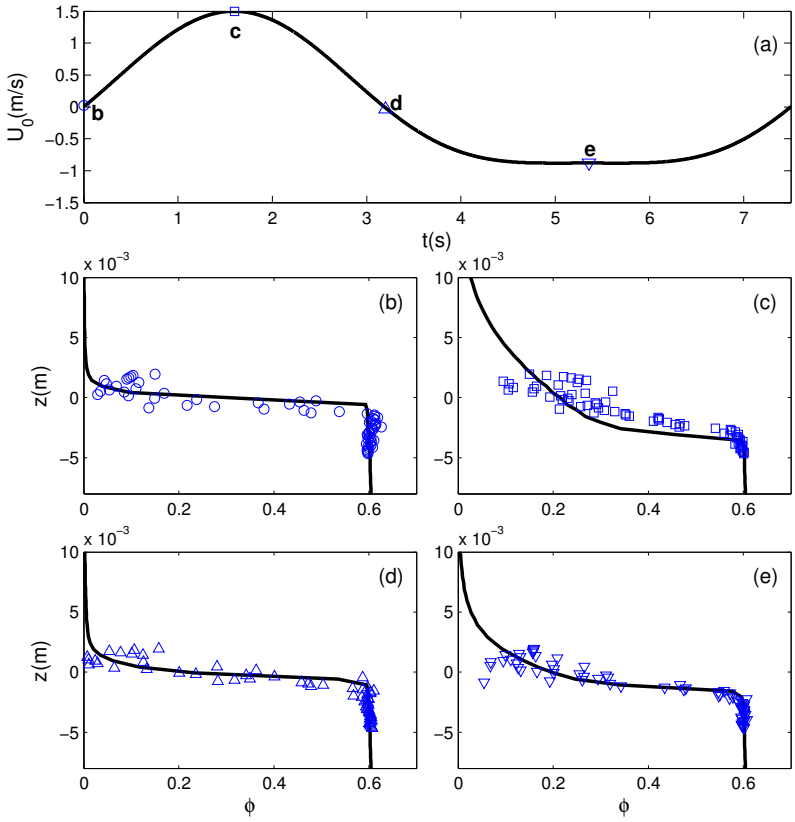

Figure 5.3: (a) Time series of free-stream velocity, in which four representative instants are indicated: (b) $t = 0$; (c) $t = 1.6$ s; (d) $t = 3.2$ s and (e) $t = 5.36$ s; The corresponding comparison of sediment concentration profiles between the numerical results (solid curve) and measured data (symbols) from O'Donoghue & Wright (2004) are presented in panel (b), (c), (d) and (e), respectively.

The concentration profiles at the four representative instants are shown in Fig. 5.3(b-d) and the corresponding phase of each panel is indicated in Fig. 5.3(a). Using the calibrated value of $B = 0.22$ without further tuning, the agreements between the model results and measured data were generally good. During the flow reversal (see Fig. 5.3 (b) and (d)), only a small amount of sediment was suspended and a sharp concentration gradient near the bed was observed. On the contrary, during the positive flow peak (see Fig. 5.3 (c)), significantly more sediment was suspended with a notably thicker suspension layer. Suspended sediment during the negative flow peak (see Fig.

5.3 (d)) was less than those during the positive flow peak and the model results also matched well with the measured data.

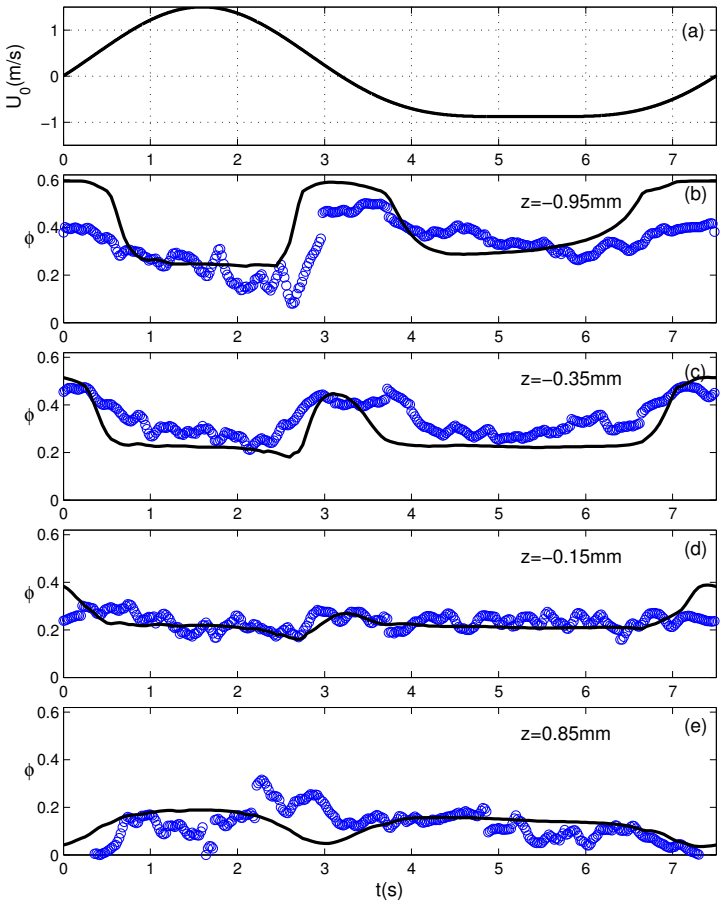

Figure 5.4: (a) Time series of free stream velocity driven by Stokes second-order wave motion (MA7515, O'Donoghue & Wright (2004)); The comparisons of concentration time series for sheet flow of medium sand at four different vertical locations are shown in (b) $z = -0.95$ mm; (c) $z = -0.35$ mm; (d) $z = -0.15$ mm and (e) $z = 0.85$ mm.

The agreement between the measured sediment concentration and model results can also be examined via the time series of sediment concentration at four representative locations near the bed (Fig. 5.4). In the pick up layer (e.g., $z = -0.95$ mm, see Fig. 5.4(b)), namely the region below the initially undisturbed bed (z <0), sediment concentration decreased from about 0.6 (concentration of immobile bed) to about 0.25 as

free-stream approaches flow peak. Sediment concentration then increased to about 0.6 as flow became weaker and approaches flow reversal. A similar feature repeated again during the wave trough although the sediment concentration only decreased to about 0.33 due to less energetic flow. Similar agreements were observed at $z = -0.35$ mm (see 5.4(c)). The model was clearly able to capture the main characteristic in the pick up layer. In the suspension layer, namely the region above the initially undisturbed bed ($z > 0$), the temporal evolution with respect to the pick-up layer reverses. The behavior was qualitatively captured by the model (see Fig. 5.4(e)). It is noted that the model cannot predict the burst events during the flow reversal (see $t = 2 - 3$ s in Fig. 5.4(e)), and the burst events may be due to the turbulence-sediment interactions, which may require a turbulence-resolving model to resolve this phenomenon. However, the model was able to reproduce the nearly constant sediment concentration occurring around the initially undisturbed bed level ($z \approx 0$, see Fig. 5.4(d)).

The erosion depth is defined as the distance between the initial bed level to the location where the particle velocity is sufficiently small ($u^s < 5$ mm/s). The modeled temporal evolution of erosion depth is similar to the measured data (Fig. 5.5), although it was also observed that the model tends to over-predict the erosion depth during positive or negative flow peak by about 0.5 mm. On the contrary, during flow reversal, the model under-predicted the erosion depth by about 1 mm. We like to also point out that a difference of 0.5 to 1 mm is roughly 2-3 grain diameters, and also it is similar to the measurement error and our numerical grid size.

The model results of velocity profiles at four different instants are shown in Fig. 5.6 (solid curves). During the experiment of O'Donoghue & Wright (2004), concurrent measurement of flow velocity was not performed for medium sand cases. However, velocity profiles of another case under the same wave condition for mixed grain sizes with the same d_{50} (X2A7515) were reported and they were also presented in Fig. 5.6 (symbols). Overall, the model predicted velocity profiles were in good agreement with the measured data. However, the numerical model slightly over-predicted the flow velocity during positive flow peak (see panel (c)). During the negative wave

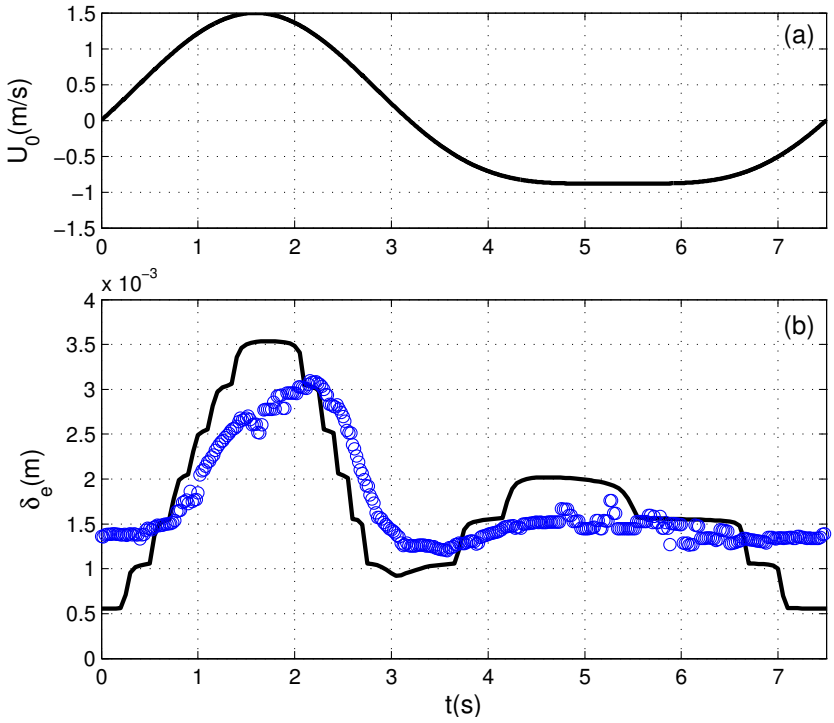

Figure 5.5: (a) Time series of free-stream velocity, and (b) Comparison of erosion depth between numerical results (solid curve) and experiment data (symbols) of MA7515 in O'Donoghue & Wright (2004).

phase, the agreement was very good (see panel (d), (e)). The same simulation for case MA7515 was also carried out for 2DV domain with $L_x = 0.4$ m. The resulting flow field was completely uniform in the streamwise direction and the modeled sediment concentration and flow velocity were almost identical to those obtained from the 1DV simulation (not shown).

5.3.3 Scour downstream of an apron

To further validate the present model for more complicated 2DV flow conditions, we simulated the scour development downstream of an apron. Following the numerical study of Amoudry & Liu (2009), the scour problem was simplified and sketched in Fig. 5.7. The flow depth is chosen to be $h_0 = 0.15$ m, and the initial bed depth is $h_b = 0.05$ m. The length of the domain downstream of the apron is chosen to be

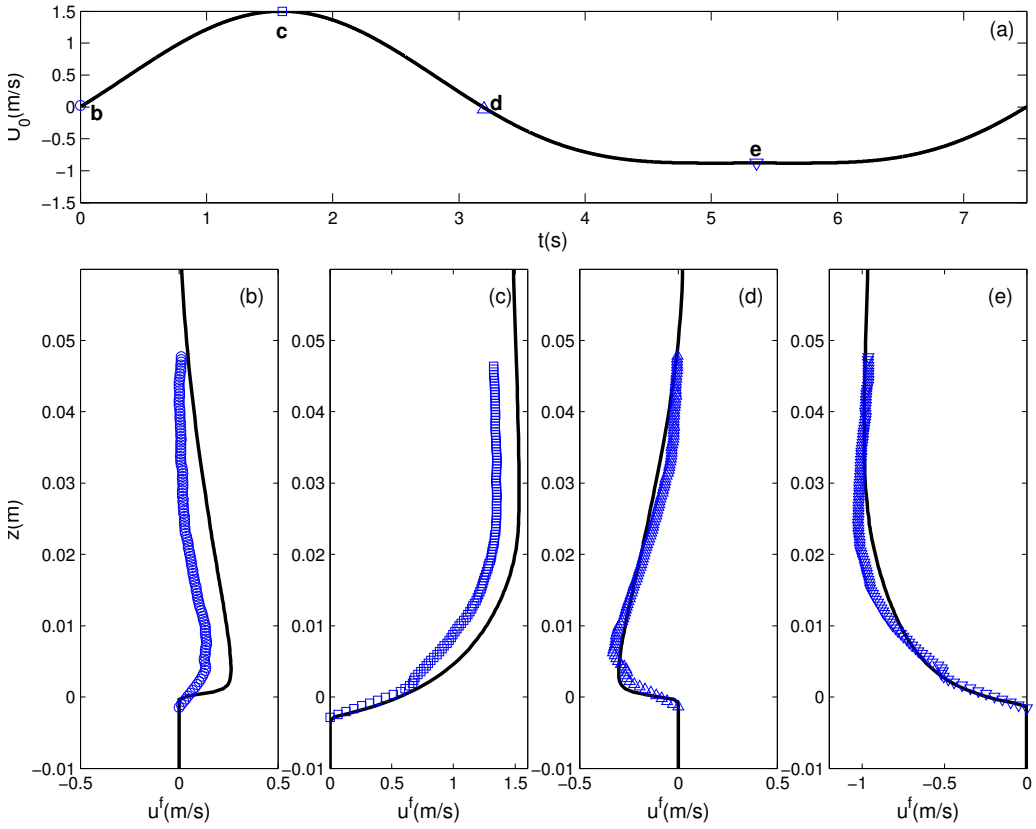

Figure 5.6: (a) Time series of free-stream velocity for MA7515 in O'Donoghue & Wright (2004), in which four representative instants are indicated: (b) $t = 0$; (c) $t = 1.6$ s; (d) $t = 3.2$ s and (e) $t = 5.36$ s; The corresponding comparison of fluid velocity profiles between the numerical results (solid curve) and measured data (symbols) at these four instants are shown in panel (b), (c), (d) and (e).

$L_x = 1$ m. Stretched grid are used in both the streamwise and vertical directions. In the vertical direction, 300 grid points are used with uniform grid size of $\Delta_z = 0.5$ mm near and below the initial bed level. The vertical grid size then increases away from the initial bed with $\Delta_{zmax} \approx 1.1$ mm near the top boundary. In the streamwise direction, finer resolution is used around the apron with $\Delta_{xmin} = 0.5$ mm. The grid size then increases gradually away from the apron with the maximum grid size of $\Delta_{xmax} = 2.5$ mm near the downstream end of the domain. A symmetric boundary condition is imposed on the top boundary, and at the step wall and bottom wall, wall

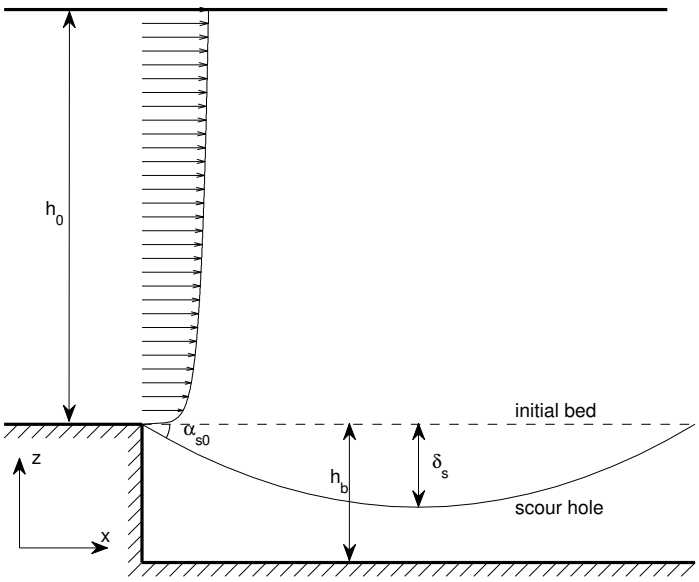

Figure 5.7: Sketch of scour downstream of an apron.

boundaries are applied for both the fluid and the sediment velocities and sediment concentration. At the downstream boundary, an outlet boundary condition is used for the velocities of both phases. When the flow is going outward, a zero gradient is imposed for the velocities. Otherwise, it is set to zero. As for the fluid pressure, when the flow is going outward, a constant pressure value is imposed. Otherwise, a zero gradient boundary condition is used. For the inlet boundary (left boundary of the domain), a zero gradient boundary condition is used for the pressure, and a rough-wall log-law velocity profile is imposed for both phases,

$$\frac{u}{u_*} = \frac{1}{\kappa} ln\Big(\frac{30z}{K_s}\Big), \tag{5.17}$$

where $u_* = 3.69$ cm/s is the frictional velocity, $\kappa = 0.41$ is the von Karman constant, and $K_s = 2.5d$ is the bed roughness with the grain size specified as $d = 0.25$ mm. With sediment specific gravity specified as $s = 2.65$, the Shields parameter was estimated to be $\theta = 0.34$. The domain is initialized with a flat bed having bed concentration of 0.61.

For the initial fluid and sediment velocities above the bed, they are set to be identical to the inlet velocity, and within the bed, both fluid and sediment velocities are set to be zero.

Fig. 5.8 shows three snapshots of sediment concentration contour and velocity profiles at four different locations down stream of the apron. At $t = 5$ s, the development of a scour hole near the inlet can be identified (see Fig. 5.8(a)). The scour angle and scour depth were both small at this instant. Several small bedforms were observed downstream of the scour hole. At $t = 15$ s and $t = 45$ s, the scour hole became sufficiently large and a return flow was observed within the scour hole (see the velocity profiles in Fig. 5.8(b),(c)). At $t = 15$ s, the maximum scour depth was located at $x = 0.1$ m. At $t = 45$ s, the maximum scour depth occurred further downstream at $x = 0.17$ m. Bedforms were also observed to migrate away from the inlet.

According to several experimental/observational studies (e.g., Breusers 1967, Breusers & Raudkivi 1991), it is clear that the development of scour hole is rapid at the initial stage, and eventually an equilibrium state can be established. An empirical formulation was suggested to describe the initial rapid development of scour depth (Breusers 1967),

$$\frac{\delta_s}{h_0} = \left(\frac{t}{T_s}\right)^{n_s}, \tag{5.18}$$

where T_s is a characteristic timescale, and the exponent n_s characterizes the speed of the scour depth growth at the initial stage. Notice that Eq. (5.18) only describes the initial development of the scour depth, and the equilibrium scour depth may not be determined from this empirical formula. The equilibrium scour shape is generally independent of the flow velocity and grain size if the Shields parameter is sufficiently larger than the critical Shields parameter. On the other hand, the development of upstream scour angle α_s can reach equilibrium rapidly. An empirical formula to describe the development of scour angle is written as (Breusers 1967),

$$\alpha_s = \alpha_{s0}\Big(1 - e^{-t/T_{\alpha s}}\Big), \tag{5.19}$$

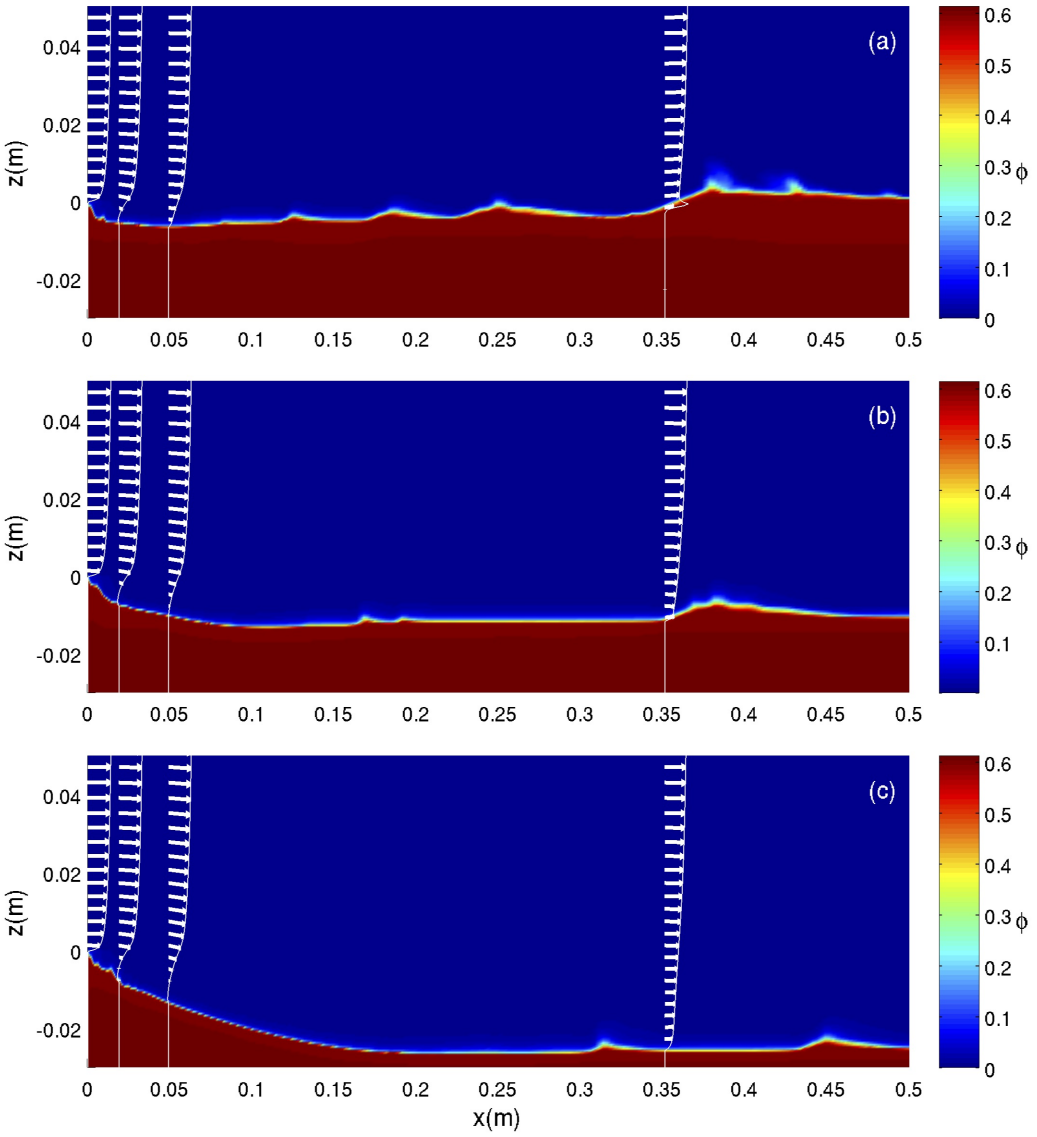

Figure 5.8: Velocity profiles at different locations downstream of the apron at (a) $t =$ 5 s, (b) $t = 15$ s, and (c) $t = 45$ s; The background is the concentration contour.

where $T_{\alpha s}$ is the equilibrium timescale of scour angle development and α_{s0} is the equilibrium scour angle. In Fig. 5.9, the modeled evolution of these two key scour quantities were compared with the empirical formulas (5.18) and (5.19). By using the least-square fit to the modeled scour depth, we observe that the model also reproduced the power law for the initial development of scour depth similar to the empirical formula with

$n_s = 0.54$ and $T_s =$ 1100 s. Similar to the model of Amoudry & Liu (2009), our model results gave a value of n_s at the high range of the reported value but still can be considered reasonable. For instance, Buchko et al. (1988) reported n_s as high as 0.6. The best fit value for the modeled scour angle was $\alpha_{s0} = -14.55°$, and $T_{\alpha s} =$ 15.2 s. Modeled α_{s0} was within the reported range of observation, $-16° < \alpha_{s0} < -9.5°$ (Breusers 1967).

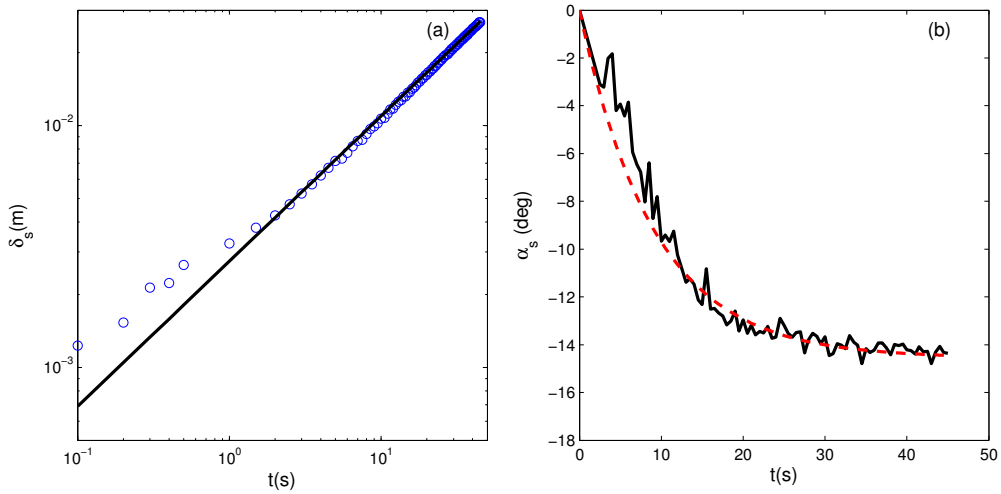

Figure 5.9: (a) Evolution of maximum scour depth for model results (symbols) and the empirical formula of Eq. (5.18) with $T_s = 1100$ s and $n_s = 0.54$ (solid line); (b) Evolution of upstream scour angle between model results (dashed curve) and Eq. (5.19) with $T_{\alpha s} = 15.2$ s and $\alpha_{s0} = -14.55°$ (solid curve).

It is worth mentioning that the predicted scour evolution coefficients are sensitive to many factors, especially the initial condition. Model experiments suggested that the sediment concentration of the initial bed has an impact on the evolution of the scour depth. It was found that a uniform bed concentration rendered a rather fast scour process as compared with the initial condition where the bed concentration was obtained directly from the steady state of 1DV results. We consider the latter to be more realistic and the results reported here were based on the established bed condition from the 1DV model. Meanwhile, the evolution of scour was also sensitive to

the B value in the turbulence modulation model (see Eq. (5.9)). With a lower value of B ($= 0.15$), numerical experiments showed that the scour process was slightly faster ($T_{\alpha s} = 14$ s), and the characteristic scour angle was slightly larger ($\alpha_{s0} = -15.56°$). The development of scour depth was also faster with $T_s = 785$ s and $n_s = 0.6$. In addition, since the bedload transport dominated the scour process, the frictional stress model may also play a role. It was found that the scour process was slightly slower (i.e., both $T_{\alpha s}$ and T_s were larger) when the coefficient m was reduced from $m = 3$ to $m = 2$ or the angle of repose θ_f was increased from 28° to 32°. However, the differences were within 15%.

5.4 Momentary Bed Failure in Sheet Flow

Several field observations (Foster et al. 2006, Conley & Inman 1992) and laboratory experiments (Sleath 1999, Flores & Sleath 1998) on wave-induced sediment transport revealed that large horizontal pressure gradients induced by the passage of steep near-breaking or broken waves can destabilize the sand bed and drive momentary bed (shear) failure. Comparing with the well-known sheet flow condition, the observed large transport (or erosion depth) cannot be solely explained by bottom shear stress (or Sheilds parameter) and hence the resulting transport rate is postulated to be enhanced by horizontal pressure gradient. This mechanism is often called plug flow (Sleath 1999) or momentary bed failure (Madsen 1974).

In the oscillating water tunnel, the horizontal pressure gradient can be expressed by free-stream flow acceleration. In order to quantify the effect of the horizontal pressure gradient, a non-dimensional parameter is used, which is often called the Sleath parameter (Sleath 1999),

$$S = \frac{\left|\partial p^f/\partial x\right|_{max}}{\rho^f (s-1) g} = \frac{U_0 \omega}{(s-1) g}. \tag{5.20}$$

The last expression converts the horizontal pressure gradient to the flow acceleration, which is only appropriate for the conditions in an oscillatory water tunnel. Madsen

(1974) and Sleath (1999) both derived similar criteria to describe the initiation of momentary bed failure using a simple force balance. These criteria give a rather large threshold value of Sleath parameter, typically around 0.33. Later, Foster et al. (2006) reported the first field evidence of momentary bed failure (or plug flow) in Duck, NC and demonstrated its occurrence at a much lower threshold value. They argue that in general the initiation of momentary bed failure must also depend on the Shields parameter. Hence, a combined sheet flow-plug flow mode, which is responsible for a large amount of sediment transport, may occur more commonly than previously believed. More recently, Holway et al. (2012) reported an oscillatory water tunnel experiment using bimodal nylon particles. Due to the low density of nylon particles ($\rho^s = 1170$ kg/m^3), the resulting Sleath parameter exceeded 0.36 and momentary bed failure occurred. In addition to the large transport rate obtained due to momentary bed failure, they observed wave-like instabilities and billows during the transport. These wave-like instabilities may play a major role in the plug flow dynamics and more quantitative investigation is needed.

In order to study the role of horizontal pressure gradient in driving momentary bed failure in sheet flow conditions, 2DV numerical investigations were performed. In Section 3.2, the numerical model was validated with medium sand ($d = 0.28$ mm) for a second-order Stokes wave motionan of O'Donoghue & Wright (2004). Here, we performed an additional simulation using the same medium sand for sinusoidal wave conditions (O'Donoghue & Wright 2004; Case 1 in Table 5.3). Model results were first validated with the measured data and then a series of numerical experiments with a wide range of Sleath parameter and Shields parameter for two different grain sizes were carried out to investigate momentary bed failure in sheet flow conditions (see Table 5.3).

To ensure the domain was tall enough to cover the wave boundary layer in different flow conditions, the domain height was set to be $L_z = 0.5$ m, which is larger than that used in Section 3.2. An initial sediment bed depth of $h_b = 0.075$ m is specified. Similar vertical spatial discretization is used with minimum Δ_z of 0.25 mm

(maximum Δ_z of 4 mm), and the total number of grid points in the z-direction is $N_z = 595$. The streamwise length of the domain is chosen to be $L_x = 0.4$ m, and a uniform grid resolution of $\Delta_x = 2$ mm with $N_x = 200$ are used.

Table 5.3: Flow conditions in the study of momentary bed failure

Cases	d (mm)	T(s)	U_m (m/s)	θ	S	bed instability	Ψ_{1D}	Ψ_{2D}
1	0.28	5	1.5	2.16	0.12	no	19.2	19.29
2	0.28	2.1	1.5	2.7	0.28	no	21.53	21.96
3	0.28	1.8	1.5	2.82	0.32	yes	17.87	256.5
4	0.28	5	2.1	3.91	0.16	no	38.59	38.6
5	0.28	5	2.7	6.12	0.21	yes	95.8	1170.8
6	0.28	1	1	1.73	0.39	yes	8.15	67.64
7	0.28	1.2	1	1.62	0.32	no	7.01	7.14
8	0.28	1.2	1.2	2.19	0.39	yes	11.23	117.7
9	0.28	1.5	1.2	2.04	0.31	no	10.22	11.3
10	0.28	2.4	1.8	3.57	0.29	yes	27.38	568.3
11	0.28	3	2	4.05	0.26	yes	34.43	500.3
12	0.28	4	2	3.77	0.19	no	33.86	34.59
13	0.2	5	1.5	2.79	0.12	no	39.23	39.27
14	0.2	2.1	1.5	3.45	0.28	yes	34.40	521.24
15	0.2	1.8	1.5	3.59	0.32	yes	32.24	639.1
16	0.2	5	2.1	5.09	0.16	yes	97.65	3049.3
17	0.2	1	1	2.15	0.39	yes	11.21	103.41
18	0.2	1.2	1	2.03	0.32	yes	11.17	119.4
19	0.2	1.2	1.2	2.76	0.39	yes	17.96	217.9
20	0.2	1.5	1.2	2.58	0.31	yes	18.34	181.29
21	0.2	1.2	0.9	1.7	0.29	no	9.57	9.55
22	0.2	3	1.5	3.14	0.19	no	39.49	39.81
23	0.2	5	1.8	3.86	0.14	no	65.43	65.51
24	0.2	6	2	4.76	0.13	no	87.99	88.05

5.4.1 1DV and 2DV sheet flow simulations

Case 1 was a sinusoidal wave with T=5 s and U_m=1.5 m/s (O'Donoghue & Wright 2004). The Sleath parameter and Shields parameters for Case 1 and other

cases investigated in this section are summarized in Table 5.3. The Shields parameter, θ, is estimated based on peak flow velocity,

$$\theta = \frac{0.5 f_w U_m^2}{(s-1)gd}, \tag{5.21}$$

where f_w is the wave friction factor, and it is calculated by (Swart 1974),

$$f_w = \exp\left[5.213\left(\frac{2.5d}{A}\right)^{0.194} - 5.977\right], \tag{5.22}$$

where $A = U_m T/2\pi$ is the semi-excursion length.

Although the simulation was carried out in 2DV, the modeled flow velocity and concentration fields remained nearly homogeneous in the streamwise direction (not shown). In Fig. 5.10, modeled sediment concentration profiles (averaged over the x-direction) at four instants during the positive wave phase were compared with the measured data of O'Donoghue & Wright (2004). The agreement is generally good. However, we can also observe that in this case, the model over-predicts the suspended sediment concentration during the flow peak (see Fig. 5.10c). This discrepancy can be due to the parameterization on the degree of particles following the fluid velocity fluctuations (see Eq. (5.9)). In this study, the empirical coefficient B associated with this parameterization is calibrated for steady sheet flow of Sumer et al. (1996) of fine sand with $d = 0.13$ mm. This value is used here for oscillatory flow of medium sand without further tuning. Meanwhile, another identical simulation was carried out in 1DV, and the model results from the 1DV simulation (also not shown) was nearly identical to the 2DV results. In summary, the estimated Shields parameter for Case 1 is 2.16, while the Sleath parameter is $S = 0.12$, which is much smaller than the critical value of 0.33. Hence, a regular sheet flow with complete homogeneity in the streamwise direction are expected. 2DV model results indeed reproduced homogeneous flow in the streamwise direction, Case 2 (see Table 3) with wave period reduced to 2.1 s and hence the Sleath parameter increased to $S = 0.28$ produced similar sheet flow results.

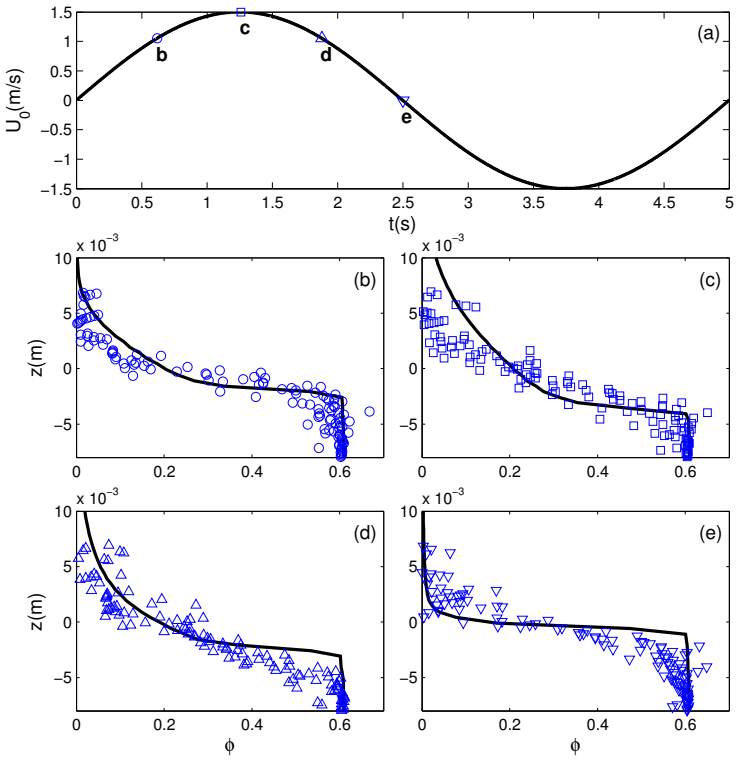

Figure 5.10: (a) Time series of free-stream velocity, in which four representative instants are indicated: (b) $t = 0$; (c) $t = 1.25$ s; (d) $t = 1.88$ s and (e) $t = 2.5$ s; The corresponding comparison of sediment concentration profiles between the numerical results (solid curve) and measured data (symbols) at these four instants for Case 1 (see Table 5.3) are shown in panel (b), (c), (d) and (e).

5.4.2 Combined sheet flow and plug flow

When the oscillatory period was reduced to $T = 1.8$ s (see Case 3 in Table 5.3), the resulting Shields parameter is 2.8. Although sheet flow is expected, model results were no longer homogeneous in the streamwise direction. Snapshots of the 2DV sediment concentration field (Fig. 5.11) showed billows associated with instabilities of the near bed transport layer. The billows had a streamwise length scale of 5 $\sim$ 10 cm. Because the billows enhance mixing, the sheet flow layer thickness is increased considerably to about 3 cm. In Case 3, the Sleath parameter is increased to $S = 0.32$ due to a shorter oscillatory period and hence a larger flow acceleration (horizontal

pressure gradient). At such large value of Sleath parameter, momentary bed failure or plug flow is expected. The present model indicated that the occurrence of momentary bed failure or plug flow is associated with the formation of the observed instability and billows near the bed.

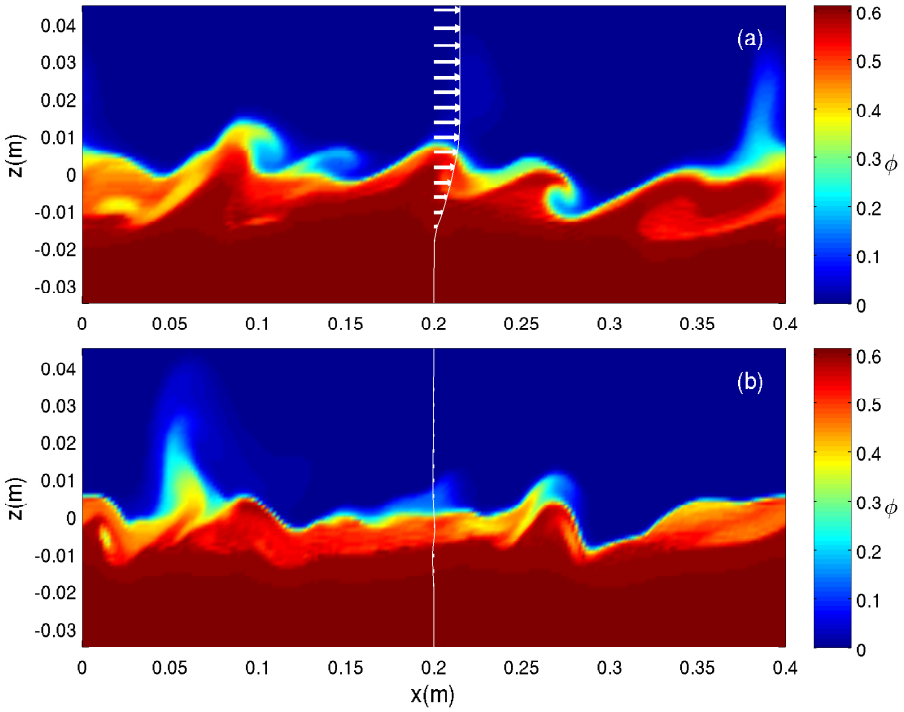

Figure 5.11: Snapshot of concentration field at (a) flow peak ($t = 0.45$ s) and (b) flow reversal ($t = 0.9$ s) for Case 3 (see Table 5.3); white arrows denotes the plane-averaged velocity vectors.

Although qualitative, the instability and billows observed in the model results seem to be consistent with several field and laboratory observations. For example, Conley & Inman (1992) described their observation of a carpet of tufts (about $O(6)$ cm, see their Fig. 5) under the crest of near-breaking waves in the surf zone. Madsen (1974) reported divers' observations of sediment bed seemingly explode just prior to the passage of the crest of near-breaking waves. As mentioned previously, similar wave-like instabilities under combined sheet flow and plug flow conditions were observed during a more recent experiment performed in a small oscillatory flow tunnel at the Naval

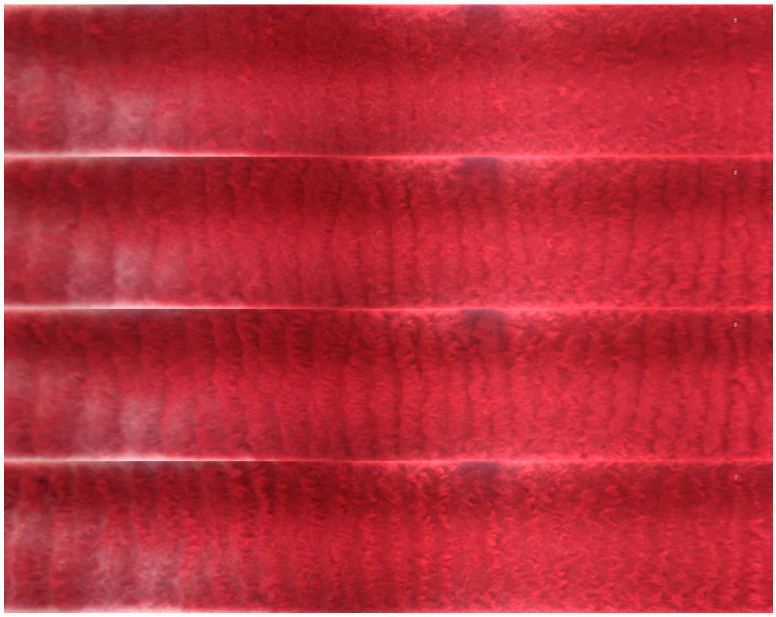

Figure 5.12: Sequence of four images (top to bottom) highlighting the development of instabilities and billows under combined sheet flow and plug flow conditions in a small oscillatory flow tunnel during half a wave cycle (Holway et al. 2012). The streamwise length (spanwise width) of the field of view in each snapshot is 128 cm (25 cm).

Research Laboratory (Holway et al. 2012). Video of sheet flow transport with a bed composed of a bimodal distribution of nylon cylinders ($\rho^s = 1170$ kg/m^3) having diameters of 0.5 mm (red) and 1.0 mm (white) demonstrated the streamwise sorting of surficial grains. Sequence of four (top view) images shown in Fig. 5.12 demonstrated the development of wave-like instabilities. Although the primary billows were more or less spanwise homogeneous, there were notable smaller 3D features suggesting that instabilities grew rapidly into turbulent features. We note that in the present 2DV Reynolds-averaged simulation, smaller 3D turbulent features are parameterized by turbulent viscosity/diffusivity and only primary 2D billows can be directly resolved.

More quantitative analysis and comparison between 1DV and 2DV simulations were performed to elucidate the effects of momentary bed failure and billows on the transport dynamics. Since the instability and billows of the near bed transport layer are inhomogeneous in the streamwise direction, the 1DV model is not adequate to simulate

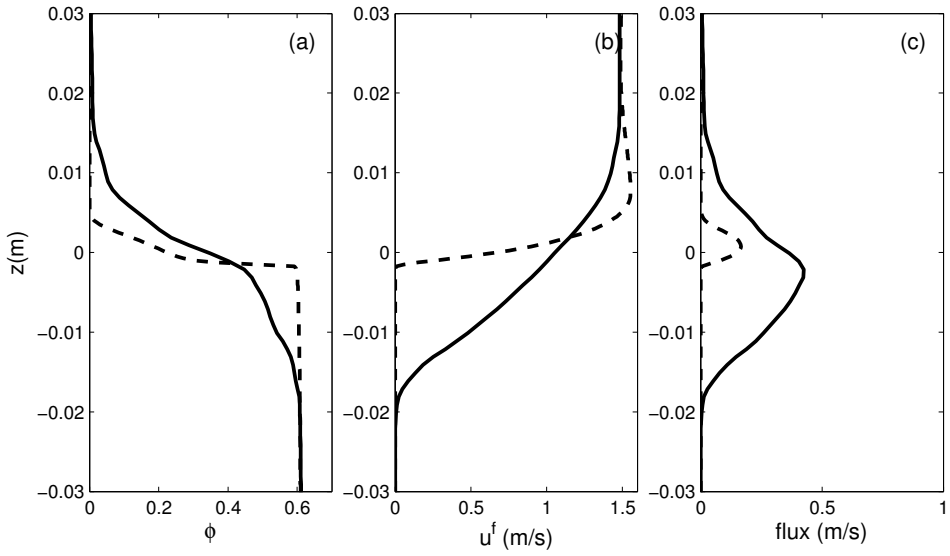

Figure 5.13: Comparison of (a) sediment concentration profiles, (b) fluid velocity profiles and (c) sediment flux profiles of 1DV (dashed curves) and 2DV (solid curves) for Case 3 at flow peak.

the process. Therefore, we carried out the same simulation of Case 3 but in a 1DV domain to understand the role of instabilities and billows on the resulting transport. In Fig. 5.13, the streamwise-averaged profiles of sediment concentration, fluid velocity and sediment flux under flow peak for Case 3 are presented along with those calculated by the 1DV model. The differences between 1DV and 2DV results for Case 3 were evident. In the 2DV results, a large dense mobile layer from $z = -0.019 \sim 0.01$ m was observed, and more sediment was mobilized, which gave considerably large sediment flux (see Fig. 5.13(c)). On the other hand, in the 1DV results the region between $z = -0.019 \sim -0.002$ m was immobile and the overall mobile layer thickness and sediment flux were several times smaller. Laboratory observation and linear stability analysis for light particle transport in steady channel flow (Charru & Mouilleron-Arnould 2002, Schaflinger et al. 1995) suggest that instability of particle transport layer may occur when the mobile layer thickness is sufficiently large. Their findings are consistent with the model results presented here.

Fig. 5.14 further contrasts the erosion depth for Case 1 and Case 3. For Case 1,

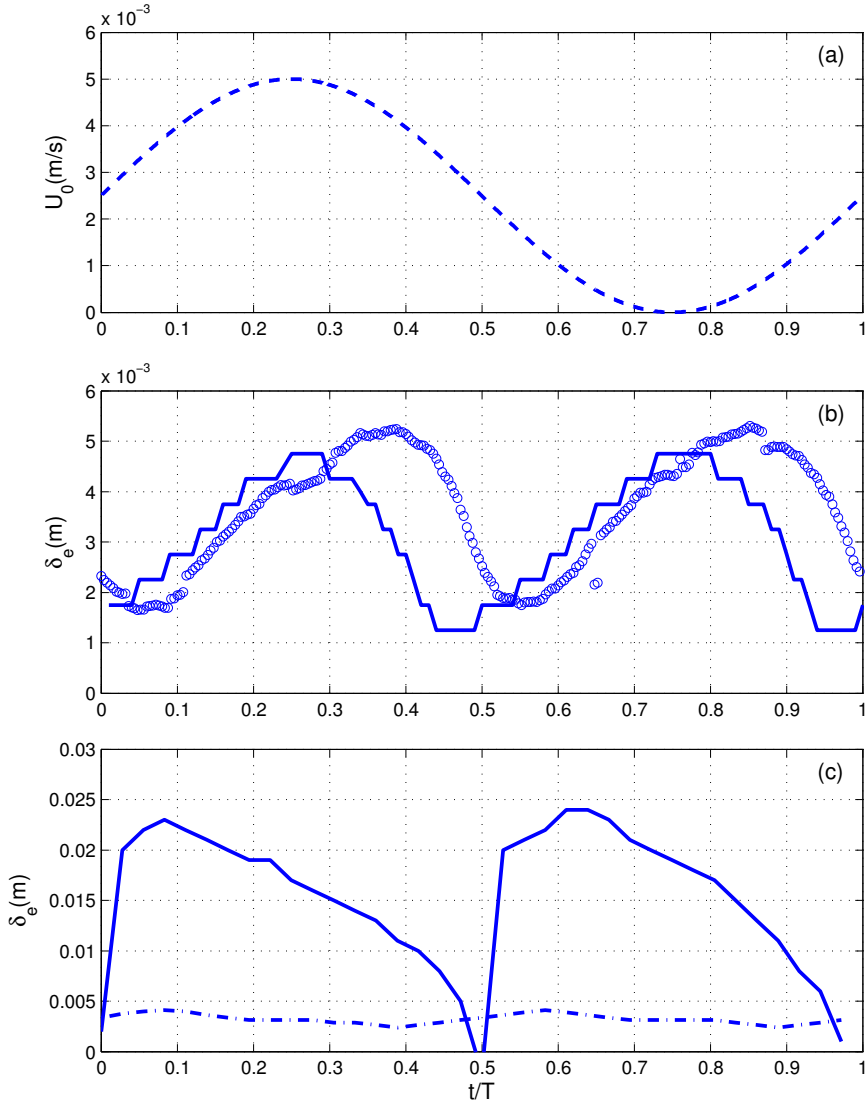

Figure 5.14: Time series of free-stream velocity (panel (a)) and numerical results of the erosion depth (solid curves) for (b) Case 1 and (c) Case 3; In panel (b), the circle symbols represent measured data from O'Donoghue & Wright (2004). In panel (c), the dash-dot curve is the 1DV result.

the model result was also compared with the measured data of O'Donoghue & Wright (2004) in Fig. 5.14(b). The measured maximum erosion depth occurred during the middle of the deceleration but the predicted peak value occurred just slightly after the peak flow. The model slightly under-predicted the maximum erosion depth by about 0.5 mm but the general agreement was good. For Case 3 where the momentary bed

failure occurred (Fig. 5.14(c)), the temporal evolution and the magnitude of erosion depth were distinctly different from that of Case 1. We observed that the erosion depth reached its maximum immediately after the flow reversal. Clearly, the rapid increase of erosion depth responded directly to the peak horizontal pressure gradient (or free-stream acceleration) at the flow reversal. Similar features have been observed by several other researchers during the occurrence of plug flow (Foster et al. 2006, Liu & Sato 2005, Sleath 1999, Flores & Sleath 1998). It is also evident that the erosion depth in Case 3 ($\delta_m \approx 22$ mm) was considerably larger than that of Case 1 ($\delta_m \approx 6$ mm). Clearly, the this major difference in erosion depth is because the Sleath parameter is sufficiently large, although the Shields parameters in Case 1 and Case 3 were similar (see Table 5.3).

5.4.3 Discussion

Sediment transport rate is the most important physical quantity to be evaluated. The present model can provide total sediment transport rate without the bedload/suspended load assumptions. To quantify how momentary bed failure can enhance the transport rate, additional simulations were carried out. A total number of 24 cases were presented in this study (see Table 5.3). Two different grain diameters (d=0.28 mm and d=0.2 mm) were considered and these 24 simulations covered Shields parameter in the range of 1.62 to 6.12 and Sleath parameter in the range of 0.12 to 0.39.

To compare sediment transport rate under sinusoidal wave motion, the half-wave averaged sediment transport rate $Q_{1/2}$ is defined as,

$$Q_{1/2} = \frac{2}{T}\int_0^{T/2}\int_0^{L_z} u^s \phi dz dt. \tag{5.23}$$

The nondimensional half-wave averaged sediment transport rate is then defined as,

$$\Psi = \frac{Q_{1/2}}{\sqrt{(s-1)gd^3}}. \tag{5.24}$$

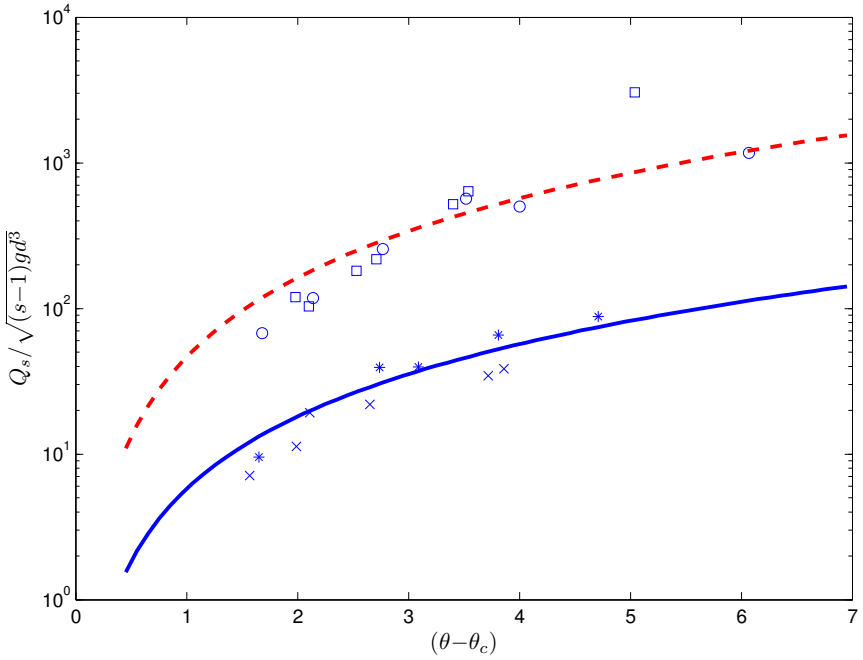

Figure 5.15: The normalized half-wave-averaged transport rate in terms of Shields parameter θ. $\times$: 2D pure sheet flow of $d = 0.28$ mm; $\circ$: 2D sheet flow with momentary bed failure of $d = 0.28$ mm; $*$: 2D pure sheet flow of $d = 0.2$ mm; $\square$: 2D sheet flow with momentary bed failure of $d = 0.2$ mm; The solid curve shows the best-fit power law for pure sheet flow predicted by the present model ($M = 5.78$, $N = 1.65$) where $\theta_c = 0.05$ is the critical shields parameter. The dashed curve shows the best-fit power law for the combined sheet flow and plug flow condition ($M = 46.55$, $N = 1.81$).

The normalized half-wave averaged transport rate calculated from the 1DV and 2DV models are both shown in Table 5.3. As long as the momentary bed failure (or plug flow) did not occur, the predicted sediment transport rate between the 1DV and 2DV results were very similar. However, when momentary bed failure/plug flow was observed, the resulting transport rate was significantly enhanced in the 2DV results. It is clear that the instabilities and billows of the transport layer observed in the 2DV simulation played a major role in the enhancement of the sediment transport rate.

The 2DV results of the normalized half-wave averaged transport rate for the 24 cases in Table 5.3 are plotted in Fig. 5.15. For typical sheet flow transport, the

Shields parameter can be used to parameterize the half-wave averaged nondimensional sediment transport rate using a power law:

$$\Psi = M(\theta - \theta_c)^N. \tag{5.25}$$

For the cases without momentary bed failure (pure sheet flow), the best fit values are $M = 5.78$ and $N = 1.65$, which are quite similar to commonly used sheet flow transport formulae (Ribberink 1998). However, when momentary bed failure in sheet flow occurred, the 2DV results predicted the transport rates that were considerably ($10 \sim 20$ times) larger than the pure sheet flow cases. Although the sediment transport rate for momentary bed failure in sheet flow may not be solely related to the Shields parameter (Nielsen 2006), we can still obtain the best-fit values as $M = 46.55$ and $N = 1.81$. Clearly, the resulting non-dimensional transport rate increases much rapidly with the Shields parameter and hence in general, we can expect that the transport rate also depends on the Sleath parameter.

It was previously found that plug flows typically occurred after the sheet flow threshold was exceeded (Foster et al. 2006). Hence, the threshold criteria for momentary bed failure, parameterized by S_{cr}, must also depend on the Shields parameter. This conjecture is confirmed by the present model (Fig. 5.16). Model experiments with a range of θ and S show that momentary bed failure/plug flow were observed at S_{cr} as large as 0.32 in mild sheet flow conditions ($\theta = 1.5$). However, in energetic sheet flow with high θ, momentary bed failure is observed at S_{cr} as low as $0.1 - 0.2$.

By rearranging the force balance on the block of sediment given in Sleath (1999), the criterion of bed mobilization is proposed as, $\left|K \cdot \theta + S\right| > C$, where K and C are coefficients, which may be related to the bed friction coefficient and bed concentration (Foster et al. 2006, Frank et al. 2015a). According to the present model results with two different grain sizes ($d = 0.2$ mm and 0.28 mm), we obtain the dashed curve shown

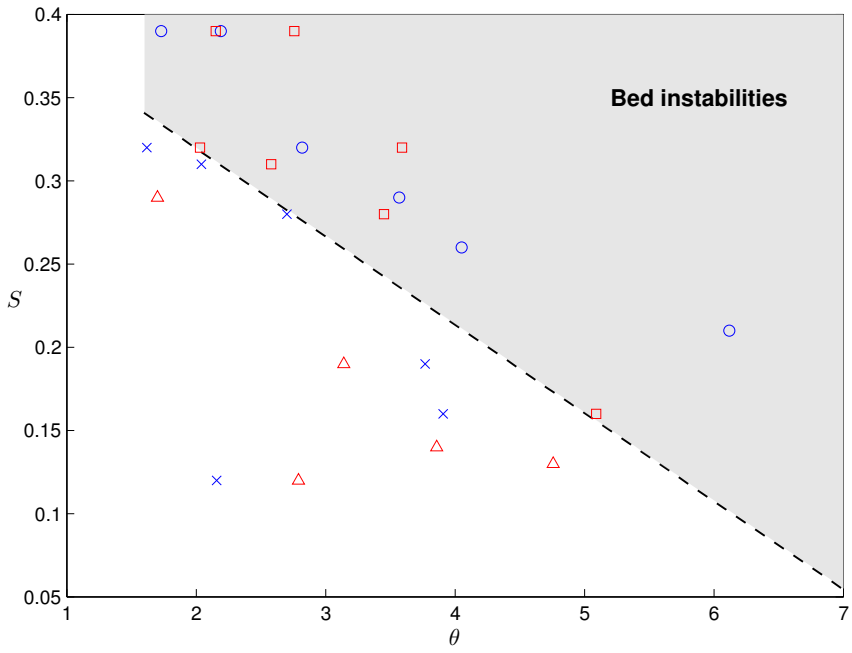

Figure 5.16: Schematic map of sheet flow with momentary bed failure in terms of Sleath parameter S and Shields parameter θ. $\times$: sheet flows of $d = 0.28$ mm; $\circ$: momentary bed failure of 0.28 mm; $\triangle$: sheet flows of $d = 0.2$ mm; $\square$: momentary bed failure of 0.2 mm; dashed curve: proposed criteria for the occurrence of momentary bed failure (Eq. (5.26)).

in Fig. 5.16 and the momentary bed failure occurs when,

$$\left|0.053\theta + S\right| > 0.426. \tag{5.26}$$

5.5 Conclusion

A multi-dimensional two-phase Eulerian model for sediment transport, called SedFoam, was developed based on the open-source CFD toolbox, OpenFOAM. The mathematical formulations follow the prior two-phase flow approach for sediment transport of Hsu et al. (2004), and several modifications to the numerical solver twoPhaseEulerFoam are introduced to make the model more robust for sediment transport applications. The model was validated for sheet flow in steady channel flow, oscillatory flow, and scour downstream of an apron.

The validated model was further used to study momentary bed failure (plug flow) in sheet flow when the horizontal pressure gradient (or flow acceleration in U-tube) is sufficiently large. Consistent with limited field and laboratory observation, model results indicate that momentary bed failure is associated with the rapid growth of large erosion depth during flow reversal. Moreover, large erosion depth further leads to instabilities and billows of the near bed transport layer and the resulting transport rate is significantly enhanced. The criteria of momentary bed failure/plug flow was investigated with a range of Shields parameter and Sleath parameter. Our numerical result was consistent with the empirical formulation proposed by Foster et al. (2006) that the threshold value for the initiation of plug flow is lower when the Shields parameter is larger. More detailed experimental investigations, especially regarding the generation of billows via instabilities and their role on the resulting transport rate are warranted. Due to the turbulence-averaging approach, the present model results are sensitive to the closure coefficients associated with the parameterization on turbulence-sediment interactions. The present study calibrated this empirical coefficient with steady sheet flow data of Sumer et al. (1996). However, when applying the model to oscillatory sheet flow, the model tends to over-predict the suspended sediment concentration during flow peak. To further improve the model and carry out fundamental investigations on turbulence-sediment interactions in sediment transport, a 3D turbulence-resolving simulation model is needed. Such model extension will also allow direct resolving the evolution and dissipation of billows associated with the momentary bed failure.

5.6 Acknowledgements

This study was supported by National Science Foundation (CMMI-1135026; OCE-1356855) and Office of Naval Research (N00014-14-1-0586). Dr. Joseph Calantoni was supported under base funding to the Naval Research Laboratory from the Office of Naval Research. Numerical simulations were carried out on MILLS at the University of Delaware. Simulations also leverage computing resource provided by Extreme Science and Engineering Discovery Environment (XSEDE) (TG-OCE100015).

We gratefully acknowledge developers involved in OpenFOAM, which is the foundation of the new solver SedFoam presented in this report. Dr. Xiao Yu provided many useful suggestions during the model development. SedFoam is publicly available via Community Surface Dynamics Modeling System (CSDMS) model repository maintained by GitHub: https://github.com/csdms-contrib/twophaseeulersedfoam

Chapter 6

A LARGE EDDY SIMULATION TWO-PHASE MODEL FOR SEDIMENT TRANSPORT

A large eddy simulation Eulerian two-phase model for coastal sediment transport applications is developed, in which a dynamic Smagorinsky sub-grid stress closure is adopted, and the sub-grid contribution to the drag force is included by a sub-grid drift velocity. The model is validated with a steady sheet flow (Revil-Baudard et al. 2015) and oscillatory sheet flow (O'Donoghue & Wright 2004). In the steady sheet flow, a reduction of the von Karman parameter in the suspension layer is reproduced by the present model, and a strong damping effect due to drag was found to be more important than the density stratification effect in the steady sheet flow condition of Revil-Baudard et al. (2015). Meanwhile, the model demonstrated that the bed intermittency is mostly related to the turbulent ejection ($u^{f\prime} < 0$ and $w^{f\prime} > 0$) and sweep ($u^{f\prime} > 0$ and $w^{f\prime} < 0$) events The numerical result shows that the turbulent ejection motions are high correlated with the bed level increasing, while the turbulence sweep events are most associated with the bed erosion. This phenomenon has also been observed by the experiment (Revil-Baudard et al. 2015). In addition, the turbulence-resolving model is able to capture the enhanced transport layer thickness for fine sand, which may be related to the burst events near flow reversal. These unique transport characteristics for fine sediments have been reported by a few other oscillating water tunnel experiments (e.g., Dohmen-Janssen & Hanes 2002). We further confirm that this phenomenon is absent for medium sand.

6.1 Introduction

The nearshore zone, defined here as the shallow coastal environment with flow depth of no more than about 10 meters, is of highly unsteady and energetic flows that can cause significant amount of sediment transport and shapes the beach morphology. Due to large bottom shear stress driven by waves and currents, small bedforms are often washed out and sediments are transported as a concentrated suspension layer called sheet flow over a relatively flat bed.

The conventional modeling approach for sediment transport splits the transport into the bedload and the suspended load layers. To adopt a single-phase modeling approach, the bedload layer is not resolved but parameterized by a bed-shear-stress-based transport rate formula while although the suspended load transport is resolved, similar bed-shear-stress-based near-bed suspension flux need to be adopted (Rijn 1984, Engelund & Fredsoe 1976). There are several challenges to model sheet flow in the nearshore zones using such conventional methodology. Firstly, major transport in sheet flow occurs within about 1 cm above the bed. Hence, the resolved suspended load layer only account for a minor portion of transport while the majority of transport predicted relies on the empirical bedload parameterization. Secondly, most of the existing formulae for bedload transport and suspension flux are developed for steady flow and hence their applicability to the highly unsteady wave-induced transport is questionable.

In the past decade, several numerical models for sheet flow sediment transport have been developed based on the Eulerian two-phase flow approach (e.g., Jenkins & Hanes 1998, Dong & Zhang 1999, Hsu et al. 2004, Revil-Baudard & Chauchat 2013). By solving the mass and momentum equations of fluid phase and sediment phase with appropriate closures on interphase momentum transfer, turbulence, and inter-granular stresses, these two-phase models are able to resolve the entire profiles of sediment transport without the assumption of bedload and suspended loads. These two-phase flow models have been adopted to study, for example, onshore sediment transport driven by nonlinear wave shapes (e.g., Dong & Zhang 2002, Hsu et al. 2004,

Liu & Sato 2006) and boundary layer streaming (Yu et al. 2010, Kranenburg et al. 2014), the parameterization of suspension flux under waves (Amoudry & Liu 2010, Yu et al. 2012), and inner-surf/swash sediment transport (Bakhtyar et al. 2010). These modeling studies successfully demonstrated that the two-phase flow approach can be an effective tool to study coastal sediment transport, however, several key improvements are warranted.

All of the aforementioned two-phase flow sediment transport models are based on turbulence-averaged approach and hence the closure of turbulence relies on eddy viscosity calculated ranging from a mixing length closure to a two-equation (e.g., $k-\epsilon$) closure. As investigated by several researchers (e.g., Amoudry et al. 2008, Kranenburg et al. 2014), the coefficients in the turbulence closure, in particular, the closure coefficients associated to the reduction or enhancement of turbulence due to the presence of sediment, is highly sensitive to the model results. A particular model coefficient is chosen and calibrated with laboratory measured sediment concentration for a given grain size of different flow intensities. However, the model's applicability to a substantially different grain size is unclear. For instance, it is well-known that in the laboratory experiments of sheet flow in oscillatory flows, measured maximum sheet flow layer thickness δ_s, when nondimensionalized by mean grain size d, scales well with the Shields parameter θ. Specifically, Dohmen-Janssen & Hanes (2002) demonstrated that for medium sand (mean grain diameter d = 0.21 mm and 0.32 mm), the resulting δ_s agrees with the well-known formula developed for steady flow (Wilson 1987), $\delta_s/d = C_\delta\theta$, with the empirical coefficient C_δ=10. However, for fine sand with d = 0.13 mm in oscillatory sheet flow, the empirical coefficient C_δ increases significantly to about 30. To our knowledge, the enhanced sheet layer thickness cannot be reproduced by the turbulence-averaged two-phase flow model unless the particular coefficient in the turbulence closure is re-calibrated for fine sand.

From the modeling perspective, it is likely that the existing closure models for turbulence, particularly turbulence-sediment interaction, is limited. To better understand the effect of sediments on modulating turbulence in sediment transport, a

turbulence-resolving two-phase flow model is required. For sediment transport applications in turbulent flows, various scales of turbulent motions and sediment structures are involved. On the contrary of direct numerical simulation (e.g., Ozdemir et al. 2010), where all scales of turbulent motions are directly resolved, it is often practical to resolve sufficient large scale eddy motions or sediment structures, and the effect of small eddies or sediment structures can be modeled with sub-grid closures. Through a 3D two-phase flow model that resolves turbulence and turbulence-sediment interaction of the energy containing eddies with appropriate sub-grid closure, i.e., Large-eddy simulation (LES), most of the turbulence-sediment interactions are directly resolved.

Recently, an open-source multi-dimensional Eulerian two-phase flow model for sediment transport, SedFoam (Cheng et al. 2016), is developed using the CFD toolbox OpenFOAM framework. Although the numerical model is developed for full 3-dimensions (3D), existing SedFoam has only been used for two-dimensional applications with turbulence-averaged formulation. The purpose of this study is to extend the SedFoam solver for 3D turbulence-resolving simulation using a large eddy simulation approach (Section 6.2). The simulations are first validated with measured data of unidirectional sheet flow transport (Revil-Baudard et al. 2015) and then it was applied to oscillatory flow for medium and fine sand reported by O'Donoghue & Wright (2004) (Sections 6.3 and 6.4). We demonstrate that the turbulence-resolving Eulerian two-phase flow simulation is able to capture turbulence-sediment interactions such as bed intermittency (Section 6.3), and enhanced sheet layer thickness for fine sand can be reproduced by the present model (Section 6.4). The present simulation results also motivate future works on improved sub-grid closure models for fluid phase, sediment phase and the coupling terms in the context of large-eddy simulation (Section 6.5).

6.2 Mathematical Formulations

6.2.1 Filtered two-phase Eulerian equations

Under the framework of typical two-phase Eulerian model for sediment transport (Cheng & Hsu 2014*b*), both fluid and particle phases are treated as continuum. In the

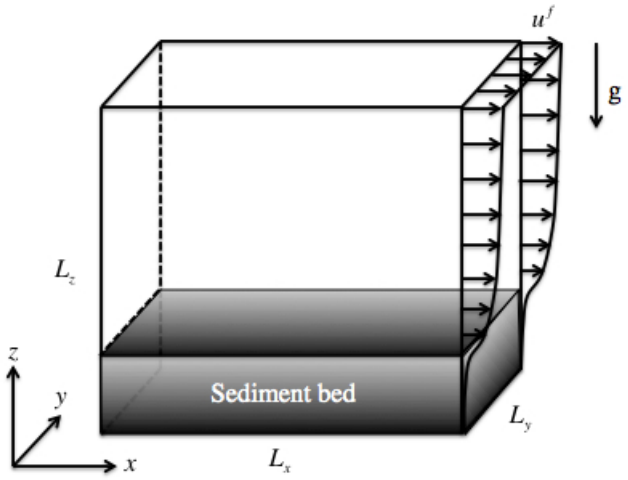

Figure 6.1: Illustration of 3D domain for turbulence-resolving Eulerian two-phase flow model

concept of LES simulation, turbulent eddies are classified into large and small scales, where the large scales are directly resolved, and the effect of the small scale motions are modeled using sub-grid closures. To achieve the separation of scales, a high-pass filter (or low-pass in frequency) is applied to the Eulerian two-phase equations for a fluid-particle system (see chapter 4). Similar to the previous studies using two-phase approach for compressible flows (e.g., Vreman et al. 1995, Galtier & Banerjee 2011), a Favre filtering concept is used, i.e. $\widehat{\phi f} = \hat{\phi}\hat{f}$, where '$\widehat{\ }$' denotes the filtering operation, and ϕ is the volume fraction of quantity f. It shall be noted that the Favre filtering operation does not commute with the partial differential operators. The Favre filtering has been demonstrated to make a negligible difference to the large-scale dynamics compared with direct filtering approaches for high Reynolds number flows (Aluie 2013). The same Favre filtering procedure is applied to both the fluid phase and sediment phase. Assuming that there is no mass transfer between the two phases, the filtered mass conservation equations for fluid phase and sediment phase can be written as:

$$\frac{\partial(1-\hat{\phi})}{\partial t} + \frac{\partial(1-\hat{\phi})\hat{u}_i^f}{\partial x_i} = 0, \tag{6.1}$$

$$\frac{\partial \hat{\phi}}{\partial t} + \frac{\partial \hat{\phi}\hat{u}_i^s}{\partial x_i} = 0, \tag{6.2}$$

where $\hat{\phi}$ is the filtered sediment volumetric concentration, $\hat{u}_i^f, \hat{u}_i^s$ are the filtered fluid and sediment velocities, and $i = 1, 2, 3$ represents streamwise, spanwise and vertical components, respectively. As a result of Favre filtering, the filtered continuity equations do not contain any sub-grid term.

The filtered momentum equations for fluid phase and sediment phase are written as:

$$\begin{aligned} \frac{\partial \rho^f (1-\hat{\phi})\hat{u}_i^f}{\partial t} + \frac{\partial \rho^f (1-\hat{\phi})\hat{u}_i^f \hat{u}_j^f}{\partial x_j} &= -(1-\hat{\phi})\frac{\partial \hat{p}^f}{\partial x_i} + \frac{\partial (1-\hat{\phi})(\hat{\tau}_{ij}^f + \hat{\tau}_{ij}^{f,sgs})}{\partial x_j} \\ &\quad + \rho^f (1-\hat{\phi}) g_i + \hat{M}_i^{fs}, \end{aligned} \tag{6.3}$$

$$\frac{\partial \rho^s \hat{\phi}\hat{u}_i^s}{\partial t} + \frac{\partial \rho^s \hat{\phi}\hat{u}_i^s \hat{u}_j^s}{\partial x_j} = -\hat{\phi}\frac{\partial \hat{p}^f}{\partial x_i} + \frac{\partial \hat{\phi}\hat{\tau}_{ij}^{s,sgs}}{\partial x_j} - \frac{\partial \hat{p}^s}{\partial x_i} + \frac{\partial \hat{\tau}_{ij}^s}{\partial x_j} + \rho^s \hat{\phi} g_i - \hat{M}_i^{fs} \tag{6.4}$$

where, ρ^f, ρ^s are fluid and sediment densities, respectively. g_i is the gravitational acceleration, and $\hat{p}^f$ is the fluid pressure. $\hat{M}_i^{fs}$ represent the filtered inter-phase momentum transfer between fluid phase and particle phase (see section 6.2.2). $\hat{\tau}_{ij}^f$ and $\hat{\tau}_{ij}^{f,sgs}$ are the fluid molecular viscous stress and sub-grid stresses associated with unresolved turbulent motions. In analogy to the fluid phase, the unresolved particle motions are also taken account by a sub-grid stress model, $\hat{\tau}_{ij}^{s,sgs}$. These sub-grid stress model will be discussed in section 6.2.3. The particle pressure $\hat{p}^s$ and particle stress $\hat{\tau}_{ij}^s$ are calculated from kinetic theory of granular flow and phenomenological closure of contact stresses (see section 6.2.4).

6.2.2 Subgrid drag model

The fluid and particle momentums are coupled with a momentum transfer term. In general, the interactions between fluid phase and particle phase include the drag force, added mass force, the Basset force, lift force (Maxey & Riley 1983) and the

effect of grain-scale turbulence fluctuations on the effective momentum transfer. We assume that the drag force dominates in sediment transport applications, and hence for simplicity, the other terms such as lift force, added mass force and Basset force are neglected. The filtered drag force can be written as a resolved part and sub-grid part:

$$\hat{M}_i^{fs} = -\widehat{\phi\beta u_i^r} \approx -\beta\widehat{\phi u_i^r} = -\beta\hat{\phi}\hat{u}_i^r - I_i^{sgs}, \tag{6.5}$$

where, $u_i^r = u_i^f - u_i^s$ is the relative velocity, and I_i^{sgs} is the sub-grid contribution to the drag. β is the drag coefficient. For the closure of drag coefficient β, we combined the model of Ergun (1952) for dense sediment concentration ($\phi \geq 0.2$) and the model of Wen & Yu (1966) for lower sediment concentration ($\phi < 0.2$) by following Ding & Gidaspow (1990):

$$\beta = \begin{cases} 150\hat{\phi}\nu^f\rho^f/[(1-\hat{\phi})d^2] + 1.75\rho^f|\hat{u}_i^r|/d, & \phi \geq 0.2 \\ 0.75C_d\rho^f|\hat{u}_i^r|(1-\hat{\phi})^{-1.65}/d, & \phi < 0.2 \end{cases} \tag{6.6}$$

where d is the grain diameter, and C_d is expressed as:

$$C_d = \begin{cases} 24(1+0.15Re_p^{0.687})/Re_p, & Re_p \leq 1000 \\ 0.44, & Re_p > 1000 \end{cases} \tag{6.7}$$

in which, $Re_p = (1-\hat{\phi})|\hat{u}_i^r|d/\nu^f$ is the particle Reynolds number, and ν^f is the fluid molecular viscosity. It was demonstrated that the existence of mesoscale structures, such as streamers and clusters, can have significant effects on the overall sediment dynamics, and these mesostructures may not be resolved by the mesh size used in the present study (O'Brien & Syamlal 1993), and the resolved drag force may be over-predicted if the sub-grid contribution of the drag force is not fully accounted for (Ozel et al. 2013). As proposed by Ozel et al. (2013), the sub-grid contribution due to the unresolved mesoscale structures can be modeled with a sub-grid drift velocity in the drag force:

$$I_i^{sgs} = \beta(\widehat{\phi u_i^r} - \hat{\phi}\hat{u}_i^r) = \hat{\phi}\beta K_i f(\Delta)h(\hat{\phi})\hat{u}_i^r, \tag{6.8}$$

where $f(\Delta) = \Delta^2/(\Delta^2 + C_f\tau_p|\hat{u}^r|)$, is a filter dependence function, and $\tau_p = \rho^s/\beta$ is the particle response time. The filter-width dependence is determined by the ratio of particle crossing length scale $l_s = \tau_p|\hat{u}_i^r|$ to the grid size. If $\Delta \gg l_s$, the sub-grid particle motions is important, and $f(\Delta) \approx 1$, otherwise when $\Delta \ll l_s$, significant portion of the particle motions are resolved, and the sub-grid contribution can be neglected, i.e., $f(\Delta) \approx 0$. The coefficient $C_f = 0.15$ is chosen by following Ozel et al. (2013) ,and $h(\hat{\phi})$ is a concentration dependent function:

$$h(\hat{\phi}) = -tanh\left(\frac{\hat{\phi}}{C_{h1}}\right)\sqrt{\frac{\hat{\phi}}{\phi_{max}}}\left(1-\frac{\hat{\phi}}{\phi_{max}}\right)^2\left[1 - C_{h2}\frac{\hat{\phi}}{\phi_{max}} + C_{h3}\left(\frac{\hat{\phi}}{\phi_{max}}\right)^2\right], \quad (6.9)$$

where $C_{h1} = 0.1$, $C_{h2} = 1.88$ and $C_{h3} = 5.16$ are determined from by following (Ozel et al. 2013), and ϕ_{max} is the max packing limit for the sediments. The function $h(\hat{\phi})$ is close to zero when the sediment concentration $\hat{\phi}$ is small ($\hat{\phi} < 0.08$) or close to packing limit ($\hat{\phi} > 0.5$), where minor sediment transport occurs. In the interval with intermediate sediment concentration $0.08 < \hat{\phi} < 0.5$, the sediment transport is most intense, and function $h(\hat{\phi})$ reaches its maximum.

The model constant K_i is adjusted dynamically to take account of the anisotropy effects on the effective drag force, and it is determined in a similar way as the dynamic Smagorinsky coefficient C_s^f by using a test filter (see section 6.2.3).

$$K_i = \frac{< D_i R_i >}{< R_i R_i >}, \quad (6.10)$$

where $D_i = \widetilde{\hat{\phi}\hat{u}_i^r} - \widetilde{\hat{\phi}}_i\widetilde{\hat{u}_i^r}$, and $R_i = f(\tilde{\Delta})h(\tilde{\hat{\phi}})\tilde{\hat{\phi}}\tilde{\hat{u}}_i^r - \widetilde{f(\Delta)h(\hat{\phi})\hat{\phi}\hat{u}_i^r}$.

6.2.3 Subgrid turbulence closure

The filtering of nonlinear convection term on the left-hand-side of Eq. (6.3) leads to an additional sub-grid tensor $\hat{\tau}_{ij}^{fsgs}$:

$$(1-\hat{\phi})\hat{\tau}_{ij}^{f,sgs} = \overline{(1-\phi)u_i^f u_j^f} - (1-\hat{\phi})\hat{u_i^f}\hat{u_j^f} \tag{6.11}$$

where ϕ, u_i^f are the unfiltered sediment concentration and fluid velocity. We further assume that $\overline{(1-\phi)u_i^f u_j^f} \approx (1-\hat{\phi})\widehat{u_i^f u_j^f}$, thus the residual momentum flux can be modeled using functional sub-grid stress model:

$$\hat{\tau}_{ij}^{f,sgs} = \widehat{u_i^f u_j^f} - \hat{u}_i^f \hat{u}_j^f = -2\nu_{sgs}^f \widehat{S}_{ij}^f \tag{6.12}$$

where $\nu_{sgs}^f = C_s^f \Delta^2 |\widehat{S}^f|$ is the sub-grid eddy viscosity, and $|\hat{S}^f|$ is defined as $\sqrt{2\widehat{S}_{ij}^f \widehat{S}_{ij}^f}$, where $\widehat{S}_{ij}^f$ is the resolved fluid strain rate tensor,

$$\widehat{S}_{ij}^f = \frac{1}{2}\left(\frac{\partial \hat{u}_i^f}{\partial x_j} + \frac{\partial \hat{u}_j^f}{\partial x_i}\right), \tag{6.13}$$

Δ is the filter width. The implicit filtering technique are adopted first, i.e., the equations are implicitly filtered by the discretization schemes and computational grid. In such technique, the filter width is typically related to the local grid cell size, here we choose the cubic root of the volume of the local cell, $\Delta = (\Delta_x \Delta_y \Delta_z)^{1/3}$. C_s^f is the Smagorinsky coefficient. A constant Smagorinsky coefficient was first used for homogeneous isotropic turbulent flows, and $C_s^f \approx (0.23)^2$ was first deduced by Lilly (1967) by matching the known value of Kolmogorov's universal constant for the inertial subrange. However, it did not work particularly well in complex turbulent flows, Deardorff

(1970) argued that the value C_s^f should be reduced to about $(0.1)^2$ as it's too dissipative. Siegel & Domaradzki (1994) investigated different turbulent flow, and the value of C_s^f varied from $(0.13)^2$ to $(0.24)^2$. To avoid the variation and flow dependency of C_s^f, a dynamic Smagroinsky model (Germano et al. 1991) is adopted in this study, where the Smagorinsky coefficient C_s^f is determined dynamically.

The dynamic Smagorinsky model involves two levels of filtering, and it assumes that the residual stress at these two levels are similar, and the Smagorinsky coefficient is determined to minimize the differences. The first level is the grid level, in which the filter size is usually the grid size. By solving the filtered Eulerian two-phase equations, this level of filtering is implicitly performed, and the residual stress at this level is:

$$\hat{\tau}_{ij}^{f,sgs} = \widehat{u_i^f u_j^f} - \hat{u}_i^f \hat{u}_j^f \tag{6.14}$$

The second filter level is the test filter, which is typically twice the grid size $\tilde{\Delta} = 2\Delta$, and '$\widetilde{\ }$' denotes the test filtering operation. This procedure is done explicitly as:

$$\widetilde{f}(\mathbf{x}, t) = \int f(\mathbf{x} - \mathbf{r}, t) G(|\mathbf{r}|; \widetilde{\Delta}) d\mathbf{r}, \tag{6.15}$$

where $G(|\mathbf{r}|; \widetilde{\Delta})$ is the filter function with a filter width $\widetilde{\Delta}$ at position $\mathbf{r}$. In this study, we used a box filtering, $G(|\mathbf{r}|; \widetilde{\Delta}) = H(\widetilde{\Delta}/2 - |\mathbf{r}|)/\widetilde{\Delta}$, where $H(\widetilde{\Delta}/2 - |\mathbf{r}|)$ is the heaviside (step) function:

$$H(\widetilde{\Delta}/2 - |\mathbf{r}|) = \begin{cases} 1, & \widetilde{\Delta}/2 - |\mathbf{r}| \geq 0 \\ 0, & \widetilde{\Delta}/2 - |\mathbf{r}| < 0 \end{cases} \tag{6.16}$$

The residual stress due to the test filtering on the grid filtered velocities is:

$$T_{ij} = \widetilde{\widehat{u_i^f u_j^f}} - \widetilde{\hat{u}_i^f} \widetilde{\hat{u}_j^f} \tag{6.17}$$

If we further apply the test filtering to equation 6.14, and Leonard identity can be defined as the difference between the test filtered equation 6.14 and residual stress due

to test filtering (equation 6.17):

$$L_{ij} = T_{ij} - \widetilde{\hat{\tau}_{ij}^{f,sgs}} = \widetilde{\hat{u}_i^f \hat{u}_j^f} - \widetilde{\hat{u}_i^f}\widetilde{\hat{u}_j^f}, \tag{6.18}$$

If we assume a uniform Smagorinsky coefficient can be used in both grid filtering level and test filtering level, we have that $T_{ij} = 2C_s^f \widetilde{\Delta}^2 |\widetilde{\widehat{S}^f}| \widetilde{\widehat{S}_{ij}^f}$, and the modeled identity (denoted as L_{ij}^m) can be expressed as:

$$L_{ij}^m = 2C_s^f \widetilde{\Delta}^2 |\widetilde{\widehat{S}^f}| \widetilde{\widehat{S}_{ij}^f} - 2C_s^f \Delta^2 |\widehat{S}^f| \widehat{S}_{ij}^f, \tag{6.19}$$

Thus the Smagorinsky coefficient C_s^f can be determined by $L_{ij} = L_{ij}^m$, and the mean square error is minimized by:

$$C_s^f = \frac{< L_{ij} L_{ij}^d >}{< L_{ij}^d L_{ij}^d >} \tag{6.20}$$

where $L_{ij}^d = 2\widetilde{\Delta}^2 |\widetilde{\widehat{S}^f}| \widetilde{\widehat{S}_{ij}^f} - 2\Delta^2 |\widehat{S}^f| \widehat{S}_{ij}^f$, and '$<\quad>$' denotes the averaging over homogeneous directions. In this study, it is assumed that the flow is homogeneous in the horizontal direction, thus a plane-average procedure is performed.

6.2.4 Closures on particle stresses

As discussed in chapter 4, the particle stresses due to collisions and frictions can be modeled with kinetic theory for granular flow (Jenkins & Savage 1983, Ding & Gidaspow 1990) and quasi-static frictional model (Johnson & Jackson 1987), so that a full transport profile including the immobile bed can be resolved. We assume that particle stress can be expressed as a sum of collisional-kinetic component (super-script 'sc') and a frictional component (super-script 'sf'),

$$\hat{p}^s = \hat{p}^{sc} + \hat{p}^{sf}, \tag{6.21}$$

$$\hat{\tau}_{ij}^{s} = \hat{\tau}_{ij}^{sc} + \hat{\tau}_{ij}^{sf}. \tag{6.22}$$

The filtered collisional-kinetic stresses can be obtained from filtered granular temperature, and its transport equation can be derived by applying the Favre filtering operation to equation **??**:

$$\begin{aligned}\frac{3}{2}\Big[\frac{\partial \rho^s \hat{\phi}\hat{\Theta}}{\partial t} + \frac{\partial \rho^s \hat{\phi}\hat{u}_j^s\hat{\Theta}}{\partial x_j}\Big] = \; & -\big(-\hat{p}^{sc}\delta_{ij} + \hat{\tau}_{ij}^{sc}\big)\tfrac{\partial \hat{u}_i^s}{\partial x_j} - A_\Theta \\ & + \tfrac{\partial}{\partial x_j}\Big(\hat{\kappa}^{sc}\tfrac{\partial \hat{\Theta}}{\partial x_j}\Big) + \tfrac{\partial B_j}{\partial x_j} \\ & - \tfrac{3}{2}\rho^s \tfrac{\partial C_j}{\partial x_j} - \hat{\gamma}_s + \hat{J}_{int},\end{aligned} \tag{6.23}$$

where, $\hat{p}^{sc}$ is the kinetic/collisional part of the particle pressure (Lun et al. 1984),

$$\hat{p}^{sc} = \rho^s \hat{\phi}[1 + 2(1+e)\hat{\phi} g_{s0}]\hat{\Theta}, \tag{6.24}$$

and g_{s0} is the radial distribution function to describe how the binary collision frequencies increase with sediment concentration $\hat{\phi}$ (Carnahan & Starling 1969),

$$g_{s0} = \frac{2 - \hat{\phi}}{2(1-\hat{\phi})^3}. \tag{6.25}$$

The kinetic/collisional part of the particle shear stress is given by Gidaspow (1994),

$$\hat{\tau}_{ij}^{sc} = \hat{\mu}^{sc}\Big[\frac{\partial \hat{u}_i^s}{\partial x_j} + \frac{\partial \hat{u}_j^s}{\partial x_i}\Big] + \big(\hat{\lambda} - \frac{2}{3}\hat{\mu}^{sc}\big)\frac{\partial \hat{u}_k^s}{\partial x_k}\delta_{ij}. \tag{6.26}$$

where the particle viscosity $\hat{\mu}^{sc}$ is calculated as,

$$\hat{\mu}^{sc} = \rho^s d\sqrt{\hat{\Theta}}\Big[\frac{4}{5}\frac{\hat{\phi}^2 g_{s0}(1+e)}{\sqrt{\pi}} + \frac{\sqrt{\pi} g_{s0}(1+e)(3e-1)\hat{\phi}^2}{15(3-e)} + \frac{\sqrt{\pi}\hat{\phi}}{6(3-e)}\Big]. \tag{6.27}$$

The bulk viscosity $\hat{\lambda}$ can be written as,

$$\hat{\lambda} = \frac{4}{3}\hat{\phi}^2\rho^s d g_{s0}(1+e)\sqrt{\frac{\hat{\Theta}}{\pi}}. \tag{6.28}$$

The diffusion of the granular temperature is assumed to be analogous to the Fourier's law of conduction, and the conductivity $\hat{\kappa}^{sc}$ is determined by,

$$\hat{\kappa}^{sc} = \rho^s d\sqrt{\hat{\Theta}}\Big[\frac{2\hat{\phi}^2 g_{s0}(1+e)}{\sqrt{\pi}} + \frac{9\sqrt{\pi}g_{s0}(1+e)^2(2e-1)\phi^2}{2(49-33e)} + \frac{5\sqrt{\pi}\hat{\phi}}{2(49-33e)}\Big]. \tag{6.29}$$

The dissipation rate due to inelastic collision is calculated based on that proposed by Ding & Gidaspow (1990),

$$\hat{\gamma}_s = 3(1-e^2)\hat{\phi}^2\rho^s g_{s0}\hat{\Theta}\Big[\frac{4}{d}\Big(\frac{\hat{\Theta}}{\pi}\Big)^{1/2} - \frac{\partial \hat{u}_j^s}{\partial x_j}\Big]. \tag{6.30}$$

where $e = 0.8$ is the coefficient of restitution during collision. The last term is fluid-sediment interaction term $J_{int} = \hat{\phi}\beta(\widehat{u_i^{fp}u_i^{sp}} - 3\hat{\Theta})$, where u_i^{fp} and u_i^{sp} are unresolved fluid velocity fluctuations and unresolved sediment motion. Due to the difficulties of estimating the sub-grid velocity fluctuations and the correlation between two phases, the term $\widehat{u_i^{fp}u_i^{sp}}$ is neglected. This assumption is valid when the particle response time is sufficiently larger than the characteristic flow time scale. The terms A_Θ, B_j and C_j are resulted from the filtering of production term (first term on the R.H.S.), diffusion term (third term on R.H.S.) and advection term (second term on the L.H.S.):

$$A_\Theta = \overline{\big(-p^{sc}\delta_{ij} + \tau_{ij}^{sc}\big)\frac{\partial u_i^s}{\partial x_j}} - \big(-\hat{p}^{sc}\delta_{ij} + \hat{\tau}_{ij}^{sc}\big)\frac{\partial \hat{u}_i^s}{\partial x_j}, \tag{6.31}$$

$$B_j = \widehat{\kappa^{sc}\frac{\partial \Theta}{\partial x_j}} - \hat{\kappa}^{sc}\frac{\partial \hat{\Theta}}{\partial x_j}, \tag{6.32}$$

$$C_j = \widehat{\phi\Theta u_j^s} - \hat{\phi}\hat{\Theta}\hat{u}_j^s \approx \hat{\phi}(\widehat{\Theta u_j^s} - \hat{\Theta}\hat{u}_j^s), \tag{6.33}$$

It is assumed that the resolved particle motion contributed most to the granular temperature, and the sub-grid contribution can negligible for fine grid resolutions (Ozel et al. 2013), and hence the unresolved terms such as A_Θ, B_j and C_j are not included in the filter granular temperature transport equation. However, the effect of these sub-grid terms may need future investigations.

When the volumetric concentration of particles becomes close to random loose packing, particles are constantly in contact with each other, and frictional stress model need to be adopted. In the present model, we adopt the simple model of Johnson & Jackson (1987) for particle pressure:

$$\hat{p}^{sf} = \begin{cases} 0, \phi < \phi_f \\ F\frac{(\hat{\phi}-\phi_f)^m}{(\phi_{max}-\hat{\phi})^n}, \hat{\phi} \geq \phi_f, \end{cases} \tag{6.34}$$

where $F = 0.05$, $m = 3$ and $n = 5$ are empirical coefficients. ϕ_{max} is the maximum sediment concentration in the bed, and ϕ_f is the concentration where particle friction start to be important. Both ϕ_f and ϕ_{max} may depend on the particle properties such as shape and size distribution. The particle stress due to frictional contact is calculated by the model of Srivastava & Sundaresan (2003),

$$\hat{\tau}_{ij}^{sf} = -2\hat{\mu}^{sf}\hat{S}_{ij}^s, \tag{6.35}$$

where $\hat{\mu}^{sf}$ is the frictional viscosity and $\hat{S}_{ij}^s$ is the deviatoric part of strain rate tensor of sediment phase,

$$\hat{S}_{ij}^s = \frac{1}{2}\Big(\frac{\partial \hat{u}_i^s}{\partial x_j} + \frac{\partial \hat{u}_j^s}{\partial x_i}\Big) - \frac{1}{3}\frac{\partial \hat{u}_k^s}{\partial x_k}\delta_{ij}. \tag{6.36}$$

d_p (mm)	ρ^s (kg/m^3)	ρ^f (kg/m^3)	w_s (cm/s)	θ_f (deg)	$u_\star$ (cm/s)	ν^f (m^2/s)
3	1192	1000	5.59	35	5.0	10^{-6}

Table 6.1: The steady sheet flow experiment conditions in Revil-Baudard et al. (2015)

where the friction viscosity to be calculated by Srivastava & Sundaresan (2003),

$$\hat{\mu}^{sf} = \frac{\sqrt{2}p^{sf}\sin(\theta_f)}{2\sqrt{S^s_{ij}\cdot S^s_{ij}}}, \tag{6.37}$$

where θ_f is the angle of repose. In sediment transport, the quasi-static component of particle pressure and particle stress play a definite role to ensure the existence of an immobile sediment bed and a low mobility layer of enduring contact (Hsu et al. 2004).

6.3 Model Validation—Steady Sheet Flow

In this section, a detailed model validation with a comprehensive dataset of coarse light sediment transport in uniform and steady sheet flow experiments (Revil-Baudard et al. 2015) is presented. The flow condition and sediment properties are listed in Table 6.1. The sediments are irregularly shaped particles with particle density $\rho^s = 1192$ kg/m^3, and the grain diameters are narrowly distributed within the range of $d = 2.5 - 3.5$ mm, and the measured mean settling velocity is $w_s = 5.59$ cm/s. It is noticed that the drag model (see equation (6.6) and (6.7)) assumes spherical shape particles, which is not consistent with the experiment condition. To match the settling velocity with the experiment, which is important for sediment transport, we introduce an shape factor of 0.5 in the drag model to take account of the non-sphericity. However, we retain the same original grain size d in the particle stress models (see section 6.2.4) to maintain the same particle inertia. In the rest of this chapter, we will take the liberty of dropping '$\widehat{\ }$' whenever there is no ambiguity.

Table 6.2: Numerical parameters for steady sheet flow experiments in Revil-Baudard et al. (2015)

u_* (cm/s)	d (mm)	d_e (mm)	L_x (m)	L_y (m)	L_z (m)	z_d (m)	z_b (m)	Δ_x (mm)	Δ_y (mm)	Δ_{zmin} (mm)	Δ_{zmax} (mm)
5	3	1.5	0.844	0.422	0.175	0.044	0.041	6.6	6.6	0.4	2.2

6.3.1 Computational domain and its discretization

To carry out a similar numerical simulation as the experiment of Revil-Baudard et al. (2015), the computational domain and coordinate system is designed as shown in figure 6.1, and the numerical parameters are listed in table 6.2. The wall boundaries are applied at the bottom boundary, and a symmetry boundary is applied on the top boundary to save computational costs. The flow is fully turbulent with a high bulk Reynolds number $Re = Uh/\nu^f = 8.8 \times 10^4$, where U is the bulk velocity and h is the flow depth. It is assumed that the flow is homogenous in the streamwise (x) and spawns (y) directions, thus periodic boundary conditions are justified if the domain in the homogeneous directions are large enough to include the largest eddies in the flow. In this study, the flow depth is $h_0 = 0.131$ m, the initial bed elevation is $z_d = 0.044$ m. At final steady state, the bed is eroded, and the immobile bed is located at $z_b = 0.041$ m, while the flow depth becomes $h = 0.134$ m. The domain size is adjusted to be $L_x = 2\pi h, L_y = \pi h$ to ensure that the velocity fluctuations are uncorrelated at a separation of one half-period in the homogeneous directions. This choice is justified by examining the two-point correlations. The normalized autocorrelation coefficients for velocity fluctuations (three components) in streamwise (panel a) and spanwise (panel b) directions are shown in figure 6.2. The plane for the two-point correlation analysis is chosen to be at $(z - z_b)/d = 12.5$, where sediment concentration is small (see figure 6.4b). We can see that the correlation coefficients drops from 1 at zero separation to nearly zero when the separation is larger than half of domain size, i.e., $\delta_x/L_x > 0.5$ and $\delta_y/L_y > 0.5$.

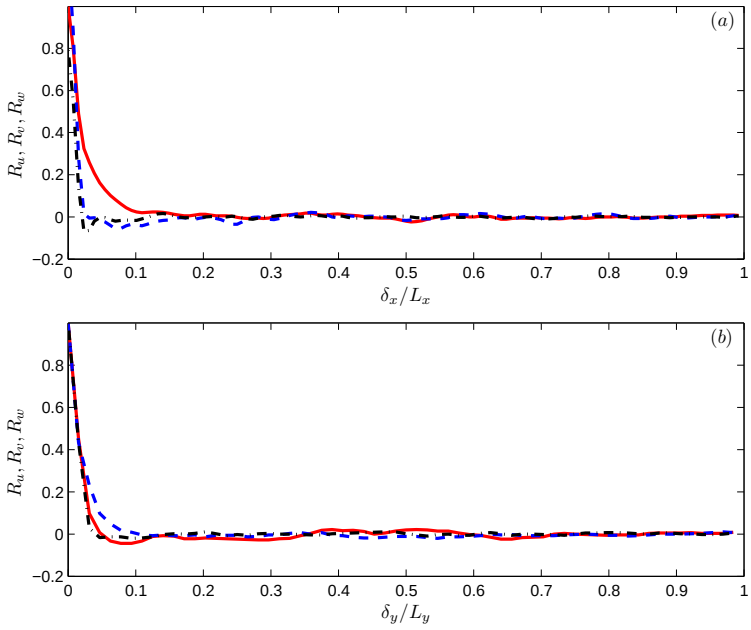

Figure 6.2: Normalized autocorrelation of streamwise (solid curve), spanwise (dash-dot curve) and vertical (dashed curve) velocity components in streamwise (panel (a)) and spanwise (panel (b)) directions

The domain is discretized into 1826816 grid points ($128 \times 64 \times 223$ in x, y, z directions), where uniform grid size $\Delta_x = \Delta_y \approx 6.6$ mm is used in streamwise and spanwise directions. Nonuniform grid resolution is used in the vertical direction, where a total of 100 uniform grid size $\Delta_{zmin} = 0.4$ mm is used around the bed elevation ($0.04 < z < 0.08$ m), and the grid is stretched to a maximum value of $\Delta_{zmax} = 2.2$ mm at the top of the domain. We confirmed that this grid resolution is able to resolve sufficient turbulent kinetic energy. To demonstrate this, the turbulent energy spectrum for each velocity components in the streamwise and spanwise directions are shown in figure 6.3. We can see that a slope of $-5/3$ is resolved in both streamwise and spanwise directions, and about two orders of magnitude of turbulent kinetic energy is resolved. However, less than one order of magnitude of turbulent energy is contained in the range of slope $-5/3$. It is noticed that the $-5/3$ was based on Kolmogorov's theory for isotropic turbulence in high Reynolds number turbulent flow in single phase fluid. A few differences between single phase flow and two-phase flow may alter the slope in

the energy spectrum. Firstly, the existence of sediment can affect the flow turbulence, and the energy transfer between sediment phase and fluid phase can change the fluid turbulence energy dissipation mechanism (see section 6.3.3). Secondly, The Favre-filtered velocity can not be straightforwardly identical to the physical velocities, thus the velocity fluctuation is difficult to link with physical turbulence. In the two-phase flows, the fluid phase and sediment phase is similar to slightly compressible flows. Galtier & Banerjee (2011) found that for isotropic fully turbulent compressible flow, the density weighted velocity ($(1-\phi)^{1/3}u_i^f$) shall follow $-5/3$ in the energy spectrum, while velocity fluctuation alone may not.

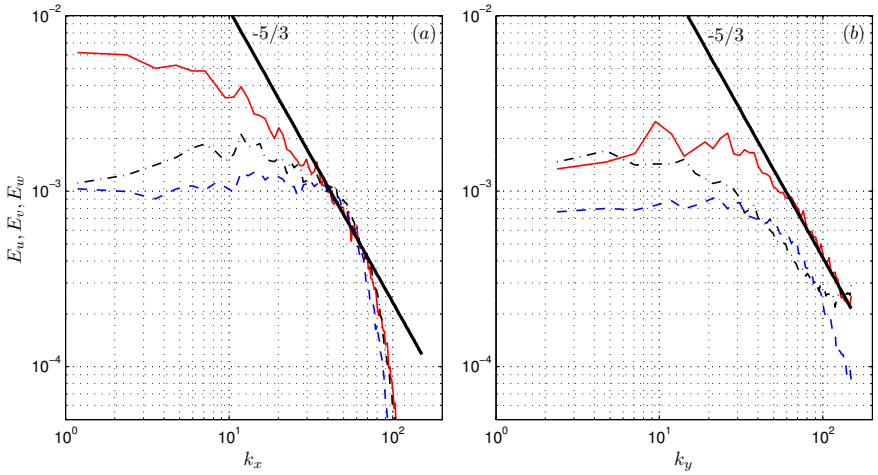

Figure 6.3: Energy spectrum of streamwise (solid curve), spanwise (dash-dot curve) and vertical (dashed curve) velocity fluctuation components in streamwise (panel (a)) and spanwise (panel (b)) directions; In both panel (a) and (b), the thick curve denotes a slope of $-5/3$

6.3.2 Mean quantities

Firstly, the model is validated with experimental result of Revil-Baudard et al. (2015) by the ensemble averaged (denoted as overbar '$\overline{\ }$') flow statistics such as the streamwise velocities, sediment concentration, root-mean-square of velocity fluctuations and Reynolds shear stress (figure 6.4). For the streamwise velocity (figure 6.4a),

the model predicts a similar linear streamwise velocity profile as the experimental result near the bed ($0 < (z - z_b)/d < 6$). In this range, the numerical prediction of the sediment concentration matches with the experimental data reasonably well (see figure 6.4b). The sediment concentration is larger than 0.08, and particle-particle collisions are important, thus the particle stresses due to collisions are properly resolved in this range. However, the model under-predicts the fluid velocity magnitude away from the sediment bed ($(z - z_b)/d > 6$), and the discrepancy increases from $(z - z_b)/d = 6$ to $(z - z_b)/d = 10$, where intense turbulence-sediment interactions occurs. Meanwhile, the predicted sediment concentration away from the bed is also smaller than the measured data. Further improvement of the sediment suspension and streamwise velocity in the dilute part may requires other sub-grid effects such as unresolved granular temperatures (see equation 6.23). Figure 6.4c shows the comparison of root-mean-square of streamwise and vertical velocity fluctuations. Overall, our model predicts similar velocity fluctuation intensities in both streamwise and vertical directions, and both measured data and numerical results indicate that the flow is anisotropic. It shall be noted that the significant overshoot of streamwise velocity fluctuations may be related to the bed variations in the streamwise direction, which will be discussed later in this paper. However, the model seems to over-predict the vertical velocity fluctuations in the dilute transport layer ($(z-z_b)/d > 5$), while under-estimate the streamwise velocity fluctuations in this layer. The Reynolds shear stress comparison is presented in figure 6.4d, which shows a good agreement with the experiment data. It is well-known that the Reynolds shear stress follows a linear distribution in the boundary layer, which is confirmed in our numerical model ($(z - z_b)/d > 5$). By matching the Reynolds shear stress distribution, we confirm that the bottom shear stress, which plays a key role in sediment transport, is consistent with the experiment condition.

A number of sediment-laden experiments have shown that the von Karman constant or the mixing length is reduced by the suspended sediment (e.g., Vanoni 1946, Wright & Parker 2004, Muste et al. 2005, Revil-Baudard et al. 2015). It has been shown that in the sheet flow sediment transport, the velocity profile in the overlapping

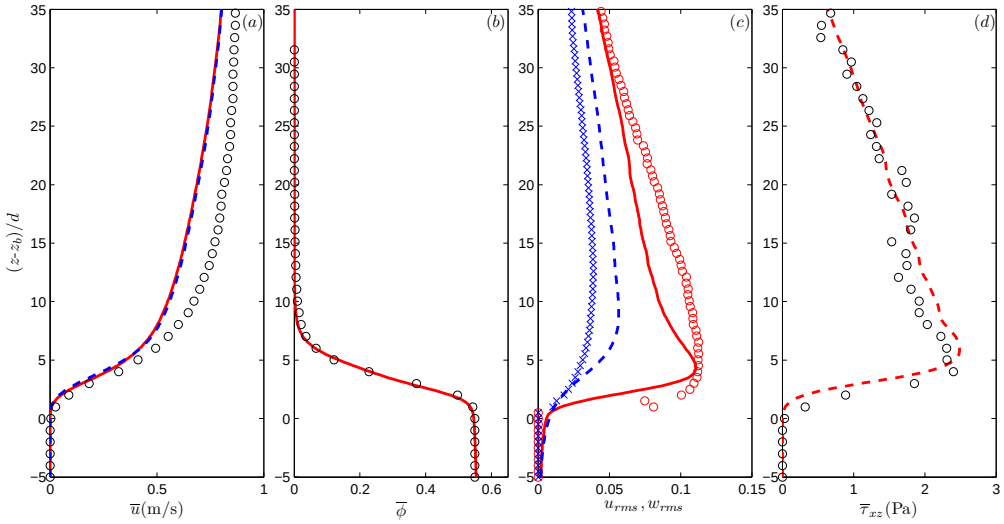

Figure 6.4: The comparison of numerical results (curves) and experiment results (symbols) of (a) Streamwise velocity (fluid velocity: solid curve, and particle velocity: dashed curve), (b) Sediment concentration, (c) Root-mean-square of velocity fluctuations and (d) Reynolds shear stress. In panel (c), cross and circle symbols denote the experiment results of the vertical and streamwise components of velocity fluctuation, while dashed curve and solid curves denote the numerical result of the vertical and streamwise components of velocity fluctuation

layer between outer layer (velocity profile scales with flow depth) and inner layer (velocity profile scales with roughness length scale) follows the logarithmic law, which the relevant local length scale is the wall distance:

$$\overline{u}^f = \frac{u_\star}{\kappa} ln\left(\frac{z - z_0}{z_{ks}}\right), \tag{6.38}$$

where $u_\star$ is the friction velocity, obtained from the linear extrapolation of Reynolds shear stress at the bed. The von Karman constant κ is universally 0.41 for clear fluid. The fitted logarithmic (using equation 6.38) profile of numerical result and experiment data are compared in figure 6.5. It is evident that the logarithmic law fits the velocity well in the range of $(z - z_b)/d > 8$ for the numerical result (solid curve), and the fitted the von Karman constant κ is about 0.25 (dashed curve), which is close to the

experimental result ($\kappa = 0.23$). Notice that the value of von Karman constant for the sheet flow sediment transport is significantly smaller than the clear fluid value (0.41), which is indicated as dash-dot curve in figure 6.5.

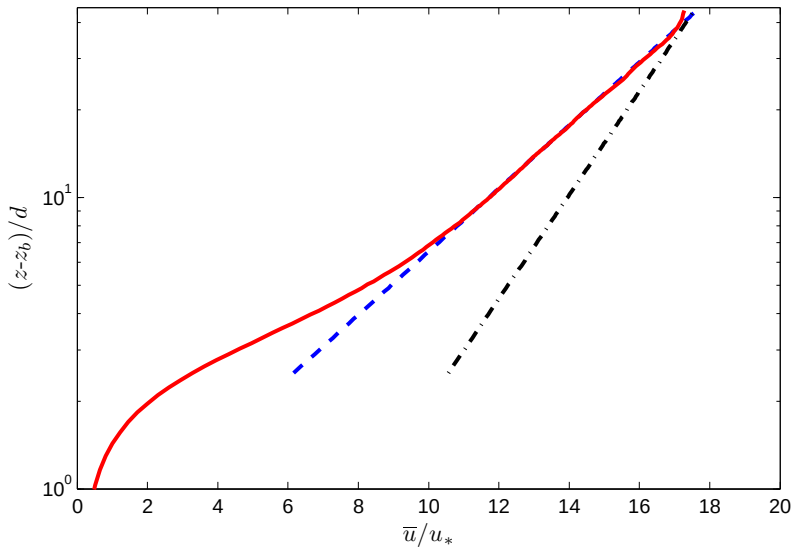

Figure 6.5: The model result (red-solid curve) of streamwise velocity profile in semi-logarithmic scale, the blue-dashed curve shows the fit with von Karman constant $\kappa = 0.25$, and the black-dashed-dot curve shows the slope of $\kappa = 0.41$ as in clear fluid.

The mixing length l_m is a characteristic length scale for the momentum transfer, and it can be evaluated by $l_m = u_\star/|\partial\overline{u}^f/\partial z|$ following the analysis of Revil-Baudard et al. (2015) (see figure 6.7). Overall, the model predicts a similar mixing length as the experimental result. Meanwhile, we can derive from the equation 6.38 that the mixing length can be written as: $l_m = \kappa(z - z_0)$ in the log-law region. The fitted curve (dash-dot for experiment result and dashed curve for model result) agrees well with the mixing length distribution ($\kappa = 0.25$). We can observe that above the bed $(z - z_b) > 0$, the mixing length can be well scaled by the grain size, and the minimum mixing length is about $d/2$. This indicates that the mean eddy sizes are limited by the grain size ($l_m > d/2$), which justifies our numerical resolution to be close to the grain size.

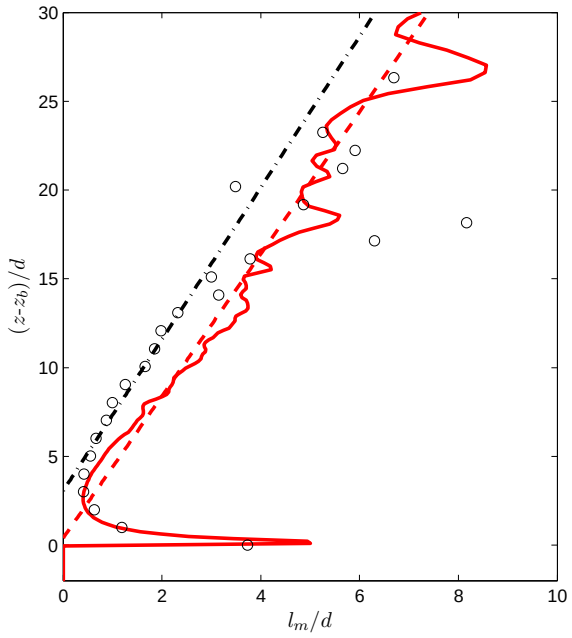

Figure 6.6: The comparison of the mixing lengths from numerical result (solid curve) and experimental results (symbols). The dashed curve is the linear fit of the mixing length for numerical result with $\kappa = 0.25$, and the dashed-dot curve shows the linear fit of measured data with $\kappa = 0.23$.

In many Reynolds-averaged models of sediment transport (e.g., Hsu et al. 2004, Revil-Baudard & Chauchat 2013, Cheng et al. 2016), the gradient transport assumptions are often adopted:

$$\overline{w^{s'}\phi'} = -\sigma_p \frac{\partial \overline{\phi}}{\partial z}, \tag{6.39}$$

where σ_p is the sediment diffusivity, which is often parameterized by the turbulent eddy viscosity, or vertical momentum diffusivity σ_m with $\sigma_p = \sigma_m/Sc$. In many sediment transport models (e.g., Hsu et al. 2003, Chen et al. 2011, Cheng et al. 2016), a constant Schmidt number is usually assumed. Amoudry et al. (2005) investigated the dependency of Schmidt number on the sediment concentration, and an improved prediction of sediment suspension was obtained by varying Schmidt number as a function of sediment concentration. It is worthwhile to evaluate this assumption by using our turbulence-resolving two-phase model. The turbulent eddy viscosity can be written as:

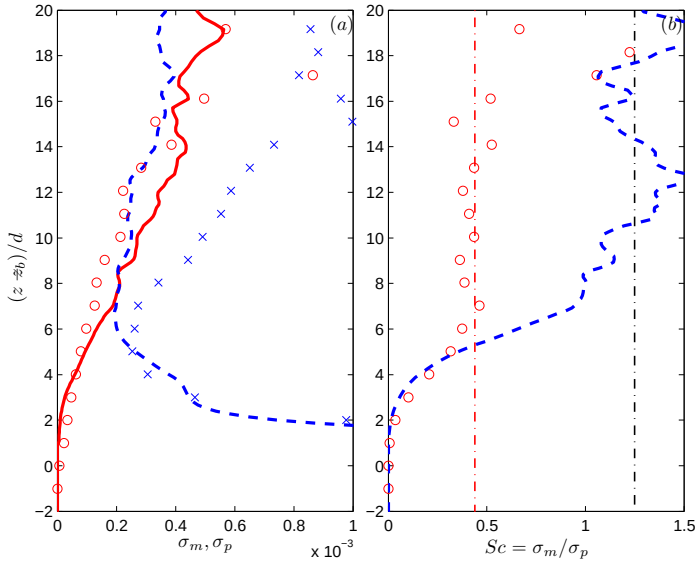

Figure 6.7: The vertical structure (panel a) of turbulent eddy viscosity (mode result: solid curve, experiment data: circle symbols) and sediment diffusivity (mode result: dashed curve, experiment data: cross symbols); The corresponding vertical structure of Schmidt number ($Sc = \sigma_m/\sigma_p$) is plotted in panel b, model result: dashed curve; experiment data: circle symbols, and the dash-dot curve shows the mean level of Schmidt number.

$$\sigma_m = \frac{-\overline{u^{f\prime} w^{f\prime}}}{\partial \overline{u}^f / \partial z}, \tag{6.40}$$

The sediment diffusivity can be evaluated alternatively using $\sigma_p = -w_s\overline{\phi}/(\partial\overline{\phi}/\partial z)$. The vertical structure of the sediment diffusivity and turbulent eddy viscosity are shown in figure 6.7(a). It is evident that the turbulent eddy viscosity agrees well with the experiment result in the range of $(z - z_b)/d < 14$. Meanwhile, our numerical model significantly under-predicted the sediment diffusivity above $(z - z_b)/d > 6$, which is consistent with the underestimation of suspended sediments. As a result, the proposed model over-predict the Schmidt number significantly from $(z - z_b)/d > 6$. However, it shall be noted that the comparison of numerical result and experiment result agree well below $(z - z_b)/d > 6$. In addition, we noticed that the Schmidt number is more or less a constant when the sediment concentration $\phi < 0.08$ either from the experiment result

(0.44) or from the numerical result (1.25). Rijn (1984) suggested that the Schmidt number can vary from 0.3 to 1, however, the value may also depend on sediment properties (such as density and grain size).

6.3.3 Turbulent kinetic energy budget

It is well-established from laboratory observations that the existence of sediment can attenuate the flow turbulence (e.g., Vanoni 1946, Chien et al. 1955, Lamb et al. 2004). The most well-known mechanism for turbulence attenuation in sediment transport is attributed to the sediment-induced density stratification (e.g., Winterwerp 2001, Ozdemir et al. 2010). However, the fluid-sediment is coupled with momentum transfer forces, and the relationship between density stratification and the momentum transfer in a complete two-phase flow system remains unclear. To investigate the mechanisms of the sediment-induced damping on flow turbulence, specifically the turbulence attenuation due to the drag force, and its relative importance to the density stratification, the turbulent kinetic energy budget is first derived. The resolved turbulence can be quantified by the velocity fluctuation about the ensemble averaged velocity: $k^f = 1/2\overline{u_i^{f'} u_i^{f'}}$, where $u_i^{f'} = u_i^f - \overline{u}^f$. Based on the fluid momentum equation, the resolved turbulent kinetic energy (TKE) transport equation is derived:

$$
\begin{aligned}
\frac{\partial k^f}{\partial t} = & \underbrace{-\overline{u_i^{f'} u_j^{f'}} \frac{\partial \overline{u}_i^f}{\partial x_j}}_{\text{(I) production}} \underbrace{-\overline{(\nu^f + \nu_{sgs}^f)(\frac{\partial u_i^f}{\partial x_j} + \frac{\partial u_j^f}{\partial x_i}) \frac{\partial u_i^{f'}}{\partial x_j}}}_{\text{(II) viscous dissipation}} \\
& \underbrace{+\overline{\frac{\phi\beta[1 + K_i f(\Delta) h(\phi)]}{\rho^f (1-\phi)} (u_i^s - u_i^f) u_i^{f'}}}_{\text{(III) drag induced dissipation}} \\
& \underbrace{-\frac{1}{\rho^f} \overline{u_i^{f'} \frac{\partial p^{f'}}{\partial x_i}}}_{\text{(IV) pressure transport}} \underbrace{-\overline{u}_j^f \frac{\partial k^f}{\partial x_j}}_{\text{(V) mean advection}} \underbrace{-\frac{1}{2} \overline{u_j^{f'} \frac{\partial u_i^{f'} u_i^{f'}}{\partial x_j}}}_{\text{(VI) turbulent advection}} \\
& \underbrace{+\overline{\frac{1}{1-\phi} \frac{\partial}{\partial x_j} \left[(1-\phi)(\nu^f + \nu_{sgs}^f) u_i^{f'} (\frac{\partial u_i^f}{\partial x_j} + \frac{\partial u_j^f}{\partial x_i}) \right]}}_{\text{(VII) turbulence diffusion}}
\end{aligned}
\tag{6.41}
$$

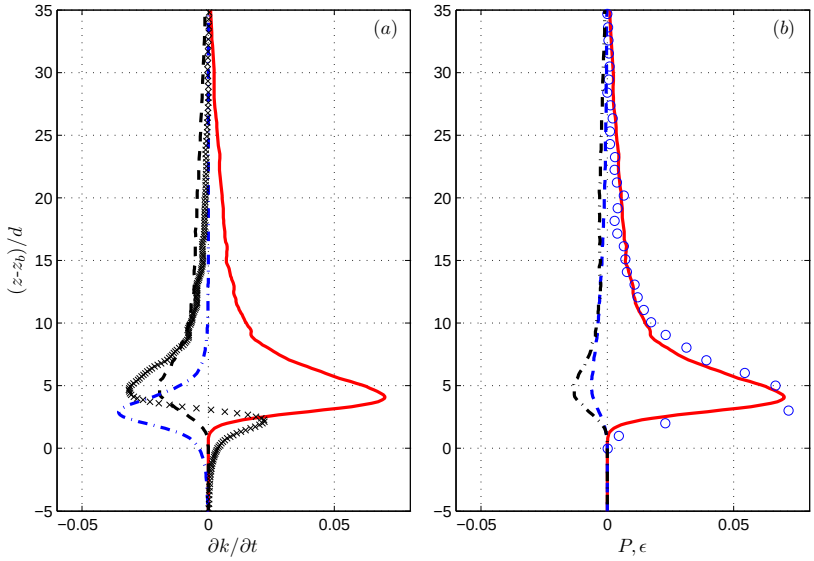

Figure 6.8: The panel (a) shows the TKE budget for fluid phase. The turbulent production (solid curve), viscous dissipation (dashed curve), drag-induced dissipation (dash-dot), total transport (cross symbols); The comparison of production (numerical result: solid curve; experimental data: symbols) and energy dissipation (resolved dissipation: dashed curve; modeled dissipation: dash-dot curve) are shown in panel (b).

where, the term on the L.H.S. is the time derivative of the resolved turbulent kinetic energy. The seven terms on the R.H.S. of equation 6.41 are (I) turbulence production, (II) viscous dissipation, (III) drag-induced dissipation, (IV) pressure transport, (V) advection due to mean flow, (VI) turbulent advection and (VII) turbulence diffusion. For convenience of discussion, the last four terms, namely pressure transport, advection due to mean flow, turbulent advection and turbulence diffusion are collectively called total transport. When the flow reaches steady state, the terms on the R.H.S. should be balanced so that $\partial k/\partial t = 0$.

The TKE budget are plotted in figure 6.8(a). The turbulent production is a positive source term for the turbulent kinetic energy, and it increases from the sediment bed and reaches its peak at about $(z - z_b)/d = 4.5$, and then drops in the upper water column to match with the turbulent production. Correspondingly, the turbulent dissipation is always negative, and serves as a sink of turbulent kinetic energy. The

turbulent dissipation reaches its peak at about $(z - z_b)/d = 5.5$, and its magnitude also drops in the upper water column. In the upper column ($(z - z_b)/d > 8$), the total energy dissipation nearly balances the turbulent production, and other terms are negligible. On the other hand, in the lower water column ($(z - z_b)/d < 5$), the magnitude of viscous dissipation drops significantly. More importantly, the turbulent interactions term due to drag prevails the viscous dissipation term, and balances the turbulence production and total transport.

Furthermore, we compared the resolved and modeled energy dissipation (see figure 6.8b), which is defined as:

$$\epsilon = -\nu\overline{(\frac{\partial u_i^f}{\partial x_j} + \frac{\partial u_j^f}{\partial x_i})\frac{\partial u_i^{f'}}{\partial x_j}}, \tag{6.42}$$

and the modeled viscous dissipation is calculated as:

$$\epsilon_{sgs} = -\overline{\nu_{sgs}^f(\frac{\partial u_i^f}{\partial x_j} + \frac{\partial u_j^f}{\partial x_i})\frac{\partial u_i^{f'}}{\partial x_j}}. \tag{6.43}$$

We can see that overall the modeled energy dissipation is larger than (about 2 times of) the resolved dissipation, which is expected for a large-eddy simulation. However, their magnitudes are significantly smaller than the turbulent energy production. It is expected that other mechanisms of turbulent attenuation must exist, such as density stratification and drag-induced turbulence damping. The density stratification has been identified by many earlier works as an important turbulence damping mechanisms induced by the sediments. Its damping effect on the fluid turbulence can be quantified by the gradient Richardson number or the flux Richardson number. The flux Richardson number is defined as the ratio of turbulence dissipation caused by the density stratification to the turbulence production:

$$Ri_f = \frac{(s-1)g\overline{\frac{\partial \phi'}{\partial z}}}{-\overline{u^{f'}w^{f'}}\frac{\partial \overline{u}^f}{\partial z}}, \tag{6.44}$$

Alternatively, the flux Richardson number can be estimated using the gradient transport assumption, and thus it becomes the gradient Richardson number:

$$Ri_g = -\frac{(s-1)g\frac{\partial\overline{\phi}}{\partial z}}{|\frac{\partial\overline{u}}{\partial z}|^2}, \tag{6.45}$$

The numerical results of flux Richardson number (dashed curve) and gradient Richardson number (dash-dot curve) are compared with the experimental result of the gradient Richardson number (symbols) in figure 6.9. We can see that the model result is very similar to the experimental data in the suspension layer $(z - z_b)/d > 5$, and the magnitude is relatively small (< 0.1). The gradient Richardson is also similar to the flux Richardson number, which confirmed that they are equivalent indicator of density stratification effect. On the other hand, following the similar idea, we can introduce an non-dimensional number E_d to quantify the drag-induced damping effect, which can be defined as the ratio of turbulent interactions to turbulent production:

$$E_d = \frac{\overline{\frac{\phi\beta[1+K_i f(\Delta)h(\phi)]}{\rho^f(1-\phi)}(u_i^s - u_i^f)u_i^{f'}}}{-\overline{u^{f'}w^{f'}}\frac{\partial\overline{u}^f}{\partial z}}, \tag{6.46}$$

The profile of E_d is also plotted in figure 6.9. We can see that, in the dilute transport layer ($(z - z_b)/d > 7$), the magnitude of E_d is very similar to the gradient Richardson number and flux Richardson number. However, in the denser layer ($(z - z_b)/d < 5$), E_d is much larger than than the Richardson numbers (either Ri_f or Ri_g). This indicates that in the denser (near bed) layer, the turbulence interactions due to drag dominates, and has a larger damping effect than the density stratification term on the turbulent kinetic energy.

6.3.4 Turbulence-sediment interactions

As discussed in the previous section, the existence of sediment has significant effect on flow turbulence. On the other hand, the turbulent flow motions also affect the sediment dynamics. The turbulence-sediment interactions have been studied by many

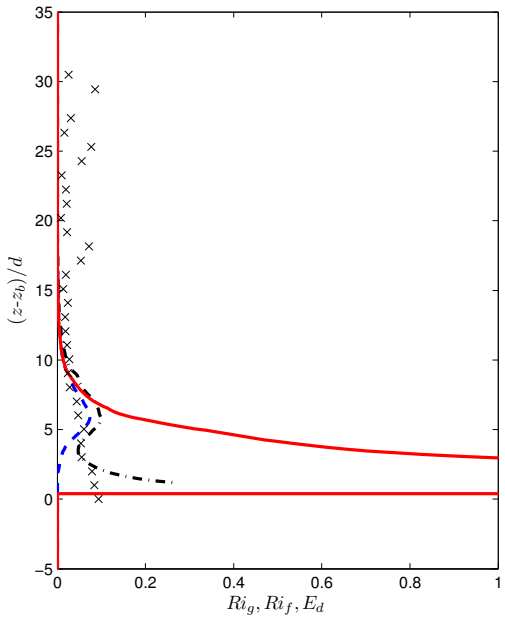

Figure 6.9: The comparison of density stratification effect (flux Richardson number: dashed curve; gradient Richardson number: dash-dot curve) and turbulence interactions (solid curve) due to drag. The gradient Richardson number obtained from the experiment is denoted as cross symbols.

laboratory experiments (e.g., Revil-Baudard et al. 2015) and turbulence-resolving numerical simulations (e.g., Wang & Maxey 1993, Schmeeckle 2014), and critical insights were obtained. In this chapter, we discuss major findings from the present turbulence-resolving Eulerian two-phase model.

To better illustrate the turbulence-sediment interactions, the fluid velocity fluctuations are classified into four quadrants (see figure 6.10): outward interactions (Q_1): $(u^{f'} > 0, w^{f'} > 0)$, ejections (Q_2): $(u^{f'} < 0, w^{f'} > 0)$, inward interactions (Q_3): $(u^{f'} < 0, w^{f'} < 0)$, sweeps (Q_4): $(u^{f'} > 0, w^{f'} < 0)$. It has been reported that the ejection events (Q_2) and sweeping events (Q_4) make the largest contribution to the Reynolds shear stress (Wallace 2016). Figure 6.11 shows the contribution of $(\overline{u^{f'}w^{f'}})_i/\overline{u^{f'}w^{f'}}$, where $i = 1, 2, 3, 4$ denotes the conditionally averaged correlations of $u^{f'}$ and $w^{f'}$ corresponding to the Q_{1-4} events. We define a conditionally averaged

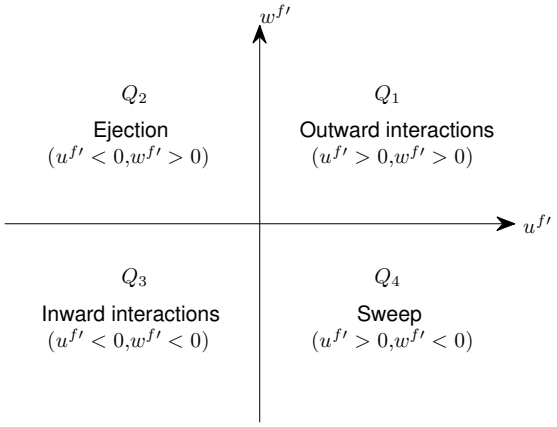

Figure 6.10: Diagram illustrating the quadrant analysis of turbulent motions: Q_1, outward interactions $(u^{f'} > 0, w^{f'} > 0)$; Q_2, ejection $(u^{f'} < 0, w^{f'} > 0)$; Q_3, inward interactions $(u^{f'} < 0, w^{f'} < 0)$; Q_4, sweep $(u^{f'} > 0, w^{f'} < 0)$

quantity $(\overline{A})_i$ under the condition of quadrant event Q_i:

$$(\overline{A})_i = \frac{\sum A dt, [Q_i]}{T_{total}}, \tag{6.47}$$

where $\sum A dt, [Q_i]$ only sums Adt when the event Q_i occurs, and $T_{total} = \sum dt$ is the total time for the temporal average. For steady flows, the ensemble average can be assumed to be identical to the temporal average, we have $\overline{A} = \sum_{i=1}^{4} (\overline{A})_i$. We can see that the Q_2 and Q_4 events contributes over 50% of the Reynolds shear stress (see figure 6.11a), and its magnitude is about 5 times of the contribution of Q_1 and Q_3 events (see figure 6.11b). This feature is similar to the clear fluid turbulent channel flow at low Reynolds number (Kim et al. 1987, Moser et al. 1999). However, the experimental result of (Revil-Baudard et al. 2016) shows that the mobile bed dynamics reduces the ratio $-(\overline{u^{f'} w^{f'}})_{2,4}/(\overline{u^{f'} w^{f'}})_{1,3}$ to about 2 (see figure 6.11b). Our model is unable to capture this reduction of $-(\overline{u^{f'} w^{f'}})_{2,4}/(\overline{u^{f'} w^{f'}})_{1,3}$, which may be due to the lack of proper closure for sediment effect on the sub-grid closure or incomplete description of interphase momentum transfer. Meanwhile, the ratio of ejection over sweeping

events are shown in figure 6.11c. We can see that in the near-bed region, the ejection contribution is slightly less than sweeping events, and the ratio increase nearly linearly further away from the bed. The crossing point of ratio $(\overline{u^{f\prime}w^{f\prime}})_2/(\overline{u^{f\prime}w^{f\prime}})_4 = 1$, locates at about $(z - z_b)/d = 18$, which is similar to the experimental result.

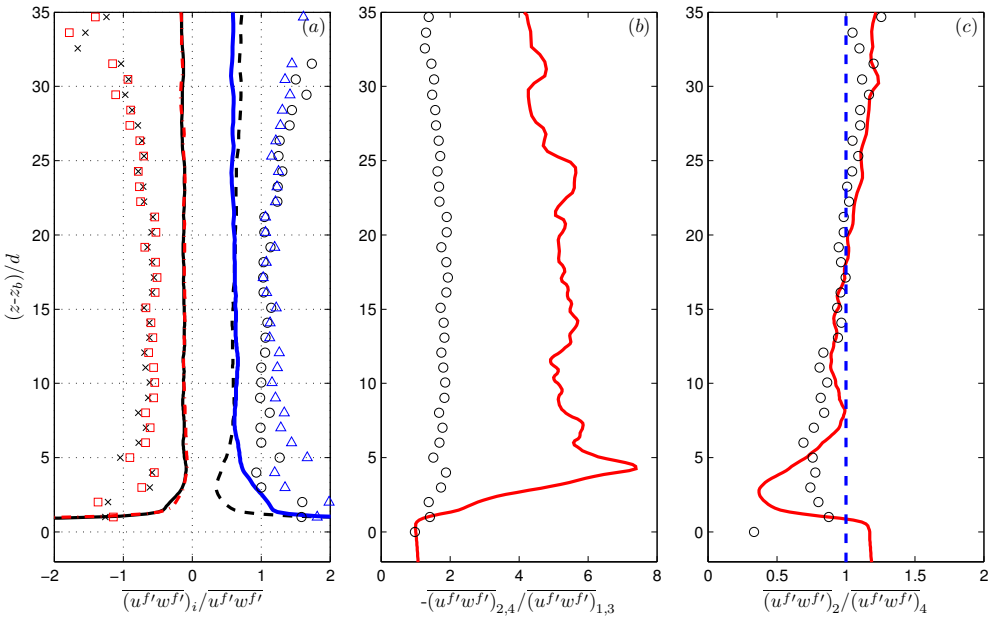

Figure 6.11: Panel (a) is the comparison of ratio $(\overline{u^{f\prime}w^{f\prime}})_i/\overline{u^{f\prime}w^{f\prime}}$ due to upward interactions ($i = 1$, numerical: thin solid curve; experiment: cross), ejection ($i = 2$, numerical: dashed curve; experiment: circles), downward interaction ($i = 3$, numerical: dash-dot curve; experiment: squares) and sweep events ($i = 4$, numerical: thick solid curve; experiment: triangles); The ratio of ejection/sweep contribution over interactions is shown in panel (b) and the ratio between ejection and sweep events is shown in panel (c), in both panel (b) and (c), the circle symbols denotes the measured data

Moreover, in order to further understand the effect of quadrant events on the erosion or deposition of sediment, the vertical sediment fluxes associated with each quadrant events are investigated in figure 6.12. The vertical flux due to turbulent suspension $(\overline{w^{s\prime}\phi^{\prime}})$ is shown in figure 6.12a, where an upward vertical flux is resulted from the turbulence-sediment interaction, and this upward turbulent flux will balance the downward settling flux $(\overline{w^s}\overline{\phi})$ at the steady state. As a result of this balance, the

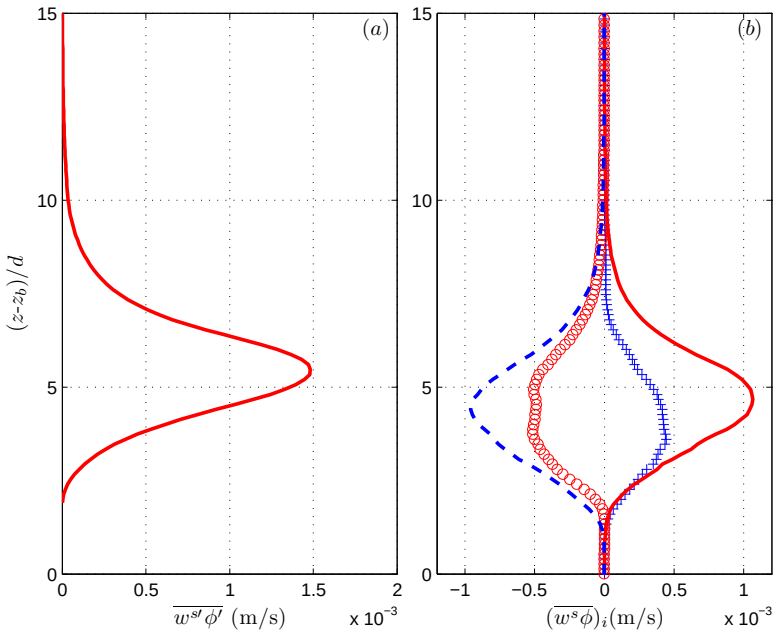

Figure 6.12: The panel (a) shows the sediment vertical turbulent flux ($\overline{w^{s\prime}\phi^{\prime}}$), which is positive in upward direction. Panel (b) shows the the contribution to the total vertical sediment flux ($(\overline{w^s\phi})_i$) due to upward interactions (1, '+'), ejection (2, solid curve), downward interaction (3, circles) and sweep events (4, dashed curve).

total sediment flux at each elevation will becomes zero. However, it is interesting to study the contributions of each quadrant event to the total vertical sediment flux, which is shown in figure 6.12b. It is evident that the contribution to the total vertical flux from the ejection is a upward, which may be responsible for the sediment erosion, while the sweep events cause a significant downward flux, which may result in the sediment deposition. The contribution of outward and inward interactions are less significant compared with ejection or sweep events.

As indicated above, the ejection and sweep events cause strong upward/downward sediment flux, which may further result in intermittent bed level evolution. As reported by Revil-Baudard et al. (2016), the bed intermittency is mainly caused by the turbulent ejection and sweep events. To better illustrate this relationship, a 2D contour of sediment concentration field is plotted against time and vertical elevation in figure

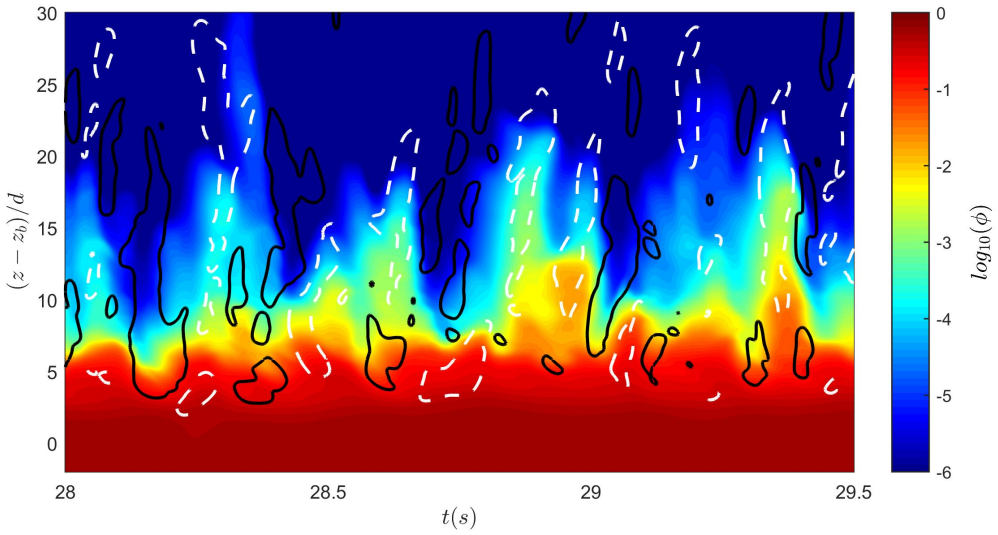

Figure 6.13: A 2D contour of sediment concentration field in terms of vertical elevation $(z - z_b)/d$ and time t (s). The sediment concentration is plotted in logarithmic scale, and the contours of ejection (dashed contour) and sweep (solid contours) events are also plotted. The contour level for the ejection and sweep are both chosen to be $-\overline{u^{f\prime}w^{f\prime}} = 0.001$.

6.13. We can see that there is a significant variation of bed elevation on the order of a few grain diameters. Such mobile bed effect can cause an enhanced bed roughness (Dohmen-Janssen et al. 2001). On top of the sediment concentration, the contours of ejection and sweep events are plotted. It is evident that the increase of bed level is coincident with the ejection events (white dashed contours), while the bed erosion is highly correlated with sweep events (black solid contours). However, the bed intermittency frequency is much higher than the experiment of Revil-Baudard et al. (2016). This frequent bed intermittency may explain the difference of our under-prediction of streamwise velocity profile.

6.4 Applications to Oscillatory Sheet Flow

In this section, we further apply the turbulence-resolving Eulerian two-phase model to idealized flow conditions in nearshore environments, namely, the oscillatory sheet flow. O'Donoghue & Wright (2004) measured sediment concentration of sheet

Case	U_m (m/s)	T (sec)	d (mm)	L_x (m)	L_y (m)	L_z (m)	z_b (m)	Δ_x (mm)	Δ_y (mm)	Δ_{zmin} (mm)	Δ_{zmax} (mm)
M512	1.5	5	0.28	0.2	0.1	0.18	0.05	1.04	1.04	0.45	2.66

Table 6.3: Numerical parameters for oscillatory sheet flow experiments in O'Donoghue & Wright (2004)

flow in an oscillating water tunnel with flow velocity and period similar to field conditions for three different sand grain sizes. In this study, we carried out numerical simulations of a medium sand under sinusoidal wave conditions reported in O'Donoghue & Wright (2004). As a preliminary turbulence-resolving investigation of sand transport in oscillatory sheet flow, the sub-grid contribution to the drag is modeled using a simpler closure than that discussed in section 6.2.2,

$$\widehat{\phi u_i^r} - \hat{\phi}\hat{u}_i^r = -\nu_{sgs}^f \frac{\partial \phi}{\partial x_i}, \tag{6.48}$$

This closure is essentially the gradient transport formulation, which is very similar to the turbulent suspension term in the turbulence-averaged models (Cheng et al. 2016). Firstly, a detailed validation are carried out for medium sand in section 6.4.2, and a numerical experiment for fine sand is presented in section 6.4.3.

6.4.1 Model setup

In the numerical simulations, the oscillatory flow is driven by a mean streamwise pressure gradient. Outside the wave boundary layer, the shear stress vanishes, and the momentum equation reduces to:

$$\frac{1}{\rho^f}\frac{\partial \overline{p}^f}{\partial x} = -\frac{\partial U_0}{\partial t}, \tag{6.49}$$

where U_0 is the free stream velocity. For sinusoidal wave, $U_0 = U_m sin(\omega t)$, U_m is the free-stream velocity magnitude, $\omega = 2\pi/T$ is the wave frequency, and T is the wave period. Relevant physical parameters are summarized in table 6.3.

The Stokes boundary layer thickness is $\delta = \sqrt{2\nu^f/\omega} = 1.26$ mm, and a similar 3D domain as the steady sheet flow is used (see figure 6.1). The domain size in streamwise and spanwise is chosen to be about 160δ and 80δ, respectively. In vertical direction, the bed depth z_b is about 40δ, and the water depth is about 100δ. This domain size is estimated to be sufficient to resolve the turbulent boundary layer. The domain is discretized into $N_x \times N_y \times N_z = 192 \times 96 \times 240$, and uniform grid sizes ($\Delta_x = \Delta_y = 1.04$ mm) are used in the streamwise and spanwise directions. In the vertical direction, nonuniform grids are used with high grid resolution ($\Delta_{zmin} = 0.45$ mm) near the initial bed level, and coarser grid resolution in the free-stream region ($\Delta_{zmax} = 2.66$ mm).

6.4.2 Medium sand

To validate the turbulence-resolving model for oscillatory sheet flow, the medium sand transport in the experiment of O'Donoghue & Wright (2004) is simulated(see table 6.3). Figure 6.14 shows the comparison of sediment concentration profiles at four different instants. The turbulence-resolving simulation results (solid curve) are also compared with the turbulence-averaged model results (Cheng et al. 2016)(dashed curve). Overall, both the turbulence-averaged model and turbulence resolving model predicts the sediment concentration profile well. However, several differences can be also identified. In the acceleration phase ($t = 0.56$ s, see figure 6.14b), turbulence-averaged model over-predicts sediment suspension, which may be due to the simple parameterization of the turbulence suspension and turbulence-sediment interaction. However, around the flow peak, the flow turbulence is strong, both models tend to slightly over-predict the sediment suspension. However, We should also keep in mind about the accuracy of CCM in measuring dilute concentration. Another difference is the near-bed region ($-0.007 < z < -0.004$ mm), where the turbulence-resolving model seems to be superior to the turbulence-averaged model (see Figure 13c to e). This better performance in the near bed region may be due to proper resolving of sediment-turbulence interactions.

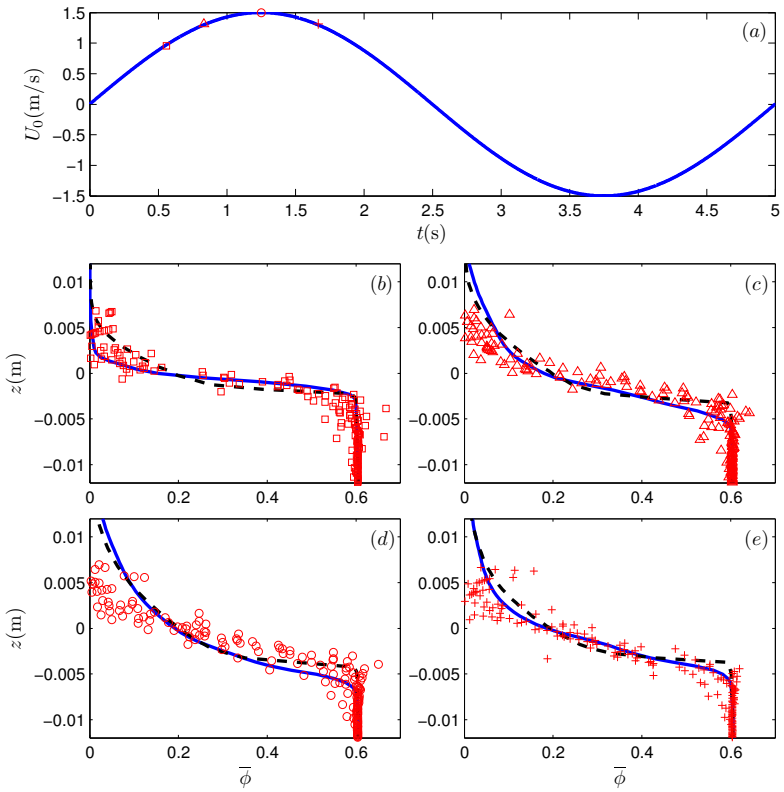

Figure 6.14: Panel (a) shows the free-stream velocity time series, and the comparison of sediment concentration profiles between turbulence-averaged model(dashed curve), turbulence-resolving model (solid curve) at four different instant are shown in (b) $t = T/12$; (c) $t = T/6$; (d) $t = T/4$; (e) $t = T/3$.

The time series of sediment concentration in three different vertical elevations are also compared with the measured data (O'Donoghue & Wright 2004). In the pick-up layer ($z = -1.85$ mm, see figure 6.15a), as the flow is accelerated ($0 < t < T/4$), sediment initially at the bed starts to be picked up ($t = 0.5$ s) and suspended to the suspension region (see figure 6.15c at $z = 0.85$ mm). Thus, a drop of sediment concentration at the pickup layer and an increase of sediment concentration in the suspension layer can be observed. On the other hand, when the flow decelerates ($T/4 < t < T/2$), the flow turbulence becomes insufficient to suspend such amount of sediment, and they start to settles from the suspension layer to the pickup layer. We can see that the turbulence-averaged model seems to predict a rather rapid sediment suspension

process (see $0 < t < 1$ s in figure 6.15c). Meanwhile, as the flow decelerates, the settling process in the turbulence-averaged model also seems to be more rapid than the turbulence-resolving model results. Close to the initial bed level, due to the settling and suspension processes across this elevation, the variation of the sediment concentration is mild, and both turbulence-averaged model and turbulence-resolving model are able to capture this feature. Overall, the main difference between the turbulence-averaged and turbulence-resolving model results is during the flow reversal. As we will demonstrate next, such feature is more pronounced for finer sand.

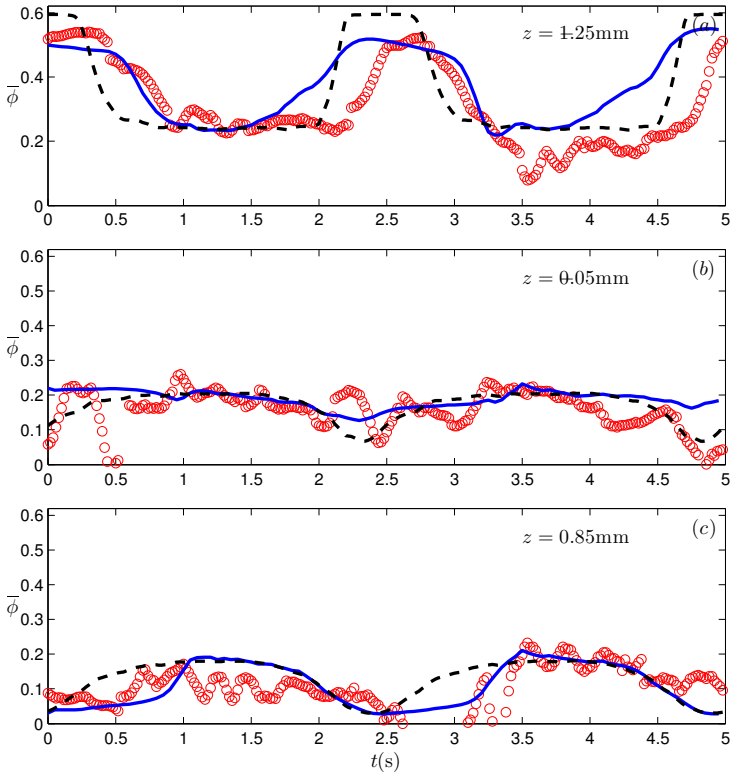

Figure 6.15: The comparison of time series of sediment concentration against measured data (O'Donoghue & Wright 2004, symbols), turbulence-averaged model results (dashed curve), turbulence-resolving model (solid curve) at (a) $z = -1.25$ mm (pick-up layer); (b) $z = -0.05$ mm (near initial bed); (c) $z = 0.85$ mm (suspension layer).

6.4.3 Fine sand burst events

It has been reported that short duration of concentration peaks occurs during flow reversal above the pick-up layer, and this peak is generally strongest for fine sand (Dohmen-Janssen 1999, O'Donoghue & Wright 2004). This different response due to grain size can be responsible for the enhanced sheet layer thickness for fine sand observed in the experiments. To investigate the sediment burst event, and enhanced sheet layer thickness fine sand transport ($d = 0.15$ mm) under the same wave condition as the medium sand case presented in section 6.4.2 is simulated. The isosurface of fine sand and medium sand during flow peak and flow reversal are compared in figure 6.16, where two sediment concentration iso-surfaces. $\phi = 0.57$ and $\phi = 0.005$ are shown. In Dohmen-Janssen et al. (2001), the sheet layer thickness is defined as the layer between the level where the mean sediment concentration is about 8% and the immobile bed. Here we determine the sheet layer thickness as the distance from the mean concentration 8% and 57%, where the particles are constantly in contact with each other and the mobility is very low. For medium sand, the sheet layer thickness at the flow peak (figure 6.16a) is much larger than that in the flow reversal (figure 6.16b), and the isosurface of 8% at the flow peak is more irregular than the flow reversal. However, for fine sand case the sheet layer thickness at the flow reversal (figure 6.16c) is similar to that at the flow peak (figure 6.16d), and the isosurface of 8% at the flow reversal is more irregular than the flow peak. In fact, several sediment bursts can be observed at the flow reversal for fine sand, which is absent for the medium sand. In summary, turbulence-resolving simulation predict much energetic sediment transport for fine sand during flow reversal. Such energetic condition during flow reversal can be associated with high shear during flow reversal that can further trigger flow instabilities. These features cannot be captured by turbulence-averaged k-ϵ models.

6.5 Conclusion

A turbulence-resolving Eulerian two-phase model is developed for sediment transport applications. The effects of the unresolved subgrid turbulence motion are

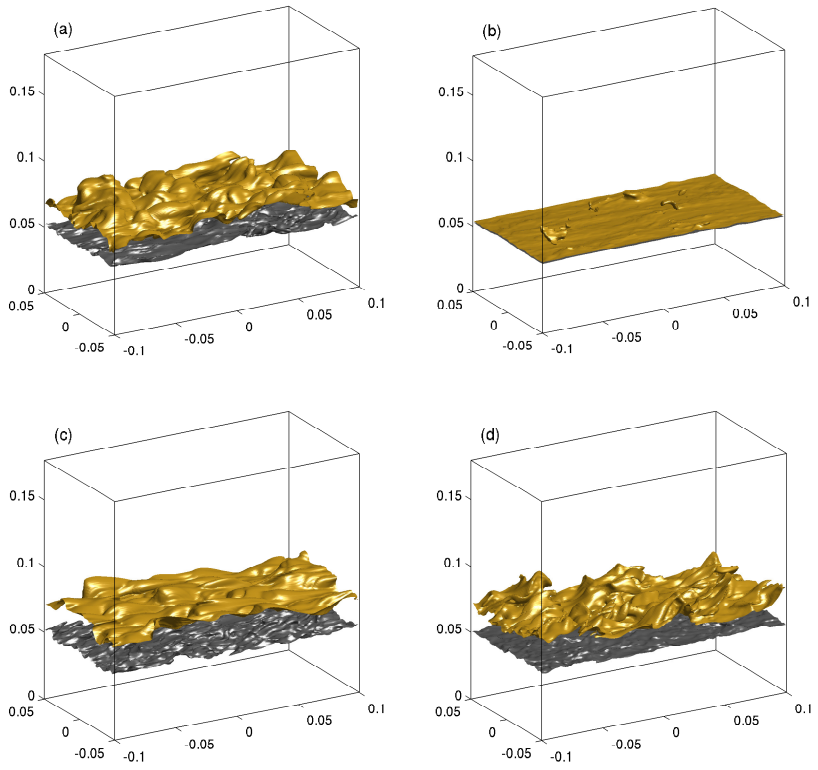

Figure 6.16: Iso-surfaces of concentration at $\phi = 0.005$ (brown) and $\phi = 0.3$ (dark gray) during flow peak (panel (a)) and flow reversal (panel (b)) for medium sand (Case M512, see table 6.3). Similar iso-surfaces of sediment concentration for fine sand (Case F512, see table 6.3) during flow peak and flow reversal are also plotted in panel (c) and (d), respectively.

modeled with a dynamic Smagorinsky sub-grid closure (Germano et al. 1991), and the effects of particle structures such as streamers and clusters are modeled with a sub-grid drift velocity model in the drag force (Ozel et al. 2013). The model is first validated with a novel acoustic high-resolution measurements in an unidirectional steady sheet flow experiment, where time-resolved profiles of collocated two-component velocities (streamwise and vertical), sediment concentration and the bed interface positions are provided (Revil-Baudard et al. 2015). A reduction of the von Karman parameter in the suspension layer is reproduced by the present model, and a strong damping effect due to the sediment-turbulence interactions is quantified in the fluid turbulence kinetic

energy budget. The drag induced turbulence damping effect is more significant than the density stratification in the flow conditions studied by Revil-Baudard et al. (2015). The contributions of velocity fluctuations to the sediment suspensions are evaluated by quadrant analysis, and their relation to the bed intermittencies were investigated. The numerical result showed that the turbulent ejection motions are highly correlated with the increase of bed level, while the turbulence sweep events are most associated with the bed erosion. Similar phenomenon has also been observed in the experiment (Revil-Baudard et al. 2015).

We further applied the model to study the oscillatory sheet flow reported by O'Donoghue & Wright (2004). The model performance for the medium sand is similar to the turbulence-averaged model, except that the turbulence-resolving model seems to be superior to the turbulence-averaged model during acceleration and decelerating phases. In addition, the turbulence-resolving model is able to capture the fine sand burst events near flow reversal. These unique transport characteristics for fine sediments have been reported by a few other oscillating water tunnel experiments (e.g., Dohmen-Janssen & Hanes 2002). We further confirm that this phenomenon is absent for medium sand.

However, there are several limitations of this model and following future work is recommended. For example, in the steady sheet flow, the model seems to under-predict the streamwise velocity and sediment concentration in the dilute region ($\phi < 8\%$). This inadequacy may be due to the simple sub-grid closure, which neglected the sediment effects. Meanwhile, more sophisticated sub-grid drift velocity closure may be needed to better resolve the effect of sub-grid sediment meso-structures. The bed intermittency from the numerical result is more frequent than the experiment measurement, The mechanisms of triggering bed intermittency can be further elucidated, especially for typical sand particles., and the relation of micro-scale (particle-scale) dynamics to the macro-scale behavior of sediment transport still needs more investigation. Further investigation on fine sand transport in oscillatory sheet flow is also warranted in order to improve existing parameterization for wave-induced transport.

6.6 Acknowledgements

This study was supported by National Science Foundation (CMMI-1135026; OCE-1356855) and Office of Naval Research (N00014-14-1-0586). Numerical simulations were carried out on MILLS at the University of Delaware. Simulations also leverage computing resource provided by Extreme Science and Engineering Discovery Environment (XSEDE) (TG-OCE100015). We gratefully acknowledge developers involved in OpenFOAM, which is the foundation of the new solver SedFoam presented in this report. Dr. Julien Chauchat and Dr. Tibaud Revil-Baudard provided many useful suggestions and experiment measurements during the model development.

Chapter 7

FUTURE WORKS, DISCUSSION AND RECOMMENDATIONS

In this thesis, several key mechanisms of sediment transport in nearshore environments, particular to boundary layer processes, were investigated. Coastal sediment transport involves processes at multiple scales due to various particle sizes and flow conditions, which necessitates the use of different numerical models ranging from turbulence-averaged model to turbulence-resolving models. Though the multi-dimensional Eulerian two-phase models succeeded in studying multi-dimensional processes such as scour or bed instabilities, several assumptions and closures on grain-scale processes are used. It is critical to realize the limitations due to these assumptions, and their effect on model results. In this chapter, several assumptions that could limit the applicability of the Eulerian two-phase models are elucidated, and future works on the improvement of these elements are discussed. Finally, recommendations for future numerical model development and laboratory measurements are given to aid the development of more accurate sediment transport predictions.

7.1 Grain Size Distribution

In nature, a range of grain sizes co-exist and depending on the particular type of environment, the size distribution can be very wide. However, it is practical to assume that the grain size is uniform in numerical studies of sediment transport (with a mean grain size d_{50} used) due to the difficulties in representing mixed grain size distributions. A lot of research effort has been devoted into studying the effect of mixed grain sizes. One well-known phenomenon of nonuniform grain sizes under sheared flows is the size segregation. Several driving mechanisms were identified. In the rapid granular transport layer, the differences in granular temperatures for dispersed particles can cause

the segregation (Jenkins & Mancini 1989, Van Wachem et al. 2001), while in the dense layer, the particle geometry plays an important role, and the smaller particles can pass through the voids between larger particles due to the percolation (Savage & Lun 1988, Ottino & Khakhar 2000). As a result, the smaller particles moves downwards, while the larger particles preferentially cover the sediment bed, which is called the armoring effect. It was found that due to the armoring effect, the critical shear stress for the onset of the bed erosion can be significantly increased (Gomez 1994, Hong et al. 2015). Liang et al. (2007) studied near-bed sediment transport over a sand-silt mixed sediment bed and showed that as large amount of fine sediment is suspended, the presence of sand can armor the bed, which prevent further suspension of fine sediment while in the meantime forming sand ripples. The sand ripples significantly increase near-bed turbulence and roughness through secondary flows and vortex shedding (Hooshmand et al. 2015). In short, the mixed grain size may have a noticeable effect on the overall sediment transport.

In the Eulerian framework, several attempts were made to study the effect of mixed grain size. Based on a single phase model for the fluid hydrodynamics, the sediment bed can be divided into inactive layer and active bed (Reed et al. 1999, Harris & Wiberg 2001, Lee et al. 2007). The active layer is mixed with both smaller and larger grain sizes available for entrainment. The entrainment of mixed sediments is calculated as a fraction-weighted average of discrete resuspension equations, and the armoring effect can be accounted by different entrainment rate parameterized by bottom shear stresses. Jenkins & Mancini (1989) developed a kinetic theory for a bimodal particle mixture, and size segregation was studied successfully. Van Wachem et al. (2001) further incorporated the kinetic theory for a bimodal mixture in an Eulerian two-phase flow model and studied fluidized beds with bimodal particle distribution. Reasonable numerical results were obtained when compared with experiment data. However, considering the complicated interactions between particles of different grain sizes, it remains difficult to develop a poly-dispersed Eulerian two-phase model for realistic particle size distributions.

To avoid the difficulties in modeling particle interactions using a Eulerian description, the particle-particle interactions of different grain sizes can be modeled explicitly using discrete particle method (DEM). Calantoni & Thaxton (2008) carried out simulations of bimodal mixtures of coarse grains using DEM, and studied sediment transport rate under nearshore wave conditions. They proposed a power law for the transport ratio between two different grain sizes. This power law can be well suited for more realistic morphodynamic modeling by considering the transport ratios of different grain sizes. Recently, preliminary efforts have been made to extend the multiphase modeling framework to study the effects of size distribution and grain shape. We consider contrasting the effect of particle size distribution by considering uniform, narrow to wide grain size distributions but having the same d_{50}. The model extension begins with an open-source CFDEM code (Goniva et al. 2012). After examining the structure of the code and particularly the coupling between the continuum fluid phase and the discrete particle phase, we implemented the fluid phase and the coupling between the fluid-sediment interaction as developed in SedFOAM while retained the DEM based on LIGGGHTS (Kloss et al. 2012). It is noted that the model development and extension is still underway. The purpose of this section is to demonstrate the capability of coupled fluid-DEM scheme in solving critical sediment transport problems using a preliminary solver. Four comparative cases are carried out as shown in table 7.1. As a baseline case, Case 0 is chosen to be of uniform grain size, $d_{50} = 0.51$ mm. According to the experiment of O'Donoghue & Wright (2004), Case A1 is designed to match the distribution used during the experiment with a nearly log-normal distribution. It is found that the particle size could be very small if we follow the log-normal distribution, which is time-consuming for discrete particle simulation. As a workaround, d_0 is extrapolated using d_5 and d_{10}, and the same approach is used to obtain d_{100}. To further emphasize the effect of particle distribution, Case A2, A3, A4 are designed to have different broadness of grain size distributions.

Figure 7.1 shows the snapshot of sediments in the bed at $t = 0$ (see figure 7.1a) and after a few waves (see figure 7.1b) for case A2 (see table 7.1). It is evident that the

Table 7.1: List of simulations presented in the study of particle size distribution.

Case	d_0(mm)	d_{10}(mm)	d_{50}(mm)	d_{90}(mm)	d_{100}(mm)	Ψ
0	NA	NA	0.51	NA	NA	0.7267
$A1$	0.33	0.36	0.51	0.67	0.86	0.6445
$A2$	0.25	0.32	0.51	0.8	1.1	0.616
$A3$	0.2	0.27	0.51	0.92	1.4	0.348
$A4$	0.38	0.42	0.51	0.62	0.69	0.7005

sediment bed is well-mixed initially before the wave motion drives the sediment bed to dilate due to the wave-driven shear flow. Due to different responses to the shear flows from different grain sizes, the large particles moves upward and eventually covers the sediment bed (armoring phenomenon).

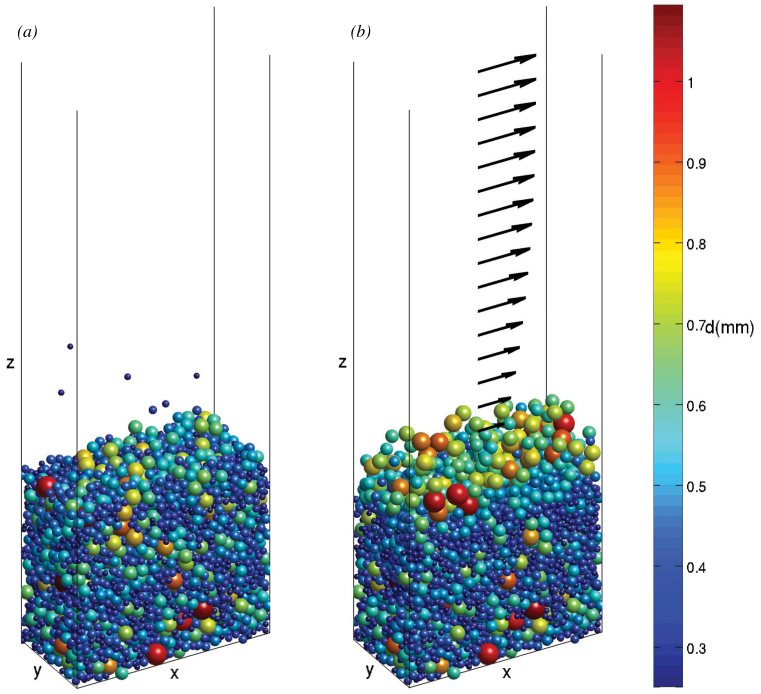

Figure 7.1: Illustration of the armoring effect in Case A2, where (a) is the initial bed, and (b) is the bed at flow peak when the flow is quasi-steady state. The particles are colored with the respective diameter, and the vectors denote the velocity.

As a resulting of the coarse particles armoring the bed, the sediment transport rate becomes lower than that using a uniform grain size with the same d_{50}. The time series of sediment transport rate for case A0-A4 are compared in figure 7.2b, and the free-stream velocity time series used as flow forcing is shown in figure 7.2a. Generally, the sediment transport rate is reduced due to the armoring effect. This reduction is more pronounced during the positive flow peak, and less effective during the negative flow peak, and as a result, the net positive (onshore) sediment transport rate is reduced (see table 7.1). This reduction is most significant for case A3, where the size distribution is the widest, and the net onshore transport rate is reduced by a factor of 2. This series of numerical experiments demonstrated that coupled fluid-DEM approach can be a very effective tool to study coastal sediment transport with emphasis on heterogeneity of sediment properties. In the next section, we further demonstrate the effect of non-spherical grain shape using the coupled fluid-DEM.

7.2 Effect of Particle Shape

Another assumption that is usually made in the Eulerian two-phase sediment transport models is the spherical particle shape. Evidently, natural sand grain is rarely of spherical shape, and its uncertainties on the sediment transport remain unclear due to the difficulties to model the exact particle shapes in the numerical models. The additional complexity may come from the rotational asymmetry of non-spherical particles, thus the particles may have a preferential orientation exerted to certain flow directions. Consequently, the fluid-particle coupling forces such as drag and lift force cannot be fully parameterized by the particle diameters (Corey 1949, Haider & Levenspiel 1989). Meanwhile, the contact force may not necessary pass through the geometry center of particles, and inter-particle locking may occur. As a result, the angle of repose becomes different from that of spherical grain. As shown by Calantoni et al. (2004), the angle of repose may increase with particle non-sphericity. In these regards, the response of particles to the fluid motion, particularly the wave motion, may differ from the spherical particles.

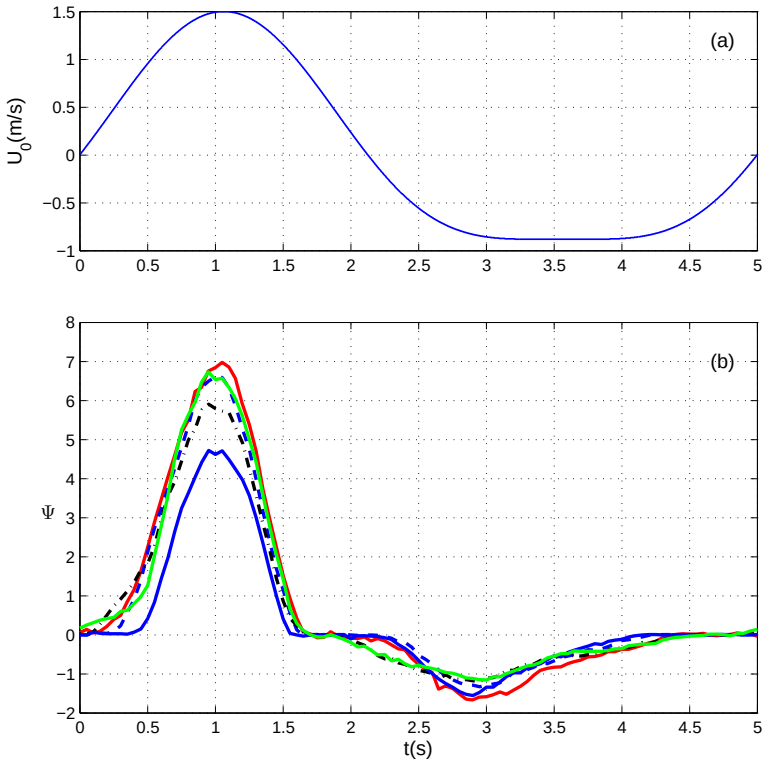

Figure 7.2: (a) Time series of the free-stream velocity. (b) Comparison of the time series of sediment transport rate for Case 0 (red solid curve), Case A1 (blue dashed curve), Case A2 (black dash-dot curve), Case A3 (blue solid curve) and Case A4 (green solid curve).

To investigate the effect of particle shape, the DEM approach is the best option because non-spherical particle shapes are considered explicitly. In the literature, two major mothedology are introduced to study non-spherical particles. One describes the particles to be a given shape, such as a cylinder, an ellipsoid and a disk, and the contacts are detected by solving the underlying mathematical equations (Wait 2001). However, detecting the contact with the neighboring particles, and the calculation of the overlap area, intersection and contact points are nontrivial (Dziugys & Peters 2001). The other method is the multi-sphere model, in which the non-spherical particles are represented as a composite of a number of spheres, with or without overlaps. The composite particles are then treated as rigid bodies (Calantoni et al. 2004). Here, we

follow Calantoni et al. (2004) and the latter method, and consider a composite particle with two spherical particles with/without overlaps, as illustrated in figure 7.3(a). The ratio of the two original particle radius is $R_1/R_2 = 2$, and as shown in table 7.2, three different (composite) particle shapes are considered by varying the volume of overlapping (the overlapped volume is not double counted). The spherical particles are also computed as a baseline scenario, and hence four particle shapes are investigated in total (see figure 7.4). Though this approach may not represent the real shape of the sediment grains, it is a critical first step to study the effect of grain shape on sediment transport.

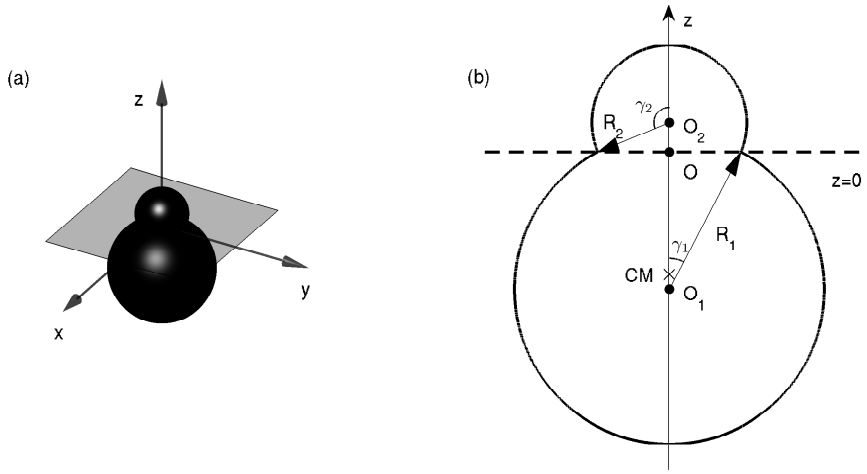

Figure 7.3: Illustration of the composite particle; (a) 3D view of the composite particle, the plane coincide with the intersection plane of the two partial spheres; (b) plan view of the composite particle, where $z = 0$ is located at the intersection plane of the two partial spheres, and z-axis coincide with the center of the two partial spheres (O_1, O_2, respectively), and it intersects with the intersection plane at the origin of the coordinate O. R_1, R_2 are the radius of the two partial spheres, respectively, and the angles γ_1 and γ_2 are measured from the positive z-axis about the center of each respective partial spheres. CM is the center of mass for the composite particle.

With the cross-section geometry illustrated in 7.3(b), the center of mass and moment of inertia can be easily calculated. The drag coefficient is modified by considering

Table 7.2: List of simulations presented in the study of particle shape.

Case	R_2/R_1	R_1(mm)	$d_{sph} = 2R$(mm)	γ_2	CSF	η	Ψ
0	NA	0.2550	0.51	NA	1.0	1.0	0.7267
$B1$	1/2	0.2534	0.51	$3\pi/8$	0.93	0.9923	0.6732
$B2$	1/2	0.2480	0.51	$5\pi/8$	0.84	0.9473	0.6405
$B3$	1/2	0.2452	0.51	π	0.8	0.8653	0.5996

the non-sphericity as suggested by Haider & Levenspiel (1989).

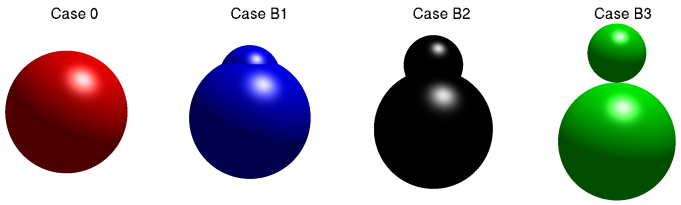

Figure 7.4: Illustration of particle shape of Case 0, B1, B2 and B3 (see Table 7.2).

The same 2nd-order Stokes wave (see section 7.1) is considered, and the transport rate time series for the four different particle shapes are presented in figure 7.5. The Case B1 and B2 show a similar transport rate as case 0, though a slightly smaller transport rate can be found during the flow peak. For the extreme example without overlaps (Case B3), the largest difference from case 0 is obtained, and the net transport over the entire wave is reduced by 20%. This preliminary investigation indicates that the non-spherical particle has minor effect on the sediment transport rate as compared to wider size distribution typically encountered in natural environment.

As a short summary of section 7.1 and 7.2, the discrete particle model is shown to be an effective tool to study the effect of particle size distribution and particle shape. The armoring due to coarse particles on top of the finer fraction may hinder the sediment entrainment, and reduce the sediment transport rate. On the other hand, the particle shape has a relatively minor effect on the overall transport rate, even though

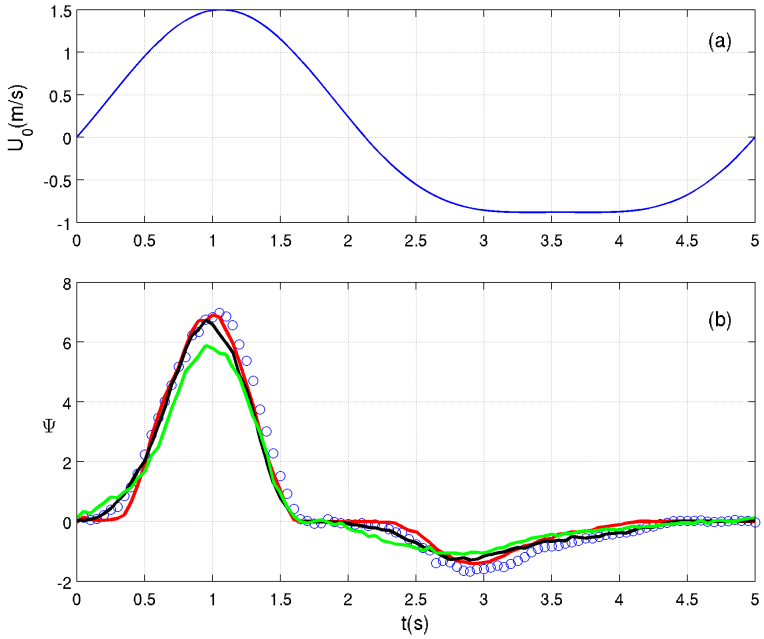

Figure 7.5: (a) Time series of the free-stream velocity; (b) Comparison of the time series of the sediment transport rate for Case 0 (circle symbols), Case B1(red solid curve), Case B2 (black solid curve), Case B3 (green solid curve)

a reduction of sediment transport caused by the non-sphericity. In the present study, the fluid phase is only solved in 1DV with a turbulence-averaged formulation, and the bedform evolution cannot be simulated. In addition, the turbulence suspension associated with flow turbulencewas not included, thus the suspended load associated with flow turbulence is ignored. Suspended load by turbulence may contribute significantly to the total sediment transport, especially for medium to fine sand particles. Future works on improvement in these directions are needed.

7.3 Effect of Progressive Surface Waves

In the scope of this thesis, no free-surface was considered, and all the model validations are limited to the laboratory experiments in tunnel (e.g., Sumer et al. 1996, O'Donoghue & Wright 2004, Revil-Baudard et al. 2015). Flow field in an oscillating tunnel is different from the progressive waves in several respects. One major distinction

is the near-bed wave orbital motions. Under progressive waves, the wave boundary layer is not homogeneous in the direction of wave propagation, and the horizontal momentum will be transported vertically due to the wave boundary layer streaming. However, in oscillatory flow tunnels (U-tube), the wave-induced near-bed motion is idealized by a horizontally uniform oscillating flow, while the vertical component is absent. As a result, the wave-included bottom current (wave streaming) cannot be reproduced. Meanwhile, the difference in the surface elevation will induce horizontal pressure gradient, which can be directly related to the $\partial\eta/\partial x$, where η is the surface elevation. This pressure gradient force is clearly missing without resolving the free surface. It has been shown that under steep waves, the pressure gradient is critical in the sediment transport prediction (Mieras et al. 2016). In addition, most of the research efforts are devoted to study sediment transport due to bottom boundary layer, however, surface-wave breaking may generate turbulent coherent structures. The so-called oblique descending eddies may touch the sediment bed and cause severe sediment suspension (Sumer et al. 2011, Zhou et al. 2014). To resolve the sediment transport under progressive waves, future works that includes the surface effects are warranted.

7.4 Momentary Bed Failure/Plug Flow

The term 'plug flow' is used to describe the situation where sediment starts to move as a block, which is usually associated with a large pressure gradient (Sleath 1999). An ideal analysis can be carried out to study the motion of the sediment block exerted by the flow pressure and shear stress (Sleath 1999). However, several unknown parameters, for example, thickness of the moving block, bottom friction coefficient inside the sediment bed, and vertical pore pressure was neglected in the analysis. A different term, 'momentary bed failure' was used by Madsen (1974), which may relates to the same physical processes. Another method to analyze the relevant bed response was given by Charru & Mouilleron-Arnould (2002) and Schaflinger et al. (1995), they suggest that instability of particle transport layer may occur when the mobile layer thickness is sufficiently large. However, the mobile layer thickness again is unclear as

a priori.

In chapter 5, the enhanced sediment transport caused by the momentary bed failure was successfully studied by a series of numerical experiments, and an attempt to provide a criterion for the occurrence of the momentary bed failure was made. However, there are several difficulties to describe the momentary bed failure or plug flow using a continuum model, since solid mechanisms are key element in the onset of the plug flow, treating solid block by assume a fluid property may be problematic. Specifically, the Eulerian two-phase model employs a highly empirical frictional stress model to ensure a solid-fluid like sediment bed. More sophisticated methods are needed to better resolve the particle-particle interactions inside the sediment bed. One possible way to study the onset of plug flow may be the discrete particle model (see Section 7.1), where the particle-particle interactions are directly resolved.

7.5 Experimental/DNS Data for Turbulence-resolving Model Assessment

In the development of the present turbulence-resolving sediment transport model, we have faced several difficulties. On the one hand, theoretical foundations on the sediment-turbulence interactions are not well established for concentrated condition, which in turn is one of purposes to develop the turbulence-resolving model. As a result, the model validation become critical. However, due to the lack of detailed and accurate 3D experiment data, the model calibration is not straightforward either. Revil-Baudard et al. (2015) provide us valuable collocated streamwise and spanwise velocity profiles, and sediment concentration profiles, However, this (and most others) experiment measurement is only at one location, and thus the spatial correlation information is lacking. In the present numerical model, we assumed that the horizontal directions are homogeneous. However, due to the bed intermittency, and possibly bedforms, this assumption is limited. Further experiment measurement resolving the spatial flow structures and sediment information would be important to evaluate this assumption. Meanwhile, the measurement frequency is also a vital issue. As the turbulent time scale is of wide

range, and high frequency signals may not be well resolved. Evidently, these difficulties lie in the development of high fidelity measurement equipment.

The approach of direct numerical simulation (DNS) can be an efficient method for the model assessment. In DNS, the complete details carrier flow turbulence and dispersed particles can be obtained. As discussed in chapter 6, the large eddy simulation model does not perform well when the sediment concentration is lower than 0.08, which may be due to a poor consideration of turbulence-sediment interactions in the sub-grid scale. A DNS simulation with a dilute to moderate concentration suspension of particles will be desirable, in which mesh size is as fine as the particle size and thus the fluid motion at the particle scales is fully resolved. It is useful to describe the particle motion using the Lagrangian scheme, and therefore no errors due to averaging will be included. However, the computational cost for such DNS simulation is high, and numerical schemes that fully tracks each individual particles may be complicated (Simeonov & Calantoni 2012), However, it may be achievable in the near future, as the computation technology is developing rapidly.

BIBLIOGRAPHY

Aluie, H. (2013), 'Scale decomposition in compressible turbulence', *Physica D: Nonlinear Phenomena* **247**(1), 54–65.

Amoudry, L., Hsu, T.-J. & Liu, P.-F. (2005), 'Schmidt number and near-bed boundary condition effects on a two-phase dilute sediment transport model', *Journal of Geophysical Research: Oceans* **110**(C9).

Amoudry, L., Hsu, T.-J. & Liu, P.-F. (2008), 'Two-phase model for sand transport in sheet flow regime', *Journal of Geophysical Research: Oceans (1978-2012)* **113**(C3).

Amoudry, L. & Liu, P.-F. (2009), 'Two-dimensional, two-phase granular sediment transport model with applications to scouring downstream of an apron', *Coastal Engineering* **56**(7), 693–702.

Amoudry, L. O. (2014), 'Extension of k-ω turbulence closure to two-phase sediment transport modelling: Application to oscillatory sheet flows', *Advances in Water Resources* **72**, 110–121.

Amoudry, L. O. & Liu, P. L.-F. (2010), 'Parameterization of near-bed processes under collinear wave and current flows from a two-phase sheet flow model', *Continental Shelf Research* **30**(13), 1403–1416.

Arakawa, A. & Lamb, V. R. (1981), 'A potential enstrophy and energy conserving scheme for the shallow water equations', *Mon. Wea. Rev.* **109**(1), 18–36.

Asano, T. (1990), 'Two-phase flow model on oscillatory sheet-flow', *Coastal Engineering Proceedings; No 22 (1990): Proceedings 22nd Conference on Coastal Engineering, Delft, The Netherlands.* .

Bagnold, R. (1966), 'An approach to the sediment transport problem', *General Physics Geological Survey, Prof. paper* .

Bakhtyar, R., Barry, D. A., Yeganeh-Bakhtiary, A., Li, L., Parlange, J.-Y. & Sander, G. (2010), 'Numerical simulation of two-phase flow for sediment transport in the inner-surf and swash zones', *Advances in water resources* **33**(3), 277–290.

Balachandar, S. & Eaton, J. K. (2010), 'Turbulent dispersed multiphase flow', *Annual Review of Fluid Mechanics* **42**, 111–133.

Berryman, J. G. (1983), 'Random close packing of hard spheres and disks', *Phys. Rev. A* **27**(2), 1053–1061.

Bever, A. J., McNinch, J. E. & Harris, C. K. (2011), 'Hydrodynamics and sediment-transport in the nearshore of Poverty Bay, New Zealand: Observations of nearshore sediment segregation and oceanic storms', *Cont. Shelf Res.* **31**(6), 507–526.

Bouillard, J. X., Lyczkowski, R. W. & Gidaspow, D. (1989), 'Porosity distributions in a fluidized bed with an immersed obstacle', *AIChE J.* **35**(6), 908–922.

Breusers, H. (1967), 'Time scale of two-dimensional local scour', *Proc. 12th IAHR Congress, Ft. Collins* **3**, 275–282.

Breusers, H. & Raudkivi, A. J. (1991), *Scouring*, Balkema Rotterdam.

Buchko, M., Kolkman, P., Pilarczyk, K. & Hydraulics, D. (1988), *Investigation of local scour in cohesionless sediments using a tunnel-model*, Delft Hydraulics.

Byun, D.-S. & Wang, X. H. (2005), 'The effect of sediment stratification on tidal dynamics and sediment transport patterns', *J. Geophys. Res.* **110**(C3), C03011.

Calantoni, J., Holland, K. T. & Drake, T. G. (2004), 'Modelling sheet-flow sediment transport in wave-bottom boundary layers using discrete-element modelling', *Philosophical Transactions–Royal Society of London. Series A: Mathematical, Physical and Engineering Sciences* **362**, 1987–2002.

Calantoni, J. & Puleo, J. A. (2006), 'Role of pressure gradients in sheet flow of coarse sediments under sawtooth waves', *Journal of Geophysical Research: Oceans* **111**(C1).

Calantoni, J. & Thaxton, C. S. (2008), 'Simple power law for transport ratio with bimodal distributions of coarse sediments under waves', *Journal of Geophysical Research* **113**(C3).

Cantero, M. I., Balachandar, S., Cantelli, A., Pirmez, C. & Parker, G. (2009), 'Turbidity current with a roof: Direct numerical simulation of self-stratified turbulent channel flow driven by suspended sediment', *J. Geophys. Res.* **114**(C3).

Cantero, M. I., Balachandar, S. & Garcia, M. H. (2008), 'An Eulerian-Eulerian model for gravity currents driven by inertial particles', *Int. J. Multiphase Flow* **34**(5), 484–501.

Carnahan, N. F. & Starling, K. E. (1969), 'Equation of state for nonattracting rigid spheres', *The Journal of Chemical Physics* **51**(2), 635–636.

Chakraborty, P., Balachandar, S. & Adrian, R. J. (2005), 'On the relationships between local vortex identification schemes', *J. Fluid Mech.* **535**, 189–214.

Charru, F. & Mouilleron-Arnould, H. (2002), 'Instability of a bed of particles sheared by a viscous flow', *Journal of Fluid Mechanics* **452**, 303–323.

Chen, C. P. & Wood, P. E. (1985), 'A turbulence closure model for dilute gas-particle flows', *Can. J. Chem. Eng.* **63**(3), 349–360.

Chen, X., Li, Y., Niu, X., Chen, D. & Yu, X. (2011), 'A two-phase approach to wave-induced sediment transport under sheet flow conditions', *Coastal Engineering* **58**(11), 1072–1088.

Cheng, Z. & Hsu, T.-J. (2014*a*), A multi-dimensional two-phase Eulerian model for sediment transport—TwophaseEulerSedFoam (version 1.0), Technical Report CACR-14-08, Center for Applied Coastal Research, University of Delaware.

Cheng, Z. & Hsu, T.-J. (2014*b*), 'A turbulence-resolving eulerian two-phase model for sediment transport', *Coastal Engineering Proceedings; No 34 (2014): Proceedings of 34th Conference on Coastal Engineering, Seoul, Korea, 2014* .

Cheng, Z., Hsu, T.-J. & Calantoni, J. (2016), 'Sedfoam: A multi-dimensional eulerian two-phase model for sediment transport and its application to momentary bed failure', *Submitted to Coastal Engineering* .

Cheng, Z., Yu, X., Hsu, T.-J., Ozdemir, C. E. & Balachandar, S. (2015a), 'On the transport modes of fine sediment in the wave boundary layer due to resuspension/deposition: A turbulence-resolving numerical investigation', *J. Geophys. Res. Oceans* **120**(3), 1918–1936.

Cheng, Z., Yu, X., Hsu, T.-J. & Balachandar, S. (2015b), 'A numerical investigation of fine sediment resuspension in the wave boundary layer–uncertainties in particle inertia and hindered settling', *Computers & Geosciences* **83**, 176–192.

Chien, N., Einstein, H. A., Einstein, H. A., Einstein, H. A. & Hydraulicien, S. (1955), *Effects of heavy sediment concentration near the bed on velocity and sediment distribution*, Missoury River Division, Corps of Engineers, US Army.

Chorin, A. J. (1968), 'Numerical solution of the Navier-Stokes equations', *Math. Comput.* **22**(104), 745–762.

Chou, Y.-J. & Fringer, O. B. (2010), 'A model for the simulation of coupled flow-bed form evolution in turbulent flows', *Journal of Geophysical Research* **115**(C10), C10041.

Conley, D. C. & Inman, D. L. (1992), 'Field observations of the fluid-granular boundary layer under near-breaking waves', *Journal of Geophysical Research* **97**(C6), 9631–9643.

Corey, A. (1949), 'Influence of shape on the fall velocity of sand grains [unpublished m. sc. thesis]: Colorado a&m college', *Fort Collins, Colorado* .

Cortese, T. A. & Balachandar, S. (1995), 'High performance spectral simulation of turbulent flows in massively parallel machines with distributed memory', *Int. J. High Perform. C.* **9**(3), 187–204.

Curran, K., Hill, P., Milligan, T., Mikkelsen, O., Law, B., de Madron, X. D. & Bourrin, F. (2007), 'Settling velocity, effective density, and mass composition of suspended sediment in a coastal bottom boundary layer, Gulf of Lions, France', *Cont. Shelf Res.* **27**(10-11), 1408–1421.

Dankers, P. & Winterwerp, J. (2007), 'Hindered settling of mud flocs: Theory and validation', *Cont. Shelf Res.* **27**(14), 1893–1907.

Danon, H., Wolfshtein, M. & Hetsroni, G. (1977), 'Numerical calculations of two-phase turbulent round jet', *International Journal of Multiphase Flow* **3**(3), 223–234.

Deardorff, J. W. (1970), 'A numerical study of three-dimensional turbulent channel flow at large reynolds numbers', *Journal of Fluid Mechanics* **41**(02), 453–480.

Ding, J. & Gidaspow, D. (1990), 'A bubbling fluidization model using kinetic theory of granular flow', *AIChE J.* **36**(4), 523–538.

Dohmen-Janssen, C. M. (1999), Grain size influence on sediment transport in oscillatory sheet flow; phase lags and mobile-bed effects, PhD thesis, Delft University of Technology.

Dohmen-Janssen, C. M. & Hanes, D. M. (2002), 'Sheet flow dynamics under monochromatic nonbreaking waves', *Journal of Geophysical Research* **107**(C10), 3149–.

Dohmen-Janssen, C. M., Hassan, W. & Ribberink, J. S. (2001), 'Mobile-bed effects in oscillatory sheet flow', *Journal of geophysical research. Pt. C: Oceans* **106**(11), 27.103–27.115.

Dong, P. & Zhang, K. (1999), 'Two-phase flow modelling of sediment motions in oscillatory sheet flow', *Coastal Engineering* **36**(2), 87–109.

Dong, P. & Zhang, K. (2002), 'Intense near-bed sediment motions in waves and currents', *Coastal Engineering* **45**(2), 75–87.

Drake, T. G. & Calantoni, J. (2001), 'Discrete particle model for sheet flow sediment transport in the nearshore', *Journal of Geophysical Research: Oceans* **106**(C9), 19859–19868.

Dyer, K. & Manning, A. (1999), 'Observation of the size, settling velocity and effective density of flocs, and their fractal dimensions', *J. Sea. Res.* **41**(1), 87–95.

Dziugys, A. & Peters, B. (2001), 'An approach to simulate the motion of spherical and non-spherical fuel particles in combustion chambers', *Granular matter* **3**(4), 231–266.

Einstein, H. A. (1950), *The bed-load function for sediment transportation in open channel flows*, 1026, US Department of Agriculture.

Engelund, F. & Fredsoe, J. (1976), 'A sediment transport model for straight alluvial channels', *Nordic Hydrology* **7**(5), 293–306.

Ergun, S. (1952), 'Fluid flow through packed columns', *Chem. Eng. Prog.* **48**, 89–94.

Fan, S., Swift, D. J., Traykovski, P., Bentley, S., Borgeld, J. C., Reed, C. W. & Niedoroda, A. W. (2004), 'River flooding, storm resuspension, and event stratigraphy on the northern California shelf: observations compared with simulations', *Mar. Geol.* **210**(1), 17–41.

Ferry, J. & Balachandar, S. (2001), 'A fast Eulerian method for disperse two-phase flow', *Int. J. multiphase flow* **27**(7), 1199–1226.

Ferry, J., Rani, S. L. & Balachandar, S. (2003), 'A locally implicit improvement of the equilibrium Eulerian method', *Int. J. Multiphase Flow* **29**(6), 869 – 891.

Flores, N. Z. & Sleath, J. F. (1998), 'Mobile layer in oscillatory sheet flow', *Journal of Geophysical Research: Oceans (1978-2012)* **103**(C6), 12783–12793.

Foster, D. L., Bowen, A. J., Holman, R. A. & Natoo, P. (2006), 'Field evidence of pressure gradient induced incipient motion', *J. Geophys. Res.* **111**(C5), C05.

Frank, D., Foster, D., Sou, I. M. & Calantoni, J. (2015b), 'Incipient motion of surf zone sediments', *J. Geophys. Res. Oceans* **120**(8), 5710–5734.

Frank, D., Foster, D., Sou, I. M., Calantoni, J. & Chou, P. (2015a), 'Lagrangian measurements of incipient motion in oscillatory flows', *Journal of Geophysical Research: Oceans* **120**(1), 244–256.

Fredsoe, J. & Deigaard, R. (1992), *Mechanics of coastal sediment transport. Advanced Series on Ocean Engineering*, Vol. 3, World Scientific, Singapore.

Friedrichs, C. & Wright, L. (2004), 'Gravity-driven sediment transport on the continental shelf: implications for equilibrium profiles near river mouths', *Coast. Eng.* **51**(8-9), 795–811.

Gallagher, E. L., Elgar, S. & Guza, R. (1998), 'Observations of sand bar evolution on a natural beach', *Journal of Geophysical Research: Oceans* **103**(C2), 3203–3215.

Galtier, S. & Banerjee, S. (2011), 'Exact relation for correlation functions in compressible isothermal turbulence', *Physical Review Letters* **107**(13), 134501.

Germano, M., Piomelli, U., Moin, P. & Cabot, W. H. (1991), 'A dynamic subgrid-scale eddy viscosity model', *Physics of Fluids A* **3**(7), 1760–1765.

Geyer, W. R., Trowbridge, J. H. & Bowen, M. M. (2000), 'The dynamics of a partially mixed estuary*', *Journal of Physical Oceanography* **30**(8), 2035–2048.

Gidaspow, D. (1994), *Multiphase flow and fluidization: continuum and kinetic theory descriptions*, Academic press.

Goldsmith, S. T., Carey, A. E., Lyons, W. B., Kao, S.-J., Lee, T.-Y. & Chen, J. (2008), 'Extreme storm events, landscape denudation, and carbon sequestration: Typhoon Mindulle, Choshui River, Taiwan', *Geology* **36**(6), 483–486.

Gomez, B. (1994), 'Effects of particle shape and mobility on stable armor development', *Water Resour. Res.* **30**(7), 2229–2239.

Goniva, C., Kloss, C., Deen, N. G., Kuipers, J. A. & Pirker, S. (2012), 'Influence of rolling friction on single spout fluidized bed simulation', *Particuology* **10**(5), 582–591.

Haider, A. & Levenspiel, O. (1989), 'Drag coefficient and terminal velocity of spherical and nonspherical particles', *Powder technology* **58**(1), 63–70.

Hale, R., Ogston, A., Walsh, J. & Orpin, A. (2014), 'Sediment transport and event deposition on the Waipaoa River Shelf, New Zealand', *Cont. Shelf Res.* **86**(0), 52–65.

Harris, C. K., C. K. & Wiberg, P. L. (1997), 'Approaches to quantifying long-term continental shelf sediment transport with an example from the Northern California STRESS mid-shelf site', *Cont. Shelf Res.* **17**(11), 1389–1418.

Harris, C. K. & Wiberg, P. (2002), 'Across-shelf sediment transport: Interactions between suspended sediment and bed sediment', *J. Geophys. Res.* **107**(C1), 8–1–8–12.

Harris, C. K. & Wiberg, P. L. (2001), 'A two-dimensional, time-dependent model of suspended sediment transport and bed reworking for continental shelves', *Computers & Geosciences* **27**(6), 675–690.

Heald, J., McEwan, I. & Tait, S. (2004), 'Sediment transport over a flat bed in a unidirectional flow: simulations and validation', *Philosophical Transactions of the Royal Society of London A* **362**, 1973–1986.

Hedges, J., Keil, R. & Benner, R. (1997), 'What happens to terrestrial organic matter in the ocean?', *Org. Geochem.* **27**(56), 195–212.

Henderson, S. M., Allen, J. S. & Newberger, P. (2004), 'Nearshore sandbar migration predicted by an eddydiffusive boundary layer model', *Journal of Geophysical Research: Oceans* **109**(C6).

Hill, P. S., Milligan, T. G. & Geyer, W. (2000), 'Controls on effective settling velocity of suspended sediment in the Eel River flood plume', *Cont. Shelf Res.* **20**(16), 2095–2111.

Hoefel, F. & Elgar, S. (2003), 'Wave-induced sediment transport and sandbar migration', *Science* **299**(5614), 1885–1887.

Hoffmans, G. & Pilarczyk, K. (1995), 'Local scour downstream of hydraulic structures', *Journal of Hydraulic Engineering* **121**(4), 326–340.

Holway, K., Thaxton, C. S. & Calantoni, J. (2012), 'Application of a simple power law for transport ratio with bimodal distributions of spherical grains under oscillatory forcing', *Advances in Water Resources* **48**, 47–54.

Hong, A., Tao, M. & Kudrolli, A. (2015), 'Onset of erosion of a granular bed in a channel driven by fluid flow', *Physics of Fluids (1994-present)* **27**(1), 013301.

Hooshmand, A., Horner-Devine, A. R. & Lamb, M. P. (2015), 'Structure of turbulence and sediment stratification in wave-supported mud layers', *J. Geophys. Res. Oceans* **120**(4), 2430–2448.

Hsu, T.-J. & Hanes, D. M. (2004), 'Effects of wave shape on sheet flow sediment transport', *Journal of Geophysical Research: Oceans* **109**(C5).

Hsu, T.-J., Jenkins, J. T. & Liu, P. L. (2003), 'On two-phase sediment transport: Dilute flow', *Journal of Geophysical Research* **108**(C3).

Hsu, T.-J., Jenkins, J. T. & Liu, P. L.-F. (2004), 'On two-phase sediment transport: sheet flow of massive particles', *Proceedings of the Royal Society of London. Series A: Mathematical, Physical and Engineering Sciences* **460**(2048), 2223–2250.

Hsu, T.-J., Ozdemir, C. E. & Traykovski, P. A. (2009), 'High-resolution numerical modeling of wave-supported gravity-driven mudflows', *J. Geophys. Res.* **114**(C5), C05014.

Hu, K., Ding, P., Wang, Z. & Yang, S. (2009), 'A 2d/3d hydrodynamic and sediment transport model for the yangtze estuary, china', *Journal of Marine Systems* **77**(12), 114–136.

Hunt, M. L., Zenit, R., Campbell, C. S. & Brennen, C. E. (2002), 'Revisiting the 1954 suspension experiments of r. a. bagnold', *Journal of Fluid Mechanics* **452**, 1–24.

Jacobsen, N. G., Fuhrman, D. R. & Fredsoe, J. (2012), 'A wave generation toolbox for the open-source CFD library: Openfoam', *International Journal for Numerical Methods in Fluids* **70**(9), 1073–1088.

Jenkins, J. & Mancini, F. (1989), 'Kinetic theory for binary mixtures of smooth, nearly elastic spheres', *Physics of Fluids A: Fluid Dynamics (1989-1993)* **1**(12), 2050–2057.

Jenkins, J. & Savage, S. (1983), 'A theory for the rapid flow of identical, smooth, nearly elastic, spherical particles', *Journal of Fluid Mechanics* **130**, 187–202.

Jenkins, J. T. & Hanes, D. M. (1998), 'Collisional sheet flows of sediment driven by a turbulent fluid', *Journal of Fluid Mechanics* **370**, 29–52.

Jensen, B., Sumer, B. & Fredsoe, J. (1989), 'Turbulent oscillatory boundary layers at high reynolds numbers', *J. Fluid Mech.* **206**, 265–297.

Jimenez, J. A. & Madsen, O. S. (2003), 'A simple formula to estimate settling velocity of natural sediments', *J. Waterw. Port, Coast. Ocean Eng.* **129**(2), 70–78.

Johnson, P. C. & Jackson, R. (1987), 'Frictional-collisional constitutive relations for granular materials, with application to plane shearing', *Journal of Fluid Mechanics* **176**, 67–93.

Kampf, J. & Myrow, P. (2014), 'High-density mud suspensions and cross-shelf transport: On the mechanism of gelling ignition', *J. Sediment. Res.* **84**(3), 215–223.

Kim, J., Moin, P. & Moser, R. (1987), 'Turbulence statistics in fully developed channel flow at low reynolds number', *Journal of fluid mechanics* **177**, 133–166.

Kineke, G., Sternberg, R., Trowbridge, J. & Geyer, W. (1996), 'Fluid-mud processes on the amazon continental shelf', *Cont. Shelf Res.* **16**(5-6), 667–696.

Kloss, C., Goniva, C., Hager, A., Amberger, S. & Pirker, S. (2012), 'Models, algorithms and validation for opensource dem and cfddem', *Progress in Computational Fluid Dynamics, an International Journal* **12**(2-3), 140–152.

Kniskern, T. A., Mitra, S., Orpin, A. R., Harris, C. K., Walsh, J. & Corbett, D. (2014), 'Characterization of a flood-associated deposit on the waipaoa river shelf using radioisotopes and terrigenous organic matter abundance and composition', *Cont. Shelf Res.* **86**, 66–84.

Kolker, A. S., Li, C., Walker, N. D., Pilley, C., Ameen, A. D., Boxer, G., Ramatchandirane, C., Ullah, M. & Williams, K. A. (2014), 'The impacts of the great Mississippi/Atchafalaya River flood on the oceanography of the Atchafalaya Shelf', *Cont. Shelf Res.* **86**(0), 17–33.

Kranenburg, C. (1994), 'The fractal structure of cohesive sediment aggregates', *Estuar. Coast. Shelf S.* **39**(6), 451–460.

Kranenburg, W. M., Hsu, T.-J. & Ribberink, J. S. (2014), 'Two-phase modeling of sheet-flow beneath waves and its dependence on grain size and streaming', *Advances in Water Resources* **72**, 57–70.

Lamb, M. P., D'Asaro, E. & Parsons, J. D. (2004), 'Turbulent structure of high-density suspensions formed under waves', *J. Geophys. Res.* **109**(C12).

Lanckriet, T., Puleo, J., Masselink, G., Turner, I., Conley, D., Blenkinsopp, C. & Russell, P. (2013), 'Comprehensive field study of swash-zone processes. ii: Sheet flow sediment concentrations during quasi-steady backwash', *J. Waterway, Port, Coastal, Ocean Eng.* **140**(1), 29–42.

Lee, C., Schwab, D. J., Beletsky, D., Stroud, J. & Lesht, B. (2007), 'Numerical modeling of mixed sediment resuspension, transport, and deposition during the march 1998 episodic events in southern lake michigan', *Journal of Geophysical Research: Oceans* **112**(C2).

Lesser, G., Roelvink, J., van Kester, J. & Stelling, G. (2004), 'Development and validation of a three-dimensional morphological model', *Coastal Engineering* **51**(89), 883–915.

Li, L. & Sawamoto, M. (1995), 'Multi-phase model on sediment transport in sheet-flow regime under oscillatory flow', *Coastal Engineering in Japan* **38**(2), 157–178.

Li, M., Pan, S. & OConnor, B. (2004), 'Acoustic back scattering measurements of sediment transport under sheet flow condition', *Department of Civil Engineering, The University of Liverpool* .

Li, M., Pan, S. & O'Connor, B. A. (2008), 'A two-phase numerical model for sediment transport prediction under oscillatory sheet flows', *Coastal Engineering* **55**(12), 1159–1173.

Liang, H., Lamb, M. P. & Parsons, J. D. (2007), 'Formation of a sandy nearbed transport layer from a finegrained bed under oscillatory flow', *Journal of Geophysical Research: Oceans* **112**(C2).

Lilly, D. K. (1967), 'The representation of small-scale turbulence in numerical simulation experiments', *In H. H. Goldstine (Ed.), Proc. IBM Scientific Computing Symp. on Environmental Sciences* pp. 195–210.

Liu, H. & Sato, S. (2005), 'Laboratory study on sheetflow sediment movement in the oscillatory turbulent boundary layer based on image analysis', *Coastal Engineering Journal* **47**(01), 21–40.

Liu, H. & Sato, S. (2006), 'A two-phase flow model for asymmetric sheetflow conditions', *Coastal Engineering* **53**(10), 825–843.

Liu, X. & Garcia, M. (2008), 'Three-dimensional numerical model with free water surface and mesh deformation for local sediment scour', *Journal of Waterway, Port, Coastal, and Ocean Engineering* **134**(4), 203–217.

Lun, C. K. K., Savage, S. B., Jeffrey, D. J. & Chepurniy, N. (1984), 'Kinetic theories for granular flow: inelastic particles in Couette flow and slightly inelastic particles in a general flowfield', *Journal of Fluid Mechanics* **140**, 223–256.

Ma, Y., Wright, L. D. & Friedrichs, C. T. (2008), 'Observations of sediment transport on the continental shelf off the mouth of the Waiapu River, New Zealand: evidence for current-supported gravity flows', *Cont. Shelf Res.* **28**(4), 516–532.

Madsen, O. S. (1974), 'Stability of a sand bed under breaking waves', *Coastal Engineering Proceedings; No 14 (1974): Proceedings of 14th Conference on Coastal Engineering, Copenhagen, Denmark, 1974* .

Maggi, F. (2007), 'Variable fractal dimension: A major control for floc structure and flocculation kinematics of suspended cohesive sediment', *Journal of Geophysical Research: Oceans* **112**(C7).

Marieu, V., Bonneton, P., Foster, D. L. & Ardhuin, F. (2008), 'Modeling of vortex ripple morphodynamics', *Journal of Geophysical Research* **113**(C9), C09007.

Maxey, M. R. & Riley, J. J. (1983), 'Equation of motion for a small rigid sphere in a nonuniform flow', *Physics of Fluids (1958-1988)* **26**(4), 883–889.

Mehta, A. (1986), Characterization of cohesive sediment properties and transport processes in estuaries, *in* A. Mehta, ed., 'Lecture Notes on Coastal and Estuarine Studies', Vol. 14, Springer New York, pp. 290–325.

Meyer-Peter, E. & Muller, R. (1948), Formulas for bed-load transport, *in* 'IHAR', IAHR.

Mieras, R. S., Puleo, J. A., Anderson, D., D., C. & Hsu, T.-J. (2016), 'Sheet flow processes on a sandbar under shoaling and breaking waves', *Submitted to Geophysical Research Letters* .

Milliman, J. D. & Farnsworth, K. L. (2011), *River discharge to the coastal ocean: a global synthesis*, Cambridge University Press.

Moser, R. D., Kim, J. & Mansour, N. N. (1999), 'Direct numerical simulation of turbulent channel flow up to Re= 590', *Phys. Fluids* **11**(4), 943–945.

Muste, M., Yu, K., Fujita, I. & Ettema, R. (2005), 'Two-phase versus mixed-flow perspective on suspended sediment transport in turbulent channel flows', *Water Resources Research* **41**(10).

Nielsen, P. (2006), 'Sheet flow sediment transport under waves with acceleration skewness and boundary layer streaming', *Coastal Engineering* **53**(9), 749–758.

Nino, Y., Lopez, F. & Garcia, M. (2003), 'Threshold for particle entrainment into suspension', *Sedimentology* **50**(2), 247–263.

Noh, Y. & Fernando, H. (1991), 'Dispersion of suspended particles in turbulent flow', *Phys. Fluids A* **3**(7), 1730–1740.

O'Brien, T. J. & Syamlal, M. (1993), 'Particle cluster effects in the numerical simulation of a circulating fluidized bed', *Circulating fluidized bed technology IV* pp. 367–372.

O'Donoghue, T. & Wright, S. (2004), 'Concentrations in oscillatory sheet flow for well sorted and graded sands', *Coastal Engineering* **50**(3), 117–138.

Ogston, A., Cacchione, D., Sternberg, R. & Kineke, G. (2000), 'Observations of storm and river flood-driven sediment transport on the northern California continental shelf', *Cont. Shelf Res.* **20**(16), 2141–2162.

Ottino, J. & Khakhar, D. (2000), 'Mixing and segregation of granular materials', *Annual Review of Fluid Mechanics* **32**(1), 55–91.

Ozdemir, C. E., Hsu, T.-J. & Balachandar, S. (2010), 'A numerical investigation of fine particle laden flow in an oscillatory channel: the role of particle-induced density stratification', *J. Fluid Mech.* **665**, 1–45.

Ozdemir, C. E., Hsu, T.-J. & Balachandar, S. (2011), 'A numerical investigation of lutocline dynamics and saturation of fine sediment in the oscillatory boundary layer', *J. Geophys. Res.* **116**(C9).

Ozdemir, C. E., Hsu, T.-J. & Balachandar, S. (2014), 'Direct numerical simulations of transition and turbulence in smooth-walled stokes boundary layer', *Phys. Fluids* **26**(4).

Ozel, A., Fede, P. & Simonin, O. (2013), 'Development of filtered euler-euler two-phase model for circulating fluidised bed: High resolution simulation, formulation and a priori analyses', *International Journal of Multiphase Flow* **55**, 43–63.

Parchure, T. M. & Mehta, A. J. (1985), 'Erosion of soft cohesive sediment deposits', *J. Hydraul. Eng.* **111**(10), 1308–1326.

Passalacqua, A. & Fox, R. (2011), 'Implementation of an iterative solution procedure for multi-fluid gas-particle flow models on unstructured grids', *Powder Technology* **213**(1-3), 174–187.

Pope, S. B. (2000), *Turbulent flows*, Cambridge university press.

Reed, C. W., Niedoroda, A. W. & Swift, D. J. (1999), 'Modeling sediment entrainment and transport processes limited by bed armoring', *Marine Geology* **154**(1), 143–154.

Revil-Baudard, T. & Chauchat, J. (2013), 'A two-phase model for sheet flow regime based on dense granular flow rheology', *Journal of Geophysical Research: Oceans* **118**(2), 619–634.

Revil-Baudard, T., Chauchat, J., Hurther, D. & Barraud, O. E. (2016), 'Interactions between the turbulence and shear-driven mobile sediment beds', *Journal of Fluid Mechanics, under review* .

Revil-Baudard, T., Chauchat, J., Hurther, D. & Barraud, P.-A. (2015), 'Investigation of sheet-flow processes based on novel acoustic high-resolution velocity and concentration measurements', *Journal of Fluid Mechanics* **767**, 1–30.

Rhie, C. & Chow, W. (1983), 'Numerical study of the turbulent flow past an airfoil with trailing edge separation', *AIAA journal* **21**(11), 1525–1532.

Ribberink, J. S. (1998), 'Bed-load transport for steady flows and unsteady oscillatory flows', *Coastal Engineering* **34**(12), 59–82.

Richardson, J. & Zaki, W. (1954), 'Sedimentation and fluidisation: Part I', *Trans. Instn Chem. Engrs* **32**(0).

Rijn, L. C. v. (1984), 'Sediment transport, part ii: suspended load transport', *Journal of hydraulic engineering* **110**(11), 1613–1641.

Roelvink, D., Reniers, A., van Dongeren, A., van Thiel de Vries, J., McCall, R. & Lescinski, J. (2009), 'Modelling storm impacts on beaches, dunes and barrier islands', *Coastal Engineering* **56**(1112), 1133–1152.

Ross, M. A. & Mehta, A. J. (1989), 'On the mechanics of lutoclines and fluid mud', *Journal of Coastal Research* pp. 51–62.

Ruessink, B. G., Kuriyama, Y., Reniers, A. J. H. M., Roelvink, J. A. & Walstra, D. J. R. (2007), 'Modeling cross-shore sandbar behavior on the timescale of weeks', *Journal of Geophysical Research* **112**(F3), F03010.

Ruessink, B. & Kuriyama, Y. (2008), 'Numerical predictability experiments of cross-shore sandbar migration', *Geophysical Research Letters* **35**(1).

Rusche, H. (2002), Computational fluid dynamics of dispersed two-phase flows at high phase fractions, PhD thesis, Imperial College London (University of London).

Sahin, C., Safak, I., Sheremet, A. & Mehta, A. J. (2012), 'Observations on cohesive bed reworking by waves: Atchafalaya Shelf, Louisiana', *J. Geophys. Res.* **117**(C9).

Sanford, L. P. (2008), 'Modeling a dynamically varying mixed sediment bed with erosion, deposition, bioturbation, consolidation, and armoring', *Comput. Geosci.* **34**(10), 1263–1283.

Sanford, L. P. & Maa, J. P.-Y. (2001), 'A unified erosion formulation for fine sediments', *Mar. Geol.* **179**(1), 9–23.

Savage, S. & Lun, C. (1988), 'Particle size segregation in inclined chute flow of dry cohesionless granular solids', *Journal of Fluid Mechanics* **189**, 311–335.

Schaeffer, D. G. (1987), 'Instability in the evolution equations describing incompressible granular flow', *Journal of Differential Equations* **66**(1), 19–50.

Schaflinger, U., Acrivos, A. & Stibi, H. (1995), 'An experimental study of viscous resuspension in a pressure-driven plane channel flow', *International Journal of Multiphase Flow* **21**(4), 693–704.

Schmeeckle, M. W. (2014), 'Numerical simulation of turbulence and sediment transport of medium sand', *Journal of Geophysical Research: Earth Surface* **119**(6), 1240–1262.

Shields, A. (1936), *Application of similarity principles and turbulence research to bed-load movement*, California Institute of Technology.

Shringarpure, M., Cantero, M. I. & Balachandar, S. (2012), 'Dynamics of complete turbulence suppression in turbidity currents driven by monodisperse suspensions of sediment', *J. Fluid Mech.* **712**, 384–417.

Siegel, D. A. & Domaradzki, J. A. (1994), 'Large-eddy simulation of decaying stably stratified turbulence', *J. Phys. Oceanogr.* **24**(11), 2353–2386.

Simeonov, J. A. & Calantoni, J. (2012), 'Modeling mechanical contact and lubrication in direct numerical simulations of colliding particles', *International Journal of Multiphase Flow* **46**, 38–53.

Sinclair, J. & Jackson, R. (1989), 'Gas-particle flow in a vertical pipe with particle-particle interactions', *AIChE Journal* **35**(9), 1473–1486.

Sleath, J. (1999), 'Conditions for plug formation in oscillatory flow', *Continental Shelf Research* **19**(13), 1643–1664.

Small, C. & Nicholls, R. J. (2003), 'A global analysis of human settlement in coastal zones', *Journal of Coastal Research* pp. 584–599.

Spalart, P. R. & Baldwin, B. S. (1989), Direct simulation of a turbulent oscillating boundary layer, *in* 'Turbulent Shear Flows 6', Springer,Berlin Heidelberg, pp. 417–440.

Srivastava, A. & Sundaresan, S. (2003), 'Analysis of a frictional-kinetic model for gas-particle flow', *Powder technology* **129**(1), 72–85.

Sternberg, R., Cacchione, D., Paulso, B., Kineke, G. & Drakez, D. (1996), 'Observations of sediment transport on the Amazon subaqueous delta', *Cont. Shelf Res.* **16**(5), 697–715.

Stevens, A., Wheatcroft, R. & Wiberg, P. (2007), 'Seabed properties and sediment erodibility along the western Adriatic margin, Italy', *Cont. Shelf Res.* **27**(3-4), 400–416.

Sumer, B. M., Kozakiewicz, A., Fredsoe, J. & Deigaard, R. (1996), 'Velocity and concentration profiles in sheet-flow layer of movable bed', *Journal of Hydraulic Engineering* **122**(10), 549–558.

Sumer, B. M., Sen, M. B., Karagali, I., Ceren, B., Fredsoe, J., Sottile, M., Zilioli, L. & Fuhrman, D. R. (2011), 'Flow and sediment transport induced by a plunging solitary wave', *Journal of Geophysical Research: Oceans* **116**(C1).

Swart, D. (1974), *Offshore sediment transport and equilibrium beach profiles*, W.D. Meinema B.V. Delft Hydraulics Laboratory.

Sweby, P. K. (1984), 'High resolution schemes using flux limiters for hyperbolic conservation laws', *SIAM Journal on Numerical Analysis* **21**(5), 995–1011.

Tardos, G. I. (1997), 'A fluid mechanistic approach to slow, frictional flow of powders', *Powder Technology* **92**(1), 61–74.

Torquato, S., Truskett, T. M. & Debenedetti, P. G. (2000), 'Is random close packing of spheres well defined?', *Phys. Rev. Lett.* **84**(10), 2064–2067.

Traykovski, P., Geyer, W., Irish, J. & Lynch, J. (2000), 'The role of wave-induced density-driven fluid mud flows for cross-shelf transport on the Eel river continental shelf', *Cont. Shelf Res.* **20**(16), 2113–2140. Oceanic Flood Sedimentation.

Traykovski, P., Trowbridge, J. & Kineke, G. (2015), 'Mechanisms of surface wave energy dissipation over a high-concentration sediment suspension', *J. Geophys. Res. Oceans* **120**(3), 1638–1681.

Traykovski, P., Wiberg, P. & Geyer, W. (2007), 'Observations and modeling of wave-supported sediment gravity flows on the Po prodelta and comparison to prior observations from the Eel shelf', *Cont. Shelf Res.* **27**(3-4), 375–399.

Trowbridge, J. & Kineke, G. (1994), 'Structure and dynamics of fluid muds on the Amazon continental shelf', *J. Geophys. Res.* **99**(C1), 865–874.

van Rijn, L. (1984*a*), 'Sediment transport, part I: Bed load transport', *Journal of Hydraulic Engineering* **110**(10), 1431–1456.

van Rijn, L. C. (1984*b*), 'Sediment pick-up functions', *Journal of Hydraulic Engineering* **110**(10), 1494–1502.

Van Wachem, B., Schouten, J., Van den Bleek, C., Krishna, R. & Sinclair, J. (2001), 'Cfd modeling of gas-fluidized beds with a bimodal particle mixture', *AIChE Journal* **47**(6), 1292–1302.

Vanoni, V. A. (1946), 'Transportation of suspended sediment by water', *Transactions of the American Society of Civil Engineers* **111**(1), 67–102.

Vinzon, S. & Mehta, A. (2000), 'Boundary layer effects due to suspended sediment in the amazon river estuary', *Proceedings in Marine Science* **3**, 359–372.

Vreman, B., Geurts, B. & Kuerten, H. (1995), 'A priori tests of large eddy simulation of the compressible plane mixing layer', *Journal of Engineering Mathematics* **29**(4), 299–327.

Wait, R. (2001), 'Discrete element models of particle flows', *Mathematical Modelling and Analysis* **6**(1), 156–164.

Wallace, J. M. (2016), 'Quadrant analysis in turbulence research: History and evolution', *Annual Review of Fluid Mechanics* **48**, 131–158.

Wang, L.-P. & Maxey, M. R. (1993), 'Settling velocity and concentration distribution of heavy particles in homogeneous isotropic turbulence', *J. Fluid Mech.* **256**, 27–68.

Warner, J. C., Sherwood, C. R., Signell, R. P., Harris, C. K. & Arango, H. G. (2008), 'Development of a three-dimensional, regional, coupled wave, current, and sediment-transport model', *Computers & Geosciences* **34**(10), 1284–1306.

Weller, H. (2002), Derivation, modelling and solution of the conditionally averaged two-phase flow equations, Technical report, OpenCFD Ltd.

Wen, C. & Yu, Y. (1966), Mechanics of fluidization, *in* 'Chemical Engineering Progress Symposium Series', Vol. 62, p. 100.

Wheatcroft, R. & Borgeld, J. (2000), 'Oceanic flood deposits on the northern California shelf: large-scale distribution and small-scale physical properties', *Cont. Shelf Res.* **20**(16), 2163–2190.

Wiberg, P. L., Drake, D. E. & Cacchione, D. A. (1994), 'Sediment resuspension and bed armoring during high bottom stress events on the northern California inner continental shelf: measurements and predictions', *Cont. Shelf Res.* **14**(1011), 1191–1219.

Wilson, K. C. (1987), 'Analysis of bed-load motion at high shear stress', *Journal of Hydraulic Engineering* **113**(1), 97–103.

Winterwerp, J. C. (1998), 'A simple model for turbulence induced flocculation of cohesive sediment', *J. Hydraul. Res.* **36**(3), 309–326.

Winterwerp, J. C. (2001), 'Stratification effects by cohesive and noncohesive sediment', *J. Geophys. Res.* **106**(C10), 22559–22574.

Winterwerp, J. C. (2006), 'Stratification effects by fine suspended sediment at low, medium, and very high concentrations', *J. Geophys. Res.* **111**(C5), C05012.

Winterwerp, J. C. (2007), On the sedimentation rate of cohesive sediment, *in* L. S. J.P.Y. Maa & D. Schoellhamer, eds, 'Estuarine and Coastal Fine Sediments Dynamics Intercoh 2003', Vol. Volume 8, Elsevier, pp. 209–226.

Winterwerp, J. C. & Van Kesteren, W. G. (2004), *Introduction to the physics of cohesive sediment dynamics in the marine environment*, Elsevier.

Winterwerp, J. C., van Kesteren, W. G. M., van Prooijen, B. & Jacobs, W. (2012), 'A conceptual framework for shear flow-induced erosion of soft cohesive sediment beds', *J. Geophys. Res.* **117**(C10), C10020.

Wright, L. D., Wiseman, W. J., Bornhold, B. D., Prior, D. B., Suhayda, J. N., Keller, G. H., Yang, Z.-S. & Fan, Y. B. (1988), 'Marine dispersal and deposition of Yellow River silts by gravity-driven underflows', *Nature* **332**(6165), 629–632.

Wright, L. & Friedrichs, C. (2006), 'Gravity-driven sediment transport on continental shelves: A status report', *Cont. Shelf Res.* **26**(17), 2092–2107.

Wright, L. & Nittrouer, C. (1995), 'Dispersal of river sediments in coastal seas: Six contrasting cases', *Estuaries* **18**(3), 494–508.

Wright, S. & Parker, G. (2004), 'Density stratification effects in sand-bed rivers', *Journal of Hydraulic Engineering* **130**(8), 783–795.

Yu, X., Hsu, T.-J. & Balachandar, S. (2013), 'A spectral-like turbulence-resolving scheme for fine sediment transport in the bottom boundary layer', *Comput. Geosci.* **61**(0), 11–22.

Yu, X., Hsu, T.-J. & Hanes, D. M. (2010), 'Sediment transport under wave groups: Relative importance between nonlinear waveshape and nonlinear boundary layer streaming', *Journal of Geophysical Research* **115**(C2).

Yu, X., Hsu, T.-J., Jenkins, J. T. & Liu, P. L.-F. (2012), 'Predictions of vertical sediment flux in oscillatory flows using a two-phase, sheet-flow model', *Advances in Water Resources* **48**(0), 2–17.

Yu, X., Ozdemir, C., Hsu, T. & Balachandar, S. (2014), 'Numerical investigation of turbulence modulation by sediment-induced stratification and enhanced viscosity in oscillatory flows', *J. Waterw. Port, Coast. Ocean Eng.* **140**(2), 160–172.

Zhou, J., Adrian, R. J., Balachandar, S. & Kendall, T. M. (1999), 'Mechanisms for generating coherent packets of hairpin vortices in channel flow', *J. Fluid Mech.* **387**, 353–396.

Zhou, Z., Sangermano, J., Hsu, T.-J. & Ting, F. C. (2014), 'A numerical investigation of wave-breaking-induced turbulent coherent structure under a solitary wave', *Journal of Geophysical Research: Oceans* **119**(10), 6952–6973.

Appendix A

IMPLEMENTATION OF TOP BOUNDARY FOR FINE SEDIMENT

In this appendix, we focus on the implementation of the top boundary condition for sediment concentration[1]. To satisfy the mass conservation at the top boundary, the no-flux boundary condition (Eqn. (3.7)) should be satisfied. Notice that the effective settling velocity may vary with x and y if hindered settling or particle inertia is considered. In the present numerical schemes, Fourier expansions are adopted in both streamwise and spanwise directions. If we transfer Eqn. (3.7) into Fourier space, convolution terms will arise from the nonlinear multiplication term (first term on left-hand-side of Eqn. (3.7)), which is difficult to handle. To resolve this problem, the sediment velocity at the top boundary is decomposed into x-y plane-averaged component $\langle w^s \rangle$ and the fluctuation component $w^{s\prime}$:

$$w^s = \langle w^s \rangle + w^{s\prime}. \tag{A.1}$$

Substituting Eqn. (A.1) into Eqn. (3.7) will result in:

$$\langle w^s \rangle \phi - \frac{1}{Re_\Delta Sc} \frac{\partial \phi}{\partial z}\Big|_{z=L_z} = -w^{s\prime}\phi\Big|_{z=L_z}. \tag{A.2}$$

However, the sediment concentration ϕ on the right-hand-side of the above equation is part of the solution, to make sure that the top boundary has the same accuracy

[1] This appendix originally serves as supplements for chapter 3

in terms of time integration, the right-hand-side term is approximated by using a second-order accurate scheme:

$$\phi^{(n*)} = \left[1 + \frac{c(n)}{c(n-1)}\right]\phi^{(n-1)} - \frac{c(n)}{c(n-1)}\phi^{(n-2)}\Big|_{z=L_z}, \tag{A.3}$$

where n denotes the time steps, and $c = \{dt/6, 5dt/24, dt/8\}$ is the coefficient for the diffusion term in the third-order low-storage Runge-Kutta method with dt being the time-step (Yu et al. 2013). In this study, the time step is chosen based on the Courant-Friedrichs-Lewy (CFL) criterion. $\phi^{(n*)}$ is the approximation of ϕ at the bottom at the n step, and $\phi^{(n-1)}$ and $\phi^{(n-2)}$ are sediment concentration at the previous two time steps $(n-1)$ and $(n-2)$, respectively.

Appendix B

INITIAL CONDITIONS FOR EULERIAN TWO-PHASE FLOW

In almost all the experiment setups for the sediment transport, special attentions should be paid to the initial conditions in order to achieve the replicability and relevance to the natural conditions. Similarly, in the numerical simulations, the initial condition also plays a vital role as sediment transport is a highly non-linear system. In the multi-dimensional numerical simulations, the initial conditions are obtained from the 1DV simulations, where the sediment bed is already established, and the flow is fully developed. In the 1DV simulations, the initial sediment concentration profile is specified by considering a momentum balance in the bed:

$$-\phi\frac{\partial p^f}{\partial z} - \frac{\partial p^{sf}}{\partial z} - \phi\rho^s g = 0, \tag{B.1}$$

where $\partial p^f/\partial z = \rho^f g$ is the hydrostatic fluid pressure initially, and p^{sf} is the frictional normal stress, which is modeled by following Johnson & Jackson (1987). Hence, we obtain

$$\frac{\partial p^{sf}}{\partial z} = F\frac{(\phi-\phi_f)^{n-1}}{(\phi_{max}-\phi)^{m+1}}[(m-n)\phi + n\phi_{max} - m\phi_f]\frac{\partial \phi}{\partial z} = -\phi(\rho^s - \rho^f)g, \tag{B.2}$$

The coefficient F,m, n, ϕ_f and ϕ_{max} are determined to give a stable bed, as discussed in chapter 5. It is evident that $m > n$ should be satisfied to ensure the sediment concentration in the bed increases with the depth. A numerical solution can be obtained for the sediment concentration in the bed, which is detailed in appendix C. However, in the limit of $\phi = \phi_f$, the sediment concentration gradient goes to infinity (see appendix C), which may be numerically problematic. Thus, it is often practical to specify a

smooth sediment concentration profile to ensure numerical stability. It is found that the following profile can provide a relatively smooth transition from ϕ_{m0} at the bed to ϕ_0 in the upper column as initial condition:

$$\phi = \phi_0 + \frac{\phi_{m0} - \phi_0}{2}[1 + tanh[A(z_b - z)]] \tag{B.3}$$

It is also found that it is practical to relax the system by setting the ϕ_{m0} to be lower than the criteria for the enduring contact, as the frictional stress increases dramatically as a function of sediment concentration above the criteria. Initially, the sediment concentration in the bed will increase due to the immersed weight, and the frictional stress will increase accordingly. Eventually the frictional pressure gradient in the bed can well balance the immersed weight of the bed.

For the fluid and sediment velocities, we assume that they are identical initially. For the steady flow, the velocity development can take a long time, and an initial rough wall log-law velocity profile is assumed:

$$\frac{u}{u_*} = \frac{1}{\kappa} ln\Big(\frac{30z}{K_s}\Big), \tag{B.4}$$

where u_* is the bottom frictional velocity, $\kappa = 0.41$ is the von Karman constant, and $K_s = 2.5d$ is the bed roughness with d being the grain size.

For the oscillatory flow, it is critical to match the velocity phase with the driving force (pressure gradient force), which may be nontrival for high-order Stokes waves, for example, 2nd-order Stokes wave:

$$U_0(t) = U_1 \sin(\omega t + \sigma_0) - U_2 \cos(2\omega t + 2\sigma_0), \tag{B.5}$$

where U_1 and U_2 are velocity amplitudes for each harmonic, $\omega = 2\pi/T$ is the oscillatory frequency, T is the oscillatory period and σ_0 is the a phase lag, which is chosen such that the free-stream velocity is zero at $t = 0$, i.e., σ_0 is the solution of $U_1 sin(\sigma_0) = U_2 cos(2\sigma_0)$, which depends on the flow asymmetry.

Appendix C

SOLUTION FOR SEDIMENT CONCENTRATION IN THE BED

In this appendix, the goal is to determine an analytical solution for the sediment concentration for in the bed as an initial condition for the Eulerian two-phase model, where the frictional normal stress balances the immersed weight of the sediment,

$$\frac{\partial p^{sf}}{\partial z} = F\frac{(\phi-\phi_f)^{n-1}}{(\phi_{max}-\phi)^{m+1}}[(m-n)\phi + n\phi_{max} - m\phi_f]\frac{\partial \phi}{\partial z} = -\phi(\rho^s - \rho^f)g. \tag{C.1}$$

The coefficient F,m, n, ϕ_f and ϕ_{max} are determined to give a stable bed, as discussed in chapter 5. The sediment concentration is the solution of the following partial differential equation:

$$\frac{\partial \phi}{\partial z} = -\frac{(\rho^s - \rho^f)g}{F}\phi\frac{(\phi_{max}-\phi)^{m+1}}{(\phi-\phi_f)^{n-1}[(m-n)\phi + n\phi_{max} - m\phi_f]} \tag{C.2}$$

The analytical solution for the sediment concentration from the above differential equation is difficult to solve. However, the sediment concentration can be solved numerically, and it is the solution of the equation $G(\phi) = f(\phi) - \partial\phi/\partial z = 0$, where $f(\phi) = -(\rho^s - \rho^f)g/F\phi(\phi_{max}-\phi)^{m+1}/(\phi-\phi_f)^{n-1}[(m-n)\phi + n\phi_{max} - m\phi_f]$. Here we sought for a solution at vertical uniform grids, where the grid size is dz, and $z_{i+1} = z_i - dz$, and the concentration gradient can be approximated using a central difference scheme, that is, the sediment concentration gradient at $(z_{i+1} + z_i)/2$ can be approximated as $\partial\phi/\partial z|_{i+1/2} = (\phi_i - \phi_{i+1})/dz$, thus the sediment concentration at $(i+1)$-th vertical grid is the solution of the equation,

$$G(\phi) = f(\frac{\phi + \phi^i}{2}) - \frac{\phi^i - \phi}{dz} \tag{C.3}$$

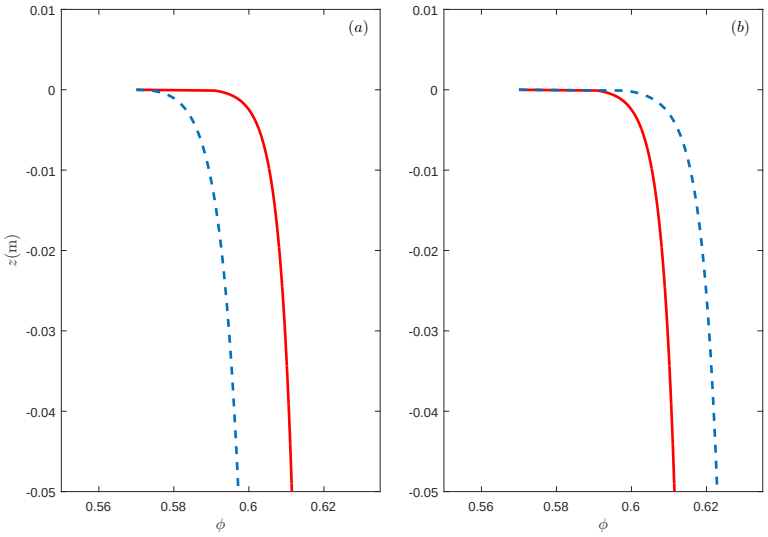

Figure C.1: (a) Sediment concentration profiles with $n = 2$ (dashed curve) and $m = 3$ (solid curve) in the frictional stress model (see equation C.1), $m = 5$, $\phi_{max} = 0.635$, and $\phi = 0.57$; (b) Sediment concentration profiles with $\phi_{max} = 0.635$ (solid curve) and $\phi_{max} = 0.65$ (dashed curve) in the frictional stress model (see equation C.1), $m = 5$, $n = 3$, and $\phi_f = 0.57$

Given the value of ϕ^i at z_i, the solution of ϕ^{i+1} can be obtained by a Newton-Raphson method, and the $(j+1)$-th attempt can be approximated by

$$\phi^*_{j+1} = \phi^*_j - \frac{G(\phi^*_j)}{G'(\phi^*_j)}, \tag{C.4}$$

where, $G'(\phi^*_j)$ is the derivative of $G(\phi)$ in terms of ϕ at $\phi = \phi^*_j$,

$$\begin{aligned} G'(\phi^*_j) \;=\; & \frac{1}{dz} - \frac{(\rho^s - \rho^f)g}{2F} \frac{(\phi_{max} - (\phi^*_j + \phi^i)/2)^m}{[(\phi^*_j + \phi^i)/2 - \phi_f]^n [(m+n)(\phi^*_j + \phi^i)/2 + n\phi_{max} - m\phi_f]} \\ & [(m-n)(n-m-3)[(\phi^*_j + \phi^i)/2]^3 + [(2n^2 - 2mn - 5n + 2m)\phi_{max} \\ & +(2m^2 - 2mn - 2n + 5m)\phi_f][(\phi^*_j + \phi^i)/2]^2 + (m-n)[n(2-n)\phi^2_{max} \\ & +(2mn - 2m + 2n - 1)\phi_{max}\phi_f - m(m+2)\phi^2_f](\phi^*_j + \phi^i)/2 \\ & -(n\phi_{max} - m\phi_f)\phi_{max}\phi_f], \end{aligned} \tag{C.5}$$

To demonstrate the sensitivity of the coefficient m and n, we assume that

$\phi_0 = 0.57$ at $z = 0$, and we choose $dz = 0.0001$ m, and consider the sediment bed thickness $z_b = 0.05$ m, which is typical in experiment condition. The resulting sediment concentration from $z = -0.05 \sim 0$ m resulting from $n = 2$ (dashed curve) and $n = 3$ (solid curve) are compared in figure C.1(a). It is evident that, both $n = 3$ and $n = 2$ gives a very minor concentration gradient within the bed. However, with typical values of ϕ_f and ϕ_{max}, the bed concentration is highly dependent on the n values, we found that $n = 3$ yields a slightly larger sediment concentration in the bed, which is closer to measured data (e.g., O'Donoghue & Wright 2004). Meanwhile, we noticed that it is possible to change the sediment concentration in the bed by tuning ϕ_{max}, which is the maximum allowed sediment concentration. The physical interpretation of ϕ_{max} can be relaxed to achieve a desired bed concentration. As illustrated in figure C.1(b), changing ϕ_{max} from 0.635 to 0.65, the bed sediment concentration will also be increased accordingly, and it is worth-mentioning that the bed concentration is much smaller than ϕ_{max}. The analysis in this appendix can be used for the initial condition of numerical simulations with a stable initial sediment bed.

Appendix D

COPYRIGHT PERMISSION LETTERS

D.1 Copyright 1

The figure 1.1 is adopted, with permission, from the article:

Yu, X., Hsu, T.-J., Jenkins, J. T. & Liu, P. L.-F. (2012), 'Predictions of vertical sediment flux in oscillatory flows using a two-phase, sheet-flow model', Advances in Water Resources 48(0), 2-17.

The image of the permission letter from Advances in Water Resources (Elsevier) is shown in figure D.1:

D.2 Copyright 2

The figure 1.2 is adopted, with permission, from the article:

Yu, X., Ozdemir, C., Hsu, T. & Balachandar, S. (2014), 'Numerical investigation of turbulence modulation by sediment-induced stratification and enhanced viscosity in oscillatory flows', Journal of Waterway. Port, Coastal and Ocean Engineering. 140(2), 160-172.

The communication from the American Society of Civil Engineers (ASCE) states that permission is granted for the reuse of this figure from Numerical investigation of turbulence modulation by sediment-induced stratification and enhanced viscosity in oscillatory flows in the thesis, and the image of the permission letter is shown in figure D.2:

D.3 Copyright 3

The abstract (in part), Chapter 1 (in part) and Chapter 2 are reproduced or modified, with permission, from the article:

Cheng, Z., Yu, X., Hsu, T.-J., Ozdemir, C. E. & Balachandar, S. (2015a), 'On the transport modes of fine sediment in the wave boundary layer due to resuspension/deposition: A turbulence-resolving numerical investigation', J. Geophys. Res. Oceans 120(3), 1918-1936.

The image of the permission letter from the Journal of Geophysical Research (John Wiley and Sons) are shown in figure D.3:

D.4 Copyright 4

The abstract (in part), Chapter 1 (in part) and Chapter 3 are reproduced or modified, with permission, from the article:

Cheng, Z., Yu, X., Hsu, T.-J. & Balachandar, S. (2015b), 'A numerical investigation of fine sediment resuspension in the wave boundary layer—uncertainties in particle inertia and hindered settling', Computers & Geosciences 83, 176192.

The image of the permission letter from Computers & Geosciences (Elsevier) are shown in figure D.4:

ELSEVIER LICENSE
TERMS AND CONDITIONS

Jul 05, 2016

This Agreement between Zhen Cheng ("You") and Elsevier ("Elsevier") consists of your license details and the terms and conditions provided by Elsevier and Copyright Clearance Center.

License Number	3902781204378
License date	Jul 05, 2016
Licensed Content Publisher	Elsevier
Licensed Content Publication	Advances in Water Resources
Licensed Content Title	Predictions of vertical sediment flux in oscillatory flows using a two-phase, sheet-flow model
Licensed Content Author	Xiao Yu,Tian-Jian Hsu,James T. Jenkins,Philip L.-F. Liu
Licensed Content Date	November 2012
Licensed Content Volume Number	48
Licensed Content Issue Number	n/a
Licensed Content Pages	16
Start Page	2
End Page	17
Type of Use	reuse in a thesis/dissertation
Portion	figures/tables/illustrations
Number of figures/tables/illustrations	1
Format	both print and electronic
Are you the author of this Elsevier article?	No
Will you be translating?	No
Order reference number	
Original figure numbers	figure 1
Title of your thesis/dissertation	A MULTI-DIMENSIONAL TWO-PHASE FLOW MODELING FRAMEWORK FOR SEDIMENT TRANSPORT APPLICATIONS
Expected completion date	Aug 2016
Estimated size (number of pages)	256
Elsevier VAT number	GB 494 6272 12
Requestor Location	Zhen Cheng 515 Wharton Dr. NEWARK, DE 19711 United States Attn: Zhen Cheng

Figure D.1: Permission letter from Advances in Water Resources (Elsevier) for the reuse of figure 1 in the article by Yu et al. (2012)

Zhen Cheng <zcheng@udel.edu>

Copyright permission request for Figure in ASCE articles

Fogleson, Joann <jfogleson@asce.org> Mon, Jul 18, 2016 at 9:50 AM
To: Zhen Cheng <zcheng@udel.edu>

Dear Zhen Cheng:

Permission is granted for you to reuse one figure from “Numerical investigation of turbulence modulation by sediment-induced stratication and enhanced viscosity in oscillatory flows” for you thesis.

A full credit line must be added to the material being reprinted. For reuse in non-ASCE publications, add the words "With permission from ASCE" to your source citation. For Intranet posting, add the following additional notice: "This material may be downloaded for personal use only. Any other use requires prior permission of the American Society of Civil Engineers.”

Regards,

Joann

Joann Fogleson

Manager, Product and Subscription Services

American Society of Civil Engineers

1801 Alexander Bell Drive

Reston, VA 20191

PERMISSIONS@asce.org

703-295-6112

E-mail: jfogleson@asce.org

Internet: www.asce.org/pubs | www.ascelibrary.org | http://ascelibrary.org/page/rightsrequests

A full credit line must be added to the material being reprinted. For reuse in non-ASCE publications, add the words "With permission from ASCE" to your source citation. For Intranet posting, add the following additional notice: "This material may be downloaded for personal use only. Any other use

Figure D.2: Permission letter from ASCE for the reuse of figure 1 in the article by Yu et al. (2014)

JOHN WILEY AND SONS LICENSE TERMS AND CONDITIONS

Jul 05, 2016

This Agreement between Zhen Cheng ("You") and John Wiley and Sons ("John Wiley and Sons") consists of your license details and the terms and conditions provided by John Wiley and Sons and Copyright Clearance Center.

License Number	3902761228280
License date	Jul 05, 2016
Licensed Content Publisher	John Wiley and Sons
Licensed Content Publication	Journal of Geophysical Research: Oceans
Licensed Content Title	On the transport modes of fine sediment in the wave boundary layer due to resuspension/deposition: A turbulence-resolving numerical investigation
Licensed Content Author	Zhen Cheng,Xiao Yu,Tian-Jian Hsu,Celalettin E. Ozdemir,S. Balachandar
Licensed Content Date	Mar 26, 2015
Licensed Content Pages	19
Type of use	Dissertation/Thesis
Requestor type	Author of this Wiley article
Format	Print and electronic
Portion	Full article
Will you be translating?	No
Title of your thesis / dissertation	A MULTI-DIMENSIONAL TWO-PHASE FLOW MODELING FRAMEWORK FOR SEDIMENT TRANSPORT APPLICATIONS
Expected completion date	Aug 2016
Expected size (number of pages)	256
Requestor Location	Zhen Cheng 515 Wharton Dr. NEWARK, DE 19711 United States Attn: Zhen Cheng
Publisher Tax ID	EU826007151
Billing Type	Invoice
Billing Address	Zhen Cheng 515 Wharton Dr. NEWARK, DE 19711 United States Attn: Zhen Cheng
Total	0.00 USD
Terms and Conditions	

Figure D.3: Permission letter from the Journal of Geophysical Research (John Wiley and Sons) for the reuse of the article by Cheng et al. (2015a)

ELSEVIER LICENSE
TERMS AND CONDITIONS

Jul 05, 2016

This Agreement between Zhen Cheng ("You") and Elsevier ("Elsevier") consists of your license details and the terms and conditions provided by Elsevier and Copyright Clearance Center.

License Number	3902770487348
License date	Jul 05, 2016
Licensed Content Publisher	Elsevier
Licensed Content Publication	Computers & Geosciences
Licensed Content Title	A numerical investigation of fine sediment resuspension in the wave boundary layer—Uncertainties in particle inertia and hindered settling
Licensed Content Author	Zhen Cheng,Xiao Yu,Tian-Jian Hsu,S. Balachandar
Licensed Content Date	October 2015
Licensed Content Volume Number	83
Licensed Content Issue Number	n/a
Licensed Content Pages	17
Start Page	176
End Page	192
Type of Use	reuse in a thesis/dissertation
Intended publisher of new work	other
Portion	full article
Format	both print and electronic
Are you the author of this Elsevier article?	Yes
Will you be translating?	No
Order reference number	
Title of your thesis/dissertation	A MULTI-DIMENSIONAL TWO-PHASE FLOW MODELING FRAMEWORK FOR SEDIMENT TRANSPORT APPLICATIONS
Expected completion date	Aug 2016
Estimated size (number of pages)	256
Elsevier VAT number	GB 494 6272 12
Requestor Location	Zhen Cheng 515 Wharton Dr. NEWARK, DE 19711 United States Attn: Zhen Cheng
Total	0.00 USD

Figure D.4: Permission letter from Computers & Geosciences (Elsevier) for the reuse of the article by Cheng et al. (2015b)